Title
Safety and core design of large liquid-metal cooled fast breeder reactors

Author
Qvist, Staffan Alexander

Publication Date
2013

Peer reviewed|Thesis/dissertation

Safety and core design of large liquid-metal cooled fast breeder reactors

by

Staffan Alexander Qvist

A dissertation submitted in partial satisfaction of the
requirements for the degree of
Doctor of Philosophy

in

Engineering - Nuclear Engineering

in the

Graduate Division

of the

University of California, Berkeley

Committee in charge:

Professor Ehud Greenspan, Chair
Professor Per Peterson
Professor Thomas Devine
Associate Professor Peter Hosemann

Spring 2013

Safety and core design of large liquid-metal cooled fast breeder reactors

Abstract

Safety and core design of large liquid-metal cooled fast breeder reactors

by

Staffan Alexander Qvist

Doctor of Philosophy in Engineering - Nuclear Engineering

University of California, Berkeley

Professor Ehud Greenspan, Chair

In light of the scientific evidence for changes in the climate caused by greenhouse-gas emissions from human activities, the world is in ever more desperate need of new, inexhaustible, safe and clean primary energy sources. A viable solution to this problem is the widespread adoption of nuclear breeder reactor technology. Innovative breeder reactor concepts using liquid-metal coolants such as sodium or lead will be able to utilize the waste produced by the current light water reactor fuel cycle to power the entire world for several centuries to come.

Breed & burn (B&B) type fast reactor cores can unlock the energy potential of readily available fertile material such as depleted uranium without the need for chemical reprocessing. Using B&B technology, nuclear waste generation, uranium mining needs and proliferation concerns can be greatly reduced, and after a transitional period, enrichment facilities may no longer be needed.

In this dissertation, new passively operating safety systems for fast reactors cores are presented. New analysis and optimization methods for B&B core design have been developed, along with a comprehensive computer code that couples neutronics, thermal-hydraulics and structural mechanics and enables a completely automated and optimized fast reactor core design process. In addition, an experiment that expands the knowledge-base of corrosion issues of lead-based coolants in nuclear reactors was designed and built.

The motivation behind the work presented in this thesis is to help facilitate the widespread adoption of *safe* and *efficient* fast reactor technology.

To my family

Contents

List of Figures

List of Tables

Specific contributions and highlights

- Two completely new systems for inherent fast reactor safety (the *ARC* systems) are introduced in Chapter 6. The ARC-systems operate passively based only on natural laws and have no moving mechanical parts. In the event of a temperature excursion, the systems inject a neutron poison (^{6}Li) in to the core and quickly shuts off the neutron chain reaction. As the analysis of Chapters 5 and 6 of this dissertation shows, such systems are necessary to enable the safe and efficient operation of breed & burn type cores. While they are a necessity in breed and burn systems, ARC-systems can be used to improve the safety and economics of any type of fast reactor core.

- A comprehensive new computer code for the automated design of optimized fast reactor cores (ADOPT) was developed and is introduced in Chapter 7. With ADOPT, the entire fast reactor core design process is automated and optimized. Any combination of single-phase coolant, fuel and structural material can be used as input. The code can either define or reverse-engineer an optimal core geometry down to individual fuel pins based on user-defined constraints (max. temperature, pressure drop, etc.) and a limited amount of user-defined general core parameters (power, overall size etc.).

- The *extended neutron balance* method (ENB) for breed & burn reactor core analysis is introduced in Section 2.6. The ENB method is a powerful new way of estimating the impact of design variables on the performance of breed and burn systems.

- The optimum shape, geometry and performance limits of liquid metal cooled breed & burn type core design are defined in Section 7.6.

- New correlations for the elastic modulus and density of the U-Zr fuel alloy were developed and are presented in Sections 4.3.6 and 7.4.3 respectively.

- A new methodology for the calculation of fuel axial expansion reactivity of metallic fuel is introduced in Section 4.3 and further analyzed in Sections 4.8.2 and 4.8.8.

- The design and function of the ICE-II experiment, a unique experimental station enabling the study of irradiation effects on corrosion protection of steel subjected to liquid metals, is introduced in Chapter 8.

Acknowledgments

Firstly, I would like to thank Professor Ehud Greenspan, for being my advisor, mentor and friend. By believing in and supporting me, Ehud made this possible.

Thanks to Professor Peter Hosemann, for being both a mentor and a friend.

Thanks to Professor Janne Wallenius of KTH, for inspiring me to pursue a nuclear engineering degree and for his undying optimism and energy.

Thanks to my colleagues and friends in the UC Berkeley neutronics group. For helping and supporting me in my work and making my stay at Berkeley a fantastic time in my life.

Thanks to my friends back home in Sweden, for caring, visiting and supporting me throughout my time in the US..

This work was supported by the US Department of Energy Nuclear Energy University Programs (NEUP) and by TerraPower LLC.

Chapter 1

Introduction and motivation

In light of the scientific evidence for changes in the climate caused by greenhouse-gas emissions from human activities, the world is in ever more desperate need of new, inexhaustible, safe and *clean* primary energy sources. A viable solution to this problem is the widespread adoption of nuclear breeder reactor technology. Innovative breeder reactor concepts using liquid-metal coolants such as sodium or lead will be able to utilize the waste produced by the current light water reactor fuel cycle to meet global energy demand for several centuries to come.

World energy and electricity demand are expected to rise steeply over the coming decades, as population numbers soar and nations such as China and India continue to expand their economies and raise their populations out of poverty. By 2035, global primary energy demand is expected to have risen by 40% and electricity consumption by 67% compared to today (2012). Following the reference scenario of the US Energy Information Administration (**EIA**), greenhouse-gas (**GHG**) emitting fossil fuels such as coal, oil and gas will continue to provide around 80% of the primary energy [1]. The projected world primary energy supply is shown in Figure 1.1. For a sustainable future, a majority of the world energy supply will need to be replaced by clean new energy sources such as new nuclear and renewables, as existing fossil plants and older nuclear plants are phased out. Around 40% of world energy is supplied by the burning of coal. Apart from being a major contributor to global warming by GHG-emissions, coal power plant emissions such as sulfur dioxide (SO_2) and nitrogen oxides (NO_x) take a significant toll on the health and longevity of millions of people around the world. In the US, fine particle pollution from coal power plants is estimated to cause 13200 premature deaths, 9700 additional hospitalizations and more than 20000 heart attacks annually [2]. In Europe, coal power plant emissions cause an estimated 18200 premature deaths each year [3]. In China, the World Health Organisation (**WHO**) estimates up to 600000 premature deaths annually due to coal plant emissions [4]. Summed globally, the death toll from coal pollution may be as high as one million people per year. In addition to this, there are estimates of up to 250000 deaths in coal mining accidents in China alone in the period 1949-2007 [5]. To meet new energy demand and the retirement of older plants, as of January

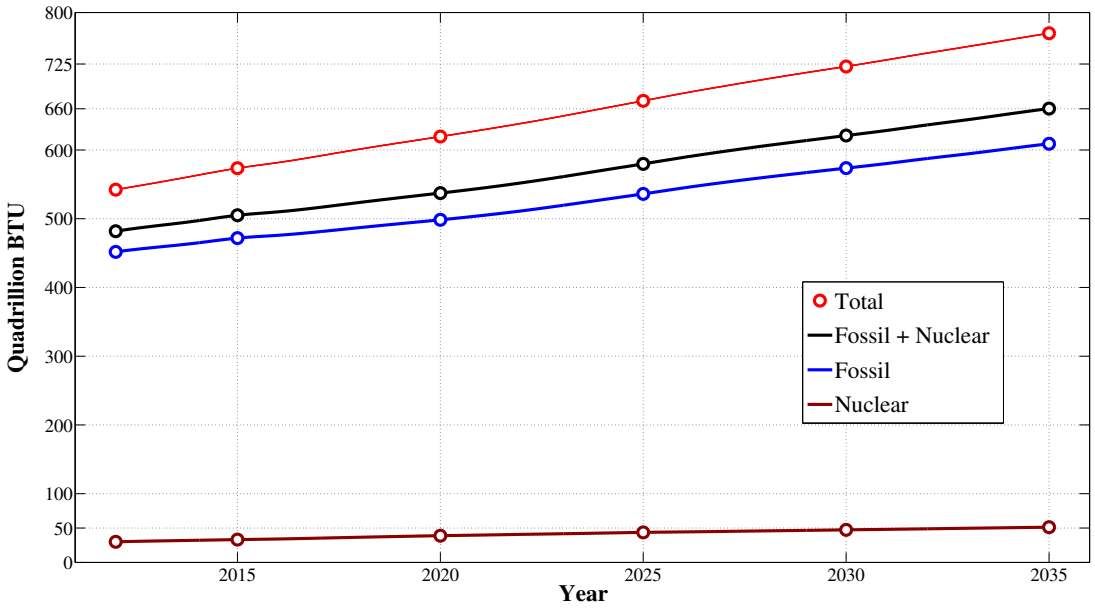

Figure 1.1: World energy production projection [1]

2012, there are 48 new coal plants either planned or under construction in the US, while China is adding about one major new coal plant to the electricity grid every week [6].

A very aggressive push toward renewable energy sources such as wind and solar can help to reduce the fraction of fossil energy sources such as coal from the global energy mix. However, the low power density (and corresponding massive land use), high cost and intermittent nature of these sources mean they will at most play a minor role in global energy supply over the coming century. Hydropower is and will likely remain the major clean renewable energy source.[1] There is, however, very limited room for future growth for hydropower, as most suitable locations in the developed world have already been utilized.

Light water nuclear reactor technology (**LWR**) is a steady source of reliable and GHG-free electricity, currently providing about 15% of world electricity and 6% of the worlds primary energy [1]. Replacing the fossil fuel energy production with clean production sources, an ever more urgent necessity, requires a large expansion of nuclear power production. If conventional LWR nuclear power is to provide a major fraction of world energy, the current resources of economically recoverable uranium is a seriously limiting factor. While utilizing thorium as a fuel form and mining the oceans for uranium can provide LWR fuel for cen-

[1]The burning of biomass constitutes about 65% of *renewable* energy, but emits massive amounts of air pollution in much the same way as fossil energy sources, it can thus not be labelled *clean*.

turies, other characteristics of the LWR fuel cycle make it an unattractive option. LWRs require fuel that is enriched in fissile isotopes and typically reach a uranium utilization[2] of a mere 0.6% [7]. The corresponding volume of waste and need for enrichment facilities will be very large. In stark contrast, integrated fast reactor fuel cycles such as the one developed in the Integral Fast Reactor (**IFR**) project in the US and commercialized by General Electric as the S-PRISM plant can achieve nearly 100% uranium utilization, but requires fuel reprocessing.

Breed and burn (B&B) reactors operating on a once-through fuel cycle (without reprocessing) can reach a uranium utilization of ∼20%, more than 30 times higher than what is achievable with LWR technology. Using proliferation-resistant limited-separations fuel processing, the utilization could be raised above 50%. Total fuel cycle waste generation can be reduced and after a transitional period, uranium enrichment facilities may no longer be needed. In addition, there is little need for uranium mining, since these reactors will use the ample waste already generated in the current LWR fuel cycle as fuel.

B&B technology offers a path forward to an emissions-free, proliferation resistant global energy supply with maximized resource utilization. The B&B fuel cycle can achieve this without the need for fuel reprocessing involving the extraction or separation of actinides from most of the solid fission products. The motivation behind the work presented in this thesis is to help facilitate the much needed widespread adoption of novel and safe fast reactor technology.

[2]Uranium utilization is defined as ratio of heavy metal mass fissioned to total uranium mass used for making fuel.

Part I

Fast reactor physics and safety

Chapter 2

Breed-and-burn reactor physics

2.1 Introduction

2.1.1 Definition and physical principle

Breed-and-burn reactors (B&B) are designed to produce (breed) and burn (fission) plutonium & minor actinides without chemical separation in the fuel cycle. B&B cores require fissile fuel, typically enriched uranium or transuranics from spent light water reactor (LWR) fuel, to establish initial criticality. After a transition period, the equlibrium cycle of a B&B reactor can be fed solely by fertile fuel such as depleted uranium (DU). All reactors fueled with some amount of fertile material will produce and fission fissile isotopes from the fertile material. In this broad sense, all reactor concepts, including conventional LWRs, do breed & burn. To clearly distinguish the type of reactors that is referred to when talking about B&B reactors, the following can be used as a full definition:

> "A reactor system that breeds and burns fissile material without chemical separation in the fuel cycle, where external supply of fissile fuel is only required for establishing initial criticality; after reaching an equilibrium state a B&B system can maintain criticality indefinitely when fed only by fertile material such as depleted uranium."

This effectively means that the majority of the energy output of B&B systems comes from a combination of the fission of fertile isotopes and fissile isotopes bred in from the fertile isotopes of the feed fuel. This definition encompasses all concepts that have been defined as B&B systems in the past, while it excludes similar systems such as conventional fast breeder reactors (FBR). The general idea of a breed-and-burn reactor, consistent with the definition given above, was proposed as early as 1958 by S. Feinberg and E.P. Kunegin, published in a discussion comment in the Proceedings of the International Conference on the Peaceful Uses for Atomic Energy at the United Nations in Geneva [8]. The physical principle of a B&B system is that it is possible to ignite a self-sustaining wave of breeding & burning through fertile "feed" material using an enriched volume of "starter" (or "seed") fuel. After a transition period, the importance of the starter fuel diminishes and the core reaches a self-sustaining equilibrium condition where the core remains in a critical state without the need for additional added fissile material. This is possible because excess neutrons produced in fission reactions in the starter fuel leak out in to the feed (fertile) material where they are absorbed causing either nuclear transmutation or another fission reaction. After capturing a neutron, the fertile fuel undergoes a nuclear transmutation chain that results in the creation of a fissile isotope, according to eq. 2.1 and eq. 2.2 for uranium and thorium based systems respectively.

$$^{238}\mathrm{U}\,(n,\gamma)\,^{239}\mathrm{U} \xrightarrow[23.5m]{\beta^-} {}^{239}\mathrm{Np} \xrightarrow[23.5m]{\beta^-} {}^{239}\mathrm{Pu} \tag{2.1}$$

$$^{232}\mathrm{Th}\,(n,\gamma)\,^{233}\mathrm{Th} \xrightarrow[21.8m]{\beta^-} {}^{233}\mathrm{Pa} \xrightarrow[27d]{\beta^-} {}^{233}\mathrm{U} \tag{2.2}$$

As the fraction of fissile isotopes build in the feed fuel, the probability of fission increases. Eventually, the initially fertile fuel becomes a net producer of neutrons primarily due to fissions in the bred fissile isotopes (with a significant contribution by fertile isotope fission). The excess neutrons leaking out of this region after this point are effectively propagating a continuous "burning wave" through the fertile fuel region. This unique mode of operation allows B&B-type reactors to unlock the vast energy potential of natural or depleted uranium (and potentially thorium) without the use of chemical separation processes in the fuel cycle (see the following section for a comparison with breeder reactors). Many different avenues of engineering implementation have been explored over the past 55 years, but B&B reactors come in just 2 basic varieties; Standing-wave reactors (SWR) or Traveling-wave reactors (TWR). The difference is in the way the burning wave propagates through the fuel. In the TWR, the breeding/burning wave moves through the fuel that is static, in the SWR, fuel is shuffled in and out of the burning zone, thus effectively making it stationary. The details of these concepts are explored in the following sections.

2.1.1.1 B&Bs vs. Conventional Fast Breeder Reactors

In the broadest of sense, all B&B reactors could also be said to belong to the family of fast breeder reactors, defined as fast reactors with a conversion ratio greater than unity. In practice, realistic B&B cores also tend to be similar to conventional large FBR designs. There are however very important design differences that enable the completely distinct fuel cycle concept employed in B&Bs. In a conventional fast breeder reactor (FBR), the core is driven by a "seed" region of fuel assemblies loaded with ∼10-30% of fissile material (^{235}U or TRU). Specialized "blanket" assemblies, consisting of fertile material (^{238}U or ^{232}Th) are located either at the radial periphery (heterogeneous design) or interspersed (homogeneous design) in the core. As the blankets absorb neutrons leaking out of the seed fuel, fissile isotopes are created through nuclear transmutation (breeding), as explained in the previous section. These principles are common for both B&Bs and FBRs. The assemblies of a conventional FBR are periodically taken out of the core and are chemically reprocessed, separating plutonium and higher actinides from uranium and fission products. The separated fissile material bred in the blanket assemblies is then used to create new seed assemblies. In such a way, FBRs can in principle fission 100% of the initial uranium, while loading the core with seed fuel of high fissile content. Because FBRs can be loaded with a varying fraction of fissile isotopes in the fuel, the neutron economy requirements are not that strict.

More recently, fast breeder core designs such as the Encapsulated Nuclear Heat Source (ENHS) [9] have been developed for long life operation without the use of blankets. ENHS-type cores can operate without refuelling for over 20-years with essentially no change in core fissile content and no burnup reactivity swing. The ENHS core has excellent safety and profileration resistance, but the uranium utilization of such cores when operating on a once-through fuel cycle offers only modest improvements compared to the LWR fuel cycle.

While an FBR typically has a neutron leakage probability of ∼15-25%, a B&B mode of operation can in general not be sustained with a leakage above ∼10% (explained and quantified in Section 2.6). The FBR core is made up of two distinct types of fuel assemblies, seed & blanket, where the blanket type assemblies produce little power and have a very high fuel volume fraction. In an SWR B&B core, all assemblies need to be identical, as each individual assembly will fill both the function of blanket and seed fuel at some point during its time in the core. The burning wave will either pass through the assembly (TWR) or the assembly will pass through the burning wave (SWR). The stringent requirements on the B&B neutron economy lead to large low-leakage designs with a single uniform fuel assembly design with a maximized fuel volume fraction. This distinguishes the B&B designs from conventional FBRs. A notable degradation of the passive reactivity safety performance is seen as the nominal neutron leakage probability is reduced. It is finding solutions to this issue that prompted much of the work presented in this thesis. The major advantage of the B&B system over a conventional FBR is that it does not require the economically and politically expensive step of chemical reprocessing of used fuel. Since additional B&B reactors may be able to be fueled by discharged fuel from previous B&B reactors that undergoes limited reconditioning, there is no need for enrichment facilities apart from providing seed-fuel in the initial phasing-in of B&B technology. As the preferred feed-fuel is readily available depleted uranium, there is no further need for uranium mining. B&B technology thus eliminates both enrichment, reprocessing and mining out of the nuclear fuel cycle, substantially reducing environmental and proliferation concerns, while enabling a highly effective use of uranium (or thorium) resources.

2.2 Breed-and-burn reactor concepts

2.2.1 Standing and Traveling wave reactors (SWR & TWR)

In a *traveling wave reactor* (TWR) reactor, a small fissile fuel region provides the ignition for a nuclear fission deflagration wave that propagates through a region of fertile fuel material once ignited. Properly configured, a small enriched fuel-region axially adjacent to a large fertile fuel region can initiate a self-propagating wave of breeding and burning that moves at a very slow and constant velocity through the fertile fuel. Theoretically, such a concept would, once the impact of the initial fissile region diminishes, reach and maintain a steady state until the burning wave reaches the end of the fertile-fuel region. In principle, such a core maintain constant core parameters (reactivity, flux shape etc.) during an essentially arbitrarily long fuel cycle, only limited by the length of the fertile fuel region. The problem with such a design is that a large fraction of the neutrons are inevitably lost in the wake of the wave, and less neutrons are available to help to propagate the wave forward. The resulting requirements for average and peak discharge burnup and fast fluence are far beyond what any structural material, such as a cladding or duct steel, can tolerate. A nuclear fission deflagration wave can be made to propagate through a fast reactor core with a high

fuel volume fraction at an average burnup level of ∼40% FIMA [10]. The peak damage to structural materials in such a core could approach 1000 dpa. Periodic replacement of steel components in the active core and continuous venting of fission gases have been proposed as methods to handle this situation. However, this would require periodic shutdown for extended periods of time and the feasibility and economic viability of periodically replacing for example the fuel rod cladding remains to be proven. It appears that a standing wave type reactor is a superior alternative if periodic outages and fuel handling is unavoidable.

In a standing wave reactor (SWR), a nuclear burning wave is ignited and is then kept going by feeding fertile material in to the wave and extracting burnt fuel out of the wave. The relative motion of the nuclear burning wave and the fertile fuel remains the same as in the TWR concept, but the wave is stationary and the fuel is moving. In a standing wave reactor, the fertile fuel blanket surrounds an inner burning region radially, and neutrons that leak out from the inner region have a high probability of transmuting material in the fertile blanket to fissile isotopes. In a TWR, only neutrons that leak in the forward direction of the burning wave contribute to propagating the wave. Radially and backwards leaking neutrons are essentially lost. Consequently, SWRs make much more efficient use of the neutrons leaking out of the burning region, and require only about half the fluence/burnup/dpa of a TWR to "propagate" the wave [11].

The history of major breed and burn research projects have been summarized in Figure 2.2. The legend explaining Fig. 2.2 is given in Figure 2.1. While this figure may not capture all B&B research efforts that have been carried out during the last 55 years, it is the result of an extensive review of published scientific literature on the subject.

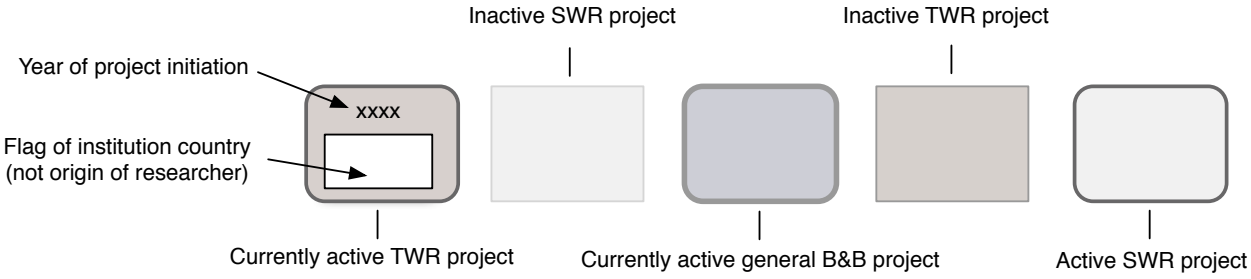

Figure 2.1: The legend to Figure 2.2.

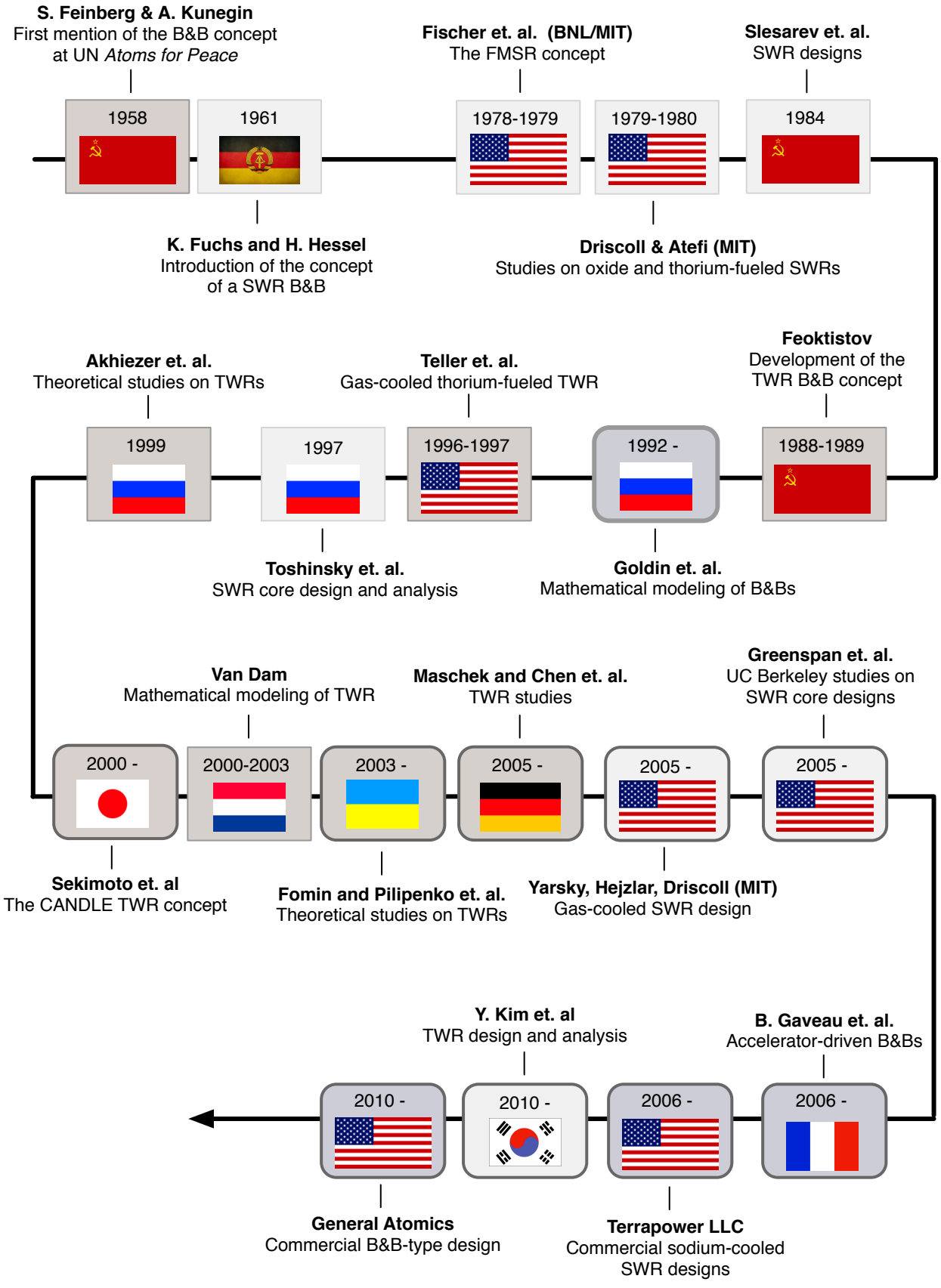

Figure 2.2: The research history of B&B systems

2.2.2 TWR research background

The earliest research on TWR-type B&B concepts were made in Russia by L. P. Feoktistov, with the studies of *"self-regulating fast reactors in traveling-wave mode"* in 1988 & 1989 [12][13]. In Ukraine, V. Ya Goldin et. al studied TWR concepts with a series of papers starting in 1995 [14].

2.2.2.1 The *Teller et. al.* travelling wave reactor

The TWR was presented in its most well-known and publicized form in a three-part paper in 1996 by american physicists E. Teller, M. Ishikawa and L. Wood [15]. The original *Teller et. al* concept consists of cylindrical thorium fuel sticks with an enriched ignitor section on one end, surrounded by a graphite neutron reflector. The core, seen in Figure 2.3, would be cooled by pipes filled with pressurized helium gas. The design featured a very innovative passive safety system, which was part of the inspiration for the new safety system presented in this thesis in chapter 6. The *Teller et. al* safety system is presented in detail in section 5.5.1.

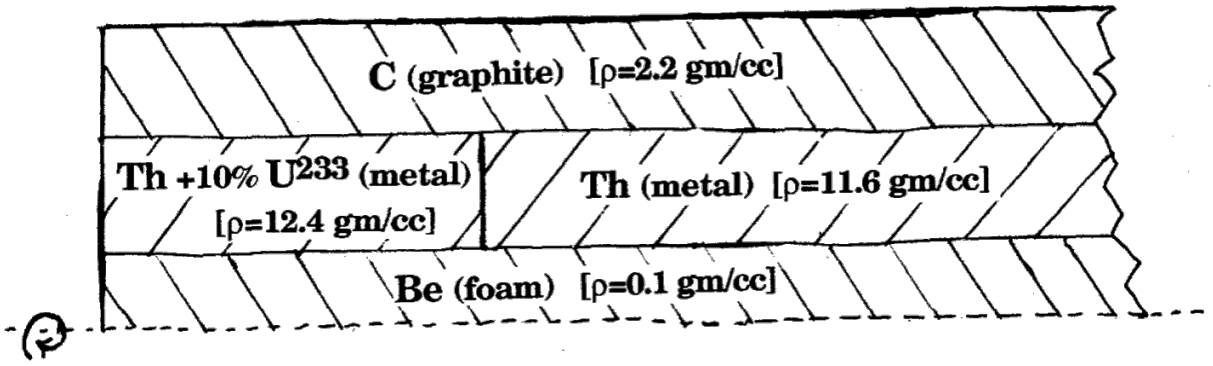

Figure 2.3: A diametral plane section of the *Teller et. al* TWR core concept (from ref. [15])

2.2.2.2 CANDLE

During the 1990s, *Hattori et. al* produced a design for the *4S* reactor where the fission region of the core is moved axially upward along a fuel column through the slow mechanical movement of a radial reflector [16]. In the early 2000s, *Sekimoto* realized that the fission region could be made to move in a similar manner without a moving reflector by utilizing the traveling fission wave principle. *Sekimoto* and colleagues began working on a traveling-wave based concept called *"Constant Axial shape of Neutron flux, nuclide densities and power shape During Life of Energy Energy production"* - CANDLE [17]. The first concepts were large lead or lead-bismuth eutectic (LBE) cooled reactors with nitride fuel, but *Sekimoto* and others have now produced a wide variety of reactor designs utilizing the CANDLE travelling-

wave burnup principle. The CANDLE concept has been investigated with several different coolants and power levels and research is ongoing.

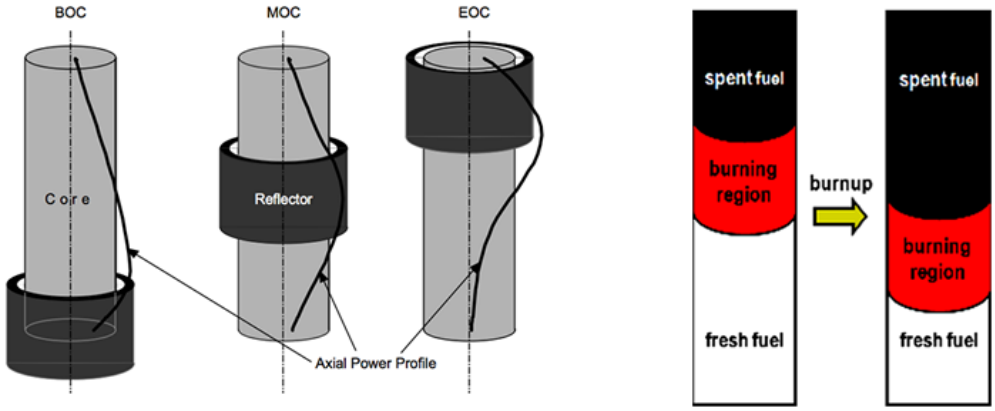

Figure 2.4: The S4 (left) and CANDLE (right) burnup concepts (from ref. [18] and [10])

2.2.2.3 General Atomics Energy Multiplier Module (EM^2)

The EM^2 is small modular gas-cooled reactor concept rated at 240 MWe (500 MWth) [19][20]. It is cooled by helium gas with a core outlet temperature of 850°C and is fully enclosed in an underground containment structure. The reactor uses carbide fuel, a composite of silicon carbide as cladding material and beryllium carbide and graphite as neutron reflector material. The reactor unit is coupled to a helium gas turbine which in turn drives a generator for the production of electricity. The core is made up of starter fuel of uranium enriched to an average of 11.4% ^{235}U with axial blankets of depleted uranium. The ^{235}U of the initial fuel loading dominates the fission rate for the first ∼10 years of operation. After about 10 years, enough ^{239}Pu has been bred in the blanket for it to start dominating the fission rate. At the end of core life after 32 years, ∼23% of the initial HM loading has been consumed (∼14% fissioned and ∼9% converted) and the fuel is discharged and can be used to manufacture starter fuel for additional EM^2 units. The peak discharge burnup of the starter fuel is ∼300 MWd/kg. While it is not a pure B&B system in its once-through version (according to the definition of Section 2.1.1), the EM^2 can be said to utilize the B&B principle. If a subsequent core starter fuel loading can be manufactured without chemical reprocessing directly from the discharged fuel of an EM^2 module, the total family of EM^2 reactors can be said to be operating collectively in a B&B mode.

2.2.2.4 Korean TWR core design and analysis

At the Korean Institute of Science and Technology (KAIST), Prof. *Yonghee Kim et. al* are currently designing and analyzing liquid metal cooled TWR cores [21][22].

2.2.2.5 Mathematical analysis

Analytical insights to travelling fission waves were provided in 2000 by *Van Dam* [23] and *Seifritz* [24]. Among others, *Fomin et. al.* in the Ukraine and *Chen et. al* in Germany continue investigating the mathematical and physical principles of traveling fission waves [25][26].

2.2.3 SWR research background

2.2.3.1 Fuchs and Hessel SWR studies

As early as 1961, famous Manhattan-project physicist and soviet spy Klaus Fuchs and colleagues studied natural uranium fueled breed and burn systems. In their studies, natural uranium feed fuel was continuously added to the core while burnt fuel was being removed at the same rate [27].

2.2.3.2 The Fast Mixed Spectrum Reactor

The first core design studies on SWR reactors were conducted at Brookhaven National Laboratory (BNL) in collaboration with the Massachusetts Institute of Technology (MIT) in the late 1970s [28]. The Fast Mixed Spectrum Reactor (FMSR), developed in this collaboration, is a system design based on the B&B principle [29][30]. The FMSR is a variation of the previously studied coupled fast/thermal breeder reactor concept [31], in which unmoderated (fast) core zones are neutronically coupled to moderated (thermal) core zones in the sense that neutrons born in each of the zones will cause fission in the other. If a significant portion of the fission events occur in the thermal region, the combined system will have a substantially longer prompt neutron lifetime than in an all-fast configuration. This can be achieved with only a small reduction in breeding ratio. However, the FMSR core design (shown in Figure 2.5) is heavily weighted toward the fast region and hence, the prompt neutron life-time is more characteristic of a fast reactor. In subsequent studies of B&B reactors, the fast/thermal concept was dropped in favor of all-fast systems similar in design to conventional fast breeder reactors (FBR). Many of the principles employed in present day B&B core design were identified in the development of the FMSR. This includes fuel shuffling strategies and the use of metallic fuel with fission gas venting.

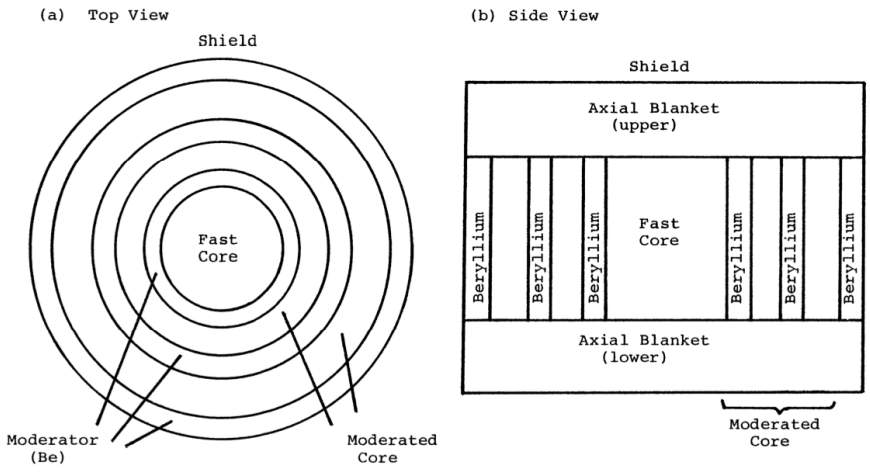

Figure 2.5: The FMSR concept (from ref. [30])

2.2.3.3 Slesarev and Toshinsky designs

In Russia, *Slesarev et. al* published research on B&B SWRs starting as early as 1984 [32]. *Toshinsky et. al.* introduced a SWR core design concept in 1997 [33].

2.2.3.4 TerraPower LLC

In 2006, an "invention session" was held at the intellectual property giant Intellectual Ventures LLC on the topic of global energy issues. Attending the session were, among others, Bill Gates (founder of Microsoft), Nathan Myhrwold (founder of Intellectual Ventures) and physicist Lowell Wood, co-author of the 1996 study on traveling wave reactors headed by Edward Teller (see section 2.2.2.1). The meeting concluded with a decision to finance a study looking in to the practical engineering implementation and limitations of such a system. In 2008, the private company TerraPower LLC was founded as an Intellectual Ventures subsidiary and began developing a commercial traveling-wave reactor. Initially the design was a TWR (and they still retain this acronym), but the TerraPower team did not find a practical engineering implementation of the traveling-wave burnup principle. The reactors developed by present day TerraPower are in fact SWRs, similar in design to large conventional sodium fast reactors (SFR).

TerraPower aims to commercialize B&B technology through a two-stage approach, beginning with a prototype plant followed by the commercial design. The TerraPower Prototype Reactor (TWR-P) is a 1200 MW-thermal plant aimed to serve as the last step in the structural material and fuels qualification program for the commercial TWR. It will also demonstrate key plant equipment, validate computer codes and form the licensing basis for the commercial design. The TerraPower TWR designs are estimated to suffer a peak displacement-per-atom (dpa) damage in the structural materials (cladding & duct) of 550-600 dpa [34]. The stated

time-line for the start-up of the TWR-P plant is ∼2022. This requires both a reactor vendor partner and a host country to be defined. The second step of the TerraPower plan is to introduce a larger (3 GW_{th}) TWR-C plant to the commercial market.

2.2.3.5 Recent MIT SWR research

After the initial work based on the sodium-cooled FMSR in the late 1970s and early 1980s, B&B research was restarted at MIT in 2005, primarily focusing on gas cooled concepts [35] [36] [37].

2.2.3.6 UC Berkeley SWR research

UC Berkeley B&B research has been primarily focused on SWRs. Core design, safety and fuel cycle characteristics of SWR B&B systems operating on a once-through fuel cycle or with limited separations using melt-refining (see Figure. 4.34 for a description) have been developed and presented in a number of papers, conference proceedings and dissertations. The work presented in this dissertation builds on and is a continuation of this work. Selected UCB SWR B&B references for further reading: [11][38][39][40][41][42][43][44][45][46].

2.3 The neutron balance concept

The concept of a neutron economy analogous to that of the monetary economy is highly applicable to B&B system analysis. There are five important steps in the neutron balance analysis, these are detailed in Section 2.3.0.7 along with their analogies in the monetary economy. The concept of neutron balance for a typical B&B reactor can be visualized with typical values using a standard sodium cooled B&B assembly design with core parameters as summarized in Table 2.1.

Table 2.1: Parameters of the sample B&B core for neutron balance illustration

Volume fractions		Fuel parameters	
Fuel	43.7%	Type	Metallic U-6Zr (w. %)
Coolant + Bond (Na)	39.9%	Smear density	75%
Structure (HT9)	16.4%	Fissile content	0.2% ^{235}U
Fuel rod pitch-to-diameter ratio (P/D)			1.088

Neutron transport calculations were performed in a 0-dimensional geometry in the Serpent neutron transport code [47] using ENDF/B-VII.0 cross-sections [48]. The results are generally applicable to B&B cores, but will change with changes in the specifics of the core design. The impact of core design choices and neutron loss on the neutron economy and balance is detailed in Section 2.7. The evolution of k_∞ with burnup of a core with the design parameters of Table 2.1 is given in Figure 2.6.

The infinite multiplication factor (k_∞) of metallic depleted uranium fuel in a typical sodium cooled B&B fuel assembly is ∼0.23-0.25. The batch only gives back one neutron for every four it absorbs. As plutonium is bred in the fuel, the multiplication factor increases rapidly. At an average burnup level of ∼3-4% FIMA, k_∞ reaches unity. The maximum infinite multiplication factor plateaus around 1.20 in the burnup range ∼12-13% FIMA. The assembly remains a net neutron producer with k_∞ above unity until a burnup of roughly 40% FIMA. The average number of neutrons produced per fission ($\overline{\nu}$) for metallic depleted uranium fuel in a typical sodium cooled B&B fuel assembly is shown in Figure 2.7. Initially, the only fissionable isotopes in the fuel are ^{235}U and ^{238}U. As the average number of fission neutrons released is higher for the plutonium isotopes, $\overline{\nu}$ quickly increases and then reaches an asymptote of ∼2.92-2.93 as plutonium-fission starts to dominate the neutron production. The neutron balance approach can be used to assess the minimum and maximum achievable burnup for B&B systems, without explicitly modeling the systems themselves. When the neutron economy is balanced, the total integrated neutron absorption equals the total integrated neutron production. Introducing the variables P_{NL} as the non-leakage probability and P_{NCR} as the probability of a neutron not being absorbed in control elements, this balance

can be expressed as:

$$\int_0^{\mathrm{BU}} P_{\mathrm{NL}} \times P_{NCR} \times \text{Production rate}\,(\mathrm{BU}) = \int_0^{\mathrm{BU}} \text{Absorption rate}\,(\mathrm{BU}) \tag{2.3}$$

Two values for BU satisfy eq. 2.3, the first (smaller) gives the minimum burnup, the larger corresponds to the maximum attainable average discharge burnup. The instantaneous neutron production rate in the core, disregarding (n,2n) and (n,3n) reactions, is given by:

$$P_{\mathrm{inst}} = \phi \times \sum_i \left(\Sigma_f^i \times \nu_i\right) \quad \left[\frac{n}{cm^3 \times s}\right] \tag{2.4}$$

Where the subscript i denotes a fuel isotope, ϕ is the total neutron flux, Σ_f is the effective one-group macroscopic fission cross-section and ν is the average number of neutrons emitted per fission of isotope i. The time-integrated flux (i.e fluence ϕt) is proportional to burnup. Expressing the production per unit volume of fuel, the integrated neutron production in the core is given by:

$$P_{\mathrm{BU}} = N_{\mathrm{HM}} \int^{BU} \sum_i \left(\Sigma_f^i \times \nu_i\right) dBU \tag{2.5}$$

Where both Σ_f and ν are functions dependent on burnup. The preferred unit of burnup for neutron balance studies is Fissions Per Initial Metal Atom (FIMA). This simplifies the expressions for production, absorption and neutron balance significantly. Neutron production is directly proportional to the average number of neutrons released per fission, with an integrated total neutron production of $N_{\mathrm{HM}} \times \overline{\nu}$ per initial actinide at 100% FIMA. N_{HM} is the actinide atomic density of the initial fuel loading. The unit of N_{HM} can be chosen at will (either as a density of volume-integrated). With the burnup expressed in the unit of FIMA, eq. 2.5 simplifies to:

$$P_{\mathrm{FIMA}} = N_{\mathrm{HM}} \int^{BU} \overline{\nu}\,(\mathrm{BU})\,\mathrm{dBU} \tag{2.6}$$

$\overline{\nu}$, the average number fission neutrons generated per fission event, is defined as:

$$\overline{\nu}\,(\mathrm{BU}) = \frac{\sum_i \left(v^i \Sigma_f^i\right)}{\sum_i \left(\Sigma_f^i\right)} \tag{2.7}$$

The neutron absorption is given from the definition of k_∞ as:

$$k_\infty\,(\mathrm{BU}) = \frac{\text{Production}}{\text{Absorption}} \rightarrow \text{Absorption} = \frac{\text{Production}}{k_\infty} = N_{\mathrm{HM}} \frac{\overline{\nu}\,(\mathrm{BU})}{k_\infty\,(\mathrm{BU})} \tag{2.8}$$

Absorption (A) can then be defined as:

$$A_{\mathrm{FIMA}} = \int^{BU} N_{\mathrm{HM}} \frac{\overline{\nu}\,(\mathrm{BU})}{k_{\infty}\,(\mathrm{BU})} \mathrm{dBU} \tag{2.9}$$

The integrated net neutron balance (N), using eq. 2.6 & 2.9, is given by:

$$\begin{aligned} N &= \int^{\mathrm{BU}} (P - A)\,\mathrm{dBU} = N_{\mathrm{HM}} \int^{\mathrm{BU}} \left(\overline{\nu}\,(\mathrm{BU}) - \frac{\overline{\nu}\,(\mathrm{BU})}{k_{\infty}\,(\mathrm{BU})} \right) \mathrm{dBU} \\ &= N_{\mathrm{HM}} \int^{\mathrm{BU}} \overline{\nu}\,(\mathrm{BU}) \left(1 - \frac{1}{k_{\infty}\,(\mathrm{BU})} \right) \mathrm{dBU} \end{aligned} \tag{2.10}$$

To include the effect of neutron leakage and loss to absorption in control assemblies as introduced in eq. 2.3, the infinite multiplication factor can be replaced by an effective multiplication factor as:

$$k_{\mathrm{eff}} = k_{\infty} \times P_{\mathrm{NL}} \times P_{\mathrm{NCR}} \tag{2.11}$$

For a neutron balance analysis, it makes no difference how the neutrons are lost. An integrated loss parameter Q is introduced, defining the total neutron loss in the system as:

$$Q = (1 - P_{\mathrm{NL}}) + (1 - P_{\mathrm{NCR}}) \tag{2.12}$$

The definition given in eq. 2.12 may be modified at will. Depending on convention, the non-leakage term (P_{NL}) and the probability of non-absorption in control assemblies can be treated as connected quantities (as in eq. 2.11), giving $Q = (1 - P_{\mathrm{NL}}) + (1 - P_{\mathrm{NL}})\,(1 - P_{\mathrm{NCR}})$. With Q defined, the effective multiplication factor is then:

$$k_{\mathrm{eff}}\,(\mathrm{BU}) = k_{\infty}\,(\mathrm{BU}) \times (1 - Q) \tag{2.13}$$

To conclude, the minimum and maximum average discharge burnup where a B&B mode of operation can be sustained is given by the values of burnup (expressed in FIMA) that satisfies the following equation (henceforth the *neutron balance integral*, first published in ref. [46]):

$$\begin{aligned} 0 &= \int^{\mathrm{BU}} \overline{\nu}\,(\mathrm{BU}) \left(1 - \frac{1}{k_{\mathrm{eff}}\,(\mathrm{BU})} \right) \mathrm{dBU} \\ &= \int^{\mathrm{BU}} \overline{\nu}\,(\mathrm{BU}) \left(1 - \frac{1}{k_{\infty}\,(\mathrm{BU}) \times (1 - Q)} \right) \mathrm{dBU} \end{aligned} \tag{2.14}$$

Both $\overline{\nu}$ and k_{∞} are standard output parameters from calculations in neutron transport codes such as Serpent or MCNP. Values are calculated at discrete predetermined values of burnup. In the neutron balance analysis of this thesis, values have been calculated at ∼70-80 discrete

burnup points between 0-100% FIMA. The functional form of the burnup-dependent infinite multiplication factor and average number of neutrons produced per fission event in fertile fuel can be well represented by a 5th-order rational expression of the form:

$$k_{\infty}, \overline{\nu} \propto \frac{p_1 B^5 + p_2 B^4 + p_3 B^3 + p_2 B^2 + p_5 B + p_6}{B^5 + q_1 B^4 + q_2 B^3 + q_3 B^2 + q_4 B + q_5} \tag{2.15}$$

Where B is the burnup in FIMA and p_i and q_i are constants. The k_{∞}-evolution with burnup of the reference B&B fuel assembly is given in Fig. 2.6 along with a curve-fit based on a rational expression as given in eq. 2.15. The curve-fits, developed using the *Levenberg-Marquardt* algorithm [49], are tested until the root-mean-square error (RMSE) falls below 5×10^{-4}. At this point, given an adequate number of datapoint at early burnup steps, statistical errors in the neutron transport calculation at 1 million neutron histories are larger than errors introduced by the curve-fit. The non-integral parameters of the neutron balance analysis (1. Fuel loading, 2. Point of net neutron production and 4. Initial point of net neutron loss) can be identified immediately through Figure 2.6. The neutron balance integral has been evaluated numerically by integrating the right side of eq. 2.14 using a MATLAB script at different values for the neutron loss parameter Q. Figures 2.8-2.9, illustrating points 1-5 of section 2.3.0.7, were made with the idealized assumption of zero neutron loss (Q=0).

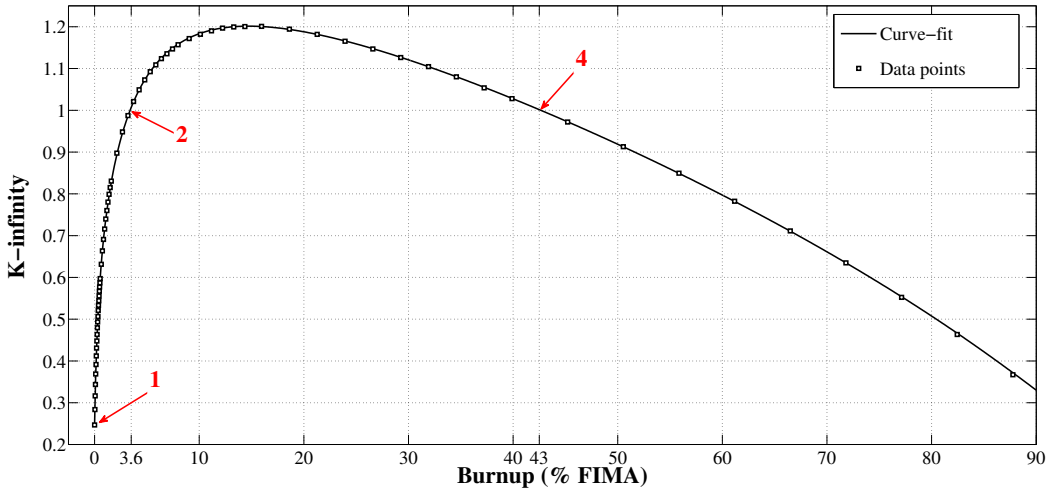

Figure 2.6: The k-infinity evolution with burnup of a depleted-uranium fueled sodium-cooled B&B reactor assembly, as defined by Table 2.1

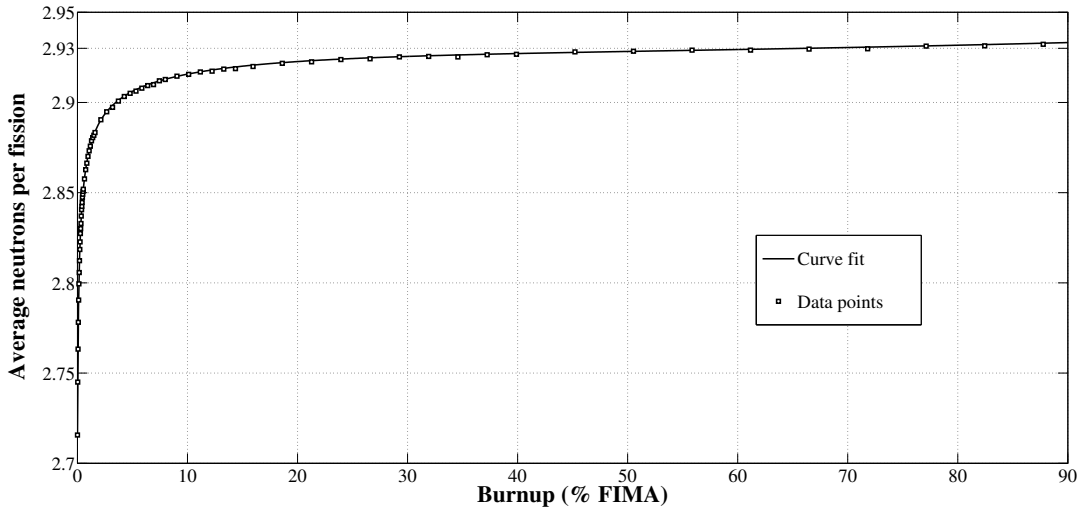

Figure 2.7: The $\overline{\nu}$-evolution with burnup of a depleted-uranium fueled sodium-cooled B&B reactor assembly, as defined by Table 2.1

2.3.0.7 The 5 steps of B&B reactor neutron balance

1. Fuel loading. A fertile fuel batch loaded to the core initially produces far less neutrons than it absorbs. The batch is borrowing neutrons from the general core neutron economy.

1 → 2 Net neutron absorption in the fuel causes breeding of fissile isotopes through nuclear transmutation of fertile isotopes.

2. Net neutron production. Once k_∞ reaches unity, the batch turns from a net neutron absorber to a net neutron producer. At this point, the neutron investment by the neutron economy has caused enough breeding for the batch to start producing excess neutrons. From this point, excess neutron production in the batch starts to pay back the initial neutron debt to the general neutron economy.

2 → 3 Net excess neutrons are being produced while breeding is continued. As the fuel approaches point 3, it reaches its most productive stage where the maximum amount of excess neutrons are being added to the system per unit burnup.

3. B&B neutron balance (1) At the burnup level where the burnup-integrated neutron production and loss (absorption + leakage) are equal, the neutron economy is *balanced*. This point corresponds to the lowest level of average batch discharge burnup that an equilibrium cycle of a B&B reactor can be operated at. The batch is now adding net excess neutrons to the economy as a whole. These excess neutrons are used by new fertile batches going through the previous stages.

3 → 4 During this period the fuel batch is a net neutron producer.

4. Net neutron absorption. Due to fission product accumulation, the excess neutron production is constantly diminishing after having reached point 3. At point 4, neutron absorption rate and losses equal production rate, and after this point the batch again becomes a net neutron absorber.

4 → 5 The fuel is a net neutron absorber. In the neutron economy, the net neutron profit accumulated between points 3 and 4 is being spent.

5. B&B neutron balance (2). Once the neutrons gained between point 3 and 4 have been consumed, the net neutron excess is again 0, and the neutron economy is *balanced* for the second time. This corresponds to the maximum level of average batch discharge burnup that an equilibrium cycle of B&B can be operated at.

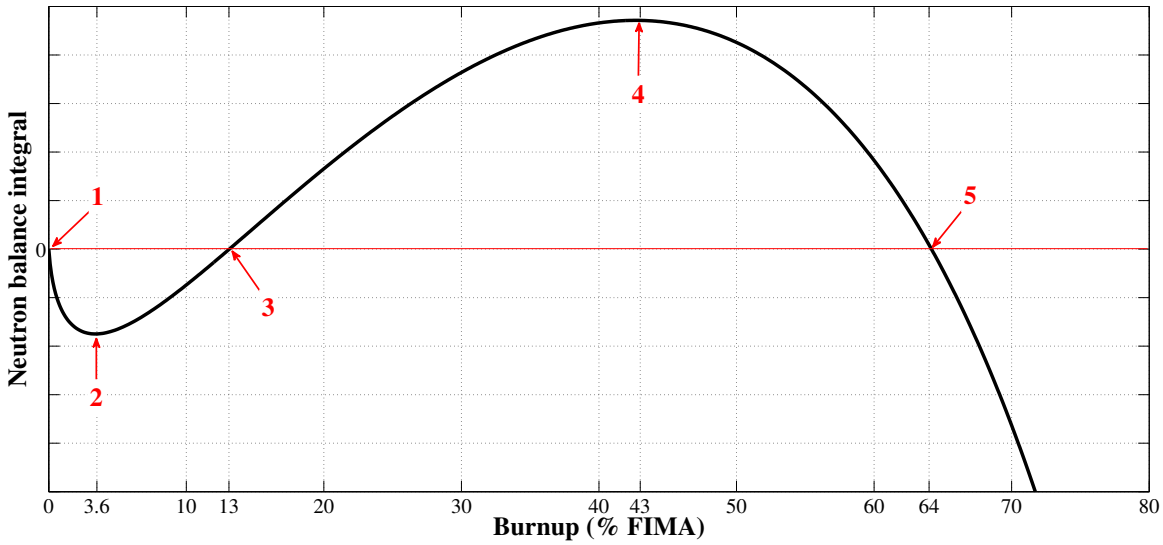

Figure 2.8: The *neutron balance integral* of a depleted-uranium fueled sodium-cooled B&B reactor assembly, as defined by Table 2.1 with Q=0

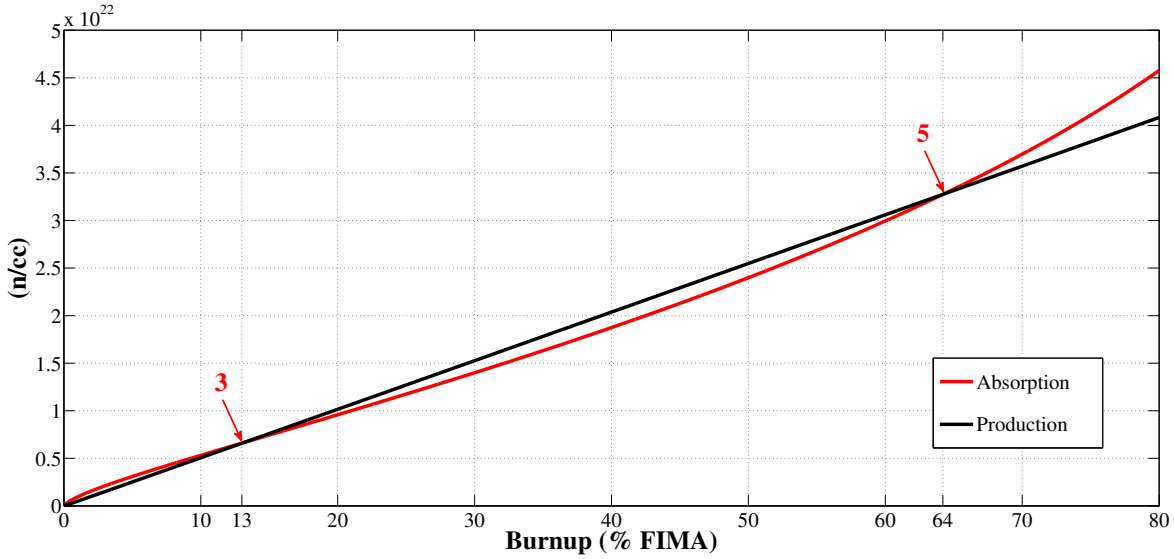

Figure 2.9: Absorption and production (neutrons/cm^3) of a depleted-uranium fueled sodium-cooled B&B reactor assembly, as defined by Table 2.1 with Q=0

2.3.1 The FIMA burnup unit - principles and problems

The standard unit for burnup is given as an amount of energy produced per unit of actinide mass loaded in the fuel (usually MWd/kg or GWd/ton). This is a straightforward unit to use for conventional analysis as it is simply a function of the actinide mass loaded in the core, power level and fuel residence time. Neutron balance analysis requires the use of the unconventional FIMA burnup unit. The conversion between the two burnup units is not straightforward. As formulated, it is dependent on the isotopic composition of the actinides producing fission. Using a set conversion unit such as X% FIMA = Y MWd/kg can produce significant errors. In reality, the conversion between FIMA and MWd/kg is a function of burnup. The differences arise because the heat deposited in the system by a fission reaction is dependent on both the isotope being fissioned and the energy of the neutron causing the fission reaction. Conversion between the two units thus requires proper averaging throughout the burnup cycle. Problems may arise because of the disparity among different literature sources for the amount of recoverable heating energy released in the fission of different isotopes (E_f). For ^{235}U, which provides the majority of fission energy in the world and is the most studied fissile isotope, textbook recommendations for E_f are given at 190 [50], 195 [51] and 200 MeV/fission [52][53], a difference of more than 5%. The values included in the latest release of Evaluated Nuclear Data File (ENDF-VII) are given in Table 2.2 [54].

Table 2.2: Components of the fission heating values (E_f) of important isotopes (MeV/fission)*, excluding neutrino energy as it leaves the reactor and is unrecoverable

Isotope	Fission products & neutrons	γ	β	Total (E_f)
^{235}U	174.05	12.93	6.50	193.48
^{238}U	174.62	14.93	8.48	198.03
^{239}Pu	181.62	11.91	5.31	198.83

* No specific dependence on average neutron energy causing fission for these values is cited

To convert MWd/kg in to FIMA, physical constants as defined in Table 2.3 are used.

Table 2.3: Physical constants for burnup unit conversion

Constant	Symbol	Value	Unit
Megawatt-day	MWd	8.64×10^{10}	J
Electron volt	eV	$1.602176565 \times 10^{-19}$	J
Avogrados constant	N_{AV}	$6.02214129 \times 10^{23}$	atoms/mol
^{235}U atomic mass	$\mathrm{M}^{235}\mathrm{U}$	235.0439231	grams/mol
^{238}U atomic mass	$\mathrm{M}^{238}\mathrm{U}$	238.0507826	grams/mol
^{239}Pu atomic mass	$\mathrm{M}^{239}\mathrm{Pu}$	239.0521565	grams/mol

The average atomic mass of the actinides in depleted uranium (DU) is:

$$M_{\mathrm{DU}} = 0.998 \times M^{238}\mathrm{U} + 0.002 \times M^{235}\mathrm{U} = 238.0447688 \ \left[\frac{\mathrm{grams}}{\mathrm{mol}}\right] \tag{2.16}$$

The number of DU-atoms per kg is:

$$\mathrm{Akg}_{\mathrm{DU}} = \frac{10^3 \times N_{\mathrm{AV}}}{M_{\mathrm{DU}}} = 2.529835594 \times 10^{24} \ \left[\frac{\mathrm{atoms}}{\mathrm{kg}}\right] \tag{2.17}$$

The heat deposited in the reactor per fission event (assuming freshly loaded DU) is given by:

$$E_{\mathrm{fuel}}\left(\mathrm{DU}\right) = \frac{\Sigma_f\left(^{235}\mathrm{U}\right) \times E_f\left(^{235}\mathrm{U}\right)}{\Sigma_f\left(^{235}\mathrm{U}\right) + \Sigma_f\left(^{238}\mathrm{U}\right)} + \frac{\Sigma_f\left(^{238}\mathrm{U}\right) \times E_f\left(^{238}\mathrm{U}\right)}{\Sigma_f\left(^{235}\mathrm{U}\right) + \Sigma_f\left(^{238}\mathrm{U}\right)} \ \left[\frac{\mathrm{MeV}}{\mathrm{fisson}}\right] \tag{2.18}$$

More generally, the *average* heat deposition by fission is given by:

$$E_{\mathrm{fuel}} = \sum_i \left[\frac{\Sigma_f^i \times E_f^i}{\sum\limits_i \left(\Sigma_f^i\right)}\right] \ \left[\frac{\mathrm{MeV}}{\mathrm{fisson}}\right] \tag{2.19}$$

Where i is a fuel actinide. The spectrum-averaged effective one-group microscopic and macroscopic cross-sections of the uranium isotopes in a core with parameters as defined in Table 2.1 are given in Table 2.4.

Table 2.4: Effective 1-group cross-sections of DU isotopes in sodium-cooled B&B reactor

Isotope	σ_f (barn)	σ_c (barn)	Σ_f (1/cm)	Σ_c (1/cm)	$\sigma_f/(\sigma_f + \sigma_c)$
^{235}U	1.6733	0.4475	5.9×10^{-5}	1.6×10^{-5}	0.789
^{238}U	0.0226	0.2346	0.4×10^{-3}	4.1×10^{-3}	0.088

Interesting to note from Table 2.4 is that ∼88% of the fission events in depleted uranium fuel is due to fission of the fertile isotope ^{238}U. Using the values of Table 2.2, 2.3 & 2.4, the average fission heating energy $\overline{E}_f$ of the freshly loaded fuel is 197.45 MeV. The burnup conversion ratio between FIMA and MWd/kg at core loading of depleted uranium fuel can then be calculated as:

$$\mathrm{Cr}_1 = \frac{0.01 \times \overline{E}_f \times \mathrm{Akg}_{\mathrm{DU}}}{\mathrm{MWd}} = 9.26 \quad \left[\frac{\%\ \mathrm{FIMA}}{\mathrm{MWd/kg}}\right] \tag{2.20}$$

As the fuel burnup progresses, ^{239}Pu is bred in and starts to dominate the fission reaction in the fuel. Thus, $\overline{E}_f$ quickly approaches the value for ^{239}Pu and then slowly increases as higher actinides are contributing more and more to the fission events. At discharge burnups typical of B&B reactors (15-20% FIMA), the cycle averaged burnup conversion ratio typically approaches ∼9.5.

2.3.2 Limitations and approximations in the neutron balance method

There are three important limitations when applying the neutron balance concept to B&B reactor analysis. In order of importance, they are:

1. Neutron loss (Q) is an unknown variable and is difficult to correctly estimate.
2. (For SWR B&Bs): The radial power peaking factor cannot be estimated without explicitly modelling the core shuffling scheme. The radial peaking factor has a profound impact on the attainable fuel volume fraction.
3. The flux spectrum and its evolution of the typically 0D or 1D simplified models used in neutron balance analysis differs from the actual flux spectrum experienced by the fuel in the reactor. The relative change in spectrum with burnup is larger in the simplified geometry.

While the neutron balance method can be adjusted for neutron loss (as described by equations 2.11 & 2.12), estimating values a value for Q (i.e. P_{NL} and P_{NCR}) for a real 3D-system can be difficult. The impact of the value of Q is profound for the performance of the system, which limits the utility of the neutron balance method for applications where Q can not be estimated. While absolute quantities (such as minimum required burnup for the system) can be difficult to estimate, the neutron balance method remains an effective tool for comparing different design options.
A severe limitation inherent in low-dimensional system analysis is that higher-dimensional effects such as power peaking factors cannot be assessed. In standing wave type reactors, fuel is moved around in the core according to a set shuffling scheme. For any "reasonable"[1]

[1] *Resonable* here means any shuffling scheme that does not place highly reactive fuel at the core periphery and thus causing an *unreasonable* amount of leakage

shuffling scheme, the effect on neutron balance is minor with a given set of core volume fractions. However, it is primarily the shuffling scheme that determines the radial power peaking in the core. As fuel assemblies across the core need to be identical, the coolant fraction needed to effectively cool the assembly position with the maximum power (the "*hot assembly*") sets the volume fractions for all assemblies. The neutron balance method can more or less accurately determine minimum required and maximum achievable burnup for a given set of volume fractions, but it cannot estimate whether these volume fractions could be used in an actual core design. Because of this drawback, neutron balance is mainly applicable as a scoping tool. For scoping analysis it is however exceptionally powerful, and it can guide core design decisions very effectively. The *extended neutron balance* method (ENB), introduced in Section 2.6 further extends the utility of this type of analysis.

The error introduced by differences in flux spectra between a simplified model and analyzing the full system is relatively minor. In a fast system, the average scattering cross section is much higher than the average absorption cross section. This means neutrons scatter in the system many times before eventually being absorbed. Because of the long neutron mean free path in a fast system, the local spectrum of a particular fuel region is influenced by adjacent regions that may be at different burnup levels depending on the shuffling scheme. In a real 3D-system, some fraction of neutrons also leak out of the system, which has an additional impact on the neutron spectrum. These influences are lost in a neutron balance analysis and also introduces a spectral error. In a real system, the spectrum in the low-fissile-content blanket assemblies that are loaded far from the fission wave is relatively soft due to the increased number of scattering reactions neutrons have undergone before reaching these assemblies. The evolution of the neutron spectrum with burnup reaches an asymptote at $\sim$5%, after which the spectrum remains all but constant up past 20% FIMA. The low and high burnup spectral evolution of a 0D system (as defined by Table 2.1) are given in Fig. 2.10 and 2.11 respectively.

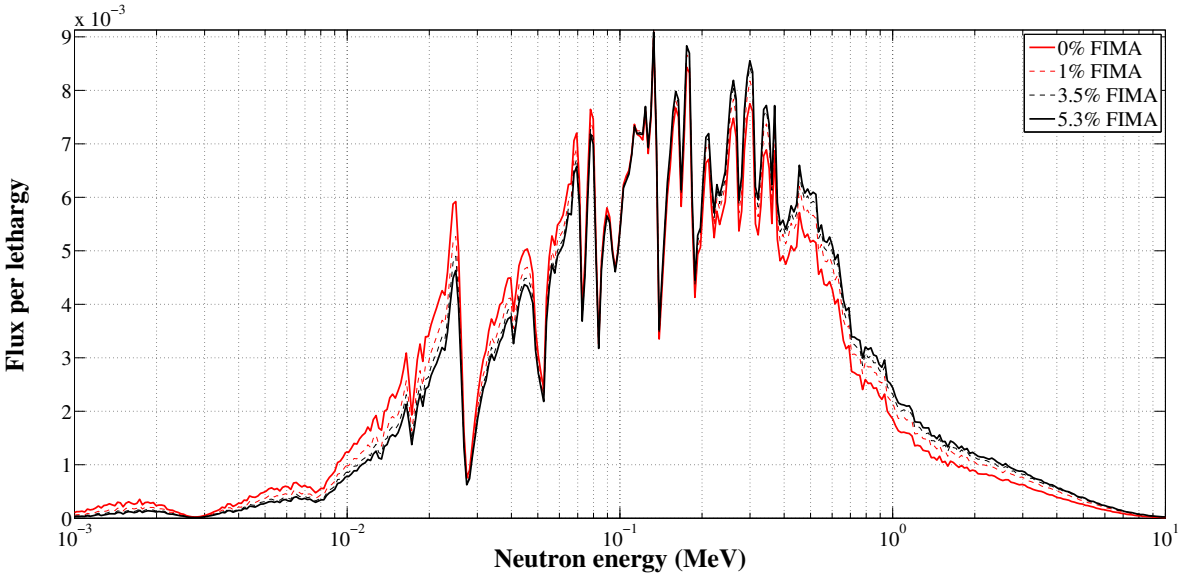

Figure 2.10: Normalized neutron flux spectrum at low burnups (core as defined in Table 2.1)

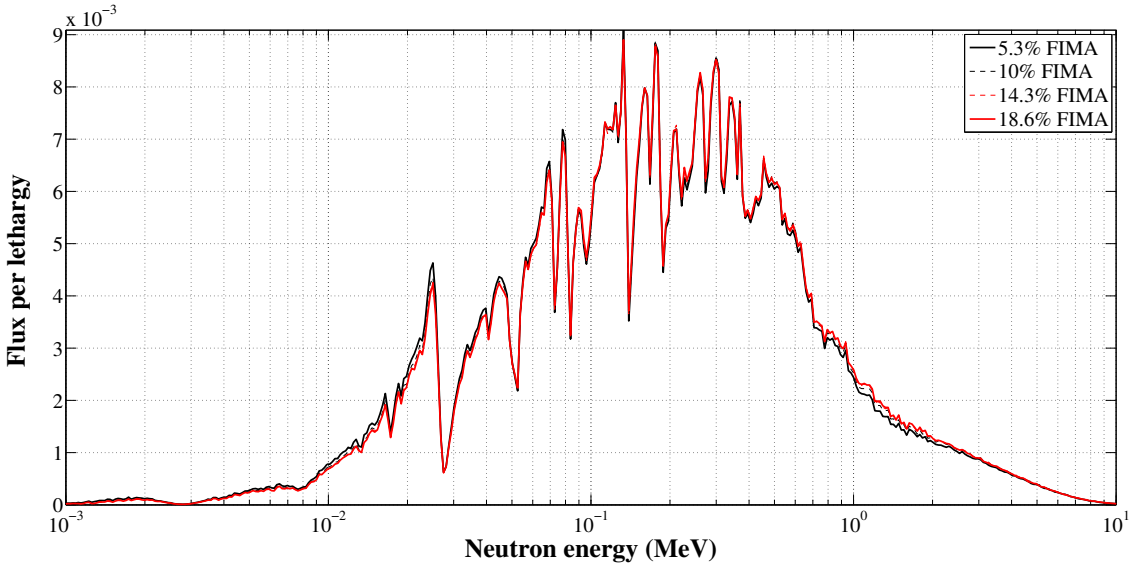

Figure 2.11: Normalized neutron flux spectrum at high burnups (core as defined in Table 2.1)

2.4 B&B burnup characteristics

2.4.1 Fuel isotopic composition

The burnup characteristics of a fertile fuel batch loaded in to a B&B core can be highlighted by looking at the evolution of isotopic concentrations and fission & absorption rates. The fuel consists of three major components: Initial actinides (primarily ^{238}U), bred actinides (primarily Pu) and fission products. The evolution of these components by burnup in the full burnup range (0-100%) in a B&B system is given in Fig. 2.12.

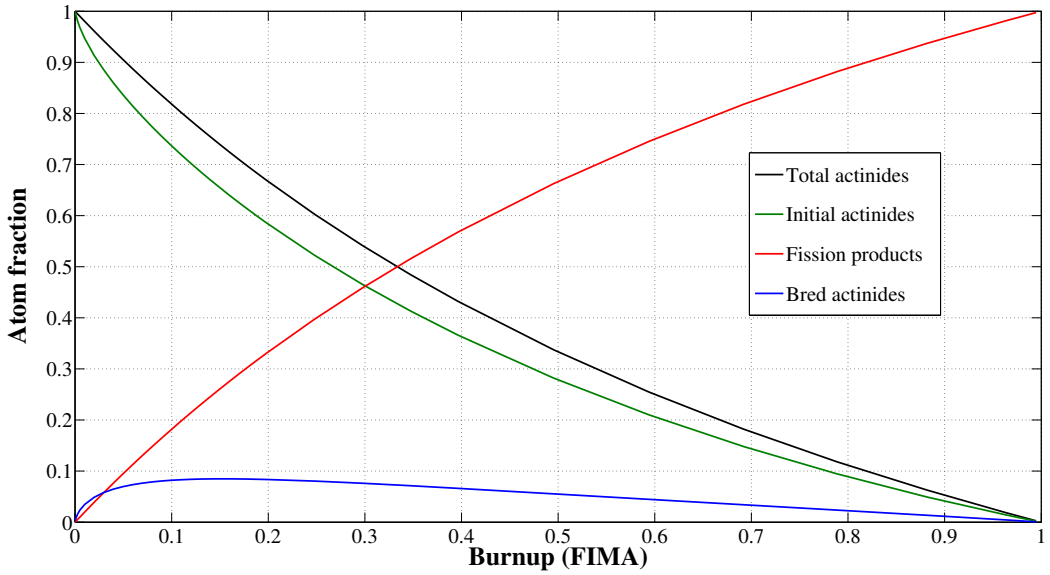

Figure 2.12: Fuel components by burnup

The individual isotopic evolutions of concentrations in the fuel are given in Figure 2.13.

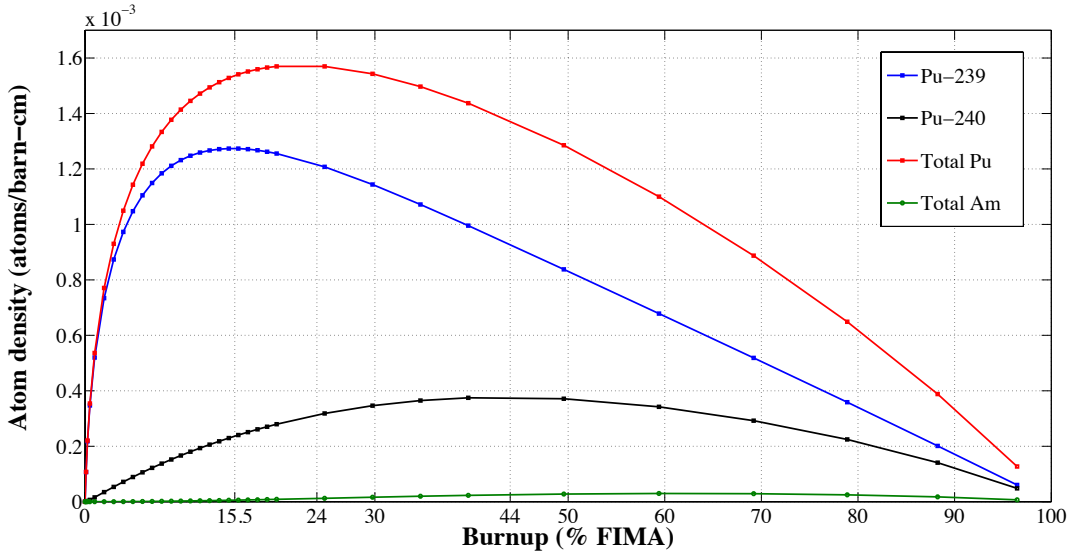

Figure 2.13: Isotopic concentrations evolution

The concentration of plutonium in the fuel peaks at ∼24% FIMA. ^{239}Pu, the dominant fissile isotope in any uranium-fueled B&B system, is most abundant at 15.5% FIMA. ^{240}Pu build up more slowly, peaking in concentration at ∼44% FIMA. The *fissile* content of the fuel is conventionally defined as the concentration of isotopes that can fission by zero-energy neutrons. These are defined by atomic-mass range in Table 2.5.

Table 2.5: Fissile isotopes

A < 235	235 < A < 244	A > 244
^{232}U	^{235}U	^{245}Cm
^{233}U	^{236}Np	^{247}Cm
	^{239}Pu	^{249}Cf
	^{241}Pu	^{251}Cf
	^{242m}Am	
	^{243}Cm	

The remaining actinides are defined as *fertile*. If a material is fertile, its probability of fission is very low in a thermal spectrum, as only a small fraction of neutron have energies above the fission threshold. These distinctions have a much more muddled meaning in a fast spectrum, as several fertile isotopes have fission-to-capture cross-section ratios above one in

a fast spectrum. The concentration ratio between fissile and fertile isotopes in the B&B system is given in Fig. 2.14.

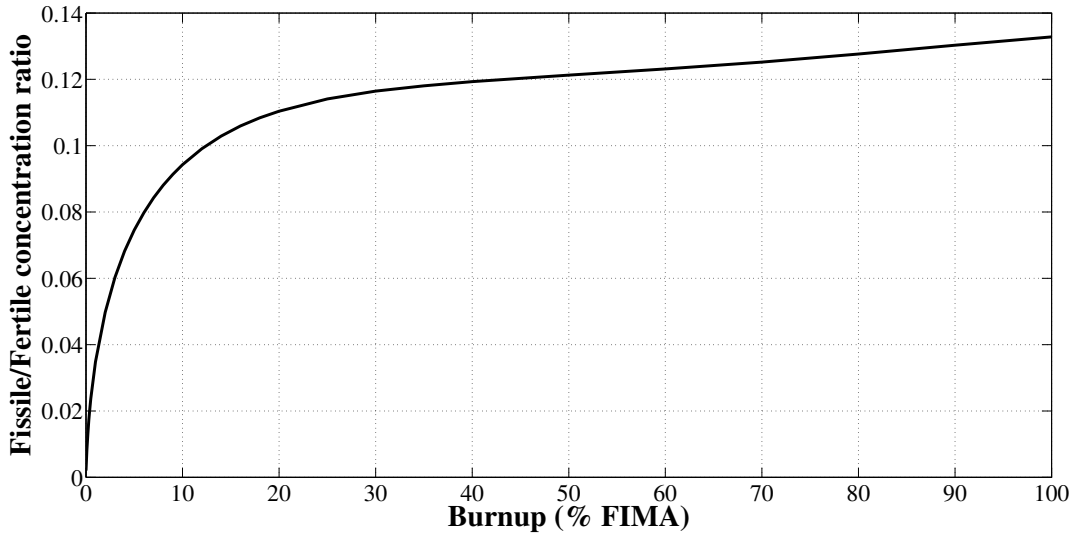

Figure 2.14: Fissile/Fertile isotopic ratio (core as defined in Table 2.1)

2.4.2 Capture and fission

The relative fraction of total fission events by different isotopes are given in Fig. 2.15. At fuel loading, fission is dominated by ^{238}U, with 88% of fission reactions, the remaining 12% of fission is provided by the tiny amount (0.2%) of ^{235}U present in depleted uranium fuel. Before 1% FIMA, ^{239}Pu, bred in by absorption reactions in ^{238}U, begins to dominate the fission reactions in the system. The relative impact of ^{235}U drops below 1% of total fission at 5% FIMA. The impact on the system by ^{235}U is at a minimum at 35% FIMA, at which point its concentration reaches a steady state value of $\sim$10% of its original value as balance is reached between capture reactions and the decay of higher actinides such as ^{239}Pu. The fission of the system past 5% FIMA is dominated by ^{239}Pu and ^{238}U, with minor but increasing contributions from ^{240}Pu & ^{241}Pu. Higher plutonium isotopes and americium are not bred in sufficient concentrations to have a major impact on system fission. The relative importance of fission in ^{239}Pu as compared to ^{238}U is given in Fig. 2.16. The distribution of absorption events by isotope is shown in Fig. 2.17 and the core-averages macroscopic fission and absorption cross-section are shown in Fig. 2.18.

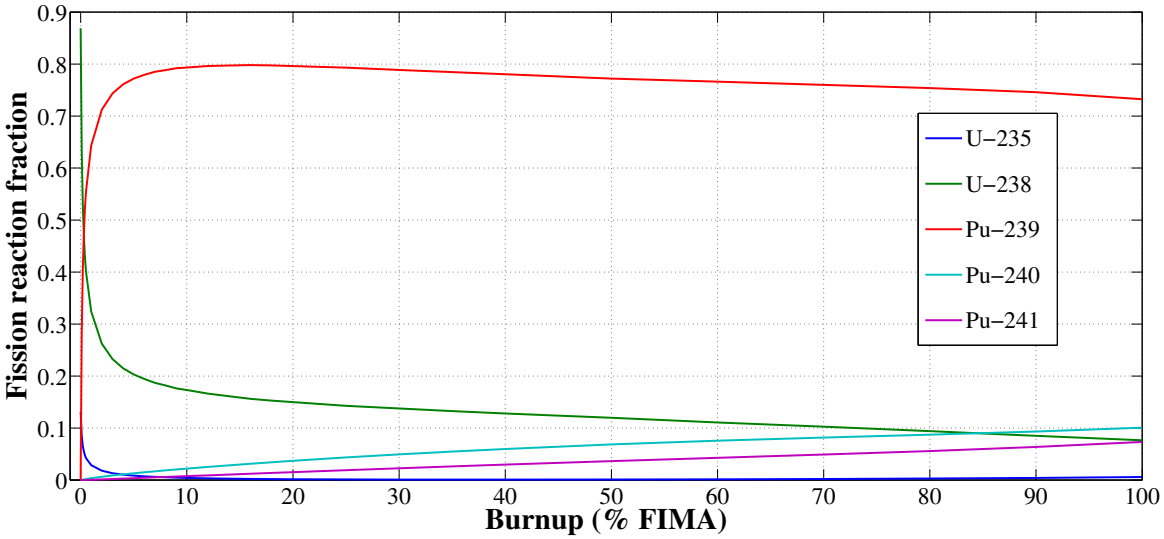

Figure 2.15: Fraction of total fission events by nuclide

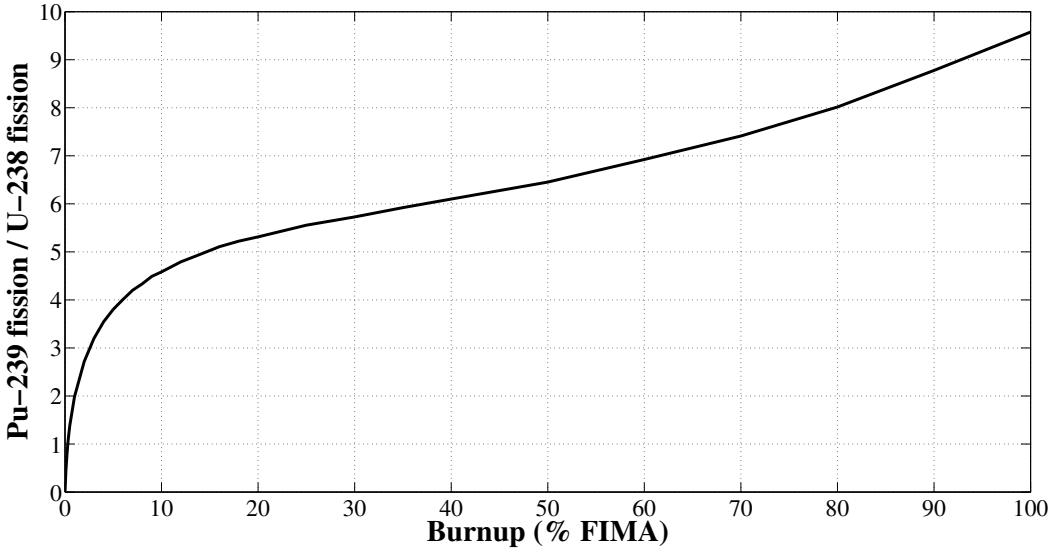

Figure 2.16: Fission reaction rate of ^{239}Pu divided by fission reaction rate of ^{238}U

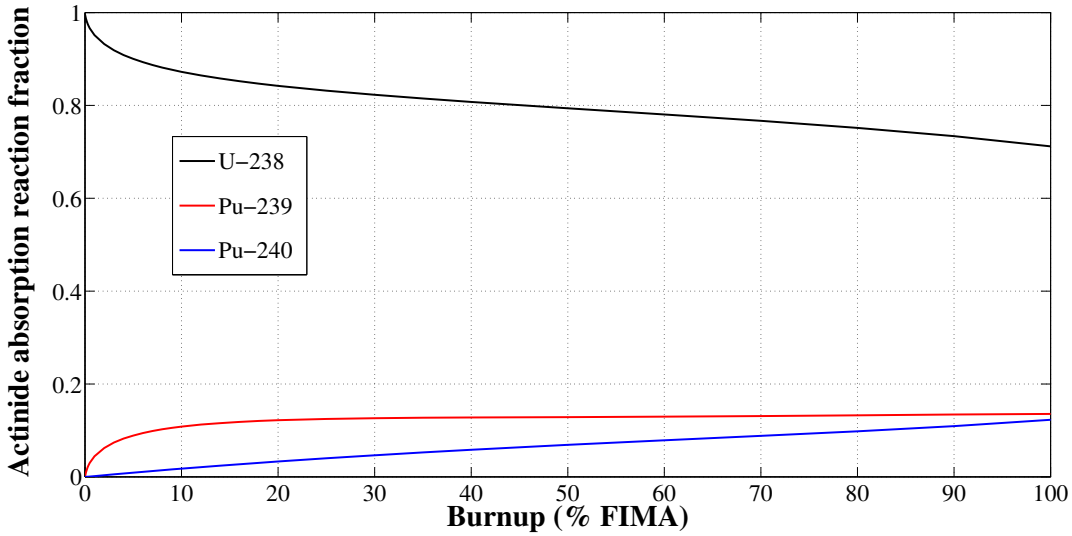

Figure 2.17: Fraction of total absorptions events in actinides

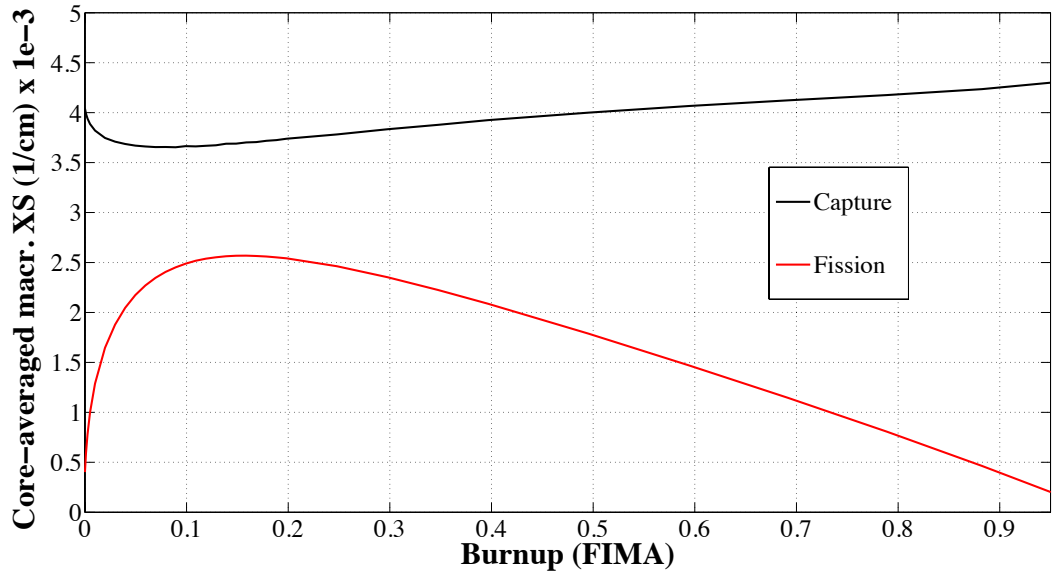

Figure 2.18: Core-averaged fission and capture macroscopic cross-sections (10^3/cm)

2.5 B&B fuel type analysis

To a first order approximation, the choice of fuel type does not impact the fuel assembly design of a B&B reactor. Any B&B reactor design will be designed for a maximized actinide density and fuel volume fraction in the core. The limitations for fuel loading are set by constraints in the heat removal system, primarily by limits imposed on coolant velocity and pressure drop. While the fuel temperature margin-to-melting of different fuel types could impact the assembly design, this constraint is typically of lesser importance. This is because B&B systems operate at a relatively low-power-density designs due their large active core size (to minimize leakage) and their need for a high actinide density loading in the core. It is therefore motivated to use the same assembly design while comparing fuel types. The choice of fuel type affects the attainable design space of a B&B reactor in three ways:

1. The actinide atom density in the core
2. The moderation of neutrons by non-actinide components of the fuel
3. The absorption of neutrons by non-actinide components of the fuel

The first and most obvious difference is the variation in actinide atom density in the core. The effective actinide density (including fabrication and smear density) of common fuel types can vary by up to 50%. The highest attainable core-averaged actinide density for a typical SFR is around $\sim$8 g/cm^3. An oxide-fuel core with the same geometry has a core-averaged actinide density of $\sim$4.5 g/cm^3. A summary of fuel and core properties, calculated for a core with a pitch-to-diameter ratio of 1.088 are given in Table 2.6[2].

Table 2.6: Fuel parameters for P/D = 1.088 cores

Fuel type	UO_2	UN	UC	U-10Zr	U-10Mo	U
Smear density [55]	85%	85%	85%	75%	75%	75%
Fabrication density [55]	94%	94%	94%	100%	100%	100%
Fuel density (g/cm^3)	10.26	13.59	12.58	15.80	16.70	18.53
Swollen fuel density (g/cm^3)	8.73	11.56	10.81	11.86	12.54	13.91
Actinide density (g/cm^3)	9.05	12.84	11.98	14.22	15.03	18.53
Swollen actinide density (g/cm^3)	7.69	10.91	10.30	10.67	11.29	13.91
Core actinide density (g/cm^3)	4.48	6.36	5.93	6.21	6.57	8.10
Core actinide density (mol/cm^3)	0.01882	0.02672	0.02492	0.02609	0.02761	0.03403

[2]A P/D-value of 1.088 corresponds to an thermal-hydraulically optimized sodium-cooled core designed using the ADOPT code (see Chapter 7) with 185 cm length of active fuel and a core-averaged power density of 200 W/cm^3. This is used here as a representative design for SWR B&Bs. Variations of these parameters are covered in detail in Sections 2.7 and 7.6.

2.5.1 Neutron moderation by non-actinides in the fuel

The presence of non-actinides in the fuel (such as oxygen, carbon, zirconium or nitrogen) both reduces fuel density and increases parasitic absorption and moderation of neutrons which has a negative effect on the neutron economy. To achieve the best possible neutron economy, the fuel form needs a minimized fraction of non-actinides and non-actinides with as high atomic number as possible. The effect on the neutron energy spectrum by elastic scattering of neutron on non-actinides in the fuel can be estimated by the *slowing down decrement* (ξ). It is defined as the mean value of the logarithm of the energy loss ratio per collision:

$$\xi = \overline{\ln\left(E/E'\right)} \tag{2.21}$$

where E and E' are the neutron energy before and after a collision. Defining the parameter α as:

$$\alpha = \frac{(A-1)^2}{(A+1)^2} \tag{2.22}$$

where A is the atomic mass, ξ can be rewritten as:

$$\xi = 1 + \frac{\alpha}{1-\alpha}\ln\left(\alpha\right) \tag{2.23}$$

Equation 2.23 can be used to calculate the number of neutron collisions needed to bring a neutron from an initial energy E_0 to an energy E_1 as:

$$n = \frac{1}{\xi}\ln\left(E_0/E_1\right) \tag{2.24}$$

Setting E_0 to 2 MeV (roughly the energy of an uncollided fission neutron) and E_1 to 0.025 eV (the neutron energy at thermal equilibrium in room temperature), eq. 2.24 simplifies to:

$$n = \frac{18.2}{\xi} \tag{2.25}$$

While eq. 2.25 accurately reflects a materials capability to slow down neutrons, it needs to be weighted by the macroscopic scattering cross-section of the material in order to show the impact on the neutron spectrum of the core. The *slowing down power* is defined as $\Sigma_s\xi$. This parameter requires the calculation of the effective one-group microscopic scattering cross-section along with the atomic density of all isotopes that make up a specific non-actinide material in the fuel. The relevant scattering parameters for zirconium, the standard alloying material of metallic nuclear fuel, are summarized in Table 2.7. Parameters have been calculated in the spectrum of a B&B core (with parameters as given by Table 2.1) at 10% FIMA burnup rather than at the freshly loaded state to better approximate the behavior of a B&B system at equilibrium.

Table 2.7: Moderating parameters of zirconium at 10% FIMA burnup

Isotope	Nat. ab.	ξ	n	σ_s (barn)	Σ_s (1/cm)	$\xi\Sigma_s$
^{90}Zr	51.45%	0.0221	824	8.4425	0.0200	4.385e-4
^{91}Zr	11.21%	0.0218	833	8.6930	0.0049	1.044e-4
^{92}Zr	17.15%	0.0216	842	9.2596	0.0077	1.555e-4
^{94}Zr	17.38%	0.0211	861	8.4790	0.0071	1.631e-4
^{96}Zr	2.80%	0.0207	879	8.4790	0.0017	3.660e-5
Zr	100%	0.0217	839	8.6052	0.0413	8.980e-4

Natural molybdenum is an alternative metallic fuel alloy to Zr, and is made up of seven isotopes: ^{92}Mo, $^{94\text{-}98}$Mo and ^{100}Mo. Its moderating characteristics are similar to that of zirconium, but a slightly higher atomic mass and a slightly smaller scattering cross-section makes its slowing down power ∼10% lower than that of zirconium. The moderating characteristics of molybdenum are given in Table 2.8.

Table 2.8: Moderating parameters of molybdenum at 10% FIMA burnup

Isotope	Nat. ab.	ξ	n	σ_s	Σ_s	$\xi\Sigma_s$
^{92}Mo	14.83%	0.0216	842	8.3253	0.0052	1.129e-4
^{94}Mo	9.25%	0.0211	861	8.2140	0.0031	0.649e-4
^{95}Mo	15.92%	0.0209	870	8.1589	0.0054	1.123e-4
^{96}Mo	16.68%	0.0207	879	8.2369	0.0065	1.341e-4
^{97}Mo	9.55%	0.0205	888	8.0047	0.0036	0.742e-4
^{98}Mo	24.13%	0.0203	897	8.1142	0.0090	1.833e-4
^{100}Mo	9.63%	0.0199	915	7.9018	0.0038	0.755e-4
Mo	100%	0.0207	879	8.1463	0.0366	7.572e-4

Oxygen exists in nature as three isotopes - ^{16}O , ^{17}O and ^{18}O. Experimental nuclear data exist for both ^{16}O and ^{17}O and is included in calculations. Unfortunately there is no available cross-section data for the scattering of ^{18}O. The available data on absorption of ^{18}O suggests its total microscopic cross-sections are significantly larger than that of ^{16}O. However, its low concentration make it less relevant for neutronic considerations. The moderating characteristics of oxygen are given in Table 2.9.

Table 2.9: Moderating parameters of oxygen at 10% FIMA burnup

Isotope	Nat. ab.	ξ	n	σ_s	Σ_s	$\xi\Sigma_s$
^{16}O	99.762%	0.1200	152	3.6799	0.0830	0.00996
^{17}O	0.038%	0.1132	161	2.5617	2.066e-5	2.34e-6
^{18}O	0.2%	0.1071	170	N/A	N/A	N/A
O	100%	0.1200	152	3.6794	0.0830	0.00996

Nitrogen in natural composition is composed of 99.634% ^{14}N and 0.366% ^{15}N. Natural nitrogen is however not used in nuclear fuel, because neutron capture in ^{14}N leads to the production of ^{14}C. Enriching the nitride in the ^{15}N isotope both reduces the radiotoxicity of the fuel and reduces parasitic absorption in the core. ^{14}C is also produced by the (n,d) reaction in ^{15}N, but the effective cross-section of this reaction is ∼13 times smaller than the (n,p) reaction in ^{14}N. Because of this, nitrogen in nuclear fuel is typically highly enriched in the ^{15}N isotope, potentially up to 99.9%. For this study the ^{15}N enrichment has been assumed to be 99%, readily achievable by chemical separation methods [56]. The difference in neutron moderation by varying the ^{14}N/^{15}N ratio is very small, since the effective scattering cross-sections of the two isotopes differ by only ∼15%. (The capture-difference is significantly larger, as ^{15}N has ∼1/5 of the microscopic capture cross-section of ^{14}N.) The moderating characteristics of natural nitrogen are given in Table 2.10.

Table 2.10: Moderating parameters of nitrogen at 10% FIMA burnup

Isotope	Nat. ab.	ξ	n	σ_s	Σ_s	$\xi\Sigma_s$
^{14}N	99.634%	0.1362	134	4.330	7.303e-04	9.946e-05
^{15}N	0.366%	0.1276	143	3.711	0.0588	0.0075
N	100%	0.1277	143	3.718	0.0595	0.0076

Carbon exists in nature in the form of two isotopes: 98.89% ^{12}C and 1.11% ^{13}C. In the ENDF/B cross-section library, carbon cross-sections are not divided up in to isotopes but are given for the element. The moderating characteristics of carbon are given in Table 2.11.

Table 2.11: Moderating parameters of carbon at 10% FIMA burnup

Isotope	Nat. ab	ξ	n	σ_s	Σ_s	$\xi\Sigma_s$
^{12}C	98.89%	0.1578	115	N/A	N/A	N/A
^{13}C	1.11%	0.1462	124	N/A	N/A	N/A
C	100%	0.1576	115	3.9381	0.0591	0.0081

Assuming that carbon exists as an element rather than individual isotopes in the core introduces a slight error in the calculations of the neutron spectrum. However, as seen in the results of ξ and n in Table 2.11, the error introduced by this approximation is negligible.

The resulting estimation of the moderating properties of the selected non-actinide components of fuel is summarized in Table 2.12 visualized in Fig. 2.19.

Table 2.12: Moderating parameters of non-actinides in fuel at 10% FIMA burnup

Element	ξ	n	σ_s (barn)	Σ_s	$\xi\Sigma_s$
Zr	0.0217	839	8.605	0.0413	8.980e-4
Mo	0.0207	879	8.146	0.0366	7.572e-4
O	0.1200	152	3.679	0.0830	9.960e-3
N	0.1277	143	3.718	0.0595	7.600e-3
C	0.1576	115	3.938	0.0591	8.100e-3

The metallic fuels moderate by elastic scattering about an order of magnitude less than the ceramic options. Zr and Mo however have significantly lower energy thresholds for inelastic scattering and higher one-group inelastic scattering cross-sections, which reduces the effective difference in spectra to the ceramic options. Among ceramic options, nitride and carbide outperform oxide. Oxygen has a smaller elastic scattering cross-section and a higher atomic mass than carbon and nitrogen. It is its chemical form (UO_2) that is the cause of the poor performance compared to mononitride (UN) and monocarbide (UC) as it has two non-actinides per actinide. The reason it is not roughly twice as moderating as carbide and nitride is that its nominal density at fabrication is ∼20-25% lower than the other ceramics, and thus the atomic density of non-actinides is correspondingly lower. The combined effect of lower density, lower scattering cross-section, higher atomic mass and two non-actinides per actinides in the fuel combine to make oxide fuel the poorest performing fuel choice with regards to moderation for B&B cores. There is only a small difference between the two metallic fuel options as well as between nitride & carbide.

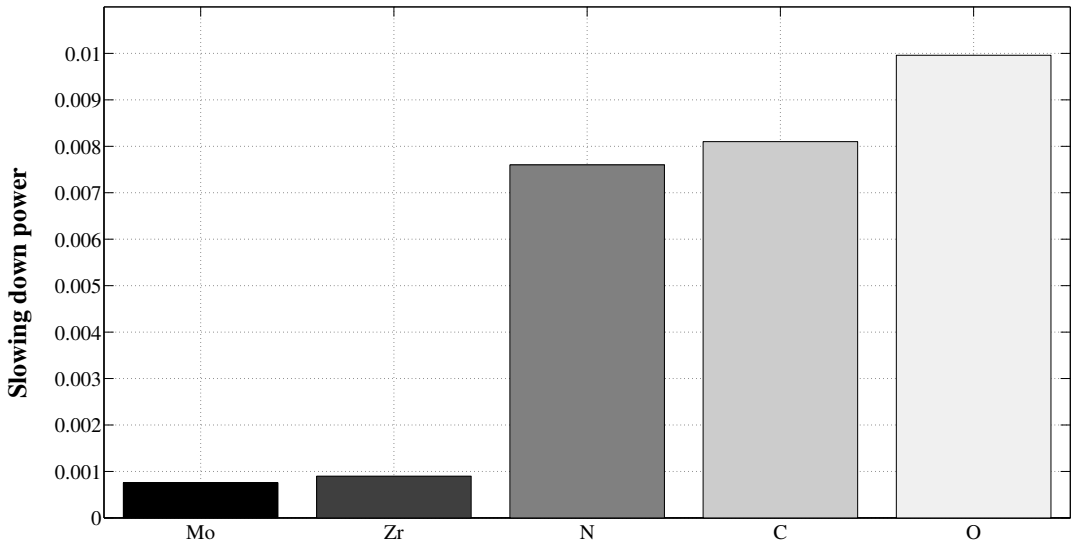

Figure 2.19: The *slowing down power* by elastic scattering of fuel non-actinides at 10% FIMA

The averaged neutron flux spectra in the unit cell (containing all core materials) collapsed to 10, 20 and 500 groups are shown in Figures 2.20-2.22. The common features of the flux spectrum (seen most clearly in Fig. 2.22) result from resonance reactions in fuel, structure and coolant. Where they differ in shape, a resonance in the chosen non-actinide component of the fuel is responsible. The most notable difference is the depletion in flux around 0.43 MeV in the oxide core. This is due to an elastic scattering resonance (shown in Fig. 2.23) in ^{16}O that causes energy shelf-shielding, depleting the flux around the resonance and enhancing it at the adjacent energy levels. A similar ^{16}O resonance is located at almost exactly 1 MeV, and its effect can also be clearly seen in Fig. 2.22.

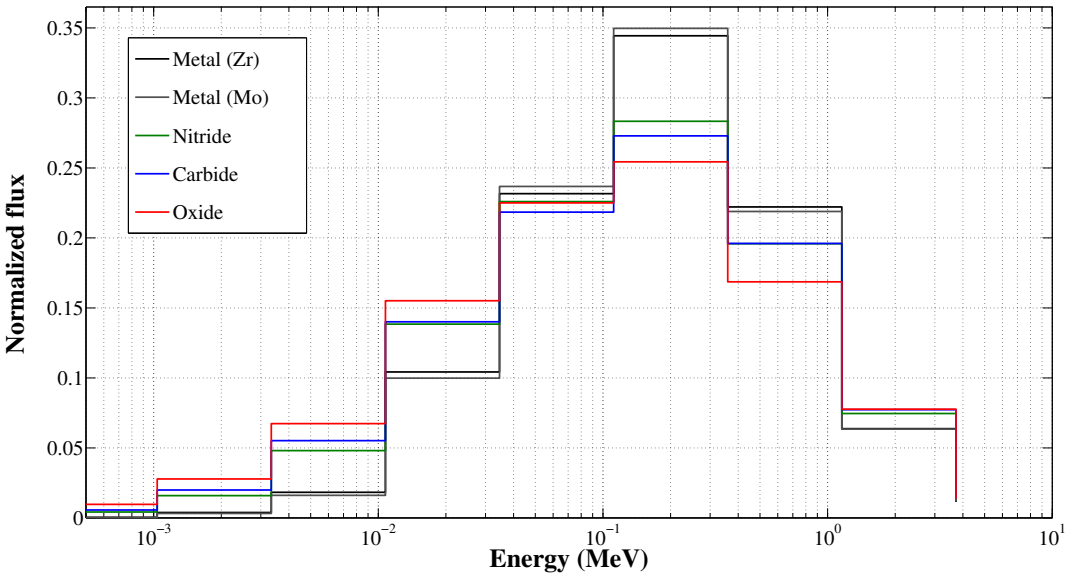

Figure 2.20: 10-group flux by fuel type

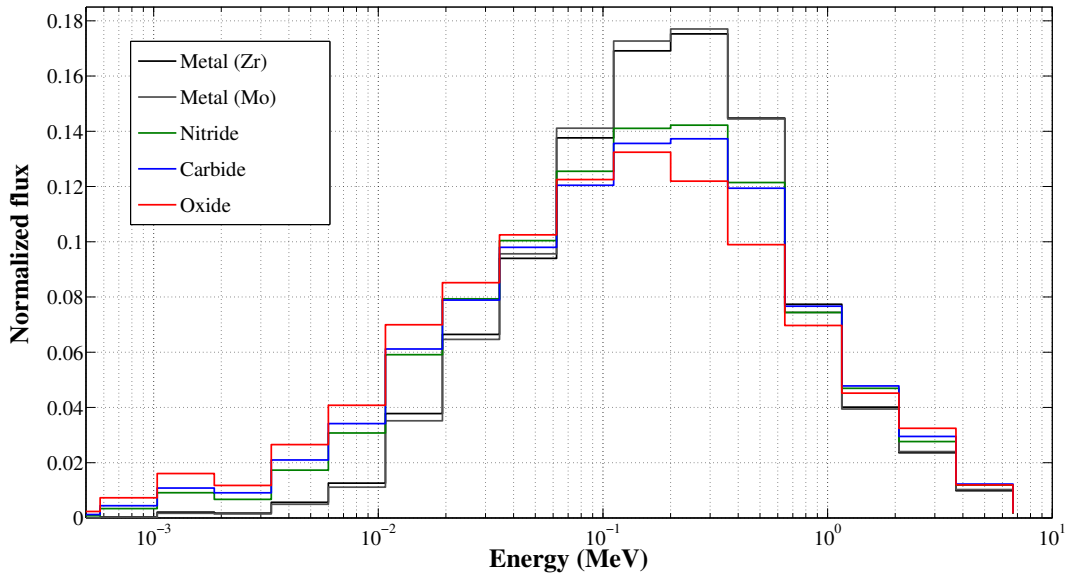

Figure 2.21: 20-group flux by fuel type

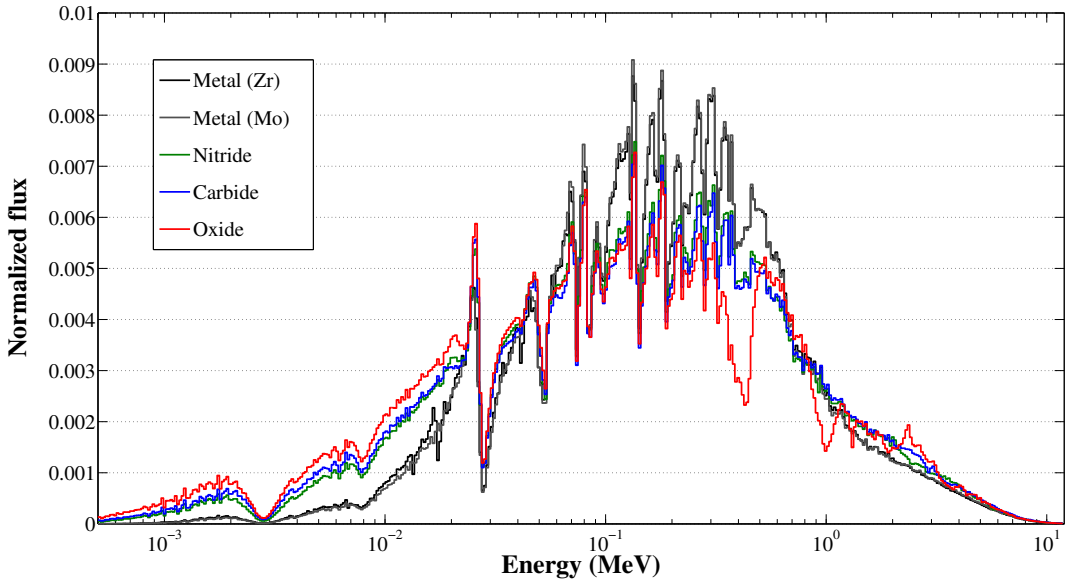

Figure 2.22: 500-group flux by fuel type

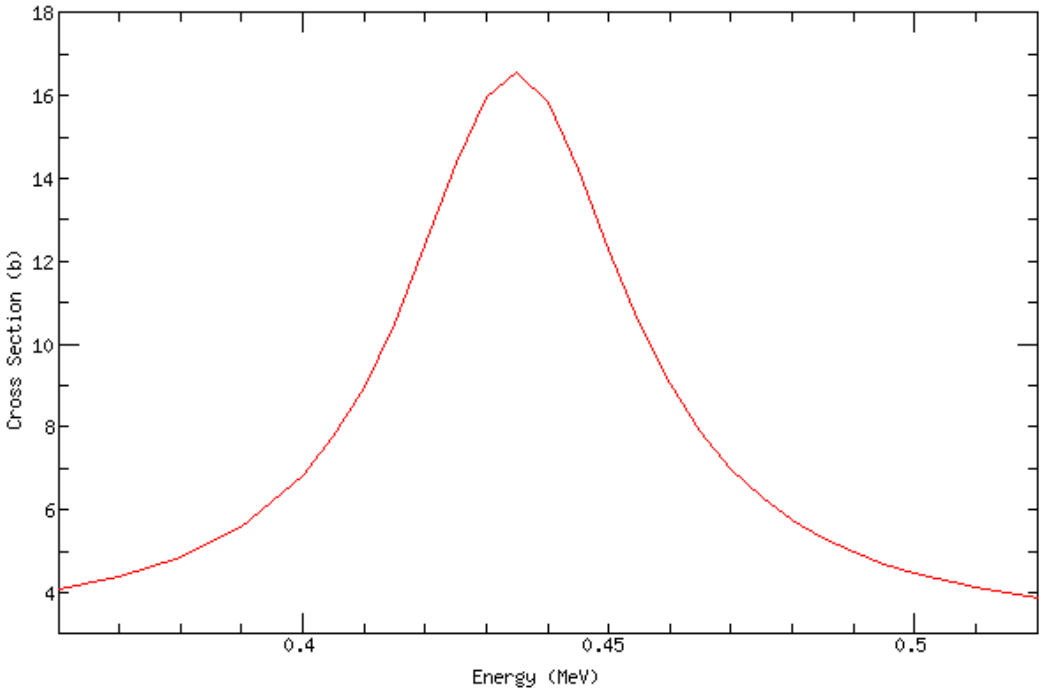

Figure 2.23: The 0.43 MeV resonance in ^{16}O (total neutron cross-section from ref. [57])

The corresponding fast (E>0.1 MeV) flux fractions are given in Table 2.13. Calculations were performed in a unit-cell using the Serpent monte-carlo neutron transport code [47] and ENDF/B-VII.0 cross-sections [48]. The fraction of fast flux using metallic fuels is ∼14% higher than carbide & nitride and ∼25% higher than in the oxide-based core. These results are in line with expectations from the moderation study and the comparison of slowing down powers.

Table 2.13: Unit cell flux fractions at 10% FIMA by fuel type

Fuel type	Flux fraction > 0.1 MeV
Metal (10-Zr)	0.6704
Metal (10-Mo)	0.6731
Oxide	0.5379
Nitride (99% N-15)	0.5918
Carbide	0.5835

Absorption in non-actinide fuel components may also play some role in determining the neutron flux spectrum. This is especially true if a non-actinide fuel isotope has a strong resonance absorption reaction at a specific energy level. However, in a fast spectrum, scattering reactions dominate the overall reaction rate completely, so any difference in absorption cross-sections will have a much smaller effect on the spectrum. Scattering events constitute around 98% of all reactions occurring in the core, which means the neutron flux spectrum is determined almost entirely by scattering. On average there are ∼45 scattering reactions for every neutron lost to capture or fission. Table 2.14 details the distribution of events in differently fueled cores at 10% FIMA burnup.

Table 2.14: Normalized reaction rates by reaction type at 10% FIMA

Fuel	Fission	Capture	Absorption	Scatter	Scatter/Absorption
Metal (Zr)	0.0086	0.0124	0.0210	0.9790	46.6
Metal (Mo)	0.0085	0.0134	0.0219	0.9781	44.7
Carbide	0.0088	0.0142	0.0230	0.9770	42.5
Nitride	0.0086	0.0136	0.0222	0.9778	44.0
Oxide	0.0088	0.0141	0.0229	0.9771	42.7

2.5.2 Neutron capture by non-actinides in the fuel

The parasitic capture of neutrons by non-actinide components in the fuel has a small impact on core performance, but it helps to explain some of the differences seen in performance between otherwise similar fuel options. In B&B reactors, with a significantly higher core-averaged fuel volume fraction than in a conventional fast reactor seed fuel assembly, differences in fuel constituents are correspondingly more important. The capture parameters of zirconium, molybdenum, oxygen, nitrogen and carbon are given in Table 2.15-2.19. The spectrum-averaged capture cross-sections of carbon, oxygen and nitrogen are near-negligible small. The metallic fuel alloying components molybdenum and zirconium have capture cross-sections 5 orders of magnitude larger. The situation is most severe for ^{95}Mo and ^{97}Mo, which have capture cross-sections of $\sim$0.2 barn, comparable to actinide cross-sections for fission and capture. Consequently, capture in fuel non-actinides is about $\sim$5 times higher in molybdenum-based fuel than in fuel alloyed with zirconium. Since both moderation and actinide density is very similar for both fuel types, some of the difference in performance stems from this difference.

Table 2.15: Capture parameters of zirconium at 10% FIMA burnup

Isotope	σ_a (barn)	Σ_a (1/cm)
^{90}Zr	0.0096	2.263e-5
^{91}Zr	0.0323	1.827e-5
^{92}Zr	0.0291	2.407e-5
^{94}Zr	0.0190	1.580e-5
^{96}Zr	0.0072	1.496e-6
Zr	0.0171	8.236e-5

Table 2.16: Capture parameters of molydenum at 10% FIMA burnup

Isotope	σ_a (barn)	Σ_a (1/cm)
^{92}Mo	0.0396	2.483e-5
^{94}Mo	0.0662	2.473e-5
^{95}Mo	0.1914	1.259e-4
^{96}Mo	0.0587	4.617e-5
^{97}Mo	0.1919	8.677e-5
^{98}Mo	0.0565	6.291e-5
^{100}Mo	0.0460	2.211e-5
Mo	0.0875	3.734e-4

Table 2.17: Capture parameters of oxygen at 10% FIMA burnup

Isotope	σ_a (barn)	Σ_a (1/cm)
^{16}O	1.4618e-07	3.2977e-09
^{17}O	5.3215e-05	4.2918e-10
O	1.6740e-7	3.7269e-09

Table 2.18: Capture parameters of nitrogen at 10% FIMA burnup

Isotope	σ_a (barns)	Σ_a (1/cm)
^{14}N	5.4196e-05	9.1402e-09
^{15}N	1.1964e-05	1.8964e-07
N	1.2407e-05	1.9878e-07

Table 2.19: Absorbing parameters of carbon at 10% FIMA burnup

Isotope	σ_a (barns)	Σ_a (1/cm)
C	5.4196e-05	9.1402e-09

2.5.3 Summary

The multiplication factor in an infinite medium with smeared materials using one-group cross-sections is given by:

$$k_\infty = \frac{\overline{\nu}\Sigma_f}{\Sigma_f + \Sigma_c} = \overline{\nu}\frac{\Sigma_f}{\Sigma_a} = \overline{\nu}\frac{N\sigma_f}{N\sigma_a} = \overline{\nu}\frac{\sigma_f}{\sigma_a} \tag{2.26}$$

The core-averaged parameters involved in determining the multiplication factor are given in Table 2.20-2.23 for 5, 10, 15 and 20% FIMA burnup. There is little change in $\overline{\nu}$ between fuel options, but the relative capture and fission cross-sections show significant differences. For the metallic fuel options, the larger absorption cross-section of molybdenum compared to zirconium gives it a noticeable disadvantage. There is little absorption in the non-actinide components of the ceramic fuel types, here the amount of spectral softening determine the relative neutron economy. The results are in line with what is expected from the slowing down comparison of Fig. 2.19, with nitride slightly better than carbide and both of them leaving oxide far behind.

Table 2.20: k_∞ components at 5% FIMA burnup

Fuel	σ_f	σ_c	σ_f/σ_c	σ_f/σ_a	$\overline{\nu}$	k_∞
Metal (Zr)	0.0022	0.0037	0.5924	0.3720	2.9052	1.0808
Metal (Mo)	0.0021	0.0038	0.5481	0.3540	2.9064	1.0290
Carbide	0.0025	0.0046	0.5337	0.3480	2.9060	1.0112
Nitride	0.0026	0.0047	0.5452	0.3528	2.9049	1.0250
Oxide	0.0020	0.0040	0.4939	0.3306	2.9036	0.9600

Table 2.21: k_∞ components at 10% FIMA burnup

Fuel	σ_f	σ_c	σ_f/σ_c	σ_f/σ_a	$\overline{\nu}$	k_∞
Metal (Zr)	0.0025	0.0037	0.6757	0.4077	2.9166	1.1892
Metal (Mo)	0.0024	0.0038	0.6377	0.3894	2.9164	1.1358
Carbide	0.0029	0.0046	0.6304	0.3837	2.9184	1.1198
Nitride	0.0030	0.0047	0.6383	0.3890	2.9178	1.1350
Oxide	0.0023	0.0040	0.5750	0.3652	2.9164	1.0651

Table 2.22: k_∞ components at 15% FIMA burnup

Fuel	σ_f	σ_c	σ_f/σ_c	σ_f/σ_a	$\overline{\nu}$	k_∞
Metal (Zr)	0.0026	0.0037	0.6938	0.4096	2.9199	1.1960
Metal (Mo)	0.0025	0.0038	0.6443	0.3919	2.9207	1.1445
Carbide	0.0029	0.0046	0.6335	0.3878	2.9227	1.1334
Nitride	0.0030	0.0047	0.6465	0.3926	2.9225	1.1475
Oxide	0.0024	0.0040	0.5864	0.3696	2.9214	1.0799

Table 2.23: k_∞ components at 20% FIMA burnup

Fuel	σ_f	σ_c	σ_f/σ_c	σ_f/σ_a	$\overline{\nu}$	k_∞
Metal (Zr)	0.0025	0.0037	0.6799	0.4047	2.9220	1.1827
Metal (Mo)	0.0024	0.0039	0.6325	0.3875	2.9228	1.1325
Carbide	0.0029	0.0047	0.6236	0.3841	2.9256	1.1237
Nitride	0.0030	0.0047	0.6364	0.3889	2.9240	1.1371
Oxide	0.0024	0.0041	0.5803	0.3672	2.9244	1.0739

The neutron balance integral of the different chemical forms of fuel, as defined by equation 2.14 (excluding U-Mo), given in moles per cm^3 is shown in Fig. 2.24. A similar study was presented by *Petroski et. al.* for a unit cell containing only fuel material [58].

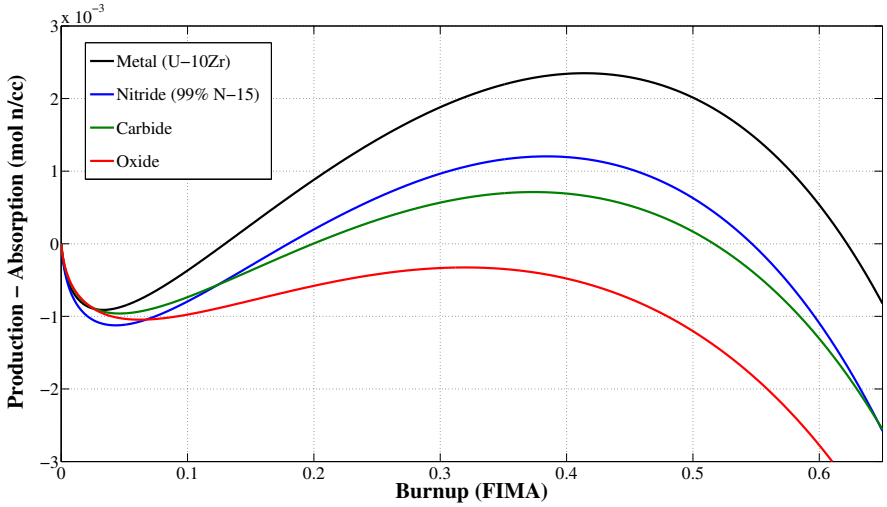

Figure 2.24: Neutron balance in moles of neutrons per cubic centimeter

2.6 The extended neutron balance method (*ENB*)

The extended neutron balance method (*ENB*) is a recently developed analysis method based on the neutron balance principle [38]. Using *ENB*, the impacts of core design variables on the available B&B design space can be defined. With it, it is also possible to develop expressions for the relative change in minimum required discharge burnup at a given level of neutron loss (leakage + loss to control elements) for any set core design parameter. The *ENB* method involves the following 9 steps:

1. Run neutron transport & depletion (0-100% FIMA) for a specific core design in a 0D-model. To ensure accuracy, 0.1% FIMA burnup-steps are used until 4% burnup, then 0.5% steps until 15% burnup and finally 5-10% steps until 100% FIMA. The total number of burnup steps is ∼70-80.

2. Collect data for the burnup-dependent value of infinite multiplication factor (k_{inf}) and the average number of neutrons released per fission (ν).

3. Develop 5^{th}-order rational curve-fits to this data using the Levenberg-Marquardt algorithm [49] until the root mean squared error (RMSE) of the fit falls below 5×10^{-4}.

4. Solve the neutron balance equation:

$$\int^{\text{BU}} \bar{\nu}\,(\text{BU}) \left(1 - \frac{1}{k_{\infty}\,(\text{BU}) \times (1-Q)}\right) \text{dBU} = 0 \tag{2.27}$$

   using the expressions developed in step (3), at increasing levels of total neutron loss (Q) until no solution is found (this point is defined as the neutron loss-limit).

5. Run steps (1-4) again while varying a design parameter (such as fuel volume fraction, Zr-content in fuel etc.). Define from the results of step (4) the minimum required burnup at each level of total neutron loss for each value of the design parameter that is being varied. Step 1-5 enables the definition of the B&B reactor design space as is shown by the area enclosed by the curves in Figure 2.25.

6. For each level of total neutron loss, develop a linear curve-fit of the type:

$$\text{BU}_{\text{min}} = p_1 X + p_2 \tag{2.28}$$

   This expression correlates the minimum required burnup (BU_{min}) and the design parameter (X).

7. Introduce a neutron loss-dependency (L) by developing double-exponential curve-fits to the values of p_1 and p_2 of the form of:

$$p_1(L) = q_1 e^{q_2 L} + q_3 e^{q_4 L} \tag{2.29}$$

$$p_2(L) = w_1 e^{w_2 L} + w_3 e^{w_4 L} \tag{2.30}$$

8. The expressions developed in step (6) can then be generalized with the neutron-loss dependent expression:

$$\mathrm{BU}_{\min} = \left(q_1 e^{q_2 L} + q_3 e^{q_4 L}\right) X + w_1 e^{w_2 L} + w_3 e^{w_4 L} \tag{2.31}$$

9. Finally, the effect of a design variable perturbation can be evaluated by differentiating the expression developed in step (8) with regards to the design variable (X).

Steps 1-9 constitute the *extended neutron balance method* (ENB) and can be used very effectively to both define the B&B reactor design space and to estimate the impact on minimum required burnup by changing certain design parameters. Figure 2.25 shows step (5) of the *ENB* process for a varying fraction of Zirconium in the fuel of a sodium cooled reactor with a P/D of 1.09 (given in detail in Section 2.7.2).

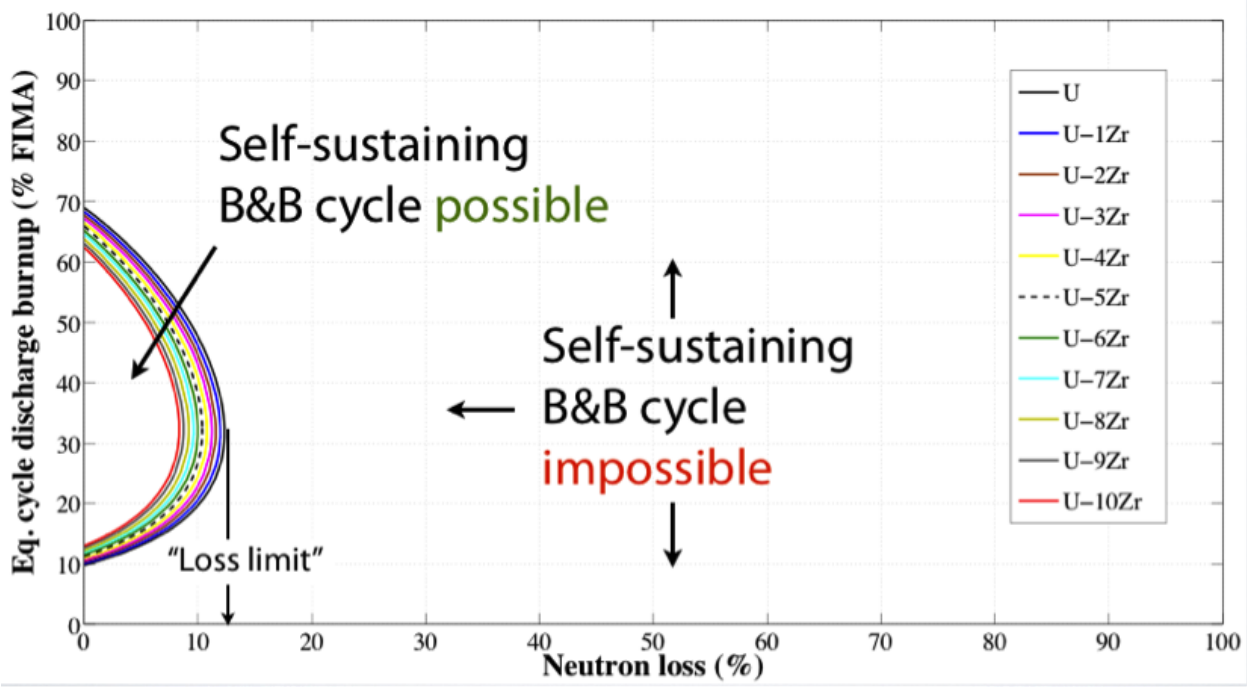

Figure 2.25: The B&B design space for with a varying design parameter (X = Zr-content in fuel)

Using step (9) of *ENB*, the effects of varying design parameters in sodium cooled B&B reactors, starting from a reference design of P/D=1.09, ^{235}U in feed fuel of 0.2%, Zr-content in fuel of 6% and a total neutron loss level of 6% is visualized in Figure 2.26. The studies performed in order to obtain the values that make up Figure 2.26 are given in the following sections.

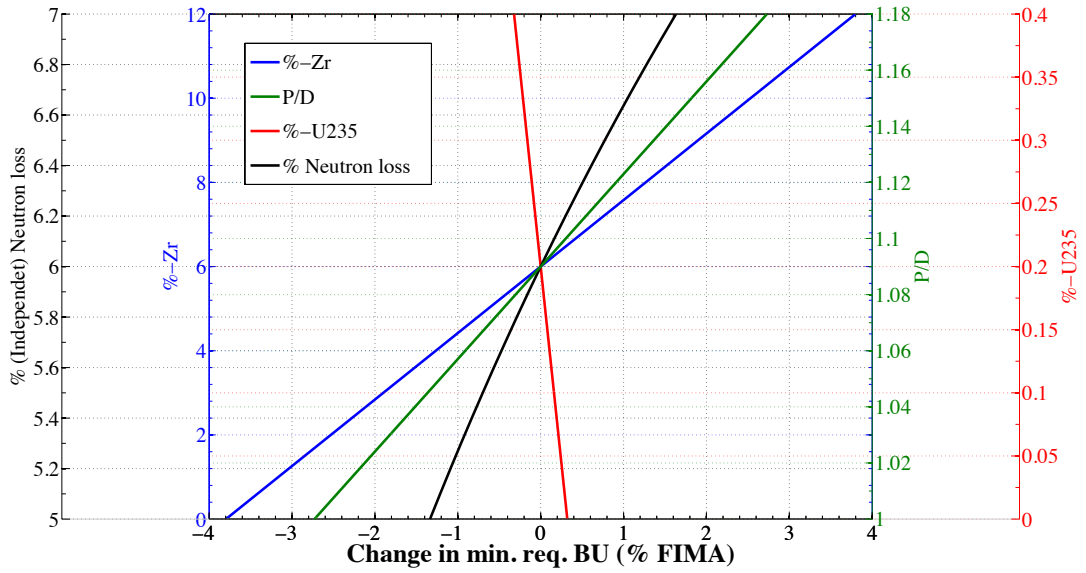

Figure 2.26: The effects of design parameter variation in a sodium-cooled B&B reactor at 6% nominal neutron loss

2.7 Core design parameter impact on neutron economy

2.7.1 Fuel type

Using the same analysis principles as explained in Section 2.6, the design space of B&B reactors by fuel type are given in Figures 2.27 and 2.28. The area to the left of the lines to the y-axis is the available design space. The superiority of metallic fuel options for B&B cores is clearly illustrated. The oxide fueled core cannot sustain a B&B mode of operation at any level of burnup even at zero neutron loss, and it is thus not shown in the graphs.

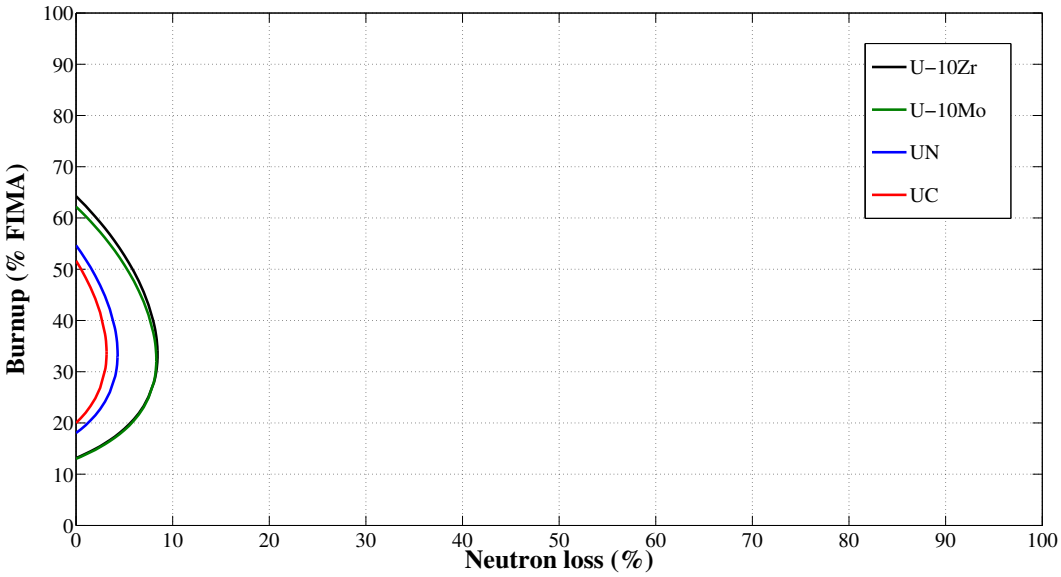

Figure 2.27: The design space of a sodium-cooled B&B reactor by fuel type

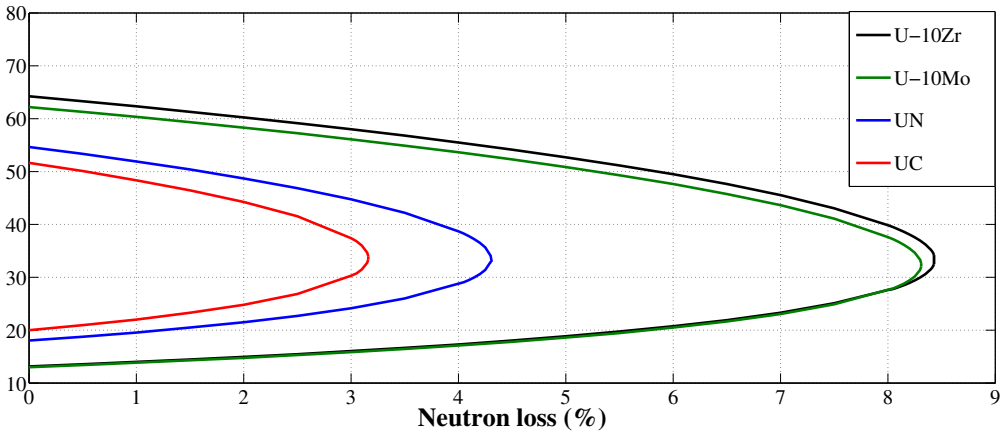

Figure 2.28: The design space of a sodium-cooled B&B reactor by fuel type

The minimum and maximum attainable B&B burnups by fuel type (matching the neutron balance analysis of Section 2.5) is given in Table 2.24. As neutron loss to leakage and control elements below 4% is not likely to be attainable, the *only* realistic fuel option for B&B cores is metallic fuel.

Table 2.24: B&B burnup and loss-limits by fuel type (P/D = 1.088)

Fuel type	Min. BU (% FIMA)	Max. BU (% FIMA)	Loss-limit (%)
U-10Zr	13.15	64.25	8.43
U-10Mo	13.00	62.20	8.31
UN	18.05	54.65	4.31
UC	20.00	51.65	3.16

2.7.2 Non-actinide content in metallic fuel

While the ceramic fuel options are more or less set in their actinide/non-actinide content (slightly sub or overstoichiometric options are possible but have a negligible impact), the non-actinide content in metallic alloys can vary freely. This design variable turns out to be one of the most important parameters for B&B reactor performance. Since uranium density is nearly three times higher than its alloying elements (zirconium or molybdenum), the alloy density falls off quickly with increasing non-actinide content (see Table 2.25).

Table 2.25: Core-averaged actinide & fuel density by fuel Zr-content (P/D = 1.088)

Zr w%	Atoms/cm^3 $\times$ 10^{22}	Moles/cm^3	Fuel density at 650°C (g/cm^3)
0	2.0482	0.0340	18.4
1	1.9938	0.0331	18.1
2	1.9411	0.0322	17.8
3	1.8900	0.0314	17.5
4	1.8405	0.0306	17.2
5	1.7926	0.0298	17.0
6	1.7461	0.0290	16.7
7	1.7009	0.0282	16.4
8	1.6571	0.0275	16.2
9	1.6146	0.0268	15.9
10	1.5721	0.0261	15.7

The neutron balance integral at 0% neutron loss is given in Figures 2.29 & 2.30 (zoomed in). To illustrate a more realistic scenario, the neutron balance is given in moles/cm^3 of core at 5% neutron loss in Figures 2.31 & 2.32 (zoomed in).

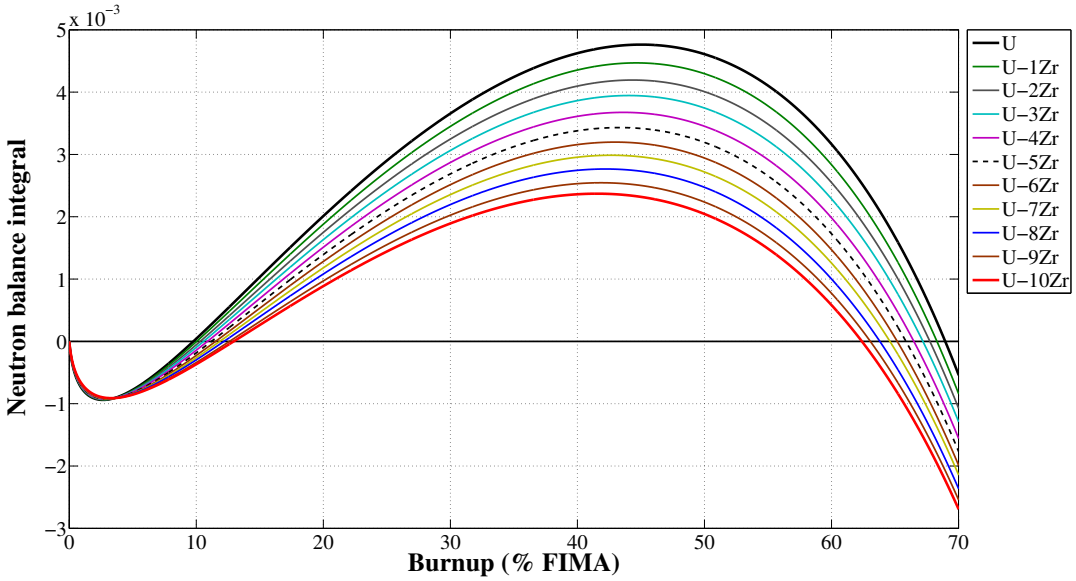

Figure 2.29: Neutron balance by non-actinide content in metallic fuel (loss = 0%) (1)

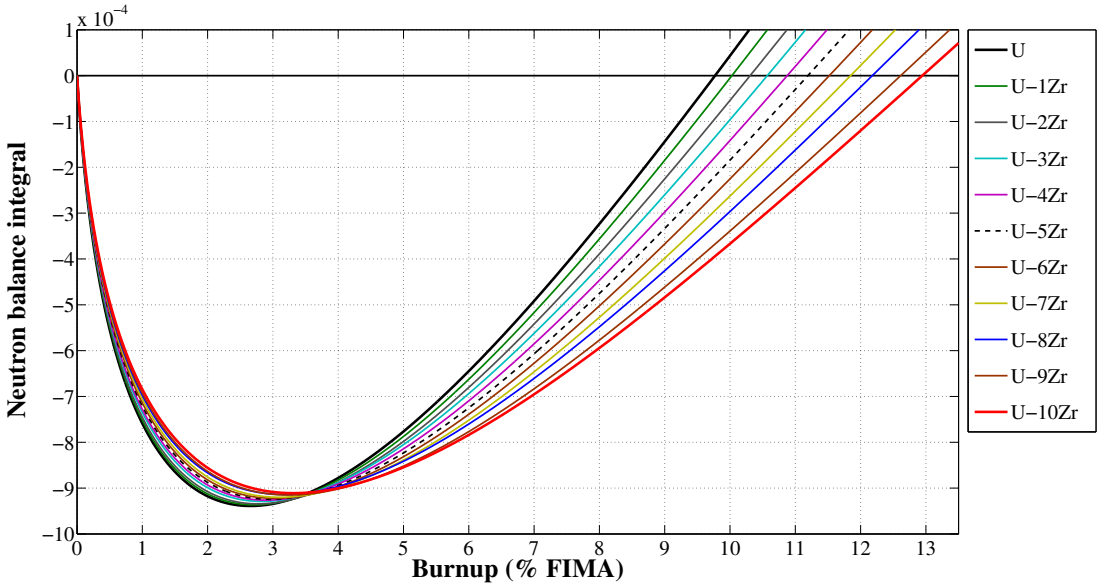

Figure 2.30: Neutron balance by non-actinide content in metallic fuel (loss = 0%) (2)

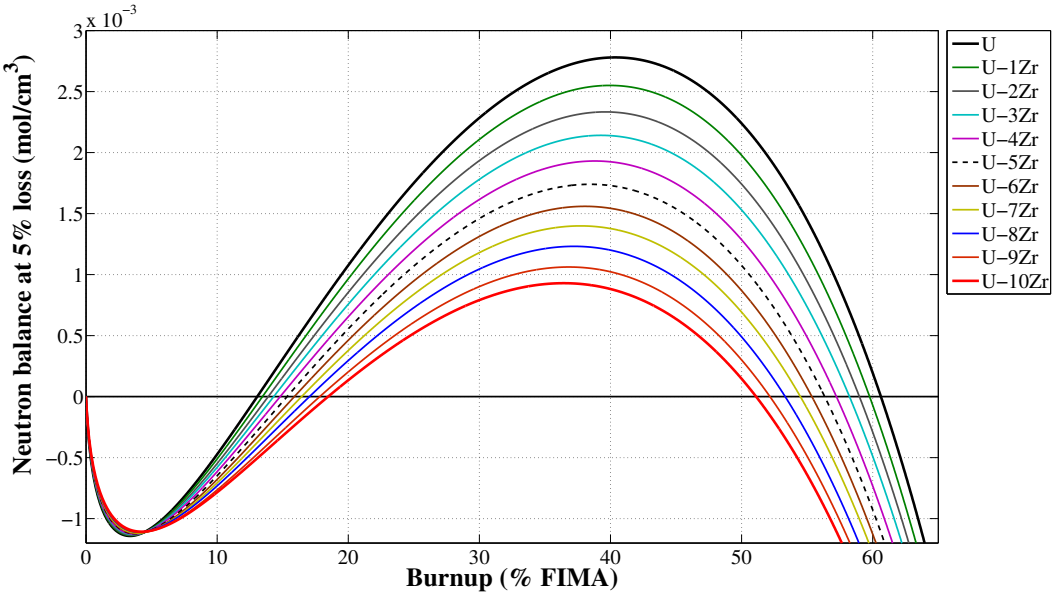

Figure 2.31: Neutron balance by non-actinide content in metallic fuel (loss = 5%) (1)

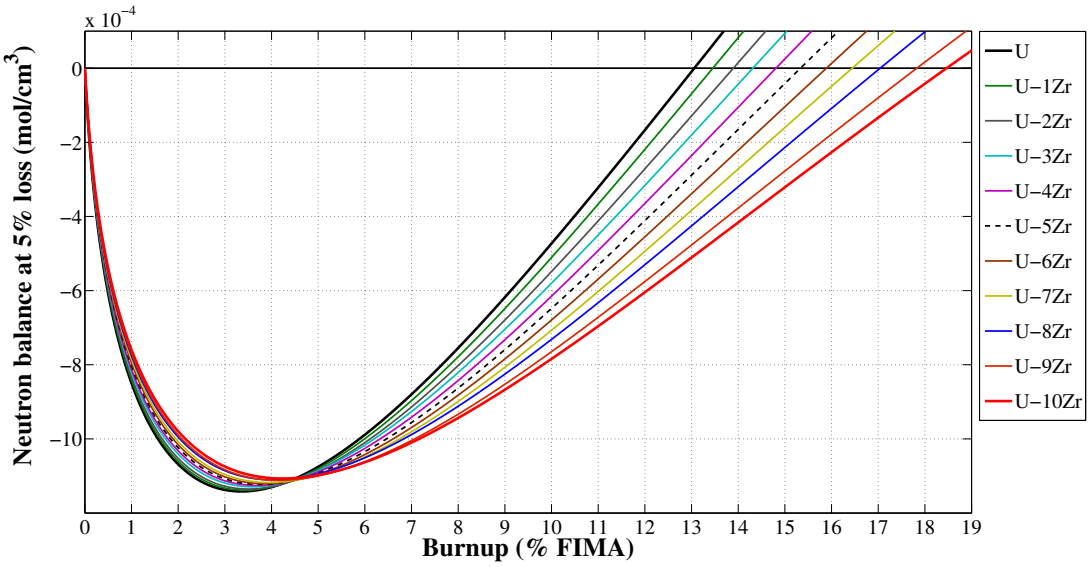

Figure 2.32: Neutron balance by non-actinide content in metallic fuel (loss = 5%) (2)

The available B&B design space at different Zr-contents in the fuel are given in Figures 2.33-2.35 at different levels of zoom. Again, the area to the left of the curves to the axis of the plot is the design space where B&B operation is possible, outside of the curves B&B operations cannot be sustained. The effect of reducing the alloying component is clearly seen in both the neutron balance and neutron design-space plots. As the average disharge burnup approaches its neutronic optima at around 32% FIMA, the differences in maximum allowable neutron loss are at its maximum (about 4% difference). The neutron *loss-limit*, the maximum amount of neutron loss in which a B&B mode of operation can be sustained at the neutronic optimum level of average disharge burnup, is given in Figure 2.36.

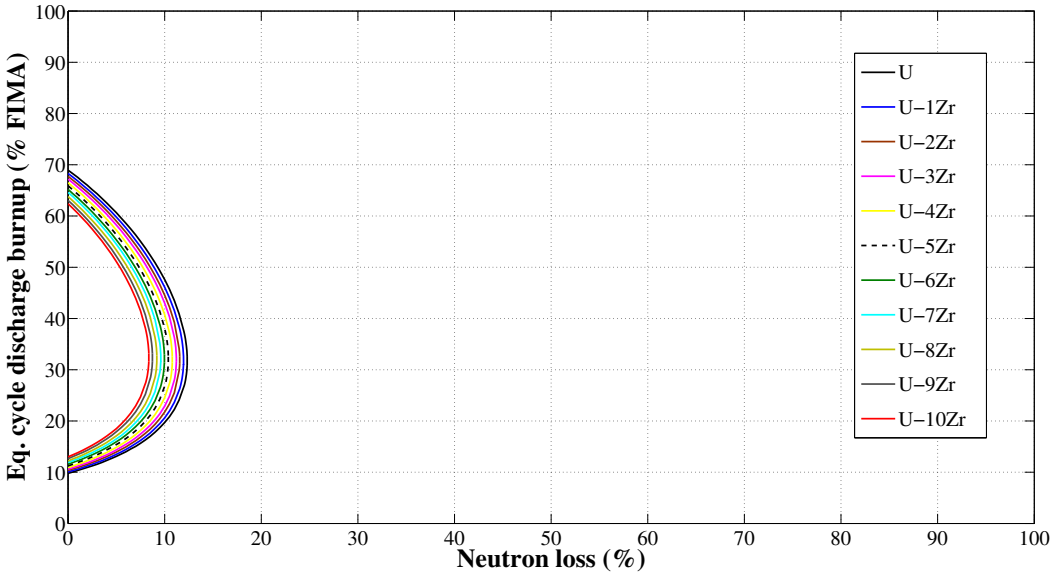

Figure 2.33: B&B design space by non-actinide content in metallic fuel (1)

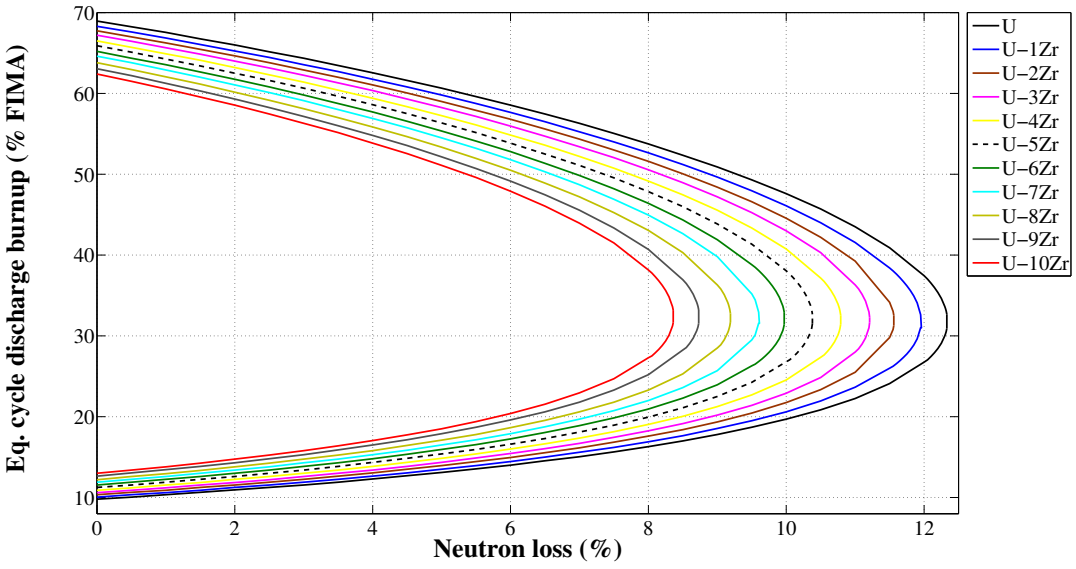

Figure 2.34: B&B design space by non-actinide content in metallic fuel (2)

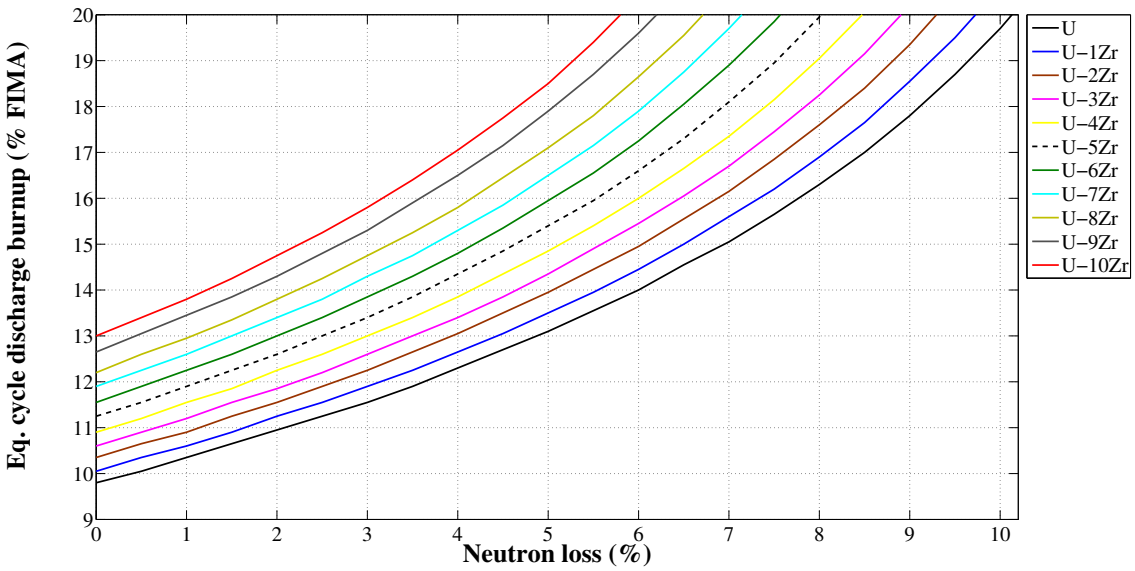

Figure 2.35: B&B design space by non-actinide content in metallic fuel (3)

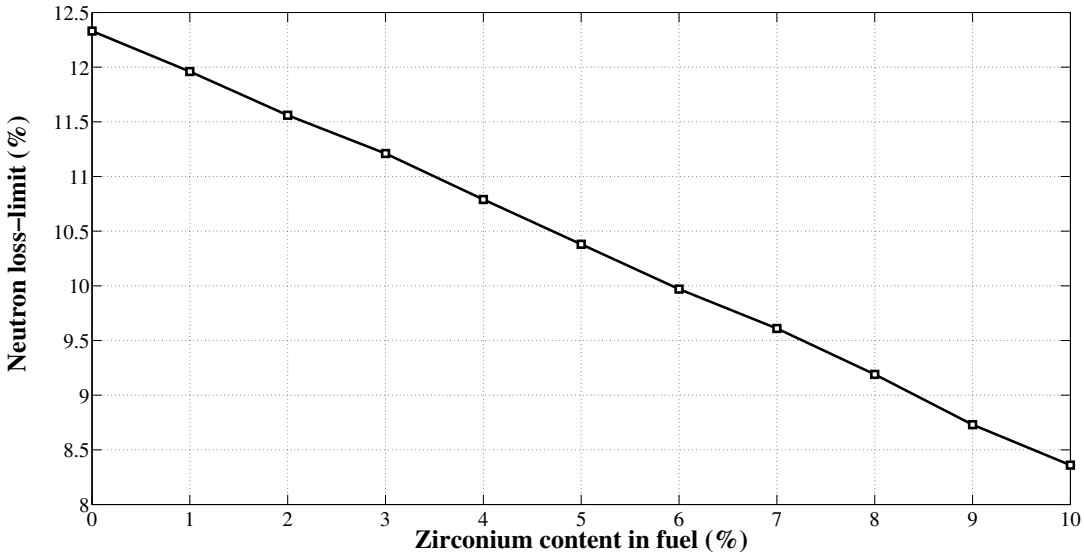

Figure 2.36: B&B loss-limit by non-actinide content in metallic fuel

The calculated values have been fitted using the methodology presented in Section 2.6.

The expression relating metallic fuel non-actinide content and minimum burnup is:

$$\begin{aligned} \mathrm{BU}_{\min} &= \mathrm{Zr}\,(\%) \times \left[0.3159 \times e^{0.0862\times \mathrm{L}} + 0.001978 e^{0.6583\times \mathrm{L}}\right] \\ &+ \left[1.229 \times e^{-0.09662\times \mathrm{L}} + 8.476 \times e^{0.07107\times \mathrm{L}}\right] \end{aligned} \tag{2.32}$$

where BU is the burnup in %-FIMA and L is the neutron loss in %. Eq. 2.32 is valid in the ranges $0 \leq Zr \leq 10\%$ and $0 \leq L \leq 8\%$.

Using eq. 2.32, the relative impact of neutron loss and actinide content can be quantified. Some of the results from using eq. 2.32 are given in Table 2.26.

Table 2.26: Burnup levels by non-actinide content in fuel (P/D = 1.088)

Case	Loss (%)	Zr-content (%)	Burnup (%FIMA)	ΔBurnup (%FIMA)
Reference	0	0	9.71	0.0
Max. loss	8	0	15.53	5.83
Max. Zr	0	10	12.88	3.18
Max Loss + Zr	8	10	25.66	15.96
Opt. B&B*	4	2	13.04	3.34
Good B&B	5	6	16.09	6.38
Ref. B&B	6	10	20.00	10.29

* Based on a large number core design studies performed as a part of the work presented in this thesis, it does not appear feasible to design a realistic B&B system with a core volume less of ∼20 m^3 with a total neutron loss level below 4%. A Zr-content below 2% is not recommended as melting temperature, fuel-cladding eutectic formation protection and dimensional irradiation stability are all negatively affected by reducing the fuel Zr-content. A level of 4% neutron loss and 2% Zr-content is therefore denoted as optimistic optimal B&B core parameters.

As is clearly seen in Table 2.26, the relative effect on burnup of the non-actinide (zirconium) content is nonlinearly dependent on the neutron loss fraction. At 0% neutron loss, the impact on burnup by going from pure uranium metal to U-10Zr is 3.18% FIMA. At 8% neutron loss, the impact has increased to 10.13% FIMA. For a leaky core, it is doubly advantageous to decrease the non-actinide content of the fuel. While the minimum required burnup is higher for a leaky core, this can more effectively be counteracted by a reduction in the non-actinide content in the fuel. Low Zr-alloy fuel (2% Zr) in a leaky core (L = 8%) has the same B&B neutronic performance as a low-leakage core (L=4%) with a more conventional metallic fuel alloy (7.5% Zr).

The relative change in minimum required burnup (in % FIMA) per % of Zr added or subtracted to/from the fuel can be evaluated by differentiating eq. 2.32 as:

$$\frac{d\,(\mathrm{Zr}\%)}{d\,(\mathrm{BU_{min}})} = 0.3159 \times e^{0.0862\times \mathrm{L}} + 0.001978 \times e^{0.6583\times \mathrm{L}} \tag{2.33}$$

Equation 2.33 is plotted in Figure 2.37. It gives the change in minimum required burnup per % of Zr. Thus, for example, the difference going from pure uranium to U-10Zr is given by simply multiplying the values of Fig. 2.37 by 10. For a B&B reactor with 6% neutron loss, a design modification from U-10Zr to pure uranium fuel would reduce the minimum required burnup by 3.3% FIMA. This corresponds to an equilibrium cycle fast fluence reduction of $\sim$1.6 $\times 10^{23}$ which corresponds to a structural material damage reduction of $\sim$90-100 dpa.

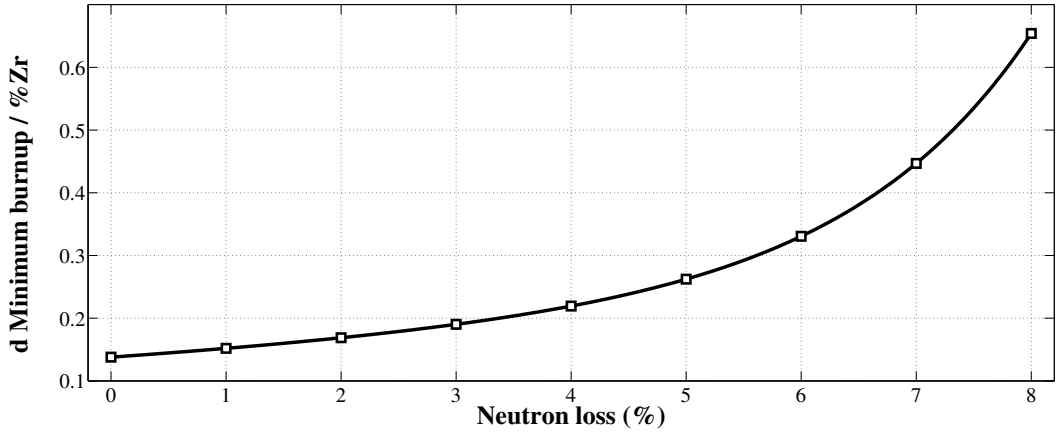

Figure 2.37: Change in minimum % FIMA burnup per %-change in non-actinide (Zr) content in metallic fuel

Note: Equation 2.32 and 2.33 is based on $\sim$1000 neutron transport calculation runs with a combined total of $\sim 10^9$ neutron histories. The data produced was then processed by 3 MATLAB scripts, hundreds of curve-fitting operations and 1 Maple script written and coupled specifically for this purpose.

2.7.3 Pitch-to-diameter (Fuel/Coolant volume ratio)

Many of the inter-connected parameters of reactor core design can be boiled down to the relative spacing between fuel rods in the assembly (the pitch-to-diameter ratio, or P/D). Metallic fuel swells and fills the radially available volume in the fuel rod at 2% FIMA. As the fuel will spend the great majority of the time in any B&B reactor in this state, the swollen volume fraction was used for this analysis. P/D ratios have been analyzed starting from a lower limit of 1.03, corresponding to a fuel volume fraction of 50.73% (as-manufactured) in the reference assembly. The P/D-relation is directly related to the fuel volume fraction and specifically to the fuel/coolant-volume ratio. However, since structural components such as clad and duct are present in the fuel assembly, no simple generalized direct link can be established between P/D and fuel or fuel/coolant volume fraction. For the reference assembly, P/D and $F_{\text{manufactured}}$[3] correlate (exactly) by the following equation:

$$F_{\text{manufactured}}\,(\%) = 1185 \times e^{-4.002\times \text{P/D}} + 101.7 \times e^{-1.135\times \text{P/D}} \tag{2.34}$$

The corresponding equation relating P/D and fuel/coolant volume ratio (as-manufactured) is:

$$\frac{F_{\text{manufactured}}}{C_{\text{Active}}} = 5.032 \times 10^{9} \times e^{-21.27\times \text{P/D}} + 85.77 \times e^{-3.76\times \text{P/D}} \tag{2.35}$$

For the reference assembly geometry, as-manufactured active (excluding inter-assembly) coolant and fuel volume fractions are equal at P/D = 1.196. The assembly contains an additional 2.24% of inter-assembly coolant, which remains unaffected by the change in P/D. The neutron balance, design space and loss-limits results are shown in Figures 2.38-2.42.

[3] $F_{\text{manufactured}}$ refers to the manufactured core fuel volume fraction at 0% fuel swelling.

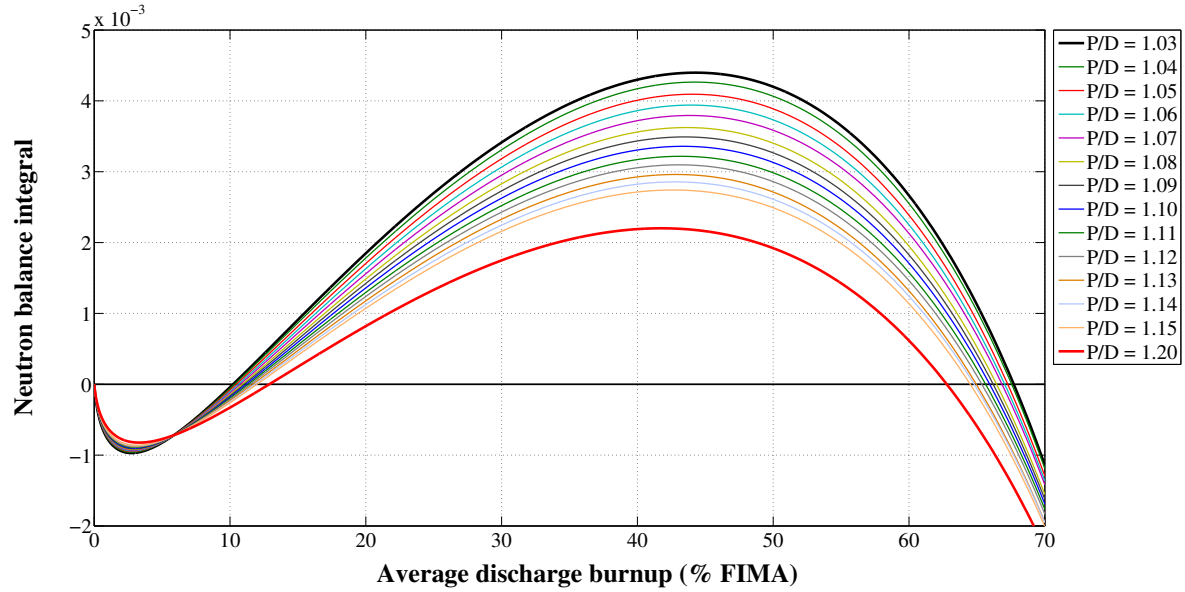

Figure 2.38: Neutron balance by P/D-ratio (loss = 0%) (1)

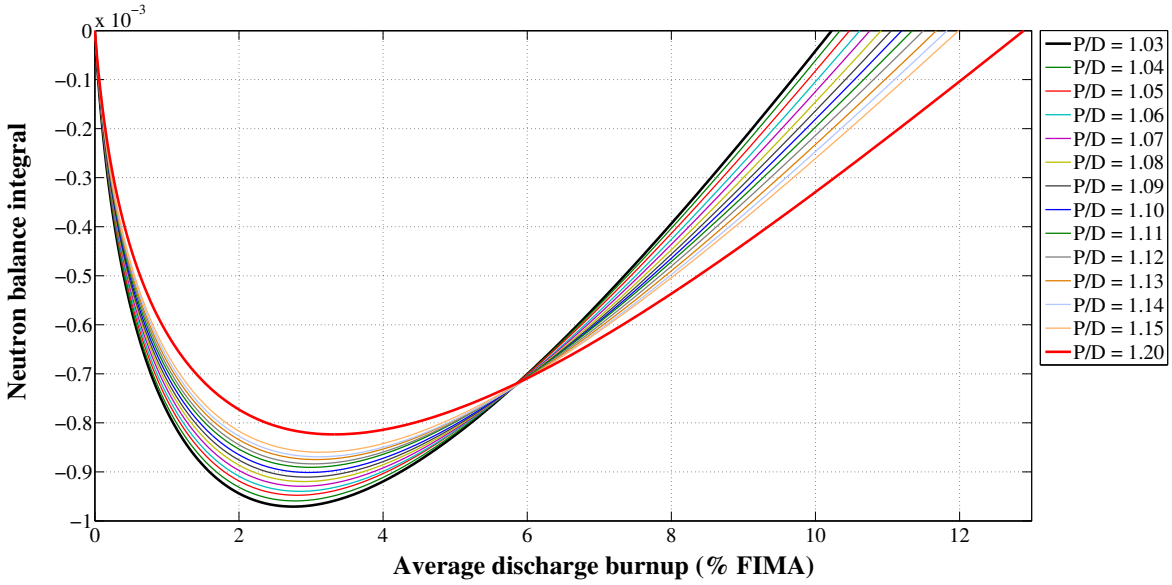

Figure 2.39: Neutron balance by P/D-ratio (loss = 0%) (2)

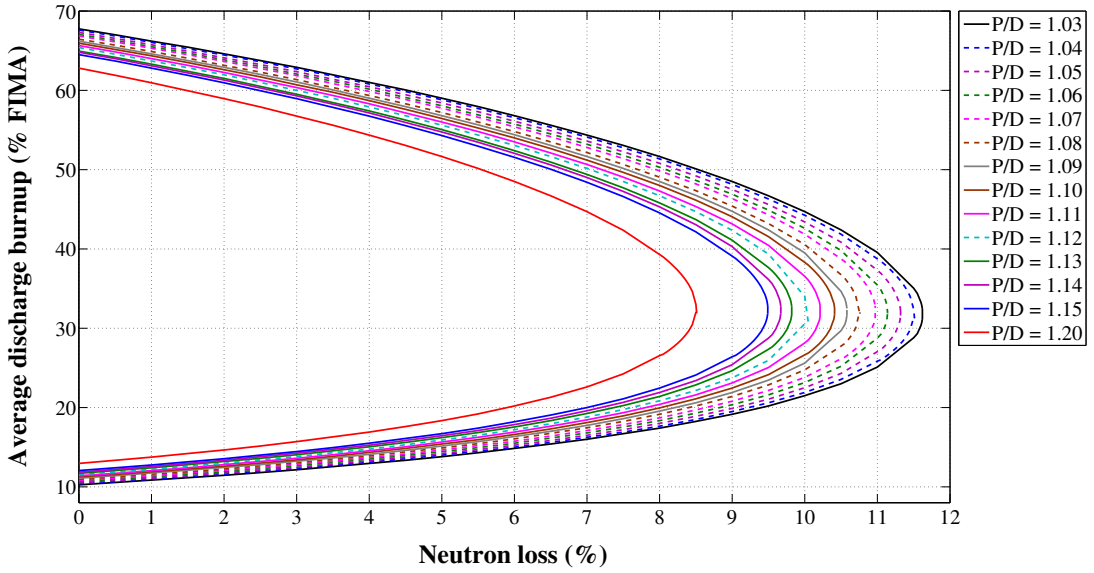

Figure 2.40: B&B design space by P/D-ratio (1)

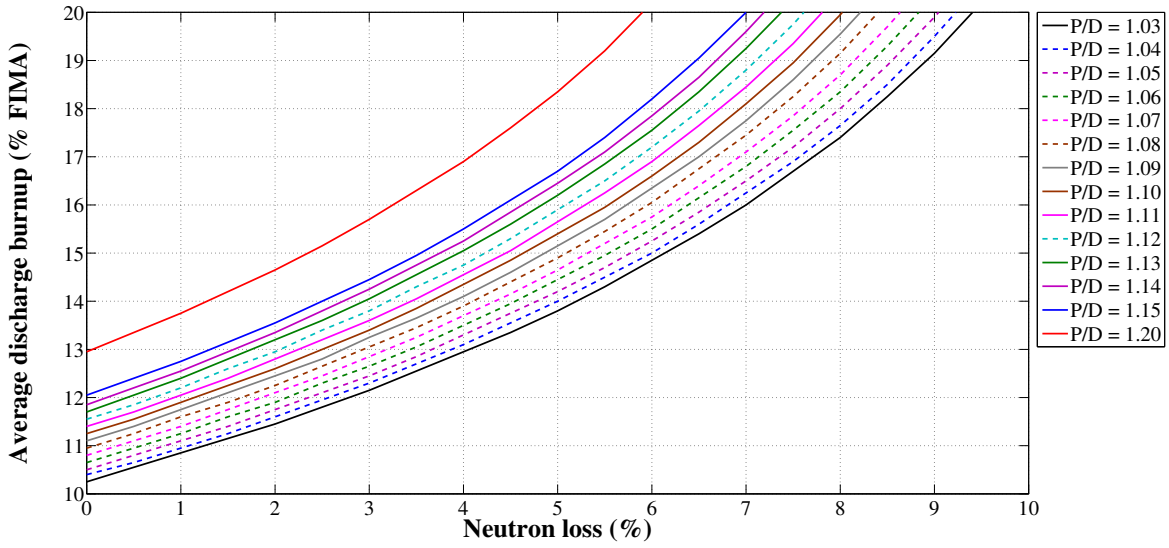

Figure 2.41: B&B design space by P/D-ratio (2)

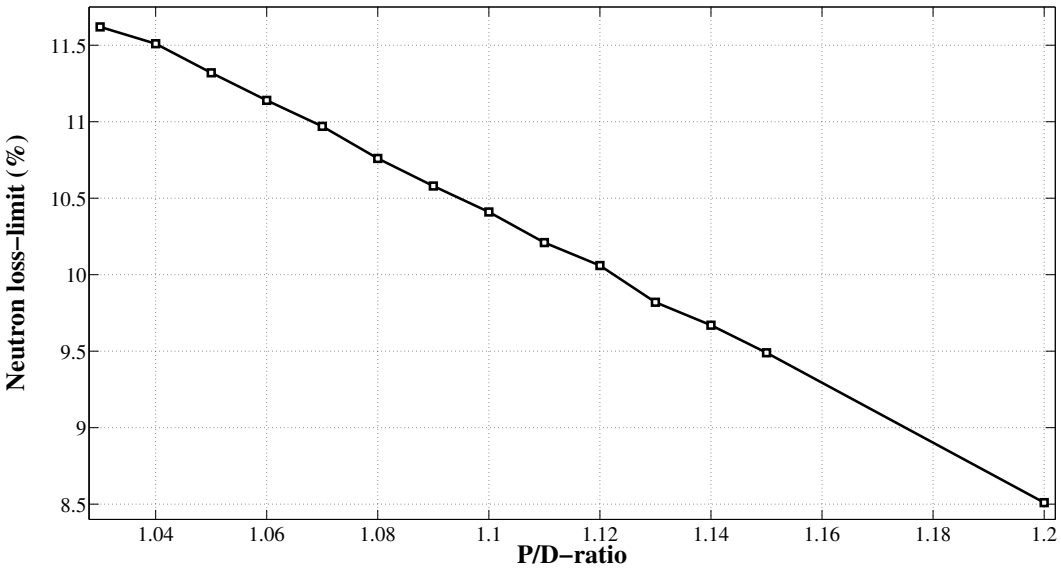

Figure 2.42: B&B loss-limit by P/D-ratio

The calculated values have been fitted using the methodology presented in Section 2.6. The expression relating P/D-ratio and minimum burnup is:

$$\begin{aligned} \mathrm{BU_{min}\,(P/D)} &= [\mathrm{P/D}] \times \left(15.34\ e^{0.09193\times L} + 0.03558 e^{0.7766\times L}\right) \\ &- \left(5.662\ e^{0.1513\times L} - 0.01171 e^{0.8966\times L}\right) \end{aligned} \tag{2.36}$$

Equation 2.36 is valid in the range $1.03 \leq \mathrm{P/D} \leq 1.20$ and $0 \leq \mathrm{L} \leq 8\%$.

Eq. 2.36 is plotted in 2.43 for both P/D and Fuel/Active coolant volume ratio.

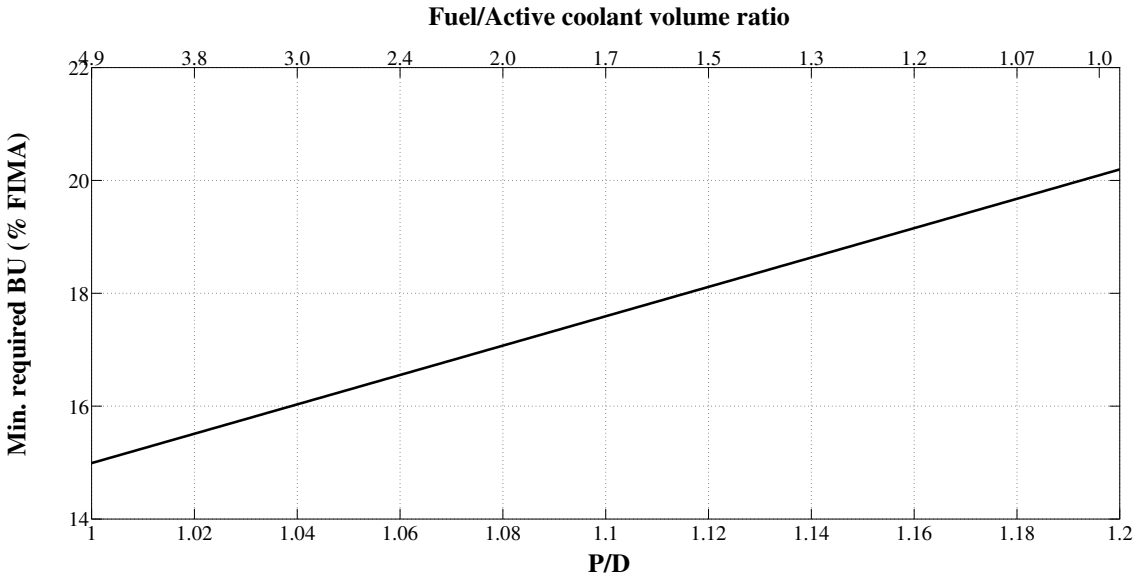

Figure 2.43: Min. required BU (% FIMA) by P/D and fuel/coolant ratio (L=5%)

Differentiating eq. 2.36 gives the relative change in minimum required burnup by 0.01-change in P/D-ratio as:

$$\frac{d\,(0.01\text{-P/D})}{d\,(\mathrm{BU_{min}})} = 0.1534 \times e^{0.09193\times \mathrm{L}} + 0.0003558 \times e^{0.7766\times \mathrm{L}} \tag{2.37}$$

Equation 2.36 gives the change in minimum required burnup by 0.01 increment steps in the P/D ratio. For example, a change in the P/D-ratio from 1.15 to 1.10 at 6% neutron loss decreases the minimum required burnup by 1.52% FIMA. It is reasonable to assume that the actual effect is slightly larger than this, as the neutron leakage probability will see some level of decrease with a larger fuel volume fraction in the core. Eq. 2.36 is plotted in Fig. 2.44.

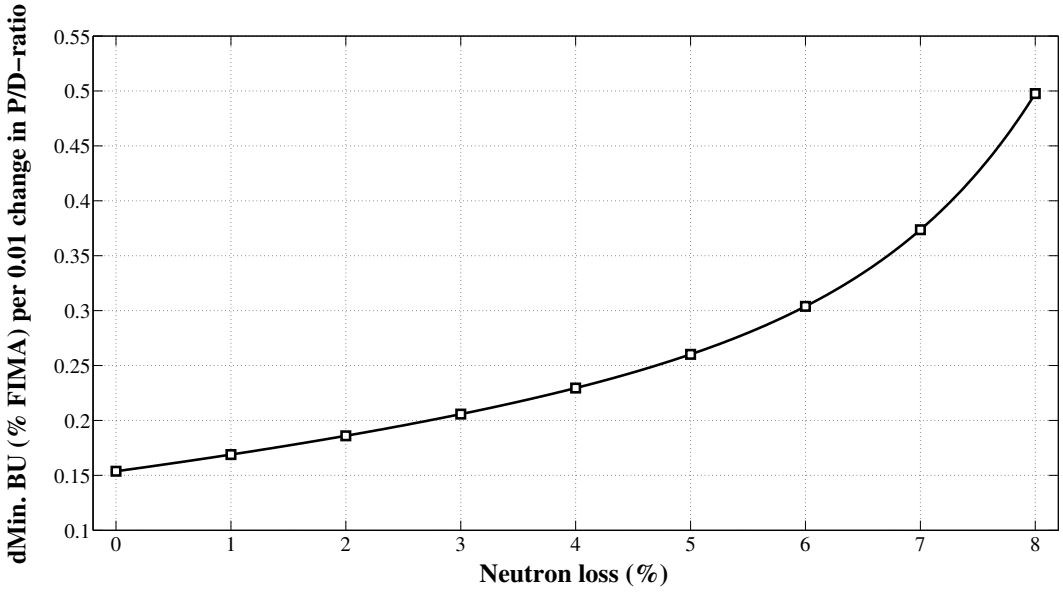

Figure 2.44: Change in min. required BU (% FIMA) by 0.01-change in P/D-ratio

2.7.4 Fissile content in feed fuel

One of the major motivations for breed & burn technology is to unlock the energy potential of fertile material such as depleted uranium without the need for chemical reprocessing. As natural uranium is enriched in the ^{235}U isotope for use in light water reactors (LWRs), large quantities of depleted uranium hexafluoride (DUF_6), known as tailings, are produced. There is no general definition of the isotopic composition of depleted uranium, other than it is uranium with a weight-concentration of ^{235}U lower than that of natural uranium (<0.72%). The composition of the tailings is dependent on the specifics of the enrichment facility and of the level of enrichment. As an example, enriching 1,000 kg of natural uranium to 5% ^{235}U produces ∼85 kg of enriched uranium hexafluoride (UF_6) and ∼915 kg of DUF_6 tailings at 0.3 percent ^{235}U. In the US, around 700000 tons of UF_6 containing about 470000 tons of depleted uranium is currently stored at facilities in Paducah (KY), Portsmouth (OH) and the ETTP facility in Tennessee. Around 8000-10000 tons of depleted uranium is added to these storage facilities annually. Most of the Department of Energy's (DOE) depleted uranium inventory contains between 0.2 to 0.4 weight-percent of ^{235}U. Details about the composition of US DU is available through the UF6 Cylinder Database [59]. It is thus of interest to estimate what impact the composition of the feed fuel has on the performance characteristics of the equilibrium B&B cycle. The ^{235}U fission-to-absorption cross-section ratio in the fast spectrum is comparable to that of the fissile plutonium isotopes (mainly ^{239}Pu and ^{241}Pu). Since a B&B system at equilibrium contains ∼100-400 times more plutonium than ^{235}U, regardless of feed-fuel enrichment in the 0-0.072% range, the ^{235}U-impact on equilibrium core performance is predictably small.

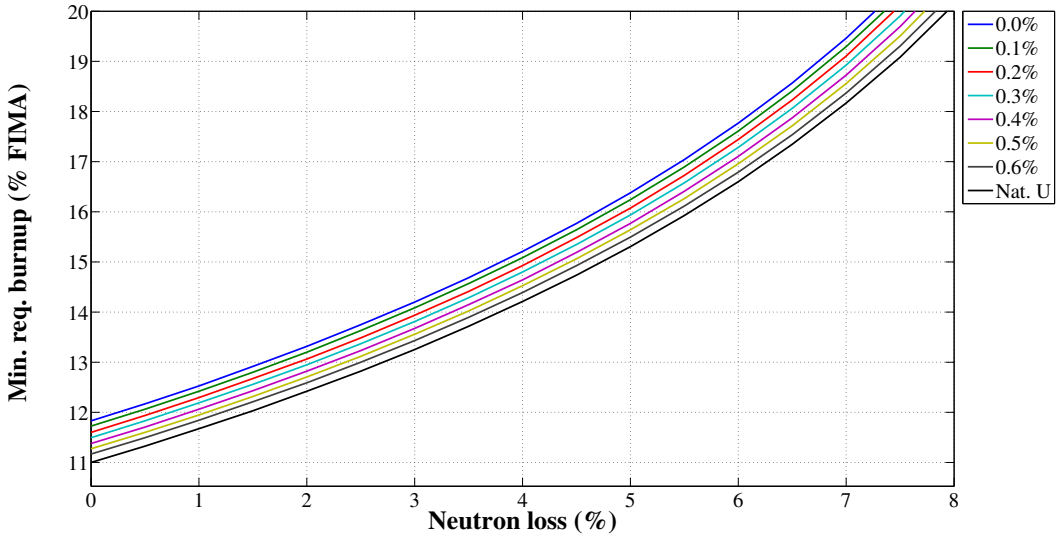

Figure 2.45: Min. required BU (% FIMA) by feed-fuel ^{235}U content

The effect on minimum burnup by a 0.01% change in the ^{235}U-content of the feed fuel, calculated using the methodology outlined in section 2.7.2 & 2.7.3, is given by the following relation:

$$\frac{d\,(0.01\%\text{-U235})}{d\,(\text{BU}_{\text{min}})} = -0.111684 \times e^{0.05189\times \text{L}} - 0.00004929 \times e^{0.8513\times \text{L}} \tag{2.38}$$

This correlation is valid for: $0.2 \leq {}^{235}\text{U} \leq 0.72\%$, $0 \leq \text{L} \leq 8\%$. Eq. 2.38 is plotted in Figure 2.46. The incremental burnup change is 0.13-0.15 % FIMA per 0.01% ^{235}U fraction in the feed fuel. Going from a feed-fuel with low-level depleted uranium (0.2% ^{235}U) to natural uranium feed (0.72% ^{235}U), means multiplying eq. 2.38 by (0.72-0.2)=0.52. The resulting reduction in the minimum burnup requirement is ∼0.78% FIMA at 6% neutron loss.

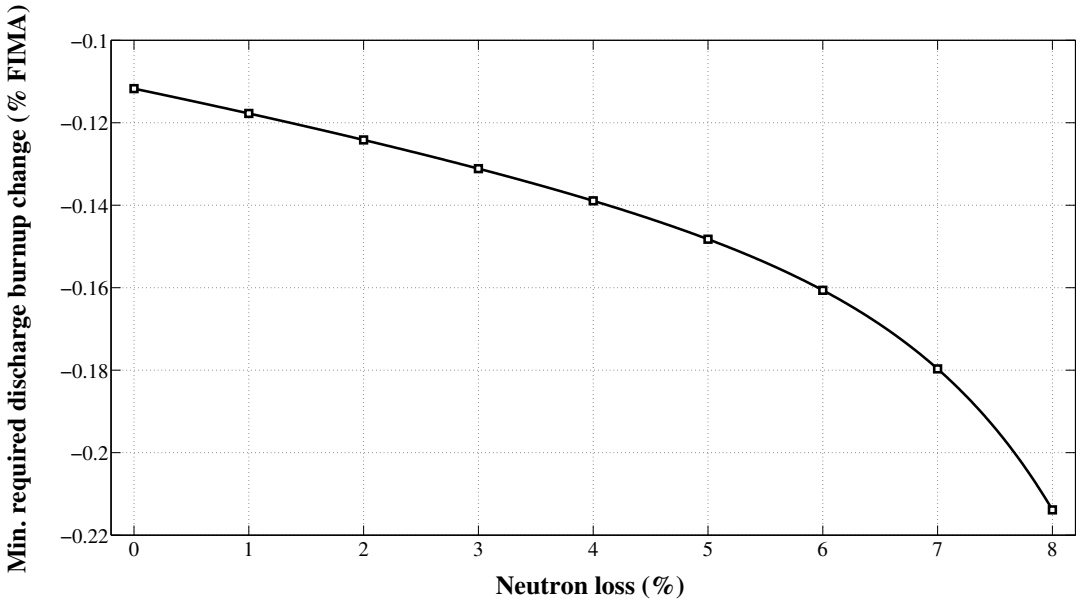

Figure 2.46: Change in min. required BU (% FIMA) per 0.01%-change in feed-fuel ^{235}U content

2.7.5 Flux/Power level

In a fast reactor, the effects of fission product poisoning are much less pronounced than in a thermal system as fission product cross-sections are many orders of magnitude lower in a fast spectrum[4]. Flux considerations in the fast spectrum depend primarily on the ratios of actinide isotope concentrations. Transmutation through radioactive decay introduces some time-dependence that connects the neutron economy to flux and power level. In a fast system, two major decay chains impact the system characteristics:

$$^{241}\mathrm{Pu} \xrightarrow[14\mathrm{y}]{\beta^-} {}^{241}\mathrm{Am} \tag{2.39}$$

$$^{238}\mathrm{U}\,(n,\gamma)\,{}^{239}\mathrm{U} \xrightarrow[23.5\mathrm{m}]{\beta^-} {}^{239}\mathrm{Np} \xrightarrow[2.35\mathrm{d}]{\beta^-} {}^{239}\mathrm{Pu} \tag{2.40}$$

A flux level lower than the optimum will see too much ^{241}Am production by the decay of ^{241}Pu. The fast spectrum fission-to-absorption ratio of ^{241}Am is a mere $\sim$0.23 compared to $\sim$0.87 for ^{241}Pu. On the other hand, if the flux level is too high, production of ^{241}Pu production from ^{239}U by the reaction sequence given in eq. 2.40 will be reduced. The fast-spectrum fission-to-absorption ratios for both decaying isotopes (^{239}U and ^{239}Np) are far lower than that of ^{241}Pu, which is the isotope that provides the majority of fission events in B&B reactors. The optimum flux level is one that allows for sufficient ^{239}Pu production while minimizing ^{241}Pu decay to ^{241}Am. Regardless of where the optimum lies, there is a set range of core-averaged flux levels that make physical sense to examine. The energy deposition from a single fission event can be averaged approximately as:

$$E_f = 200 \times 10^6 \mathrm{eV} \times \frac{\mathrm{eV}}{\mathrm{J}} = 3.204 \times 10^{11} [\mathrm{J/fission}] \tag{2.41}$$

The core-averaged fission cross-section of a hard-spectrum B&B-reactor in equilibrium is $\Sigma_f \approx 0.0027$ [1/cm][5]. Average volumetric power densities for fast reactors are conventionally in the range of 100-500 W/cm^3. The core averaged flux-level is given by:

$$\phi_{\mathrm{ave}} = \frac{\mathrm{W/cc}}{E_f \times \Sigma_f} \tag{2.42}$$

Given the above values, eq. 2.42 evaluates to:

$$1.2 \times 10^{15} \leq \phi_{\mathrm{ave}} \leq 6 \times 10^{15} \tag{2.43}$$

To increase the probability of identifying the local maxima of neutron economy by flux level, this span is expanded in this analysis to:

$$10^{13} \leq \phi_{\mathrm{ave}} \leq 10^{17} \tag{2.44}$$

[4] ^{135}Xe is the most prolific thermal-spectrum absorber. In a thermal spectrum its absorption cross-section is $\Sigma_a \approx 2.64 \times 10^6$, the corresponding fast-spectrum cross-section is $\Sigma_a \approx 7.43 \times 10^{-4}$, nearly 10 orders of magnitude smaller [60].

[5] Calculated by the Serpent monte-carlo code [47] for a sodium cooled, metallic-fueled B&B core design.

Fig. 2.47 indicates that, conveniently, the optimum flux level in a B&B core is somewhere around in the flux/power density span as set by eq. 2.43. The differences in neutron balance in the flux span corresponding to reasonable average power density levels are so small that they should have no impact whatsover on B&B design and operation considerations.

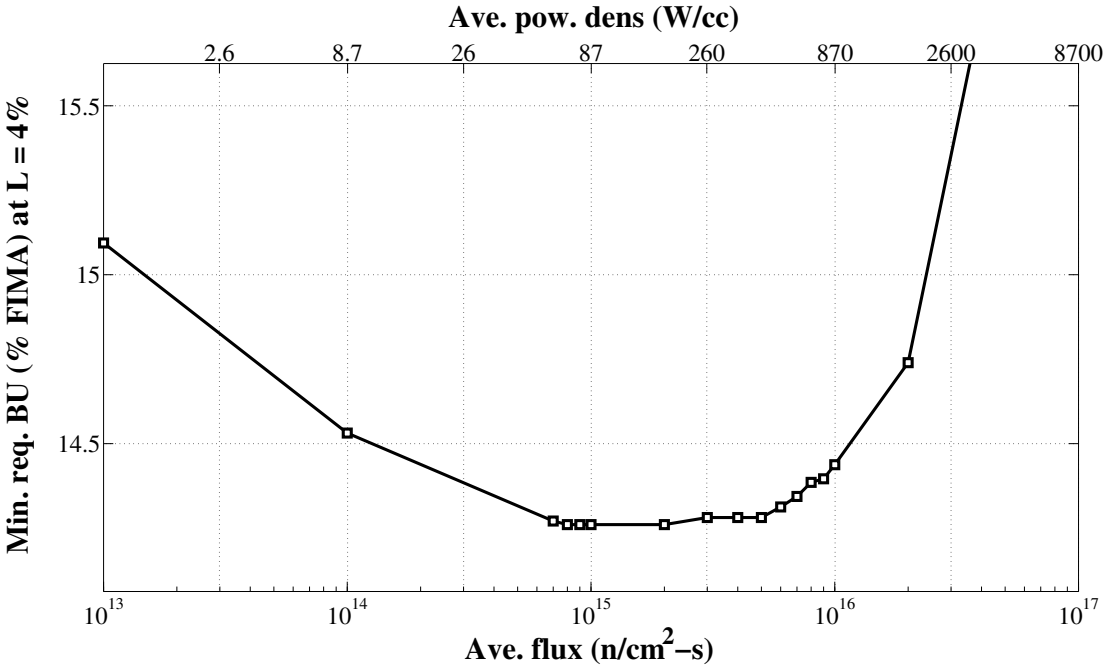

Figure 2.47: Min. req. BU dependence on flux/power level

Chapter 3

The safety of fast reactors

3.1 Introduction

This chapter serves as a short introduction to the following three chapters, which go in to detail about the physics of reactivity feedback, approaches for improving the feedback in fast reactors and the new engineered safety system *ARC*. When mentioned in this thesis, *safety* refers primarily to the safety related to reactor physics, such as *reactivity safety* and the reactivity response of the core. The engineering, design and operation of systems for *heat removal safety*, *seismic safety* etc, are not covered by the work presented in this thesis.

The focus of safety considerations for fast reactors differ from that of conventional LWR systems (PWR & BWRs), partly due to the potential of positive temperature reactivity feedback in accident scenarios. A thermal reactor core contains ∼1 critical mass and the system is close to its most reactive state in its standard geometric configuration at cold shutdown. LWRs are designed to be slightly under-moderated to ensure that a decrease of the coolant density adds negative reactivity to the system. Thus, in a properly designed LWR system, there are no positive temperature reactivity feedbacks. The only[1] way to add reactivity *and* increase temperatures in an LWR is through the withdrawal of control rods. Focus for LWR safety research is primarily concerned with providing adequate core cooling and ensuring that the core remains submerged under water during accidents scenarios. The accident progression in the Fukushima Daiichi NPP following the Tōhoku earthquake and tsunami in march of 2011 has again highlighted these issues. In contrast, a typical fast reactor core contains several critical masses and is at standard operation far from its most critical state. All fast reactors are by definition over-moderated and they are put in a state of higher reactivity if neutron moderation is decreased and the neutron spectrum is hardened (disregarding the effects of changes in the neutron leakage probability). In larger fast reactors, the positive reactivity added by spectrum hardening due to a coolant density decrease in the central region of the core is often larger than the negative reactivity by the decrease of neutron reflection. While reactivity feedback is a more serious issue in fast reactors, their operation and physical characteristics are highly favorable for heat removal in accident scenarios. Liquid metal reactors operate at atmospheric pressure and have a significant temperature margin to boiling (∼300°C for Na and ∼1300°C for Pb & LBE). In comparison, the margin to boiling in a PWR is ∼15°C, while the coolant boils in standard operation in a BWR. The nominal coolant temperature rise across the core is ∼150°C for liquid metal cooled reactors, compared to a mere ∼30-35°C in an LWR. This facilitates a much more effective natural circulation for decay heat removal. The differences affecting both *reactivity safety* and *heat removal safety* for LWRs and fast reactors are summarized

[1]Some accident scenarios involving burnable absorbers can add reactivity without a decrease in core temperatures. One example is the failure of the primary heat exhangers of a PWR, in which borated water is replaced by normal water, adding significant positive reactivity to the core. Avoiding this issue is primarily a heat-exhanger engineering problem rather than an issue for reactor physics. BWRs utilize solid burnable absorbers and thus avoid this potential issue.

in table 3.1.[2]

Table 3.1: LWR vs. fast reactor safety-analysis related characteristics

Parameter	PWR	BWR	SFR	LFR
Coolant pressure	15.5 MPa	7 MPa	∼1 atm	∼1 atm
Coolant core δT (°C)	30-40	∼10-20	150	150
Margin to boiling (°C)	15	0	300	1300
Core reactivity state	Near max	Near max	$\ll$ max.	$\ll$ max.
Natural circulation	Very low	Low-High	High	Very high
Chemical reactivity	Low	Low	High	Low
PRC* (\$ / δP/P)	-5	-5	-1	-1
Coolant boiling reactivity	Negative	Negative	Very positive	Positive

*PRC = Power Reactivity Coefficient

3.2 Passive and inherent safety

The current focus of safety design for new nuclear reactors is on inherent safety and passive safety features. Inherent safety means that the reactor's mechanical and functional design is such that the plant remains in a safe condition solely on the basis of the laws of nature; these laws ensure that the parameters remain within safe boundary values in all conceivable circumstances. This implies that no human interference, no triggering signals and no supply of external energy are required to remain in a safe condition. Passive safety features come into operation in the event of an accident without the necessity for active switching or triggering operations that requires the supply of external energy [61]. The inherent safety features are especially important when engineered systems such as the SCRAM-system for reactor shutdown are not functioning.

As most recently highlighted by the events at the Fukushima Dai-ichi nuclear power plant, the current fleet of LWRs are not inherently safe. Inherently safe design is however not limited to fast reactors. One of the first commercial reactor designs to fully incorporate inherent safety features was the PIUS PWR, developed in Sweden in the early 1980s [62]. Since then, several other thermal reactor concepts and numerous fast reactor concepts featuring

[2]When the zirc-alloy cladding of PWRs and BWRs reach around 1200°C, it will start an exothermic hydrogen-producing reaction with the coolant water. Slow processes such as the corrosion by the coolant water or lead-based coolants is not considered here from a *safety* perspective.

completely passive safety features have been developed. The focus of inherent safety is to avoid and prevent three main issues:

- Large uncontrolled increases in core power
- Insufficient cooling of the reactor core
- Rearrangement of fuel that would lead to energetic events

Fundamental phenomena are used for inherent safety, such as thermal expansion, buoyancy-driven flow, and gravity. The scenarios of primary importance for inherent safety are:

- Unprotected loss-of-flow (ULOF)
- Unprotected loss of main heat sink (ULOHS)
- Inadvertent withdrawal of reactor control rod(s) resulting in a transient overpower accident (UTOP)

The safe operation of a reactor system can be ensured by designing for two basic principles:

1. Favorable reactivity feedback
2. Passive (natural circulation) decay heat removal

During an accident, the reactivity feedback of the core should terminate the chain reaction and keep short-term temperatures of all components below safety margins even if the primary reactor shutdown system is malfunctioning. After the termination of the fission process by feedback mechanisms, the remaining decay heat should be removed through a passive cooling system until the core reaches a safe cold-shutdown mode. No operator action is required at any time during the accident progression in an inherently safe reactor. These pillars of inherent safety have been demonstrated for fast reactor system in the sodium-cooled pool-type EBR-II reactor [63].

Chapter 4

Reactivity feedback of large fast reactors

4.1 Introduction

In this chapter, the physics and calculational methodology for fast reactor core feedback mechanisms are presented. For feedback where new methodology, interpretations and methods have been developed, feedbacks are covered in detail, other feedbacks are mentioned more briefly. The change in the effective core multiplication factor (k_{eff}) due to any perturbation is governed by a combination of separable coefficients, caused by changes in geometry and physical properties of the different components that make up the reactor core. While reactivity coefficients can be expressed as functions of a change in reactor power or coolant flow, they are all fundamentally functionally dependent on temperature. To enable a straightforward physical interpretation of the values calculated and to facilitate comparisons between different types of cores, coefficients are presented in a unit based on the effective delayed neutron fraction (β_{eff}). β_{eff} is the measure of the impact on k_{eff} by neutrons released during the decay of fission products and is calculated as:

$$\beta_{\text{eff}} \equiv 1\$ = \left[k_{\text{eff}} - k_{\text{eff}}\left(\text{prompt}\right)\right] \times 10^5 \qquad [\text{pcm}] \tag{4.1}$$

The value of β_{eff}, defined in neutron kinetics studies as one dollar (1\$), is of profound importance for core safety characteristics. When reactivity, defined as the deviation in k_{eff} from a critical state, exceeds +1\$, the core is in a super-critical state without the added reactivity of delayed neutrons, and may undergo a rapid and potentially uncontrollable power excursion. Using a \$-based unit for reactivity coefficients, the safety characteristics of cores with different values of \$ (and the value of \$ can vary significantly) can be compared justly. The values of the reactivity coefficients used in this thesis are calculated using equation 4.2:

$$\alpha = \frac{k_{\text{eff}}\left(T_x\right) - k_{\text{eff}}\left(T_0\right)}{T_x - T_0} \times \frac{10^5 \times 100}{\beta_{\text{eff}}} \qquad \left[\frac{¢}{K}\right] \tag{4.2}$$

where,
T_0 is the reference (unperturbed) temperature (Kelvin)
T_x is the perturbed temperature (Kelvin)
1 cent (¢) is defined just as in currency: 1\$ = 100¢.

For some parts and discussion, the unit of reactivity (ρ) is used, defined as:

$$\rho = \frac{k_{\text{eff}} - 1}{k_{\text{eff}}} \tag{4.3}$$

The reactivity feedback from changes in temperature of the fuel, structural material and coolant can in a simplified manner be summarized by five general feedback mechanisms that together control the core response to temperature transients. The reactivity feedback of a typical fast reactor is shown in Figure 4.1. The size of the arrows following the reactivity effect boxes (ρ_{doppler} etc..) shows the characteristic magnitude of the feedback.

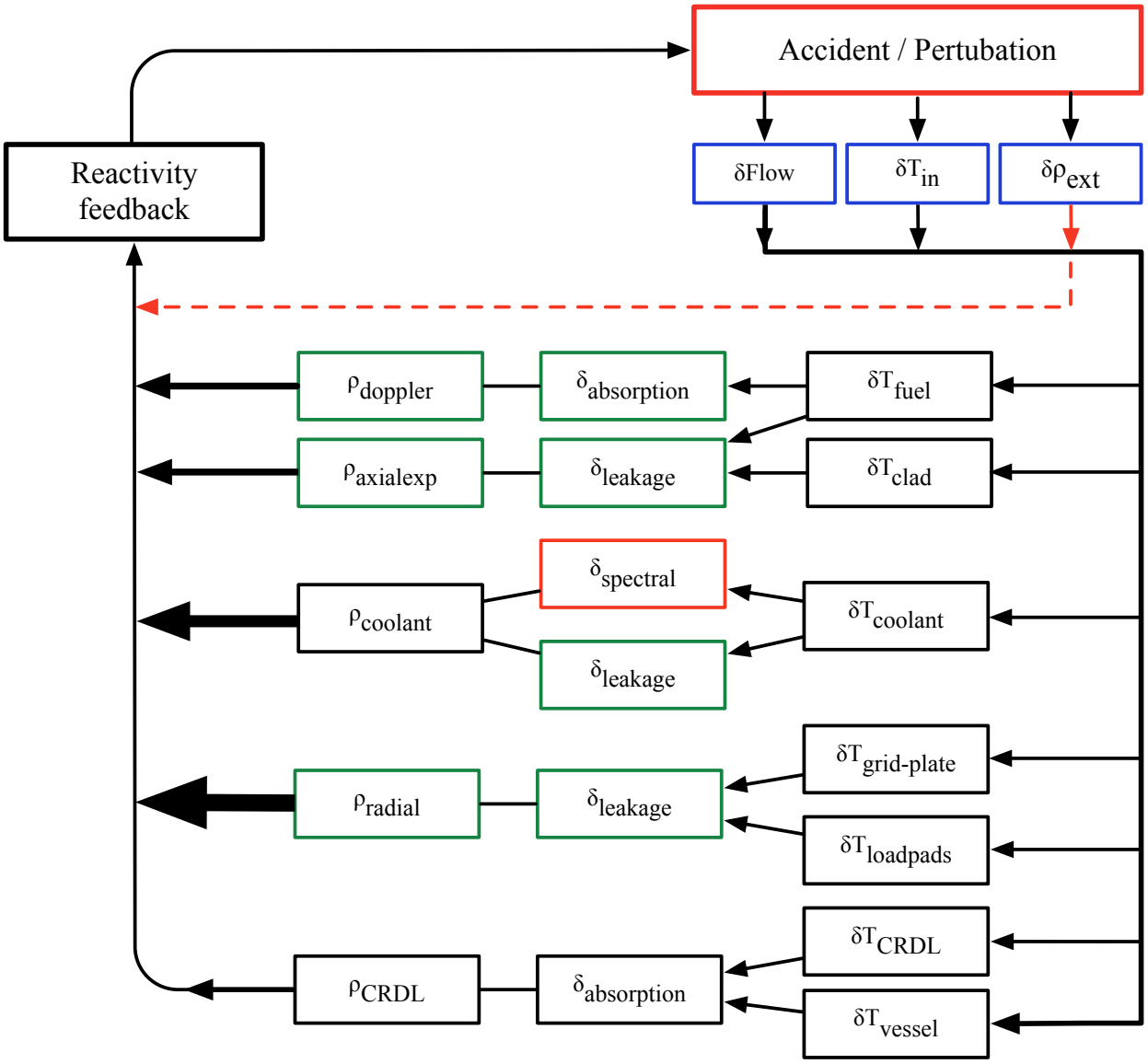

Figure 4.1: Main reactivity feedback of a fast reactor core

Note. The temperature change in each component will change both neutron absorption, leakage and spectrum to some degree. Changes in each core-component also affect all other components. The effects shown in Fig. 4.1 represent the largest and most important reactivity feedbacks effects, but do not represent all effects occuring in the core. A green-box indicates a negative temperature reactivity feedback and a red box a positive feedback. The two black boxes represent effects where the sign of the feedback is design dependent (ρ_{coolant}) or time-dependent (ρ_{CRDL} = control rod driveline expansion).

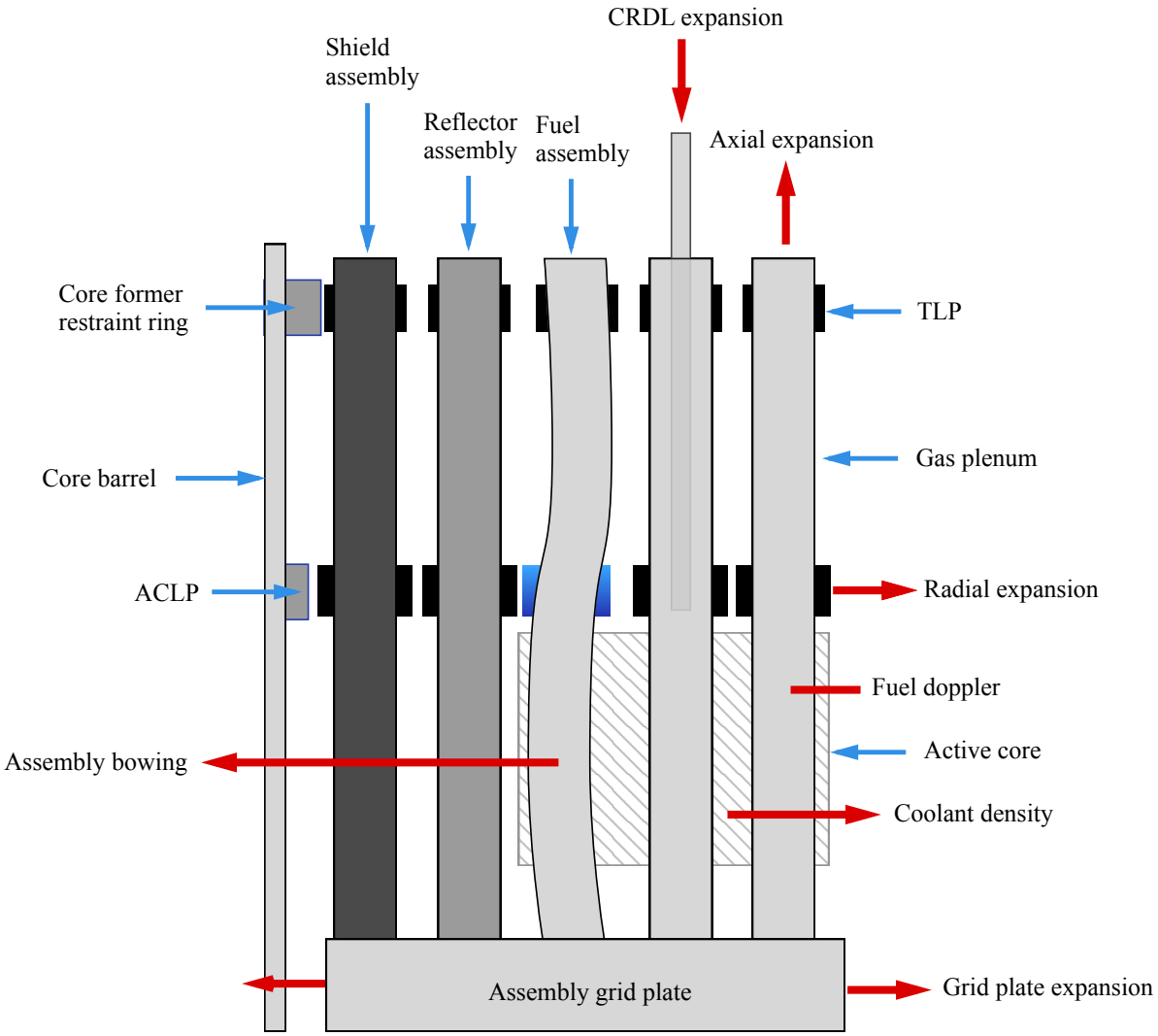

Figure 4.2: Graphical represenation of fast reactor core reactivity feedback

Note. The core structural components are indicated by blue arrows, the reactivity feedback effects are marked with red arrows and lines. The length and width of arrows do not represent any physical characteristics in this figure. TLP = Top load pad, ACLP = Above Core Load Pad.

4.2 Doppler feedback

4.2.1 Introduction

The broadening of reaction cross-sections by an increase in temperature is called the (nuclear) Doppler effect. Cross-sections for all resonances (absorption, fission, scattering) - in all materials of the core - are subject to the Doppler effect. While the total cross-section area of a resonance is always conserved, the shape of the resonance flattens with increasing temperature. This flattening is caused by an increase in the thermal oscillations of the nuclei. The range of the relative neutron/nucleus velocity widens because of the increased back-and-forth (brownian) motion of the nucleus. This effect can be seen in Figure 4.3. The Doppler broadening reduces the resonance energy self-shielding with increasing temperature, yielding an increase in effective cross sections. The negative Doppler coefficient in large fast breeder reactors (**FBR**) is primarily due to ^{238}U resonance broadening. The self-shielding effect is more important at low neutron energies (in the keV range and below), which means that the magnitude of the Doppler effect is reduced with a harder neutron spectrum. While the Doppler effect mainly occurs in the fuel, the effective absorption and scattering cross-sections of the coolant and structural materials in the core also increase with temperature due to this effect. The non-fuel Doppler effect can amount to ∼30% of the Doppler effect of the fuel, but since it is not directly tied to the temperature of the fuel it acts with a different, far larger, time constant [64]. The exact characteristics of the feedback due to this effect is determined by neutron energy spectrum and isotopic composition of the materials in the core.

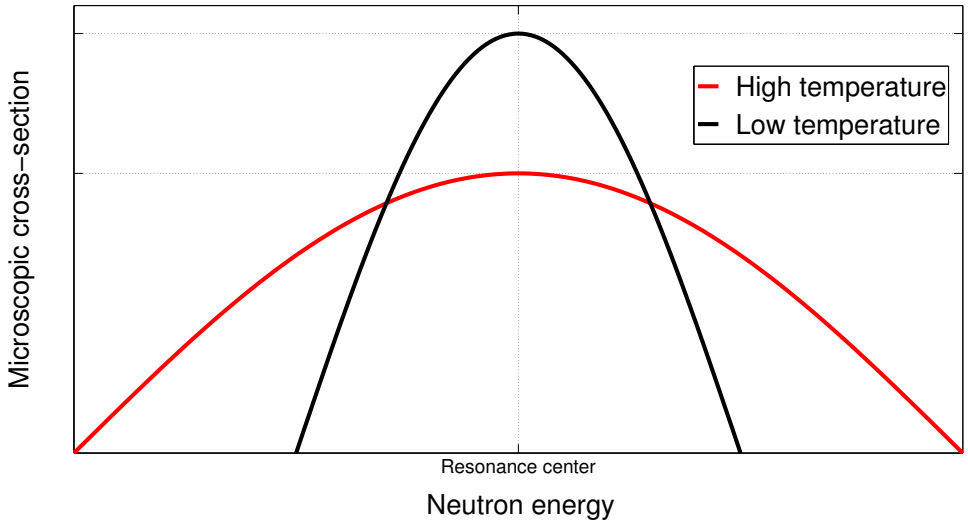

Figure 4.3: The nuclear Doppler effect visualized

The importance of resonance broadening of cross-sections decreases with neutron energy. For energies above 25 keV, the resonances are too overlapping for the Doppler effect to have any significant impact on reaction rates.

4.2.2 Fuel Doppler feedback

In uranium-based reactors with a fuel loading with some fraction of fertile fuel, the Doppler feedback of the core is dominated by the resonance absorption reaction of ^{238}U. In the B&B designs developed at UCB (see Section 4.9.1), ∼90% of the fuel Doppler effect is due to ^{238}U alone. The fuel Doppler effect is a near-instantaneous feedback and because of its negative sign it provides an inherent stabilizing effect in all nuclear reactors. Since the Doppler effect reduces the self-shielding of resonances of any type, the broadening of fission resonances means certain isotopes contribute positively to the Doppler effect. While any reactor with predominantly fertile (^{238}U or ^{232}Th) based fuel will retain a negative overall coefficient, great care must be taken with cores fueled with a high fissile content. ^{239}Pu has a positive Doppler coefficient due to its many low-energy fission resonances, leading to a near-zero overall Doppler feedback in cores high plutonium content. In a limited temperature interval from some reference state, the changes in the magnitude of the effect are small enough that it for approximate analysis can be regarded as linear. Looking at larger spans of temperature, the magnitude of the Doppler effect has a distinct temperature-dependence. A temperature-perturbation at a high temperature produces a smaller change in reactivity due to the Doppler effect than a corresponding perturbation at low temperature. The error introduced by using a linear approximation is also larger at low temperatures. To better capture the behaviour of the Doppler effect across the entire applicable temperature span, the Doppler Constant (K_D) has been introduced. The change in reactivity due to a change in the temperature of the fuel can be described approximately by:

$$T^{\alpha}\frac{d\rho}{dT} = K_D \tag{4.4}$$

In oxide-fueled fast reactors, the value for α is ≈ 1, in the harder spectrum of a metallic fueled reactor, α tends to be higher. The Doppler constant can be calculated from the results of neutron transport calculations at two different values of fuel temperature. Using the definition of reactivity given in equation 4.3, the Doppler constant is given by:

$$K_D = -\frac{\rho\left(T_x\right) - \rho\left(T_0\right)}{\ln\left(\frac{T_x}{T_0}\right)} \tag{4.5}$$

Due the prompt nature of the fuel Doppler effect, it is imperative to maintain a negative value for this coefficient. Ostensibly, the more negative a reactivity feedback is, the better the core safety characteristics. While this turns out to be true for most feedbacks, it is dependent on the specific accident scenario. When the fuel temperature drops, a negative Doppler coefficient adds positive reactivity and slows the temperature drop of the fuel. In

certain accident scenarios such as loss of flow, the absolute value of stored reactivity due to the Doppler effect in the fuel should be minimized. This will be further covered in Section 4.8. The general form of the stored fuel Doppler reactivity (**SRD**) can be defined as:

$$\text{SRD} = \delta\rho\left(T_x \rightarrow T_0\right) = K_D \int_{T_0}^{T_x} \frac{1}{T^\alpha} dT \tag{4.6}$$

where,
T_0 is the average hot standby temperature [K]
T_x is the average temperature from which the shutdown is initiated (K)
The general solution ($\alpha \neq 1$) is:

$$\text{SRD} = K_D \times \frac{T_0^{1-\alpha} - T_x^{1-\alpha}}{\alpha - 1} \tag{4.7}$$

Taking the limit $\alpha \rightarrow 1$ gives:

$$\text{SRD} = K_D \times \ln\left(\frac{T_x}{T_0}\right) \tag{4.8}$$

The stored reactivity is strongly dependent on the fuel choice through variations in K_D and T_x. The low thermal conductivity of oxide fuel means a high standard operating temperature. This presents no problems at standard operation, since the melting temperature of UO_2 is very high (T_m = 2865°C). Metallic fuel has high thermal conductivity and a low melting temperature, and operates at about half the oxide-fuel value for T_x for the same linear power density. The logarithmic temperature term in eq. 4.8 is ∼80% larger for oxide-fuel and the Doppler constant is ∼50-70% larger. Combined in equation 4.8, this results in a stored reactivity of 2.7-3.2 times that of metallic fuel. Consequently, it is much more difficult to shut down an oxide-fueled core than a metallic-fueled core. Temperatures reached in transients such as loss-of-flow are significantly higher. It is a safety advantage to operate fuel at low temperature, regardless of the specific melting temperature of the fuel type.

4.2.3 Non-fuel Doppler feedback

Compared to the Doppler feedback of the fuel, the relative importance of resonance broadening of reaction resonances in the coolant and structure are small. This is primarily because both the absolute Doppler effect is both small and not a prompt effect. Other coolant and coolant-temperature-tied reactivity effects, such as that stemming from the coolant density decrease or core thermal expansion occur on a similar timescale but has a significantly larger impact on core reactivity. Due to this, coolant and structure Doppler feedback is almost never reported as individual feedback mechanisms in core design reports.

Essentially all of the Doppler effect in sodium (which consists in natural composition of a single isotope, ^{23}Na) is due to a single elastic scattering resonance at ∼2.85 keV [65]. The

amplitude and width of this resonance at 300K can be seen in Figure 4.4, using ENDF/B-6.1 cross-section data and the KAERI plotting tool [66]. The strong flux-suppression around the 2.85 keV-resonance in Na-cooled reactors causes an increase in the flux at lower energies. As this resonance is Doppler-broadened and its effective cross-section value is increased, the flux shift to lower energies is strengthened. Since fuel isotopes such as ^{238}U have many resonances below 2.85 keV, this has the interesting effect of boosting the fuel Doppler effect (although this effect is minor).

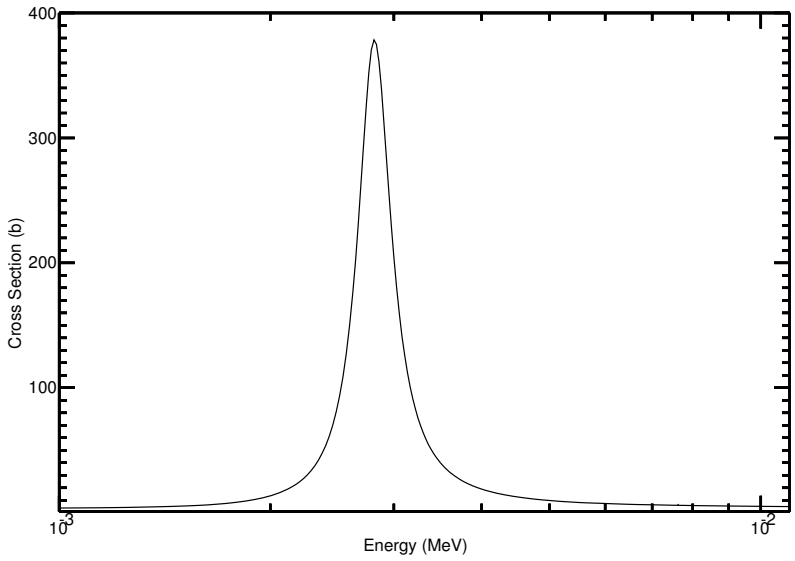

Figure 4.4: The total neutron cross-section of ^{23}Na in the energy range 1-10 keV

In addition to the fuel and coolant effects, structural materials contribute with negative reactivity due to Doppler, but this effect is small ($\leq$1/5 of the fuel effect) and time delayed. Sodium and lead-based coolants contribute negligibly to the effect, while replacing ^{238}U with ^{235}U or TRU decreases the size of the effect. Doppler coefficients and constants are calculated by generating neutron cross-sections for different temperatures and running core models for these cases, while keeping everything else constant in the model.

4.3 Fuel axial expansion

4.3.1 Introduction

As temperatures increase, the fuel rods or pellets thermally expand in all directions. The axial expansion effectively increases the height of the active core, and - since fuel mass is conservered - decreases the density of fuel in the core. The amount of fuel actinides in one radial slice of the core is decreased as the fuel expands axially, resulting in an increase in radial neutron leakage probability and a decrease in core reactivity. The reactivity effect of axial expansion is a near-prompt effect occurring essentially without time delay and is directly linked to the fuel (and sometimes cladding) temperature. The magnitude of the axial expansion reactivity effect depends on the nominal radial neutron leakage probability which in turn is determined by the core height-to-diameter ratio (H/D) and the efficiency of axial reflectors. The axial expansion reactivity effect can be decomposed in two components [67]:

$$\frac{\Delta k}{k} = A\left(\frac{\Delta H}{H}\right) - B\left(\frac{\Delta \rho_f}{\rho_f}\right) \tag{4.9}$$

The A component represents the positive feedback from the enlargement of the core. A taller core has a smaller axial flux gradient and a smaller axial neutron leakage probability, which increases core reactivity. The B component represents the reactivity effect of the reduction in the relative fuel density (ρ_f) in the core. For ceramic-fueled reactors (oxide, carbide, nitride etc.), the fuel cracks and forms inner void regions at high burnup. Because of this, the axial reactivity feedback in ceramic cores is regarded as unreliable. In metallic-fueled fast reactors, axial expansion is relied upon to give an important fast-acting negative feedback. It is of special importance in these systems since the hard neutron spectrum means that Doppler feedback is generally small. In a simplified way, the positive and negative components of axial fuel expansion are examined in the following section.

4.3.2 Physics of fuel axial expansion feedback

Using a simplified model for a homogeneous core, the relative values of the positive and negative reactivity components of axial expansion feedback and the effects of core shape can be analyzed. The core neutron multiplication factor can be expressed as:

$$k_{\text{eff}} = k_\infty \times P_{\text{NL}} \tag{4.10}$$

where P_{NL} is the non-leakage probability (the fraction of neutrons not leaking from the core) and k_∞ is the infinite multiplication factor. For simplicity, we can approximate the behavior of the core using average properties and cross-sections averaged over the energy spectrum of the core (one-group model). The infinite multiplication factor (k_∞) can be expressed as:

$$k_\infty = \frac{\nu\Sigma_f}{\Sigma_a} = \frac{\nu V_f N_f \sigma_f^f}{V_f N_f \sigma_a^f + V_c N_c \sigma_a^c + V_{\text{st}} N_{\text{st}} \sigma_a^{\text{st}}} \tag{4.11}$$

where superscripts c, f and st refer to coolant, fuel and structure respectively. V is the component volume fraction, N is the material atom density and ν is the average number of neutrons released per fission, σ_f and σ_a are the core-averaged neutron fission and absorption cross-sections respectively. Axial expansion primarily affects the fuel atom density (N_f), present in both numerator and denominator. The change in atomic density and the selective decrease in atomic density of fuel isotopes has a minor impact on the neutron spectrum and the values of ν, σ_f and σ_a. The effects of spectral change are however estimated to be small enough compared to the impact on neutron leakage probability that they can be ignored in this simple model[1]. The relative change in the infinite multiplication factor is then given by:

$$\frac{k_\infty(\text{expanded})}{k_\infty(\text{reference})} = \frac{N_f}{N_{f_o}} \times \left(\frac{V_f N_{f_o} \sigma_a^f + V_c N_c \sigma_a^c + V_{\text{st}} N_{\text{st}} \sigma_a^{\text{st}}}{V_f N_f \sigma_a^f + V_c N_c \sigma_a^c + V_{\text{st}} N_{\text{st}} \sigma_a^{\text{st}}} \right) \tag{4.12}$$

where the subscript o denotes the initial reference-state values. Since only fuel isotopes cause fission, the relative change in the nominator is larger than the change in the denominator, which means that fuel axial expansion causes a decrease in the infinite multiplication factor. With proper averaging, the infinite multiplication factor can be expressed as:

$$k_\infty = \frac{\nu N \sigma_f}{N \sigma_a} \tag{4.13}$$

The core length increase is defined by the variable x as follows:

$$H = H_o + x \rightarrow x = H - H_o \tag{4.14}$$

The expanded core height relates to the initial height as:

$$H = H_o \left(1 + \alpha \Delta T\right) \tag{4.15}$$

where ΔT is the change in temperature from the initial to the expanded state and α is the linear coefficient of fuel thermal expansion. Given the previous definition of x, the following relationship applies:

$$x = \alpha H_o \Delta T \tag{4.16}$$

The relation between the initial and expanded atom density of the fuel in the core is given by:

$$\frac{N^f}{N_o^f} = \frac{1}{1 + \alpha \Delta T} \tag{4.17}$$

The resulting change in the infinite multiplication factor, assuming microscopic cross-sections do not change, is:

$$\frac{k_{\text{eff}}}{k_{\text{eff}}^o} = \frac{\frac{1}{1+\alpha\Delta T}}{\frac{1}{1+\frac{\Sigma_a^f}{\Sigma_a}\alpha\Delta T}} = \frac{1}{1 + \alpha \Delta T} + \frac{\Sigma_a^f \alpha \Delta T}{\Sigma_a \left(1 + \alpha \Delta T\right)} \tag{4.18}$$

[1]This assumption has not been explicitly verified but is supported by the discussion and results by *Van Tuyle et. al.* [68] when calculating radial expansion effects.

Fuel-absorption in a fast spectrum reactor make up ∼95% of total absorption events [69], which means $\Sigma_a^f/\Sigma_a \approx 0.95$. As an example, the change in k_∞ by an expansion from a fuel temperature increase of 100°C ($\alpha = 2 \times 10^{-5}$) is 0.01% (10 pcm). The resulting "infinite reactivity coefficient" is on the order of 0.1 pcm/K ≈ 0.03 ¢/K. The axial expansion reactivity coefficient for a conventional SFR is on the order of 10 ¢/K [70]. The relative contribution to the reactivity coefficient by the change in fuel-atom-density in the infinite multiplication is thus on the order of 0.3%. For simplicity in the following discussion, this effect is ignored, and it is assumed that nominator and denominator of eq. 4.13 cancel. For the axial expansion study, this approximation means that the main reactivity effect is a change in the leakage probability. The non-leakage probability (P_{NL}) can be expressed in terms of geometric buckling (B_g^2) and migration area (M^2) as:

$$P_{\mathrm{NL}} = e^{-B_g^2 M^2} \tag{4.19}$$

Defining the core initial state by subscript o, and assuming as described above that there is no significant change in k_∞, the initial and axially expanded core states are given by:

$$\begin{aligned} k_o &= k_\infty e^{-B_o^2 M_o^2} \qquad \text{Reference} \\ k &= k_\infty e^{-B^2 M^2} \qquad \text{Axially expanded} \end{aligned} \tag{4.20}$$

The change in reactivity from the reference state is given by:

$$\delta\rho = \frac{k - k_o}{k} = 1 - \frac{e^{B^2 M^2}}{e^{B_o^2 M_o^2}} = 1 - e^{\left(B^2 M^2 - B_o^2 M_o^2\right)} \tag{4.21}$$

From eq. 4.21, the conditions for a core perturbation (like axial expansion) to produce a negative or positive reactivity effect can be defined as:

$$\begin{aligned} B^2 M^2 &> B_o^2 M_o^2 \rightarrow \delta\rho < 0 \\ B^2 M^2 &< B_o^2 M_o^2 \rightarrow \delta\rho > 0 \end{aligned} \tag{4.22}$$

The geometric buckling in a cylindrical core of uniform composition is:

$$B_g^2 = \left(\frac{\pi}{\tilde{H}}\right)^2 + \left(\frac{2.405}{\tilde{R}}\right)^2 \tag{4.23}$$

where $\tilde{H}$ and $\tilde{R}$ is the extrapolated height and radius of the core respectively. The first term of eq. 4.23 describes the axial buckling of the neutron flux, the second the radial. The migration area is defined as:

$$M^2 = \frac{1}{3\Sigma_{\mathrm{tr}}\Sigma_{\mathrm{a}}} \tag{4.24}$$

where Σ_{tr} and Σ_{a} are the macroscopic transport and absorption cross-sections in the core. Using core-averaged values, eq. 4.24 can be rewritten as:

$$M^2 = \frac{1}{3N^2\sigma_{\mathrm{tr}}\sigma_{\mathrm{a}}} \tag{4.25}$$

The migration area is directly inversely proportional to the square of the average atomic density in the core, which in turn for a given constant core mass is connected to the core height. The volume of a cylinder is given by:

$$V = \pi H R^2 \tag{4.26}$$

The atomic density of the core can be defined as:

$$N = N_A \times \left(\frac{M_{co}}{V \times C_{co}} \right) \tag{4.27}$$

where N_A is Avogadro's constant (6.023×10^{23} atoms/mol), M_{co} is the total mass of the core and C_{co} is the average atomic weight of all isotopes in the core. The only value that changes as the core expands is the volume. However, when modeled as a reactivity feedback, fuel axial expansion only affects the fuel (or fuel+cladding) isotopes of the core. The relative change in core atom density becomes:

$$\frac{N}{N_o} = \frac{\frac{N_A M_f}{\pi (H_o + x) R^2 C_f} + \frac{N_A M_{\text{cst}}}{\pi H_o R^2 C_{\text{cst}}}}{\frac{N_A M_{co}}{\pi H_o R^2 C_{co}}} \tag{4.28}$$

where subscript *cst* refers to values averaged over both coolant and structure. If the core consists only of fuel isotopes, eq. 4.28 simplifies to:

$$\frac{N}{N_o} = \frac{H_o}{H_o + x} = \frac{1}{1 + \alpha \Delta T} \tag{4.29}$$

The change in migration area can be expressed with total core-averaged values as:

$$\frac{M^2}{M_0^2} = \frac{\frac{1}{3 \Sigma_{\text{tr}} \Sigma_a}}{\frac{1}{3 \Sigma_{\text{tr}}^o \Sigma_a^o}} = \frac{\Sigma_{\text{tr}}^o \Sigma_a^o}{\Sigma_{\text{tr}} \Sigma_a} \tag{4.30}$$

$$\frac{\Sigma_{\text{tr}}^o \Sigma_a^o}{\Sigma_{\text{tr}} \Sigma_a} = \frac{\Sigma_{\text{tr}}^{\text{cst}} \Sigma_a^{\text{cst}} + N_f \sigma_{\text{tr}}^f \times N_f \sigma_a^f}{\Sigma_{\text{tr}}^{\text{cst}} \Sigma_a^{\text{cst}} + N_f \sigma_{\text{tr}}^f \left(\frac{1}{1 + \alpha \Delta T} \right) \times N_f \sigma_a^f \left(\frac{1}{1 + \alpha \Delta T} \right)} \tag{4.31}$$

$$= \frac{\Sigma_{\text{tr}}^{\text{cst}} \Sigma_a^{\text{cst}} + \Sigma_{\text{tr}}^f \Sigma_a^f}{\Sigma_{\text{tr}}^{\text{cst}} \Sigma_a^{\text{cst}} + \Sigma_{\text{tr}}^f \Sigma_a^f \left(\frac{1}{1 + \alpha \Delta T} \right)^2} \tag{4.32}$$

For the simplified case of a core without structural material or coolant ($\Sigma_a^{\text{cst}} = \Sigma_{\text{tr}}^{\text{cst}} = 0$), the expression becomes:

$$\frac{M^2}{M_0^2} = \frac{(H_o + x)^2}{H_o^2} = (1 + \alpha \Delta T)^2 \tag{4.33}$$

This expression can be manipulated to represent real cores with structure and coolant (that are not affected by fuel axial expansion) by weighing the expansion by the relative importance

of the fuel in determining the neutron migration area in the core. The resulting expression is:

$$\frac{M^2}{M_o^2} = \left[1 + K \times \alpha \Delta T\right]^2 \tag{4.34}$$

$$K = \left(\frac{\Sigma_a^f \Sigma_{\mathrm{tr}}^f}{\Sigma_a^{\mathrm{co}} \Sigma_{\mathrm{tr}}^{\mathrm{co}}} \right) \tag{4.35}$$

K is the importance weighing factor of the fuel. Again, subscript *co* refers to the total core macroscopic cross-section (with all materials), subscript f refers to values only for the fuel. The relative impact of a height change on the geometric buckling is dependent on the core shape. The initial and perturbed buckling is given by:

$$B_o^2 = \left(\frac{\pi}{\tilde{H}_o}\right)^2 + \left(\frac{2.405}{\tilde{R}}\right)^2 \tag{4.36}$$

$$B^2 = \left(\frac{\pi}{\tilde{H}_o + x}\right)^2 + \left(\frac{2.405}{\tilde{R}}\right)^2 \tag{4.37}$$

To describe the core shape, the parameter *HD* is introduced:

$$\mathrm{HD} = \frac{\text{Extrapolated core height}}{\text{Extrapolated core diameter}} = \frac{\tilde{H}_o}{2 \times \tilde{R}} \tag{4.38}$$

The *HD* parameter differs slightly from the geometrical H/D-ratio describing the physical core shape as it includes the extrapolation distance in both dimensions. Generally, theaxial extrapolation distance is significantly larger than the radial extrapolation distance. This leads to the following rule of thumb:

$$\mathrm{HD} > H/D \tag{4.39}$$

The smaller the value is for H/D, the greater the difference is between *HD* and H/D. The relative change in buckling can then be expressed using *HD*, $\tilde{H}_o$ and x as:

$$\frac{B^2}{B_o^2} = \frac{\frac{\pi^2}{\left(\tilde{H}_o + x\right)^2} + \frac{23.136 \times \mathrm{HD}^2}{\tilde{H}_o^2}}{\frac{\pi^2}{\tilde{H}_o^2} + \frac{23.136 \times \mathrm{HD}^2}{\tilde{H}_o^2}} \tag{4.40}$$

In the limit, where the core has no axial extent ($HD \to 0$), eq. 4.40 becomes:

$$\frac{B^2}{B_o^2}\left(\mathrm{HD} \to 0\right) = \frac{\tilde{H}_o^2}{\left(\tilde{H}_o + x\right)^2} \tag{4.41}$$

For a pure-fuel core, the minimal possible relative change in the value of geometric buckling is equal to the inverse of the core-shape-independent expression for migration area:

$$\frac{B^2}{B_o^2} \geq \frac{\tilde{H}_o^2}{\left(\tilde{H}_o + x\right)^2} \tag{4.42}$$

$$\frac{M^2}{M_o^2} = \frac{\left(\tilde{H}_o + x\right)^2}{\tilde{H}_o^2} > 1 \tag{4.43}$$

The initial inequality describing the sign of the reactivity feedback (eq. 4.23) can be re-written as follows:

$$\frac{B^2 M^2}{B_o^2 M_o^2} > 1 \rightarrow \delta\rho < 0 \tag{4.44}$$

$$\frac{B^2 M^2}{B_o^2 M_o^2} < 1 \rightarrow \delta\rho > 0 \tag{4.45}$$

For a fuel-only core, the result is:

$$\frac{B^2 M^2}{B_o^2 M_o^2} = \frac{\left(\frac{\pi^2}{\left(\tilde{H}_o + x\right)^2} + \frac{23.136\mathrm{HD}^2}{\tilde{H}_o^2}\right)\left(\tilde{H}_o + x\right)^2}{\left(\frac{\pi^2}{\tilde{H}_o^2} + \frac{23.136\mathrm{HD}^2}{\tilde{H}_o^2}\right)\tilde{H}_o^2} \geq 1 \rightarrow \delta\rho \leq 0, \quad \mathrm{HD} \geq 0 \tag{4.46}$$

Equation 4.46 gives analytical proof that axial expansion of a homogeneous core containing only fuel will *always* results in a negative reactivity feedback effect, independent of both core and flux shape.

The effect of geometric-buckling-change disappears as *HD* approaches higher values. This is easily shown mathematically as:

$$\frac{B^2}{B_o^2}\left(\mathrm{HD} \rightarrow \infty\right) = 1 \tag{4.47}$$

H/D-values of realistic fast reactor core designs generally lie in the span: $0.1 \leq \mathrm{H/D} \leq 1.0$. Fig. 4.5 gives the H/D-ratio of 33 major fast reactor concepts (17 of which were built and operated) as a function of thermal power.

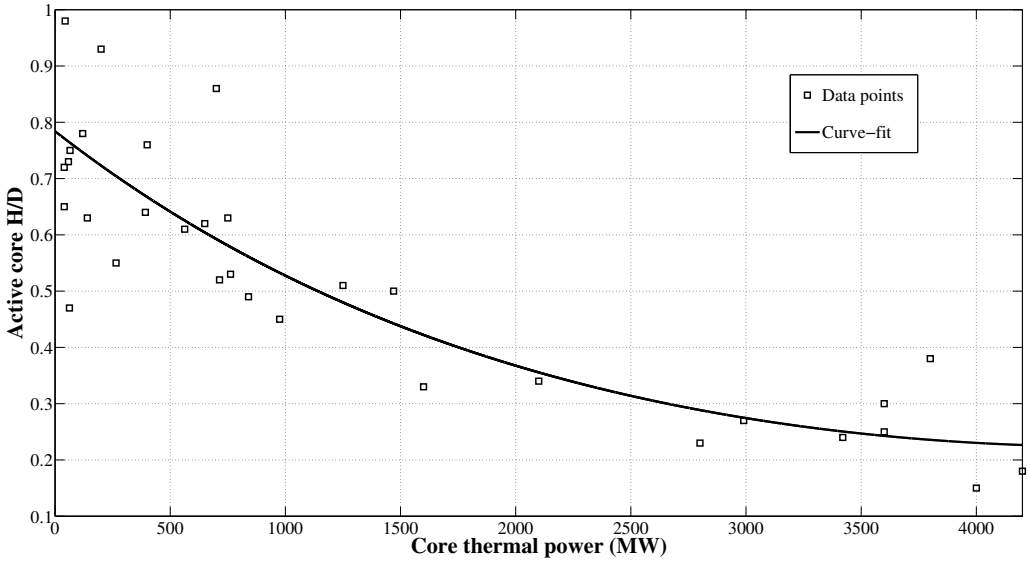

Figure 4.5: H/D ratio of 33 major fast reactor concepts (developed from data in ref. [55])

The migration-area effect is core-shape-independent, its value is simply a constant related to how large the axially expanded core is relative to the original core. The buckling changes with core shape, and the net effect determining the sign and magnitude of the reactivity impact is the relative change in both ratios. This can be seen in Fig. 4.6, where a fuel-only core is expanded by 10% of its original height. The buckling effect by itself contributes positive reactivity by reducing the axial leakage probability, the migration area effect adds negative reactivity primarily by increasing radial leakage probability. The positive reactivity added by the buckling change reaches its maximum as H/D goes to 0. For a perturbation of 10% increase in axial height, the buckling effect is essentially non-existent at H/D $\geq$ 5.

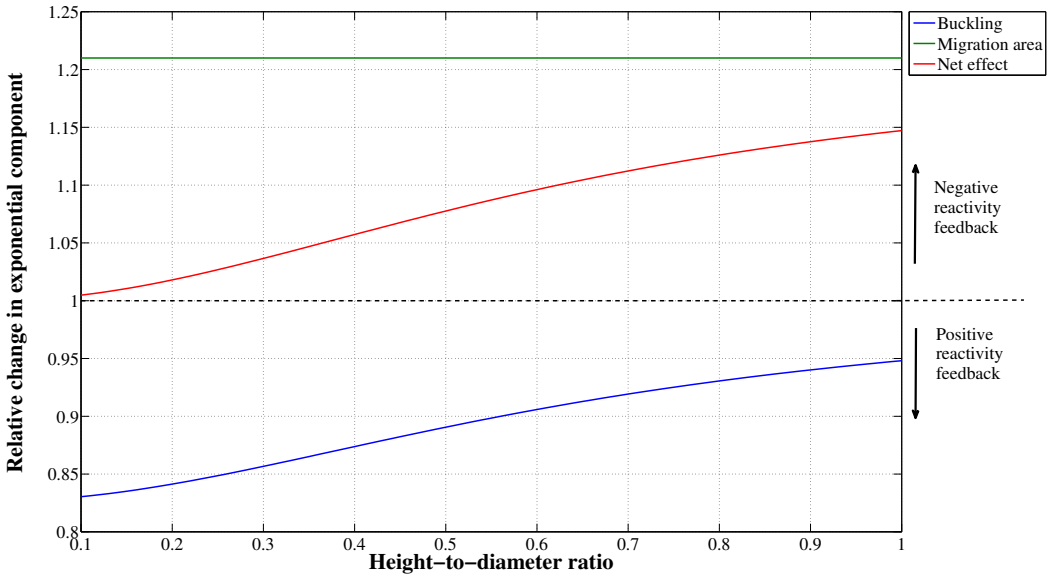

Figure 4.6: Relative change in leakage exponentials in a fuel-only core (H=100 cm, x=10 cm)

While the above analysis shows the relative positive and negative components of axial expansion and the effects of core shape, it cannot be used to quantify the reactivity effects directly. Here the crude approximation of a fuel-only core is used for simplicity. Returning to the definition of migration area, it can be written as:

$$M^2 = \frac{1}{3\sigma_{\text{tr}}\sigma_a}\left(\frac{VC_a}{N_A M_c}\right)^2 = \frac{1}{3\sigma_{\text{tr}}\sigma_a}\left(\frac{\pi R^2 C_a}{N_A M_c}\right)^2 \times H^2 \tag{4.48}$$

The change in the core height by a temperature change is given by the linear thermal expansion coefficent α (the calculation of which is described in great detail in section 4.3.4). The volume of the expanded core is:

$$V = \pi R^2 H_o \left(1 + \alpha \Delta T\right) \tag{4.49}$$

The migration area of the expanded core becomes:

$$M^2 = Q \times \left[H_o \left(1 + K\alpha\Delta T\right)\right]^2 \tag{4.50}$$

$$Q \equiv \frac{1}{3\sigma_{\text{tr}}\sigma_a}\left(\frac{\pi R^2 C_a}{N_A M_c}\right)^2 \tag{4.51}$$

where Q is added to shorten the expression to a variable and static component. The complete non-leakage exponent of the expanded core is then:

$$B^2 M^2 = Q\left(\pi^2 + \frac{2.405^2 H_o^2 \left(1 + K\alpha\Delta T\right)^2}{R^2}\right) \tag{4.52}$$

The original leakage exponential is given by simply setting ΔT=0 to remove the expansion as:

$$B_o^2 M_o^2 = QR^2 \left(\pi^2 + 2.405^2 H_o^2\right) \tag{4.53}$$

The reactivity effect stemming from an axial expansion of the core is then:

$$\delta\rho = 1 - e^{5.784 \times QR^2 H_o^2 \times \left[(1+K\alpha\Delta T)^2 - 1\right]} \tag{4.54}$$

In order to get a value out of eq. 4.54, a number of core-averaged values need to either calculated or estimated. In order to calculate the core-averaged atomic weight, one needs to know the total mass of all materials in the core:

$$M_c = \sum_i \rho_i V_i \tag{4.55}$$

where i denotes a core material. The core-average atomic weight is then given by:

$$C_a = \frac{\sum_i m_i A_i}{M_c} \tag{4.56}$$

where i denotes a core isotope and A_i the corresponding atomic weight. In addition, the core-averaged single-group absorption and transport cross-sections need to either be calculated for the specific core or estimated from known one-group cross-section tables.

4.3.2.1 Calculation examples

A typical migration length of a sodium cooled breeder reactor is ∼18 cm, giving a migration area of M=325 cm^2.[2] This calculation example is for a core with a fixed height of H_0=150 cm and a varying radius, undergoing axial expansion from a temperature increase of 500K with a metallic-fuel expansion coefficient of $\alpha = 2 \times 10^{-5} K^{-1}$. The cores are assumed to be made up of the same volume fractions of materials and have the same neutron energy spectrum, yielding a constant migration area while core radii varies. For simplicity, the value of K (eq. 4.35) is set equal to one in this example. A constant value for the effective delayed neutron fraction of 350 pcm was assumed. Table 4.1 gives the corresponding results while maintaining the total core volume at 20 m^3. It also details the separate effects of buckling and migration area changes. Notably, the reactivity coefficients of the two separate effects do not precisely sum up to the combined net effect. The net effect is slightly less negative than the sum of the coefficients for all but the most cigar-shaped core (R=100 cm).

Table 4.1: Feedback from ax. exp. by analytical model, core volume = 20 m^3

Radius (cm)	100	150	200	250
Height (cm)	636.6	282.9	159.2	101.9
H/D	3.18	0.94	0.40	0.20
k_∞	1.2164	1.1316	1.1895	1.4032
k_{eff} (ref)	1.0000	1.0000	1.0000	1.000
Leakage (ref.)	17.790%	11.629%	15.933%	28.751%
Leakage ($\delta T = 500$K)	18.101%	11.778%	16.012%	28.749%
k_{eff} ($\delta T = 500$K)	0.9962	0.9983	0.99904	0.99938
$\delta\rho$ ($\delta T = 500$K)	-0.38%	-0.17%	-0.095%	-0.060%
Reactivity coefficient (¢/K)	-0.217	-0.097	-0.054	-0.035
Separated effects				
Leakage (only buckling)	17.777%	11.559%	15.723%	28.317%
k_{eff} (only buckling)	1.002	1.0008	1.0025	1.0061
Leakage (only migration area)	18.113%	11.848%	16.226%	29.235%
k_{eff} (only migration area)	0.99607	0.99753	0.99649	0.99319
RC (¢/K) - (only buckling)	+0.009	+0.045	+0.142	+0.347
RC (¢/K) - (only migration area)	-0.223	-0.143	-0.200	-0.389

[2]Caclulated for a metallic fueled SFR using Serpent [47]

As expected, the buckling effect is smaller for nominally taller cores, while the migration effect is larger where total leakage is larger. Since H/D≈1 is the neutronically optimal core shape giving the smallest total neutron leakage probability, the migration effect reaches a minimum around this value.

4.3.3 Hybrid-analytic calculational method of axial expansion feedback

The highest fidelity method of calculating axial expansion reactivity feedback is to run a reference and perturbed core state in a neutron transport monte-carlo code such as MCNP or Serpent and evaluate the change in effective multiplication factor. To speed-up and simplify this process while maintaining acceptable (or, useful) calculational accuracy and at the same time gaining understanding of the physics involved in this feedback, a hybrid analytic/calculational method is proposed as follows:

1. Run a reference core in a neutron transport code such as Serpent or MCNP
2. Extract needed data for analytic model as presented above
3. Analytically calculate axial expansion feedback

Such a hybrid model can ensure both accuracy and a large speed-up factor, requiring only a single standard neutron transport calculation to calculate the physics of expansion feedback. The macroscopic neutron transport and absorption cross-section and axial/radial leakage is readily available as standard output from either Serpent or MCNP. The appropriate geometric buckling of a (cylindrical) core can be obtained by finding the effective extrapolation lengths in both dimensions. Normalized leakage in the radial (L_R) and axial (L_A) direction can then be expressed as:

$$L_{\mathrm{A}} = 1 - e^{B_z^2 M_o^2} \tag{4.57}$$

$$L_{\mathrm{R}} = 1 - e^{B_r^2 M_o^2} \tag{4.58}$$

Expressions for buckling in each dimension can be arrived at by assuming that the core size in the other dimension is infinite. Expressing the combined extrapolation length in the axial direction as δH and in the radial direction as δR, the geometric buckling in each dimension is:

$$B_z^2 = \left(\frac{\pi}{H + \delta H}\right)^2 \tag{4.59}$$

$$B_r^2 = \left(\frac{2.405}{R + \delta R}\right)^2 \tag{4.60}$$

Plugging in the geometric buckling expression in to eq. 4.57 and 4.58, it is possible to isolate the unknown variables δH and δR as:

$$\delta H = \pi \times \sqrt{\frac{M_o^2}{\ln\left(1 - L_z\right)}} - H \tag{4.61}$$

$$\delta R = \frac{481}{200}\sqrt{-\frac{M_o^2}{\ln\left(1-L_r\right)}} - R \tag{4.62}$$

The resulting geometric buckling, as given in the easily tallied leakage parameters, are:

$$B_o^2 = \frac{\ln\left(\frac{1}{1-L_z}\right)}{M_o^2} - \frac{\ln\left(1-L_r\right)}{M_o^2} \tag{4.63}$$

Introducing the height expansion term for the perturbed geometric buckling in the expanded core yields:

$$B^2 = \frac{\pi^2}{\left(H\left(1+\alpha\Delta T\right) + \pi\sqrt{\frac{M_o^2}{\ln\left(\frac{1}{1-L_z}\right)}} - H\right)^2} - \frac{\ln\left(1-L_r\right)}{M_o^2} \tag{4.64}$$

The original (un-expanded core) neutron migration area is given by:

$$M_o^2 = \frac{1}{3\Sigma_{\mathrm{tr}}\Sigma_{\mathrm{a}}} \tag{4.65}$$

The expanded core migration area is:

$$M^2 = M_o^2 \times \left(1 + K \times \alpha\Delta T\right)^2 \tag{4.66}$$

The non-leakage exponent can be expressed as:

$$M_o^2 B_o^2 - M^2 B^2 = M_o^2\left(1 + K \times \alpha\Delta T\right)^2 \times \tag{4.67}$$
$$\left(\frac{\pi^2}{\left(H\left(1+K\alpha\Delta T\right) + \pi\sqrt{\frac{M_o^2}{\ln\left(\frac{1}{1-L_z}\right)}} - H\right)^2} - \frac{\ln\left(1-L_r\right)}{M_o^2}\right)$$
$$-\ln\left(\frac{1}{1-L_z}\right) - \ln\left(1-L_r\right) \equiv \delta L$$

The change in reactivity, given the above definition of δL, is simply:

$$\delta\rho = \left(1 - e^{\delta L}\right) \tag{4.68}$$

Finally, the reactivity coefficient is given by:

$$\mathrm{RC}\left(¢/K\right) = \frac{100 \times \delta\rho}{\beta_{\mathrm{eff}} \times \Delta T} \tag{4.69}$$

The validity of the hybrid model remains to be verified by comparison to exact calculations using monte-carlo neutron transport calculations. Preliminary results indicate that errors as

calculated by the hybrid model varies between 3-10% for sodium cooled, metallic-fueled cores of different shapes with a fixed volume of 20 m^3. No study has been done to define the source of this discrepancy. Important to note is that calculated reactivity coefficients spanned over more than two orders of magnitude while maintaining this error span. While the monte-carlo method accurately describes the physical behavior of the core, an error is introduced when extracting a linear coefficient of reactivity from the data. Any reactivity feedback can be linearized for some span of temperature and/or geometry-change, but the coefficient will refer specifically to a pertubation from a given reference temperature. To obtain a reactivity coefficient from a monte-carlo study, the multiplication factor of a reference and perturbed core state are compared with an assumed linear behavior in between the data points. To obtain statistically significant results, the perturbed state needs to have difference in multiplication factor relative to the reference core many times larger than the properly combined statistical error of both calculations. Thus, the accuracy of the linearization of the coefficient is directly correlated to CPU-time. Assuming a very large valid linear range for the coefficient is beneficial for the computational economy but introduces an additional error (on top of statistics). The hybrid model is based solely on data at the reference (un-perturbed) state, but can in fact be expanded arbitrarily to represent any linearization interval by the choice of ΔT. As ΔT goes to 0 for the hybrid model, there is no change in calculation time but the linearization error can be completely eliminated. Errors of the magnitude as introduced by the hybrid model (3-10%) and monte-carlo linearization ($\sim$0.5%) are much smaller than uncertainties in the thermo-physical data needed to accurately calculate α for a metallic fueled system after a few percent of burnup.

4.3.3.1 Pre-computational hybrid approach

A pre-computational approach can be utilized to approximate axial expansion reactivity feedback of new core designs without the need for neutron transport at all. This is possible since the one-group cross-sections needed to calculate M_o^2 are primarily dependent on core volume fractions. If a library of one-group cross-sections are pre-calculated for given set of volume fractions, fuel compositions and burnup levels, M_o^2 can be estimated without running neutron transport. Similarly, buckling correlations for different core shapes and fuel zoning strategies could be pre-computed as well. If a new core design are within the validity range of pre-computed values, this method (along with the equations described in the previous section) can provide near instantaneous and accurate estimations of fuel axial expansion reactivity feedback.

4.3.3.2 The "virtual density" approach to calculation expansion feedback

The virtual density principle, invented by *Shikov (1959)* [71], states that the reactivity and flux distribution effects of a uniform core expansion (or contraction) can be exactly replicated by manipulating material densities with no change to core geometry. It has recently been used to replicate expansion reactivity effects with very good results using monte carlo,

diffusion and deterministic transport codes [72]. Until recently, this method represented no advance when using diffusion or monte-carlo techniques. Computing a virtual core expansion is no less computationally intensive than directly computing an actual core expansion. However, in the most recent versions of the MCNP code [73], material sensitivities can be calculated in a single run without a significant increase in calculational time, which makes the use of a hybrid virtual-density/monte-carlo calculation approach viable and effective. If this technique could be effectively implemented, it is a superior method to the hybrid method described in the preceding section.

4.3.4 Metallic fuel geometry and burnup effects

This study offers an alternative view from convention about how to accurately model fuel thermal expansion, particularly when using metallic fuel. After about 2% FIMA burnup, metallic fuel has swollen to the point that it is mechanically stuck in the cladding. Porous metallic fuel at high temperature is known to be a weak material. Because of this, many researchers have assumed that the thermal expansion of the fuel/cladding-system will not exceed that of the cladding. This is the lower bound case for the modeling of the fuel thermal expansion coefficient. Since the fuel, which by itself has a higher thermal expansion coefficient than the cladding, make up the majority of cross-sectional area, volume and mass of the rod, the actual value of the combined fuel-and-cladding thermal expansion is somewhere between that of the individual coefficients of fuel and cladding expansion. Assuming that the clad and fuel are stuck together and no sliding or plastic deformation occurs during a limited temperature transient, the combined thermal expansion coefficient can be estimated using thermo-physical data and an axial force balance. In the work of many research groups, the metallic fuel is assumed so *"weak"* that this procedure is deemed unnecessary, the fuel component in the combined expansion calculation is simple ignored by setting its elastic modulus to 0. This assumption is used by ANL (US) [74][75] , BNL (on NRC contract) (US) [68], MIT (US) [76], KAERI [77] (S. Korea), IGCAR [78] (India) and many others. It will be shown in sections 4.3.5, 4.3.6 and 4.8.8 that such an assumption introduces a significant error and is, in specific scenarios, non-conservative with regards to safety[3].

Since the fuel and cladding material feature different thermal expansion coefficients, stresses will be induced in both materials. The stress induced by thermal expansion in a restrained material is given by:

$$\sigma = \frac{F}{A} = E\epsilon \tag{4.70}$$

where σ is stress, F is force, A is the cross-sectional area, E is the elastic modulus of the material and ϵ is the resulting thermal expansion strain. The thermal expansion strain can

[3]It should be noted that in many scenarios, particularly in the early stages of transients, this is indeed a conservative assumption. Regardless, it is always better to start with the best and most accurate model model and *then* apply conservatism.

be expressed as:

$$\epsilon = \alpha \Delta T \tag{4.71}$$

where α is the coefficient of linear thermal expansion and ΔT is the change in temperature. Given eq. 4.70 and 4.71, the force in the cladding (subscript c) and fuel (subscript f) become:

$$F_c = A_c E_f \alpha_c \Delta T_c \tag{4.72}$$

$$F_f = A_f E_f \alpha_f \Delta T_f \tag{4.73}$$

Rewriting the equation, the thermal expansion coefficient can be expressed as:

$$\alpha = \frac{F}{AE\Delta T} \tag{4.74}$$

Summarizing the contributing thermal expansion coefficients and assuming that the change in temperature is the same in both materials ($\Delta T_c = \Delta T_f$) gives:

$$\alpha_{\text{combined}} = \frac{A_f E_f \alpha_f + A_c E_c \alpha_c}{A_f E_f + A_c E_c} \tag{4.75}$$

Equation 4.75 describes the actual physical expansion of the combined cladding-fuel system. The trouble is defining the components that enter in to the expression. For metallic fuel, the cross-section area ratios of the two components is a function of the initial fuel smear density and the cladding thickness. The fuel smear density (FSD) is defined as:

$$\text{FSD} = \frac{A_f}{A_{\text{ri}}} \tag{4.76}$$

where A_{ri} is the cross-sectional area of the rod inside of the cladding and A_f is the area of the fuel rod. A_{ri} is defined as:

$$A_{\text{ri}} = \left(\frac{D_{Ci}}{2}\right)^2 \times \pi \tag{4.77}$$

where D_{Ci} is the inner diameter of the cladding rod. Solving for A_f gives the freshly loaded un-irradiated fuel diameter as:

$$\frac{1}{4} \times D_f^2 \times \pi = \frac{1}{4} D_{Ci}^2 \times \pi \times \text{FSD} \tag{4.78}$$

$$D_f = \sqrt{\text{FSD}} \times D_{Ci} = \sqrt{\text{FSD}} \times (D_{Co} - 2 \times \text{CT}) \tag{4.79}$$

where D_{Co} is the outer diameter of the cladding rod and CT is the cladding thickness. From the above definitions, the area ratio between the inside of the rod and the unirradiated fuel is simply given by:

$$\frac{A_{ri}}{A_f} = \frac{1}{\text{FSD}} \tag{4.80}$$

The ratio between the total fuel rod area and the fuel area is:

$$\frac{A_{ro}}{A_f} = \frac{\left(D_{Ci} + 2\mathrm{CT}\right)^2}{\mathrm{FSD} \times D_{Ci}} \tag{4.81}$$

The actual area relations of applicability for the stress balance analysis is however the ratio between the area of the fuel and the area of the cladding. These relations are:

$$\begin{aligned} \frac{A_c}{A_f + A_c} &= \frac{\frac{1}{4}\left(D_{Ci} + 2\mathrm{CT}\right)^2 \pi - \frac{1}{4} D_{Ci}^2}{\frac{1}{4}\mathrm{FSD} \times D_{Ci}^2 \times \pi + \frac{1}{4}\left(D_{Ci} + 2\mathrm{CT}\right)^2 \pi - \frac{1}{4} D_{Ci}^2} \\ &= \frac{\frac{1}{4} D_o^2 \times pi - \frac{1}{4}\left(D_{Co} + 2\mathrm{CT}\right)^2}{\frac{1}{4}\mathrm{FSD}\left(D_{Co} - 2\mathrm{CT}\right)^2 \pi + \frac{1}{4} D_{Co}^2 \times \pi - \frac{1}{4}\left(D_{Co} - 2\mathrm{CT}\right)^2} \end{aligned} \tag{4.82}$$

$$\begin{aligned} \frac{A_f}{A_f + A_c} &= \frac{1}{4} \times \frac{\mathrm{FSD} \times D_{Ci}^2 \times \pi}{\frac{1}{4}\mathrm{FSD} \times D_{Ci}^2 \times \pi + \frac{1}{4}\left(D_{Ci} + 2\mathrm{CT}\right)^2 \pi - \frac{1}{4} D_{Ci}^2} \\ &= \frac{1}{4} \times \frac{\mathrm{FSD} \times \left(D_{Co} - 2\mathrm{CT}\right)^2 \pi}{\frac{1}{4}\mathrm{FSD}\left(D_{Co} - 2\mathrm{CT}\right)^2 \pi + \frac{1}{4} D_{Co}^2 \pi - \frac{1}{4}\left(D_{Co} - 2\mathrm{CT}\right)^2} \end{aligned} \tag{4.83}$$

The area relations essentially depend on only two variables: the fuel smear density (FSD) and the ratio between the outer cladding diameter and the cladding thickness (the *cladding thickness ratio - CTR*). These relations are shown in Fig. 4.7.

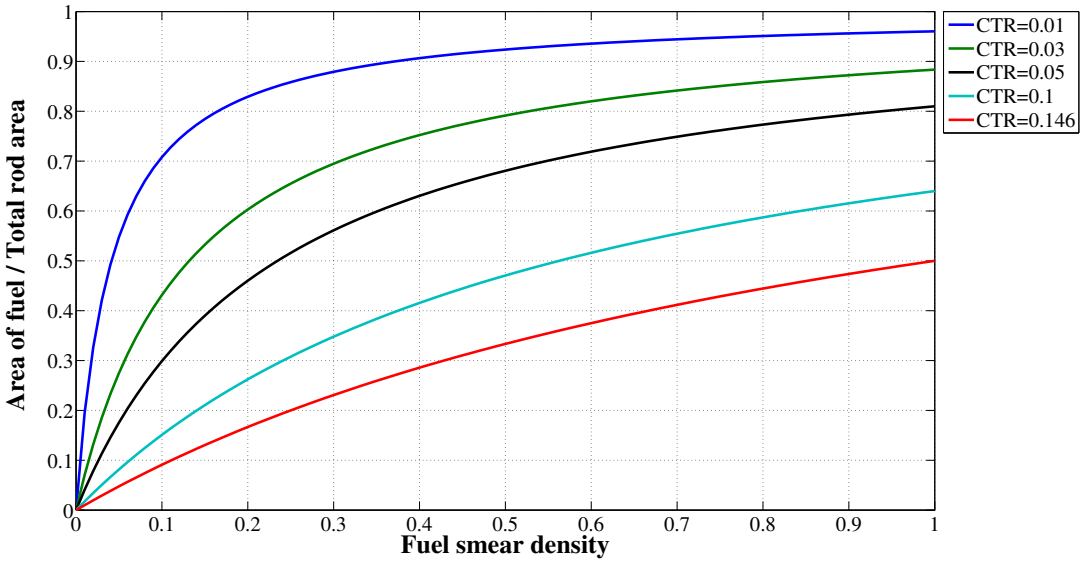

Figure 4.7: FSD and CTR dependence on fuel rod area ratios

The CTR-value is generally useful as it is a variable independent of the actual size of the fuel rod. The main property constraining the cladding thickness, the hoop stress, is linearly dependent on the fuel rod radius. Mathematically, the fully swollen fuel area fraction of the total rod area is given, independent of the rod size, by:

$$\frac{A_f}{A_f + A_c}\,(\text{FSD}{=}1) = 1 - 4\text{CTR} + 4\text{CTR}^2 \tag{4.84}$$

At CTR≈0.146, the area of the cladding and fuel is equal (also shown in Fig. 4.7). For a standard fast reactor fuel rod, the value of CTR lies within the range $0.03 \leq \text{CTR} \leq 0.07$. This value potentially has a profound effect on the reactivity feedback effect of axial fuel expansion. The geometry of metallic fuel, freshly loaded and at maximum radial swelling, is given to scale for CTR=0.05 in Fig 4.8.

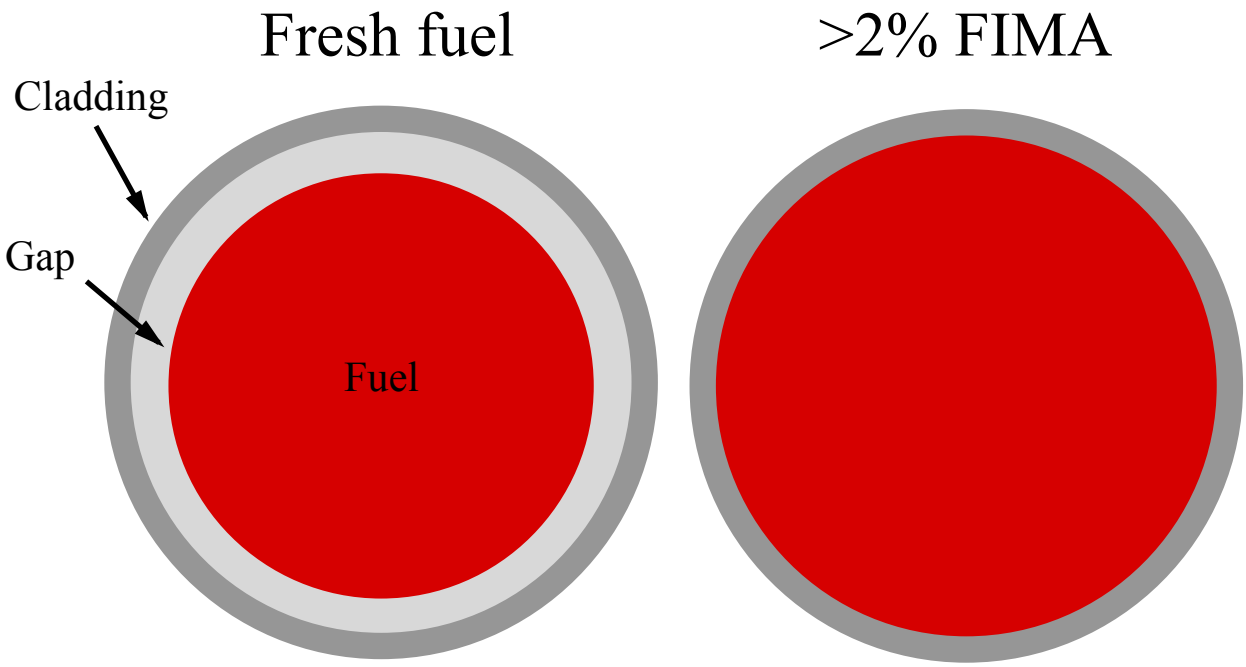

Figure 4.8: Metallic fuel geometry by burnup

In principle, the stress-balance solution (4.75) only comes in to play when the fuel has reached the swelling state as seen in the right side of Fig. 4.8. By definition then, the area ratios are at a state corresponding to $FSD{=}1$, ostensibly making the inclusion of $FSD{\neq}1$ in the above equations unnecessary. However, the level of fuel porosity has as it reaches the fuel/clad-locked state is dependent on the value of FSD. Material properties at the swollen state are heavily dependent on the amount of irradiation-induced swelling it has undergone to get there. There is little material property data reported for heavily neutron irradiated and swollen samples of metallic fuel. The data for the un-irradiated materials must therefore

be adapted for the state which is being analyzed. The most simple model to assess the change in elastic modulus by swelling is given by [79]:

$$E_1 = E_0 (1 - P) \rightarrow \delta E = -P \times E_0 \tag{4.85}$$

where P is the porosity of the material. The porosity of swollen fuel relates to the smear density as:

$$P = \frac{1}{\text{FSD}} - 1 \tag{4.86}$$

This gives the change in elastic modulus as:

$$\delta E = E_0 \left(1 - \frac{1}{\text{FSD}}\right) \tag{4.87}$$

In this very simple model, a smear density of 75% allows a final porosity of 33% giving a 33% decrease in the elastic modulus of the material once swollen. A slightly different model is recommended for use relating directly to the density change rather than porosity as [79]:

$$\delta E = E_0 \left[\frac{1}{(1+S)^2 - 1}\right] \tag{4.88}$$

$$S = \frac{\rho_0}{\rho_1} - 1 \tag{4.89}$$

Since the fuel mass does not change, the ratio $\frac{\rho_0}{\rho_1}$ can be evaluated as:

$$\frac{\rho_0}{\rho_1} = \frac{\frac{m}{V_0}}{\frac{m}{V_1}} = \frac{\left(\frac{D_{Ci}}{2}\right)^2 \pi H}{\left(\frac{\sqrt{\text{FSD}} \times D_{Ci}}{2}\right)^2 \pi H} = \frac{1}{\text{FSD}} \tag{4.90}$$

The relative change in elastic modulus can thus be given as:

$$\delta E = E_0 \times \left(\text{FSD}^2 - 1\right) \tag{4.91}$$

This model produces a stronger reduction in elastic modulus than the more basic model of eq. 4.87, and is used throughout the rest of this analysis. Introducing the re-evaluated elastic modulus that takes swelling in to account, the combined thermal expansion can be expressed as:

$$\alpha_{\text{combined}} = \frac{A_f \left[E_f \times (FSD)^2\right] \alpha_f + A_c E_c \alpha_c}{A_f \left[E_f \times (FSD)^2\right] + A_c E_c} \tag{4.92}$$

Eq. 4.92 can then be re-written with fractional area ratios as:

$$\alpha_{\text{combined}} = \frac{\frac{A_f}{A_f + A_c} \left[E_f \times (FSD)^2\right] \alpha_f + \frac{A_c}{A_f + A_c} E_c \alpha_c}{\frac{A_f}{A_f + A_c} \left[E_f \times (FSD)^2\right] + \frac{A_c}{A_f + A_c} E_c} \tag{4.93}$$

The fractional areas are given from geometry analysis as:

$$Q_f \equiv \frac{A_f}{A_f + A_c} = (2 \times \mathrm{CTR} - 1)^2 \tag{4.94}$$

$$Q_c \equiv \frac{A_c}{A_f + A_c} = 1 - (2 \times \mathrm{CTR} - 1)^2 \tag{4.95}$$

Plugging back in to eq. 4.93, the combined expansion expression becomes:

$$\alpha_{\mathrm{combined}} = \frac{Q_f \left(E_f \times \mathrm{FSD}^2\right) \alpha_f + Q_c E_c \alpha_c}{Q_f \left(E_f \times \mathrm{FSD}^2\right) + Q_c E_c} \tag{4.96}$$

4.3.5 Elastic modulus data for metallic fuel

A substantial difference in data was found in the published correlations for the elastic modulus of metallic fuel. All of the correlations that were found in a very extensive literature review are presented and evaluated here.

The elastic modulus of U-19Pu-10Zr has been reported as 85.13 GPa by Ohta et. al. [80]. The value for the same alloy was reported as 93.31 GPa in an NEA report [81], but this may be due to an error in the report, as this value corresponds to the value for the U-19Pu-10Zr-5MA-5RE alloy in ref. [80][4]. The value for U-10Mo fuel has also been reported as 85 GPa [82].

The fast reactor safety analysis code SASSYS/SAS4A contains a number of modules that reports values for the elastic modulus of metallic fuel. FPIN2 is the SASSYS/SAS4A *"Pre-Failure Metal Fuel Pin Behavior Model"*. Re-written to be in units of GPa, the correlation used in the SAS-FPIN2 computer code is given as [83]:

$$E_f\,(\mathrm{FPIN2}) = 12 \times (1 - 1.2P) \times \left(1 - 0.754 \times 10^{-3}\,(T - 588)\right) \quad \mathrm{GPa} \tag{4.97}$$

This correlation evalutates to 14.6 GPa for fully dense fuel at room-temperature. The correlation given in eq. 4.97 is not feasible, as the values are nonphysically low. The lowest elastic moduli values for metallic alloys are at least 4 times higher than the highest value as calculated from eq. 4.97. In the manual for the SAS-DEFORM4 code, the fuel elastic modulus is given as [84]:[5]

$$E_f\,(\mathrm{DEFORM4}) = 140 \quad \mathrm{GPa} \tag{4.98}$$

This is presented as an "average" value considering variation of E_f with temperature, composition, and phase. The documentation for the SASSYS/SAS4A code also gives much more

[4]Since nothing else is mentioned, it is assumed these measurements were performed at room-temperature

[5]The actual value given in ref. [84] is 1400 GPa, this is likely a typo. The DEFORM4 value is also referenced in the FPIN2 manual, stating that the DEFORM4 value is 10 times higher than that given by the FPIN2-correlation, which would mean 146 GPa.

complete expressions for elastic modulus of several metallic fuel alloys, reported in the chapter dealing with the theory of axial fuel expansion. For U-10Zr (wt.%) fuel, it is reported (in Pa) as [85]:

$$E_{f1}\,(\mathrm{T}) = 1.5123 \times 10^{11}\,(1 - 1.2P)\left(1 - 1.06\frac{T - 588}{1405}\right) \quad T \leq 923\mathrm{K} \tag{4.99}$$

$$E_{f2}\,(\mathrm{T}) = E_{f1}\,(\mathrm{T}) - 0.3 \times E_{f1}(T = 923\mathrm{K}) \quad T > 923\mathrm{K} \tag{4.100}$$

At room-temperature and 0% swelling, this evaluates to 174.9 GPa. Thus, in different sections of the SASSYS/SAS4A manual package, the elastic modulus of unswollen room-temperature U-10Zr (wt.%) is reported as 14.6, 140 and 174.9 GPa – results spanning more than an order of magnitude. As a part of the SESAME-code documentation, the following correlation is reported [86]:

$$\begin{aligned} E_f\,(\mathrm{SESAME}) &= 56 - 0.1158 \times (T - T_3) \quad T \leq T_3 \\ &= 20 - 0.1273 \times (T - T_3) \quad T_3 \leq T \leq T_6 \\ &= 31 - 0.08 \times (T - T_6) \quad T \geq T_6 \qquad [\mathrm{GPa}] \end{aligned} \tag{4.101}$$

Here temperature (T) is in °C, T_3 and T_6 are phase-transition temperatures as:
$T_3 = \alpha + \delta \rightarrow \beta + \gamma$
$T_6 = \beta + \gamma \rightarrow \gamma$

For U-10Zr fuel the transition temperatures are: $T_3 = 662$°C and $T_6 = 692$°C.
For U-19Pu-10Zr, the values are: $T_3 = 595$°C and $T_6 = 650$°C.

At operating temperatures, multiple phases will be present in the fuel. For simplicity for the moment, all correlations and values are compared at room-temperature. At room-temperature, eq. 4.101 evaluates to 133.6 GPa. In 2009, *Radhakrishnan et. al* reported a correlation for the elastic modulus of the U-10Zr (wt.%) alloy, here rewritten for the GPa unit as [87]:

$$E_{\mathrm{U10Zr}}\,(\mathrm{GPa}) = 201.1658 - 0.20859896 \times T + 0.00035424944 \times T^2 - 2.7977181 \times 10^{-7} T^3 \tag{4.102}$$

At room-temperature (T=298K), eq. 4.102 evaluates to 163 GPa. The *Radhakrishnan et. al* report cites a *Battelle Memorial Institute* report edited by *A.A. Bauer* in 1959 as a data source [88][6].

Given the immense disparity in data already seen, it is imperative to analyze the available raw data to see which, if any, correlation matches this data.

[6]It is unclear where the quadratic and cubic temperature-dependence for U-10Zr elastic modulus as given by eq. 4.102 (*Radhakrishnan et. al* [87]) comes from. It is possible the U-11.5Zr arc-melted alloy data of ref. [88] was used, since the value at room-temperature is close to that of eq. 4.102 at room-temperature (163 vs. 165 GPa).

4.3.6 A new correlation for metallic fuel elastic modulus

The disparity in the data and correlations shown in the previous section prompted the development of a new set of correlations based on the raw data that is available. The data points given in ref. [88] are used as a basis for this development. Data in *Bauer (1969)* is presented separately, divided by the methods used to produce the alloys (arc or induction melting). The production method has a noticeable but minor effect on the elastic modulus. The available data from the original source is presented in Figures 4.9 - 4.11.

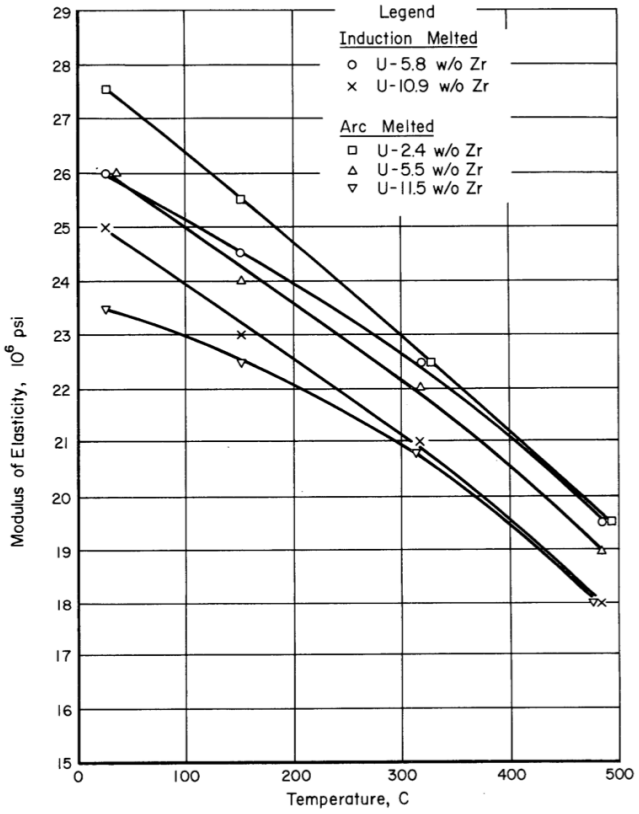

FIGURE C-12. EFFECT OF INCREASING TEMPERATURE ON MODULUS OF ELASTICITY OF SEVERAL URANIUM-ZIRCONIUM ALLOYS THAT HAD BEEN GAMMA ROLLED AND ALPHA ANNEALED FOR 24 HR AT 575 C(C-1)

Figure 4.9: Elastic modulus of U-Zr alloys (data from ref. [88], plot from ref. [89])

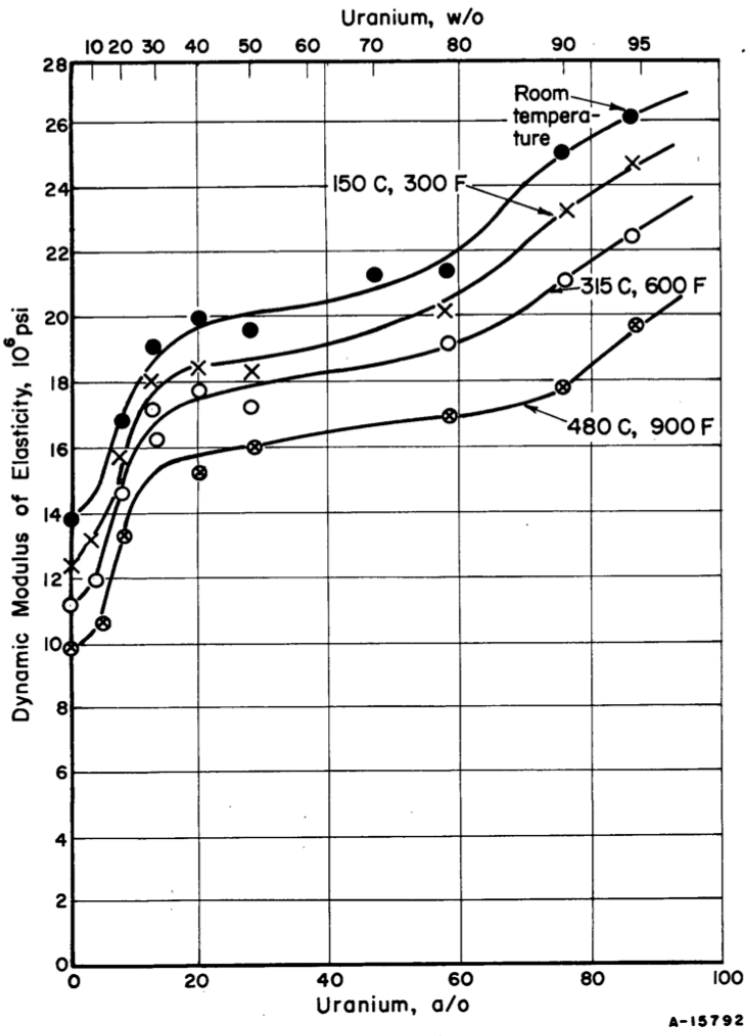

FIGURE 40. VARIATION OF DYNAMIC MODULUS OF ELASTICITY AT VARIOUS TEMPERATURES WITH URANIUM CONTENT IN INDUCTION-MELTED ZIRCONIUM-URANIUM ALLOYS

Figure 4.10: Elastic modulus of U-Zr alloys (from ref. [88])

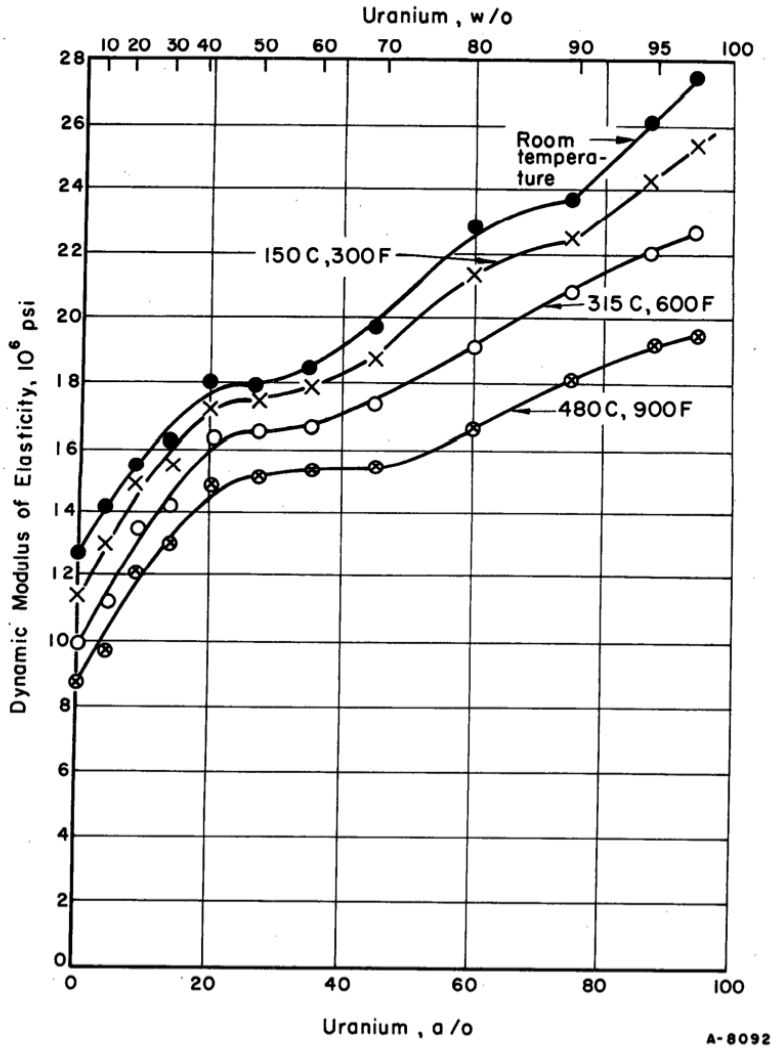

FIGURE 41. VARIATION OF DYNAMIC MODULUS OF ELASTICITY AT VARIOUS TEMPERATURES WITH URANIUM CONTENT IN ARC-MELTED ZIRCONIUM-URANIUM ALLOYS

Figure 4.11: Elastic modulus of U-Zr alloys (from ref. [88])

Note. 10^6 *psi corresponds to 6.895 GPa.*

The data in ref. [88], as given in Fig. 4.9 - 4.11 is measurement data that appears to be reliable. The reported values are in line with what is expected of a metallic alloy of this type. There are 4 temperature-datapoints each for a total of 8 different Zr-fractions for the induction melted alloys. For arc-melted alloys, the data-set contains 4 temperature datapoints at 12 different Zr-contents. For metallic breeder fuel alloys, only Zr-contents of $\leq$

20 w.% are of potential interest. This reduces the data-set to at total of 24 data-points (4 temperatures at 3 different Zr-contents for arc and induction melting respectively)[7]. This data, as extracted from the figures of ref. [88], is summarized in Table 4.2.

Table 4.2: Available data for metallic fuel elastic modulus (GPa)

Alloy	U-5.8Zr	U-5.5Zr	U-10.9Zr	U-11.5Zr	U-22Zr	U-20Zr
Manfact. type	Induction	Arc-melt	Induction	Arc-melt	Induction	Arc-melt
25°C	179.3	179.3	173.4	164.8	150.3	159.6
150°C	171.0	166.2	158.6	155.1	137.9	150.0
315°C	153.1	151.7	144.8	144.8	132.4	131.0
480°C	137.2	133.1	124.1	124.1	117.2	115.8

The dependence on temperature is approximately linear for each alloy, making it possible to produce a linear fits of the type $E_f = p_1 \times T + p_2$ to the data. The linear fits to the data of Table 4.2 are given in Table 4.3. Here temperature is given Kelvin and the validity range is $25 \leq \mathrm{T} \leq 480$°C ($298 \leq \mathrm{T} \leq 753$K).

Table 4.3: Linear data curve-fits for metallic fuel elastic modulus (GPa)

Alloy	U-5.8Zr	U-5.5Zr	U-10.9Zr	U-11.5Zr	U-22Zr	U-20Zr
Manfact. type	Induction	Arc-melt	Induction	Arc-melt	Induction	Arc-melt
p1	-0.09465	-0.1001	-0.1037	-0.08695	-0.06817	-0.09662
p2	208.9	209.1	203.4	192	169.6	188.7

Unfortunately, it is hard to define a trend and functional form for the values of p_1 from this limited data-set (3 points). It is clear from Fig. 4.10 and 4.11 that the temperature-dependence of the elastic modulus is higher at 6 w.% and 20-22 w.% Zr than at the intermediate 10 w.% data-points. Strictly speaking however, U-Zr alloys with Zr-contents higher than 10% w.% are of very limited interest for breeder reactor applications. As a very crude first-order approximation, a linear fit is applied to correlate Zr-content in fuel between the 2 data-points of 6 w.% and 10 w.%. Naturally, given there are only two data-points, there is great uncertainty in this correlation[8]. Given a second linear fit of the Zr-dependent p_1 and

[7] An additional data-set for arc-melted alloys at ~ 2.5 w.% Zr has been omitted.

[8] The "most reasonable" fit between two data-points is linear, such a fit is however of very limited value. One or more added data-points between the two data-points that are available may completely change the

p_2 values, best-estimate cure-fits with both temperature and Zr-content dependence can be developed with the following functional form:

$$E_{T,Zr}\,(\text{GPa}) = T \times (q_1 \times \text{Zr} \times +q_2) + \text{Zr} \times q_3 + q_4 \tag{4.103}$$

Evaluating the constants for the induction melted alloys yields a final expression as:

$$E_{\text{induction}}\,(\text{GPa}) = T \times (-0.001775 \times \text{Zr} - 0.08107) - 1.078 \times \text{Zr} + 215.2 \tag{4.104}$$

For the arc-melted alloys the corresponding expressions is:

$$E_{\text{arcmelting}}\,(\text{GPa}) = T \times (0.002192 \times \text{Zr} - 0.1122) - 2.85 \times \text{Zr} + 224.8 \tag{4.105}$$

These correlations are only strictly valid in the range $6 \leq \text{Zr} \leq 10$ w.% and $25 \leq \text{T} \leq 480$°C. Since the temperature-dependence is linear in this temperature range, it is reasonable to assume a linear temperature-dependence up until a phase-change occurs. For the low-Zr U-Zr alloys, this happens at about 660°C. The new developed correlations are plotted in Fig. 4.12.

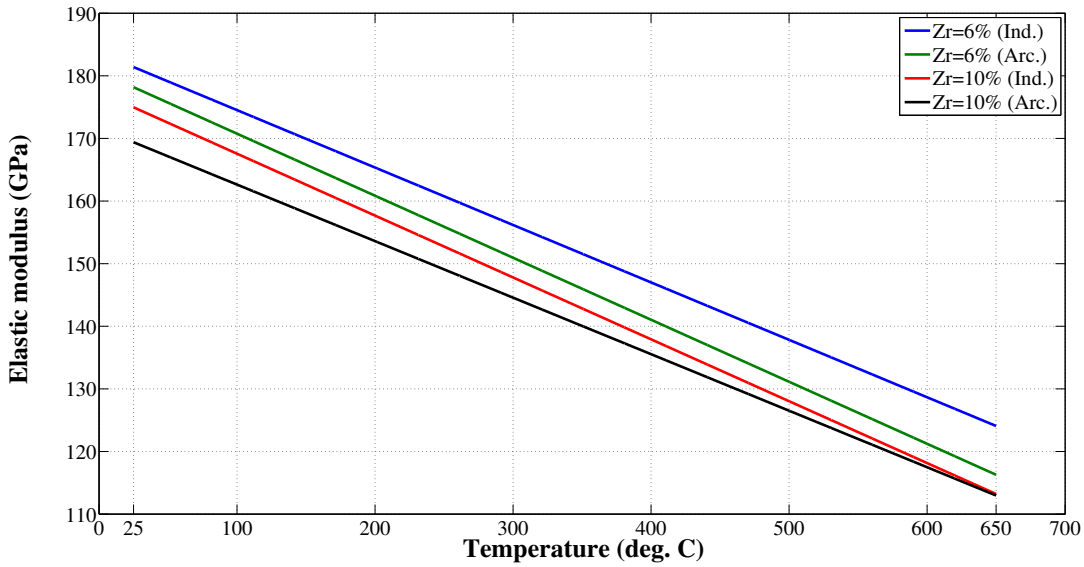

Figure 4.12: Elastic modulus of U-Zr alloys calc. by new correlations

The near-linearity of the temperature dependence of 5-10 w.% alloys can also be seen in Fig. 4.9. The effects of porosity through fuel swelling for the newly developed correlations

functional form of the fit. The fit developed is not meant to represent an actual correlation representing the true material values, it is simply the best-estimate possible from the limited data-set that exists.

(eq. 4.104 & 4.105) can be accounted for using eq. 4.91. The known independent correlations for metallic fuel elastic modulus and their applicability range are summarized in Table 4.4.

Table 4.4: Metallic fuel elastic modulus correlations data range and dependencies

Property	SAS4A	FPIN2	DEFORM	Kobayashi	Ohta	Redhakrishnan	Qvist
Zr%	10	n/a	n/a	10	10	10	0-10
Temp.	Y	Y	N	Y	N	Y	Y
Phase	N	N	N	Y	N	N	N
Porosity	Y	Y	N	N	N	N	Y
Manufacturing	N	N	N	N	N	N	Y

A summary of the values from all known data-sources for the elastic modulus of metallic fuel is given in Table 4.5.

Table 4.5: Known values for metallic fuel elastic modulus (GPa)

Source	Value at 25°C	Value at 585°C	Alloy
SASSYS/SAS4A [85]	174.9	114.3	U-10Zr
SASSYS/SAS4A [85]	135.9	88.8	U-10Zr-20Pu
FPIN2 [83]	14.6	9.6	N/A*
DEFORM4 [84]	140**	140**	N/A*
Kobayashi et. al [86]	133.6	68.7	U-10Zr
Ohta et. al [80]	85.13	n/a	U-19Pu-10Zr
Kim et. al [82]	85	n/a	U-10Mo
NEA*** [81]	93.31	n/a	U-19Pu-10Zr
Radhakrishnan et. al[87]	163.1	106.3	U-10Zr
Qvist / Bauer [88]****	175.0	119.6	U-10Zr (ind.)
Qvist / Bauer [88]	169.4	118.8	U-10Zr (arc.)

* The development effort of metallic fuels at ANL has been focused on alloys with 10 w.% Zr. The most likely alloy for this information is U-10Zr.
** The DEFORM4-value is presented as an average over temperature, it is unclear to what condition this average corresponds
*** This is likely a faulty value in the report and should probably be 85.13

**** *Bauer* does not report values for U-10Zr, these are calculated here by the correlation developed in this report (hence, ref. is Qvist/Bauer)

For the operating condition, an initial fuel smear density of 75% is assumed, giving a porosity of 33% (eq. 4.97). The average fuel operating temperature is assumed to be 585°C. The values of *Ohta et. al* and *Kim et. al* are temperature adjusted in the same way as given by *Kobayashi et. al*. For all correlations except for eq. 4.97, the swelling-adjusted elastic modulus are given by eq. 4.91. Table 4.5 gives the summarized values:

Table 4.6: Operating locked-up state metallic fuel (U-10Zr, unless otherwise mentioned) elastic modulus (GPa)

Source	585°C, 33% porosity (GPa)
ANL-FPIN2	5.77
ANL-DEFORM4	78.75
Kobayashi et. al	38.64
SASSYS/SAS4A*	0/69.0
Ohta et. al** & Kim et. al***	24.6
Radhakrishnan et. al	59.8
Qvist (2013)	66.8-67.3
HT9 (0% swelling)	154.2

* Correlation gives 69 GPa, set to 0 GPa by convention, ** U-19Pu-10Zr, *** U-10Mo

4.3.7 Implications for the value of combined axial expansion coefficient

In contrast to the wide disparity of data for elastic modulus of metallic fuel (specifically U-10Zr), there is better agreement between different sources on fuel thermal expansion data as well as of the thermophysical properties of HT9 steel. In the unit of inverse Kelvin, the thermal expansion coefficient of U-10Zr is given as [85]:

$$\alpha_{\mathrm{U10Zr}} = 1.658 \times 10^{-5} - 2.104 \times 10^{-8} T + 3.345 \times 10^{-11} T^2 \quad T < 900K \tag{4.106}$$

$$= 2.25 \times 10^{-5} \quad T \geq 900K \tag{4.107}$$

For HT9-steel it is given as [90]:

$$\alpha_{\mathrm{HT9}} = 1.62307 \times 10^{-6} + 2.84714 \times 10^{-8} T - 1.65103 \times 10^{-11} T^2 \tag{4.108}$$

The elastic modulus of HT9 steel is given as [85]:

$$E_{\mathrm{HT9}}\,(\mathrm{GPa}) = 213.7 - 0.10274 \times T \tag{4.109}$$

The combined expansion of the fuel/clad-system is given for the total range of CTR in Fig. 4.13 and zoomed-in for more reasonable fuel-rod values in Fig. 4.14. The material properties are calculated at 585°C for U-10Zr fuel with 33% porosity, and at 555°C for the HT9 cladding.

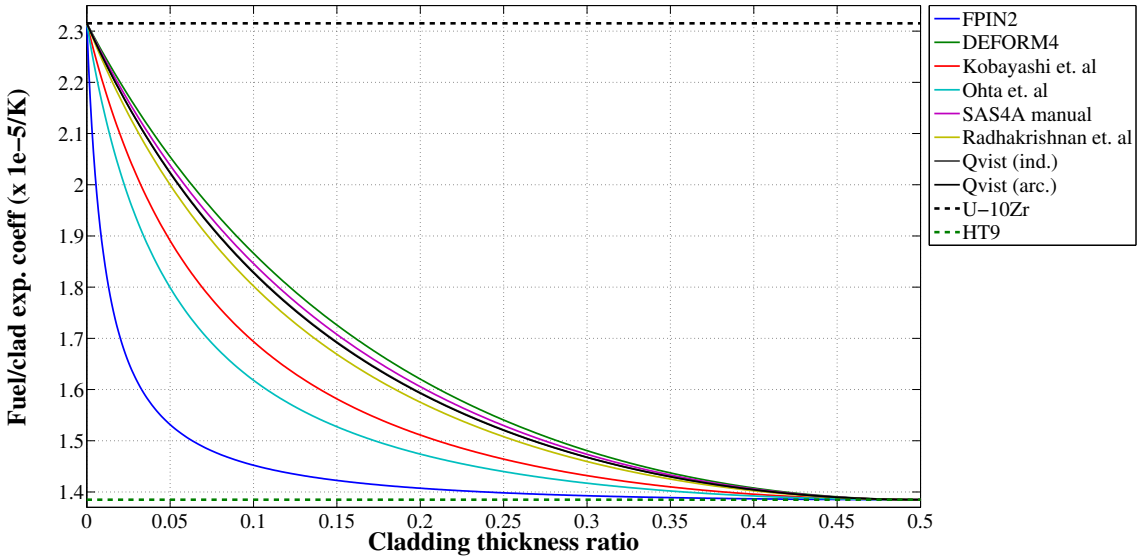

Figure 4.13: Comb. U-10Zr/HT9 exp. by all known correlations (1)

In both Fig. 4.13 and 4.14, the new correlations developed in this thesis for the induction-melted and arc-melted U-10Zr (w.%) elastic modulus are close enough that the two lines cannot be distinguished.

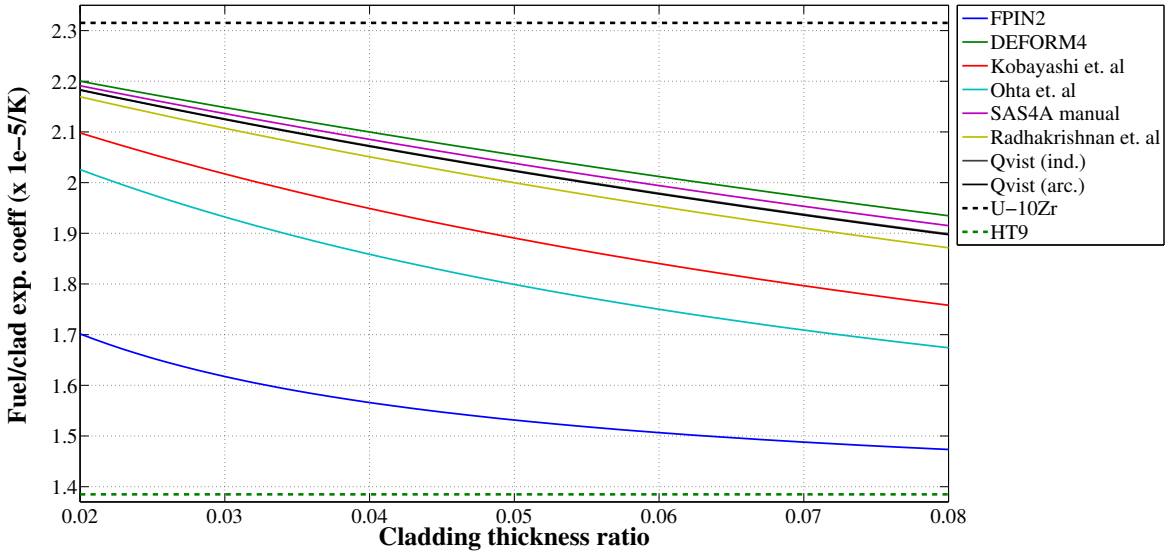

Figure 4.14: Comb. U-10Zr/HT9 exp. by all known correlations (2)

From these results, it is possible to estimate the error introduced by assuming that the fuel/clad-system expansion is determined entirely by cladding expansion. The error calculation is based on the following equation:

$$\text{Error}_1 = 100 \times \left(\frac{\alpha_{\text{combined}}}{\alpha_{\text{HT9}}} - 1 \right) \tag{4.110}$$

The error is plotted in Fig. 4.15 for the complete CTR-range and for a the applicable fuel rod range in Fig. 4.16. As expected, the limits of the error are found at CTR=0 (only fuel) as $\alpha_{\text{U10Zr}}/\alpha_{\text{HT9}} = 1.67 = 67\%$ and at CTR=0.5 (only cladding) as 0%.

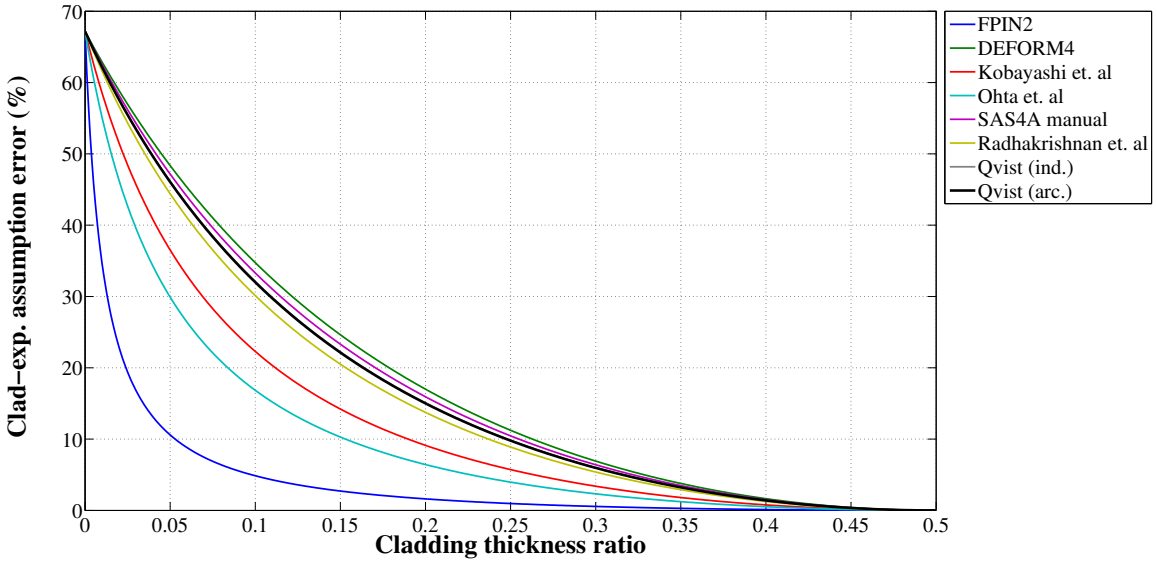

Figure 4.15: Error by assumed clad-driven exp. by all known correlations (1)

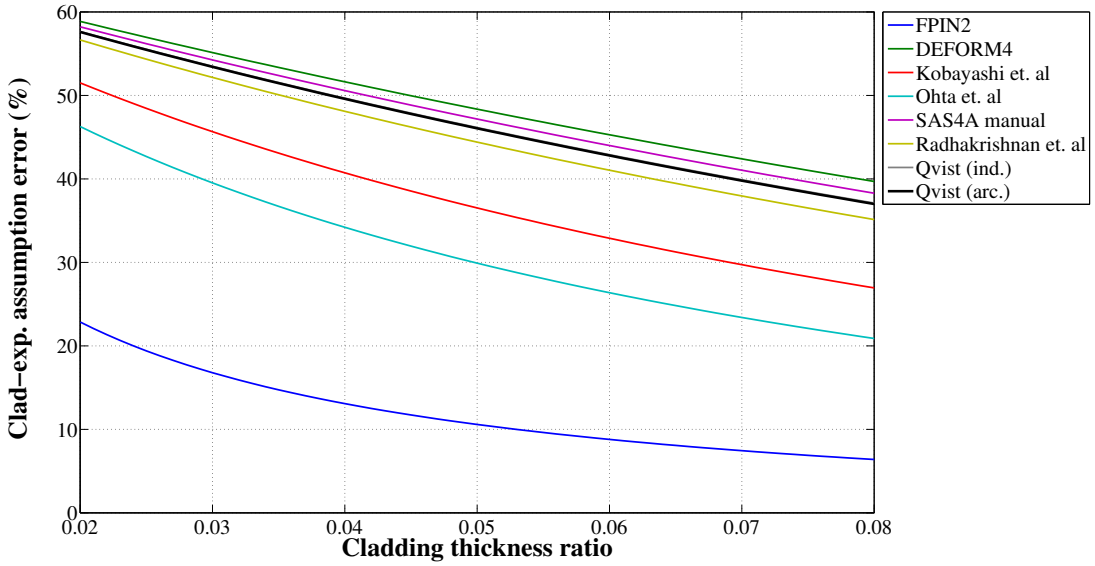

Figure 4.16: Error by assumed clad-driven exp. by all known correlations (2)

If the elastic modulus of the fuel is correctly accounted for theoretically by using the stress balance, an error is still be present by inadequate material data. Assuming that the

correlations developed in this thesis is the best estimate available, the error of using other data is given by:

$$\text{Error}_2 = 100 \times \left(\frac{\alpha_{\text{Qvist}}}{\alpha_{\text{i}}} - 1 \right) \tag{4.111}$$

where i represent another correlation or estimate. To enable this comparison, the arc-melted correlation (eq. 4.105) is used as the reference value. This is valid since the difference between the two correlations developed in this thesis is small compared to the difference to other correlations. The results are given for the full CTR range and the fuel-rod-range in Fig. 4.17 and Fig. 4.18 respectively. Naturally, the errors go to 0% at both ends of the CTR design-space, as this corresponds to only-fuel or only-clad geometries. The errors by most correlations are at or near their maximum in the range of CTR applicable for fuel rod geometries ($0.03 > \text{CTR} > 0.08$).

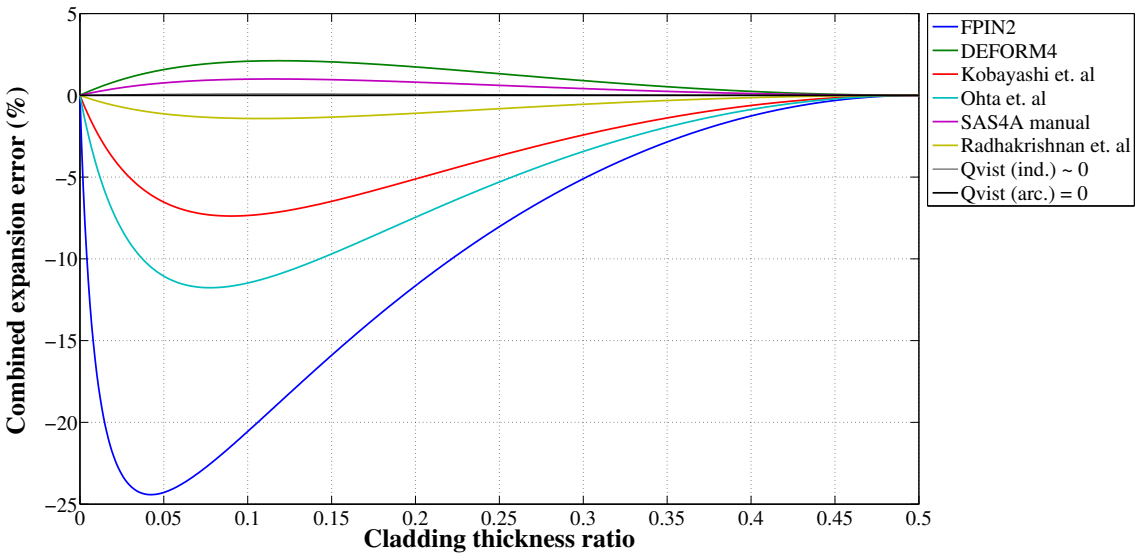

Figure 4.17: Error in fuel/clad exp. by all known correlations (1)

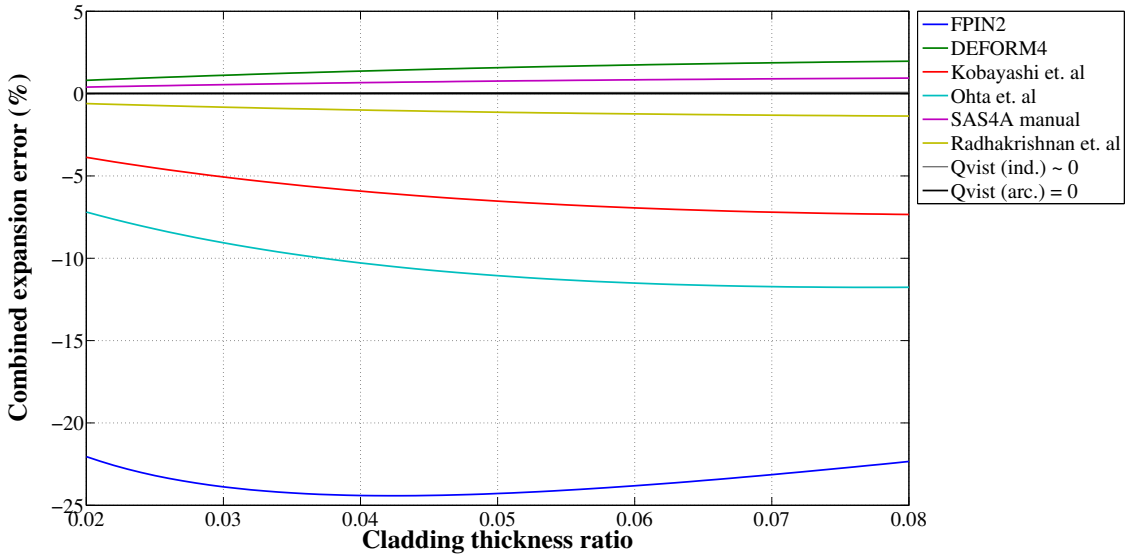

Figure 4.18: Error in fuel/clad exp. by all known correlations (2)

4.3.8 Implications for the safety of fast reactor cores

See section 4.8.8.

4.3.9 Summary and conclusions

From this extensive analysis, some general conclusions can be summarized:

1. The elastic modulus of metallic fuel alloys at fresh and irradiated state needs to be conclusively measured at a wide span of temperatures (25-1000°C).

2. Ideally, the thermal expansion coefficient of a fuel/clad system in the locked up swollen state should be measured. Since the fuel/clad-lockup occurs at as low burnup as 2%, this does not require an extensive irradiation campaign (assuming previously irradiated samples are not available).

3. The assumption of the fuel-clad system expansion being controlled only by cladding expansion is **wrong**. The best-estimate of the error introduced in the axial expansion reactivity coefficient by this assumption is up to 40% (!).

4. The $\alpha_{\text{combined}} = \alpha_c$ assumption is, for certain accident scenarios, a non-conservative assumption. Before reliable physical data for the fuel strength is available, this assumption is recommended for use when analyzing transient over-power (TOP) and

chilled inlet (CI) accidents. For loss-of-flow (LOF) and loss of heat sink (LOHS) accidents, the combined expansion coefficient should be calculated by a stress-balance. This is explained in further detail in Section 4.8.2.

4.3.10 Mechanically bonded fuel

To enable a reduction in the non-actinide alloying-material of metallic fuel and also avoid using a liquid bond in the pin, *mechanically bonded* fuel rods can be used. Using such rods has the potential for very large improvements of the neutron economy of fast reactors (see Section 2.7.2). By extruding the metallic fuel in the form of an annulus with an outer diameter matching the inner diameter of the cladding, the rod can maintain low thermal resistance from fuel to coolant without the use of a liquid bond material. The concept of an annular metallic fuel rod, with a metallic liner on the inner wall of the cladding, is shown in Figure 4.19. Similarly, the mechanically bonded rod design proposed in the Indian fast reactor program avoids the use of liquid bonds and instead uses semicircular grooves placed diametrically opposite sides inside the pin [91] (see Fig. 4.20). In both these designs, the fuel is mechanically bonded to a 125 μm Zr-liner at the inner wall of the cladding [92]. The bond is filled with helium gas instead of sodium, enabling the use of a lower gas plenum.

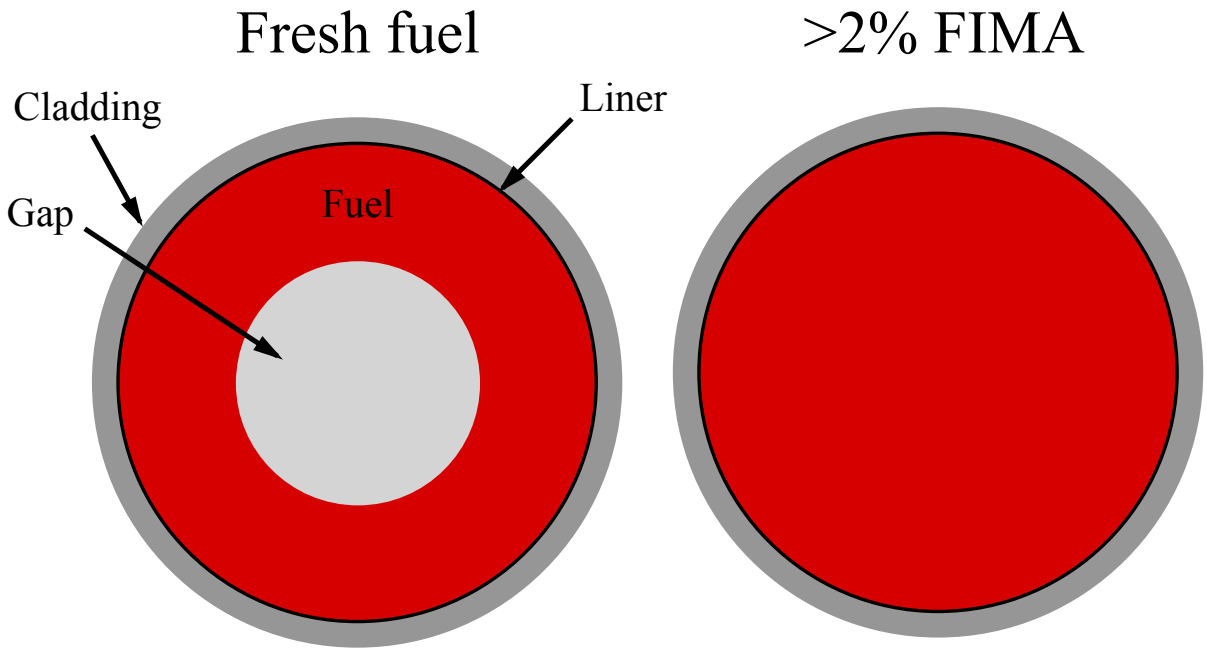

Figure 4.19: Proposed geometry of an annular metallic fuel rod (to scale)

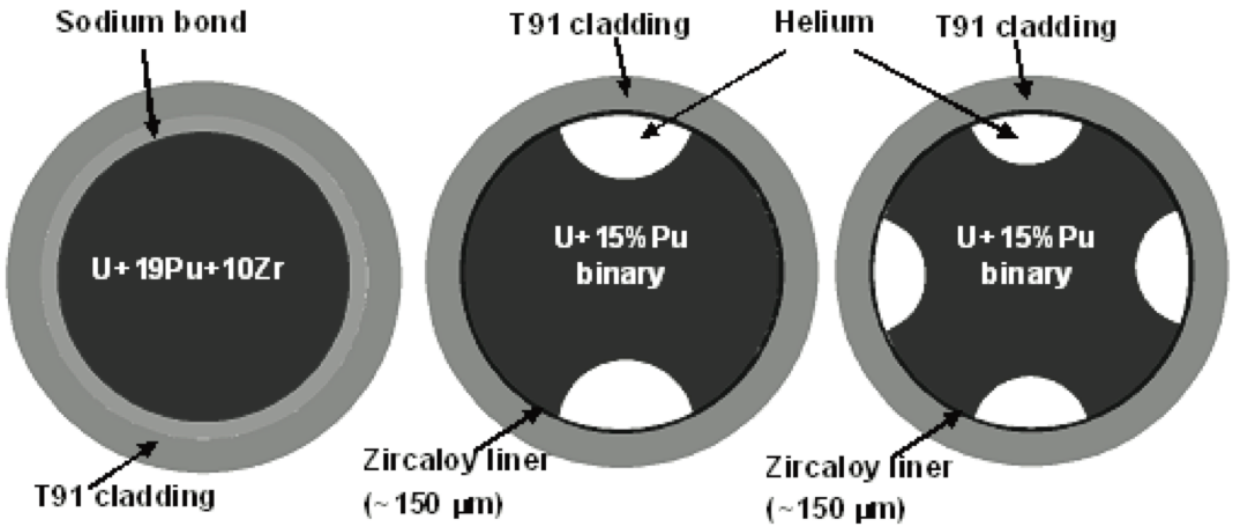

Figure 4.20: The indian FBR project *mechanically bonded* fuel concept. (Left) Conventional pin, (Middle) 85% smear density, (Right) 75% smear density [91]

For the annular pin, the geometric relations are:

$$A_f = \left(\frac{D_{Ci}}{2}\right)^2 \pi - \left(\frac{D_f}{2}\right)^2 \pi \tag{4.112}$$

where D_f is the inner diameter of the fuel annulus. The inner rod area is defined as:

$$A_{ri} = \left(\frac{D_{Ci}}{2}\right)^2 \pi \tag{4.113}$$

The relation between the inner diameter of the fuel annulus (D_f) and the smear density can be calculated as:

$$\text{FSD} = \frac{A_f}{A_{Ri}} = \frac{\left(\frac{D_{Ci}}{2}\right)^2 \pi - \left(\frac{D_f}{2}\right)^2 \pi}{\left(\frac{D_{Ci}}{2}\right)^2 \pi} \tag{4.114}$$

$$D_f = \sqrt{1 - \text{FSD}} \times D_{Ci} \tag{4.115}$$

The geometric area relations developed in Section 4.3.4 remain valid for the annular fuel concept. However, since this fuel type is in mechanical contact with the fuel at fuel-loading, the axial expansion reactivity effect of the fuel needs to calculated by a stress-balance throughout the entire burnup cycle. This means that the fuel impact on the combined fuel-clad expansion is largest at fuel loading and then diminishes as burnup progresses. The results is that the reactivity effect of fuel axial expansion is reduced within the first 2% FIMA of burnup. For conventional metallic fuel, the reduction in the axial expansion reactivity coefficient is a step-function at ∼2% FIMA, while for annular fuel it is a smooth function leveling out at

~2% FIMA. The applicable values for fuel elastic modulus at operating temperature at fuel loading is given in the right column of Table 4.5. Pure uranium has a thermal expansion coefficient of 18.18×10^{-6} $[K^{-1}]$ (calculated in the temperature range 480-680°C from data in ref. [93]). The elastic modulus of pure uranium at 580°C is 117.2 GPa [94]. The combined expansion coefficient of the fuel-clad system assuming pure uranium fuel is given in Fig. 4.21.

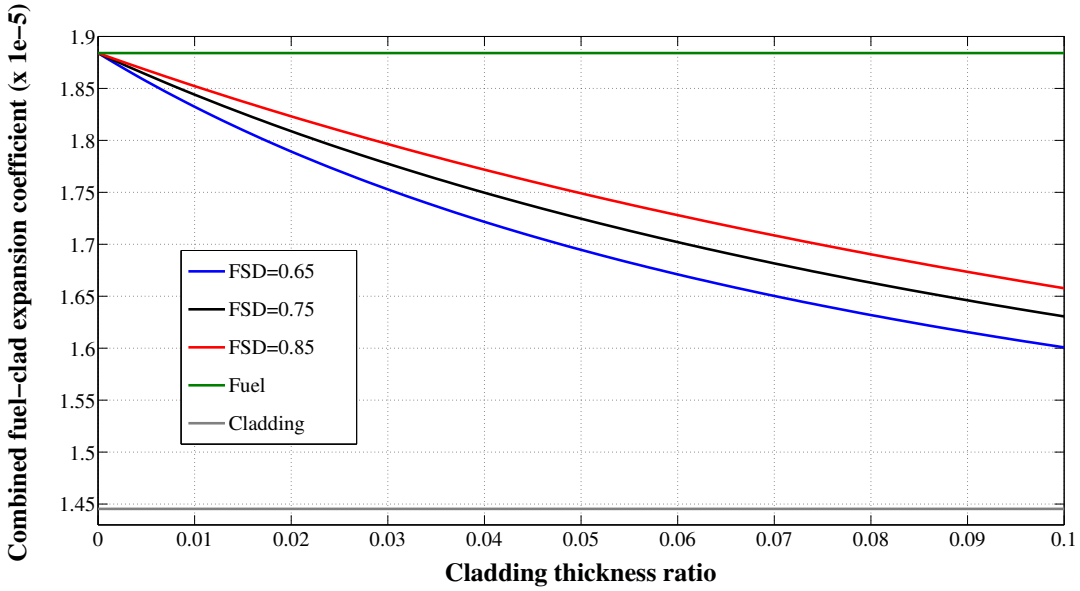

Figure 4.21: Fuel-clad combined exp. coefficient with unirradiated U-fuel, T=585°C

As is fairly obvious from Fig. 4.21, the expansion of the mechanically bonded fuel/clad system with pure uranium fuel cannot be modeled using only cladding expansion. At operating temperatures with fresh fuel, the elastic modulus of the clad is 36% higher, while the cross-sectional area of fuel is 4-5 times larger than the cladding. The expansion of the combined system is thus primarily controlled by the expansion of the fuel. The un-irradiated annular fuel model is the *only* metallic-fuel state with fuel/clad-lockup that has well defined thermophysical properties, as elastic modulus and thermal expansion data for un-irradiated pure uranium fuel and HT9 cladding are coherent and without large differences between sources. The values for individual and combined expansion of as-loaded mechanically bonded fuel are given in Table 4.7.

Table 4.7: Freshly loaded mechanically bonded fuel expansion at CTR=0.05

Component	Temperature (°C)	Elastic modulus (GPa)	Exp. coeff (x 10^{-6} K^{-1})
Cladding (HT9)	535	159.4	14.45
Fuel (U)	580	117.2	18.84
Combined system	-	-	17.25

4.3.11 Fuel radial expansion

The effect of the radial expansion of fuel inside the cladding has no direct effect on core reactivity. The outer core dimensions and total core actinide density remains the same. No actinide material is moved to a lower worth region. Metallic fuel expands and mechanically connects with the cladding within 2-3% FIMA of burnup, after which no radial fuel expansion of any significance occurs. In freshly loaded fuel, the radial expansion of the fuel displaces the bond material inside the fuel rod up in to the gas plenum. This is equivalent to a coolant density decrease which may in fact increase core reactivity. As such, radial fuel expansion in freshly loaded fuel assemblies constitute a minor but positive reactivity feedback. This size of this feedback effect after fuel/cladding contact is small enough that it can be safely ignored.

4.4 Cladding thermal expansion

The fuel rod cladding elongates in both the axial and radial direction with an increase in temperature, causing a displacement of coolant. A conventional fuel pin is attached at the bottom but is free to elongate in the axial direction. The reactivity effect of this elongation comes from the density decrease of the cladding in the active zone. The axial length increase of the cladding has no observable effect on core reactivity. The cladding also expands radially, displacing some fraction of the coolant volume between the rods. The thermal expansion and density reduction of the cladding has three main effects:

- The displacement of sodium by the radial expansion of the cladding will harden the neutron spectrum. The reduced moderation by the coolant adds positive reactivity.

- The decrease in density of the cladding in the active core will reduce cladding absorption and moderation, hardening the spectrum and increasing the number of neutrons available for fission. This will also add positive reactivity.

- The reduction in coolant flow area between the rods caused by the expanding clad decreases the heat removal efficiency which in turns raises temperatures.

In summary, cladding expansion by itself is a net positive reactivity feedback but the geometry changes that come with an increase in cladding temperature affects the cooling of the core which activates other, larger, negative feedbacks. However, by the methodology that defines seperable reactivity coefficients, cladding expansion is by definition a (very small) *positive* feedback.

Assuming the radial expansion causes an increase in the circumference of the rod, as well as an increase in the thickness of the cladding, a set of equations have been developed to describe these geometry changes.

The following definitions are used:
R_{i0},R_{i1} = Inner radius of the cladding at temperature T_0 & T_1
R_{m0},R_{m1} = Midpoint radius of the cladding at temperature T_0 & T_1
R_{o0},R_{o1} = Outer radius of the cladding at temperature T_0 & T_1
CT_0,CT_1 = Cladding thickness at temperature T_0 & T_1
C_0,C_1 = Cladding midpoint circumference at temperature T_0 & T_1
P = Fuel pin pitch (remains constant as cladding temperatures change)
PD_0,PD_1 = Pitch-to-diameter ratio at temperature T_0 & T_1
$\delta L(T_0)$ = Length expansion of the cladding steel from room. temp to T=T_0
$\delta L(T_1)$ = Length expansion of the cladding steel from room. temp to T=T_1
The initial state at temperature T_0 is known and defined from the core design process.

The variables have the following relationships:

$$R_{i0} = R_{o0} - \mathrm{CT}_0 \tag{4.116}$$

$$R_{m0} = R_{o0} - \frac{\mathrm{CT}_0}{2} = R_{i0} + \frac{\mathrm{CT}_0}{2} \tag{4.117}$$

$$C_0 = \pi \times 2 \times R_{m0} \tag{4.118}$$

$$\mathrm{CT}_1 = \mathrm{CT}_0 \times [1 + (\delta L(T_1) - \delta L(T_0))] \tag{4.119}$$

$$\mathrm{C}_1 = \mathrm{C}_0 \times [1 + (\delta L(T_1) - \delta L(T_0))] \tag{4.120}$$

$$R_{m1} = \frac{C_1}{\pi \times 2} \tag{4.121}$$

$$R_{o1} = R_{m1} + \frac{\mathrm{CT}_1}{2} \tag{4.122}$$

$$R_{i1} = R_{m1} - \frac{\mathrm{CT}_1}{2} \tag{4.123}$$

$$R_{i1} = R_{m1} - \frac{\mathrm{CT}_1}{2} \tag{4.124}$$

$$P = 2 \times R_{0o} \times \mathrm{PD}_0 \tag{4.125}$$

$$\mathrm{PD}_1 = \frac{P}{2 \times R_{o1}} \tag{4.126}$$

The geometric state at reference and elevated temperatures are shown in Fig. 4.22.

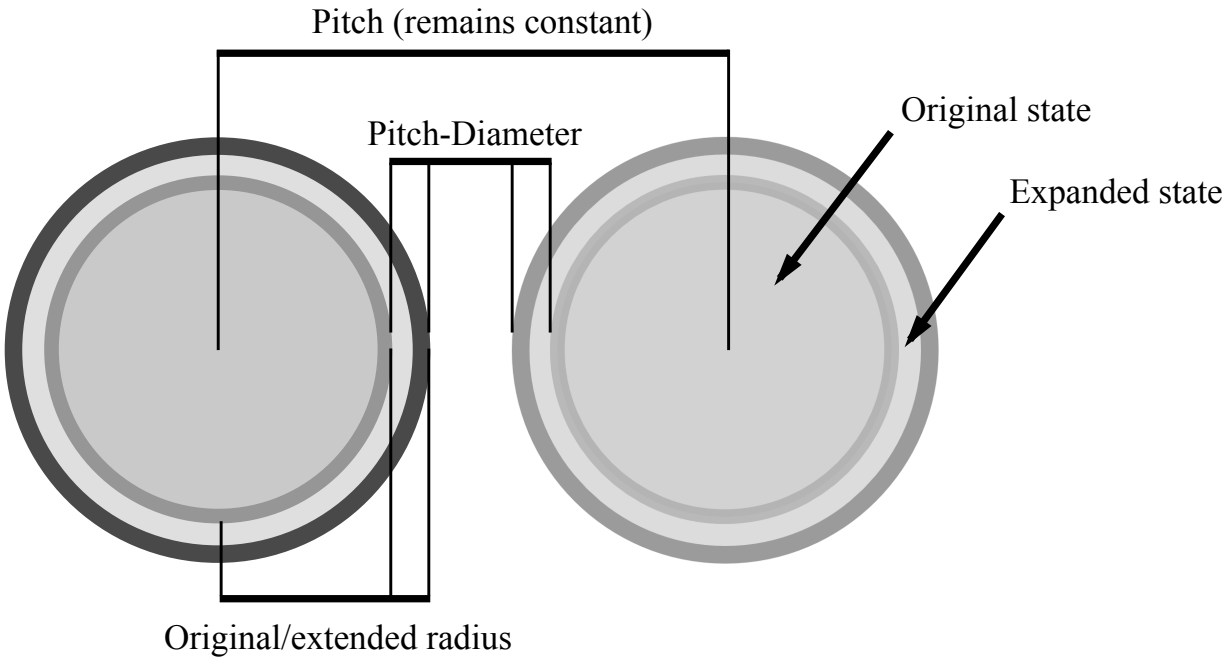

Figure 4.22: Cladding expansion geometry

Using the above equations, the complete expression for the P/D-ratio dependence on cladding temperature is given by:

$$\mathrm{PD}_1 = \frac{2 \times R_{o0} \times \mathrm{PD}_0}{2\left(R_{o0} - 0.5\mathrm{CT}_0\right)\left(1 + \delta L\left(T_1\right) - \delta L\left(T_0\right)\right) + \mathrm{CT}_0\left(1 + \delta L\left(T_1\right) - \delta L\left(T_0\right)\right)} \tag{4.127}$$

Table 4.8 gives an example of the geometrical changes induced by the cladding temperature increase for a typical sodium fast reactor fuel rod geometry with HT9 steel.

Table 4.8: HT9 SFR cladding thermal expansion example

Parameter (mm)	470°C (ref.)	570°C	670°C	1000°C
R_o	5	5.007	5.014	5.035
CT	0.5	0.5007	0.5014	0.5035
R_i	4.5	4.506	4.512	4.531
P/D	1.15	1.1484	1.1468	1.1421

The results of plotting eq. 4.127 using the reference values of Table 4.8 from the standard operating temperature (470°C) to the melting point of HT9 (1467°C) is given in Figure 4.23. To produce these results, two different correlations for the thermal expansion of HT9 steel was tried (*Leibowitz. et. al* [90], *Hofman. et. al* [95]). In the applicable temperature region $470 \leq \mathrm{T} \leq 775$°C, the correlations are near-identical, as can be seen in the small span of results in Fig. 4.23.

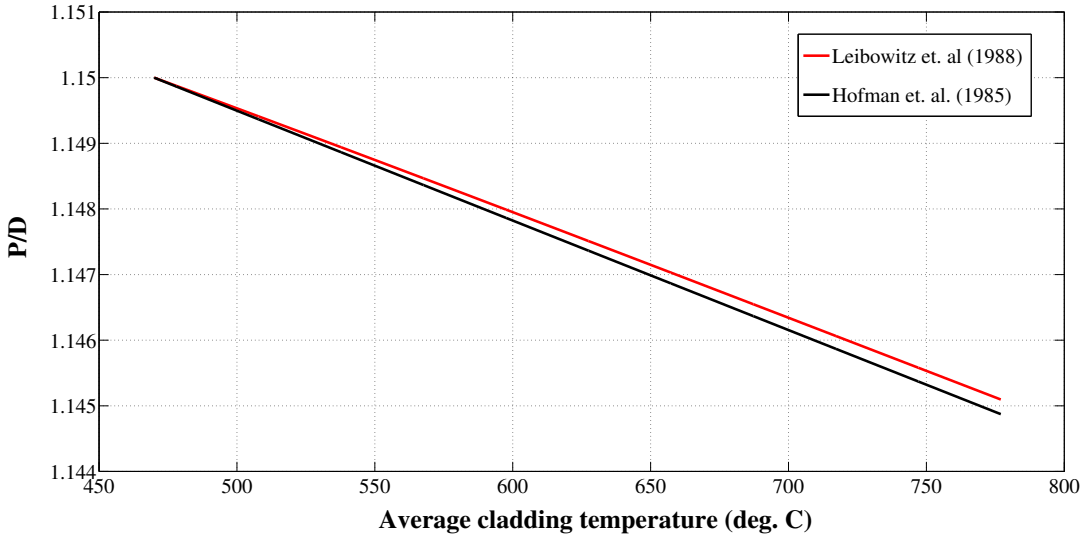

Figure 4.23: P/D dependence on HT9-cladding temperature

In the studies of large sodium-cooled B&B type reactors developed at UCB (see Section 4.9.1), the calculated value of the cladding expansion coefficient is ∼1 pcm/K, or 0.25 ¢/K. Since this feedback is about 40 times smaller than any of the major feedbacks in the core, it can be disregarded for all but the most detailed of core analysis studies.

4.5 Core radial expansion

4.5.1 Introduction

The core radial expansion reactivity feedback consists of two seperate effects: the grid plate expansion and the bowing reactivity, covered in Sections 4.5.2 and 4.5.3 respectively. See Fig. 4.1 for a graphical representation of these effects. The reactivity change from an increase in the core radius has a positive and negative component, just like the axial expansion coefficient (covered in great detail in Section 4.3). The increased in core radius decreases the radial geometric buckling which in turn decreases the radial neutron leakage probability, which is a positive reactivity feedback. The density decrease of core materials increases the axial neutron leakage probability, which is a negative reactivity feedback. The combined effect is a decrease in core reactivity.

4.5.2 Core grid plate expansion

The fuel assemblies of a fast reactor core are mechanically anchored at set positions in a grid plate at the bottom of the core. The grid plate is a large steel component, typically constructed with an upper and lower part as shown in Fig. 4.24.

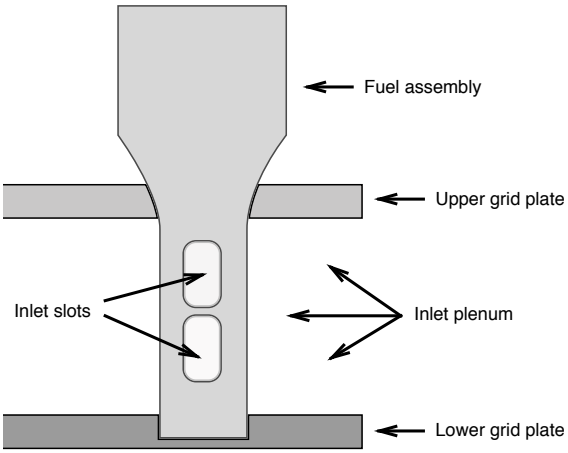

Figure 4.24: Fast reactor core grid plate geometry

As the inlet coolant temperature increases, the grid plate thermally expands which increases the pitch between fuel assemblies and the diameter of the active core. The initial expansion is axially uniform (no bending) until the above core and/or top load pads connect and restrain the outward movement of the assemblies at these axial locations. At this point, bending/bowing reactivity effects occur (covered in the following section).

4.5.3 Core radial restraint design and bowing reactivity

When temperatures of each of the six walls of any hexagonal fuel assembly duct structure are different, assembly structures will deflect from their original shape. Sides of the assembly that are exposed to higher temperatures will thermally elongate more compared to the other sides. This causes a bowed shape with the convex curvature in the direction of the higher temperature. In principle, the same effect happens for the fuel rods themselves. However, the bowing of individual pins is very limited since the rod spacer devices (wrapped wire or spacer grids) mechanically connects the rods with the duct walls. The maximum radial temperature difference across the core occurs at an axial location near the top of the active core. This gradient can be assumed constant in the axial region above the core to the top of the assembly. Below the active core, the inlet coolant is well mixed and there is no temperature gradient. If an assembly is held in place at both the bottom and the top, the bending movement of assemblies caused by the temperature gradient will be toward the center of the reactor. If the assemblies are only attached at one end, the bowing movement tends to be away from the center. These are general principles from beam theory and are not specific to a nuclear reactor core. The bowing trends of a fully clamped assembly core design is shown in Fig. 4.25. The FERMI-1 reactor featured such a design, axially and radially constrained with a hold-down mechanism at the top and a core support system at the bottom.[9] Since such a design nominally has a positive power coefficient of reactivity as the assemblies bend toward the center of the core, spacer pads were welded between assembly walls above the core mid-plane to change the bending movement and minimize the reactivity effect of the bowing.

The *free bowing/flowering* concept, in which assemblies are clamped at the bottom location, is shown in Fig. 4.26. The bowing effects of such a core design are highly complex and difficult to estimate. As radial temperature differences increase (for example, when bringing a reactor from shutdown to low power operation), the bowing is in the outward radial direction. As seen in both Fig. 4.25 and 4.26, bowing affects assemblies that are subjected to a temperature/flux gradient. Since there is essentially no gradient increase in the assemblies at the periphery of the core (usually non-fueled reflector or shield assemblies), these will maintain their initial shape. As radial temperature differences continue to increase across the core when power is increased, the outward bending assemblies will be constrained in their movement as the initial clearance space to the unbowed assemblies at the core periphery is filled.

[9]FERMI-1 was one of the first sodium cooled fast breeder reactors. Started in 1963, it reached high power ($>$ 200 MWt) operation in 1965. The core suffered a partial meltdown in 1966 due to a flow blockage. The reactor was subsequently restarted and then finally decommissioned in 1972.

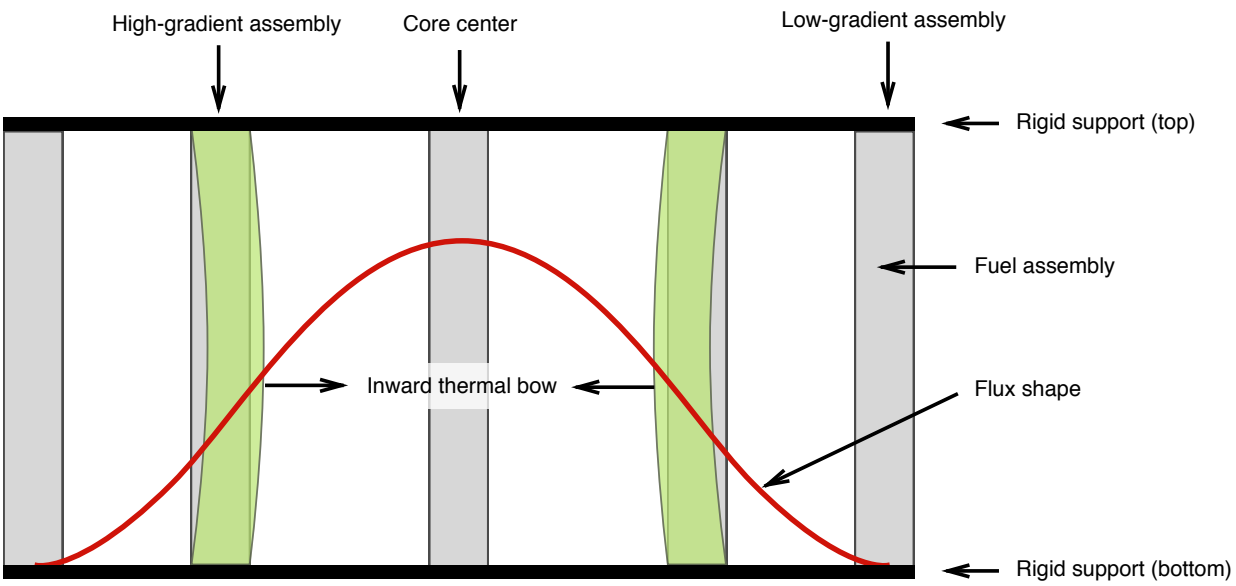

Figure 4.25: Bowing behaviour of assemblies pinned at top and bottom

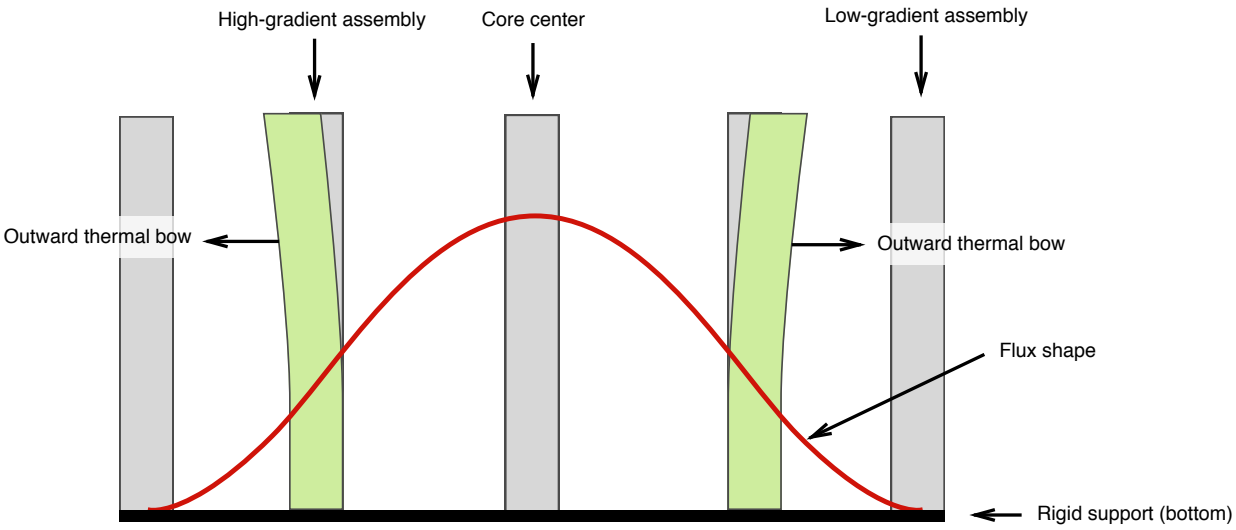

Figure 4.26: Bowing behaviour of assemblies pinned only at the bottom

When there is no more room for outward bending, the *free bow* concepts effectively turns in to a system similar to a fully clamped geometry. Further increases in radial temperature differences across the core will then cause an inward bending, giving a positive reactivity effect. To turn the power-reactivity effect of bending back to negative as temperature increase further, the assembly ducts can be thickened in the axial position at or near the top of the

active core. These thickened duct sections are henceforth denoted ACLP - Above Core Load Pads.[10] Given these physical characteristics, a properly designed *free bow* core assembly restraint design would have to following, highly complicated, power-reactivity relations:

1. Power (P): $0 \leq P \leq X\%$ ($X < 100$)
Radial temperature gradient is small (at P=0, there is no gradient), initial bowing will be in the outward direction, thus power-reactivity feedback is *negative*.

2. Power (P): $X \leq P \leq W\%$ ($X \leq W < 100$)
Outward motion of the assemblies is constrained as clearences at or near the top are taken up. Further power increases causes an inward bending movement decreasing the active core diameter, power-reactivity feedback is *positive*.

3. Power (P): $W \leq P \leq Q\%$ ($Q < W$)
As clearances at the ACLPs are taken up, the bending movement of the assemblies form an axial S-shape. As power increases, the bending movement of the active core zone continues in outward radial direction. Power-reactivity feedback is *negative*.

As an example, it was calculated that the EBR-II reactor would have an increasing core diameter as the radial temperature gradient across the outer assembly row (ΔT_m) went from 0-11°C (step 1 in the above list), followed by a strong diameter *decrease* at $11 \leq \Delta T_m \leq 17$°C (step 2). The core diameter then increases (step 3) but remains smaller than its initial value until $\Delta T_m > 33$°C, after which the core diameter reaches a value larger than at zero-power and continues to increase. Due to these characteristics, the positive reactivity gain from inward bending at full flow and 20% power exceeds the combined negative reactivity effect of all other feedbacks [67].

Because of the complexities and undesired reactivity-behaviour of *fully clamped* and *free bow/flowering* restraint designs, subsequent core-designs (to this day) employ a hybrid design strategy called *limited free bow*. Such a design have assemblies clamped in the core support structure at the bottom and employs load pads above the core (ACLPs) and top load pads (TLPs) at the axial top of the assembly. At the axial height of the TLPs, a *core restraint ring* extrudes from the core barrel which limit the possible bowing (or *flowering*) of the assemblies at the top. The gap between the TLP of the outer row of assemblies and the upper restraint ring as well as the gaps between adjacent assembly ACLPs & TLPs must be large enough to accommodate swelling and creep for the lifetime of the assembly. The bowing geometry of a *limited free bow* core design is given in Fig 4.27. For the core designs analysed and developed in this thesis, the limited free bow designs approach has been utilized. The reactivity effects of core radial expansion and bowing are discussed in the following section.

[10] In EBR-II literature, they are referred to as "buttons".

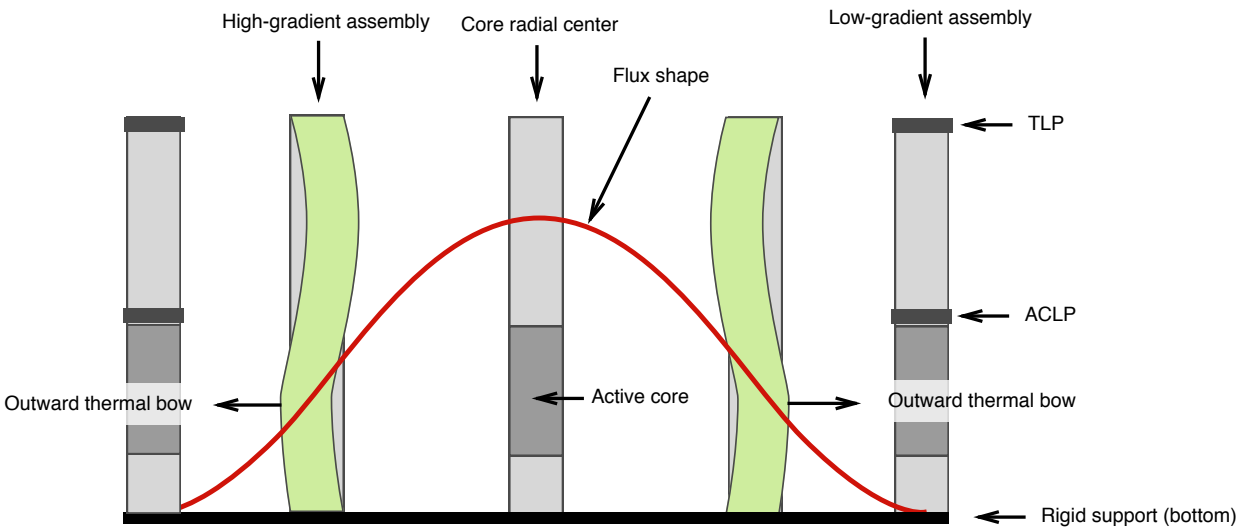

Figure 4.27: Bowing behaviour of limited free bow assemblies

4.5.4 Limited-free-bow core radial expansion reactivity

The radial expansion of the core can be separated in to three different geometric phenomena:

1. Core grid plate / lower support expansion
2. Assembly bowing
3. Core restraint ring effect

The first effect is coupled to the coolant inlet temperature, the second to the temperature rise in the core and the third effect to the temperature of the core barrel. In a limited free bow design, one of the primary objectives is to achieve a *well defined* geometry when approaching full power. This can be achieved if the top load pads (TLP) are in contact with the upper core restraint ring already at 75-80% of rated power. At this "locked" state, the radial expansion of the core is more predictable and moves in the outward radial direction in the axial region of the active core. Optionally, an additional core restraint ring can be placed at the axial location of the ACLPs to further define the geometric state. The radial expansion bowing in such a system is primarily controlled by the ACLP average temperature, which is well approximated by the coolant outlet temperature. The response of the core restraint system on radial expansion reactivity feedback from 0% power to an accident scenario can be given "chronologically" as:

1. Power & Temperature: 0-75% of rated values
Initially there is no radial temperature gradient and no assembly bowing. The assemblies are attached by the nosepiece at the lower core support structure but free to move radially at all axial positions above this. The power reactivity coefficient is *negative*, as the grid plate expands and assemblies bow upon an increase in power and temperature gradient.

2. Power & Temperature: 75-100% of rated values
The assemblies have bowed to connect the load pads with the core radial restraint rings at the corresponding axial level. The core geometry is well defined and there is no further outward flowering of the top of the assembly (only bending). The power reactivity coefficient remains *negative*, since the bending of the assemblies cause an outward radial movement within the axial level of the active core.

3. Start of transient
A transient increases the coolant outlet temperature of the core. The power could adjust up or down depending on the specifics of both the transient and the combination of reactivity coefficients in the core. Initially, negative reactivity is provided primarily by the *bowing* of assemblies. The heating of the ducts, which is causing the bending, lag the heating of the fuel pins by about 1 second [96].

4. The transient continues
The coolant has now heated up both the core grid plate and the radial constraint ring(s). The grid plate expansion further increases the diameter of the core and adds *negative reactivity*. The expansion of the constraint rings has a compacting effect on the core and adds *positive reactivity*. Typically, the ring is heated up before the grid plate. the grid plate responds to the inlet coolant temperature and has a large thermal inertia. The relative magnitude of negative reactivity added from bowing and grid plate expansion depend on the restraint system design. In a limited-free-bow core, the largest reactivity effect is typically that resulting from the uniform expansion of the grid plate. The positive effect from the restraint ring is significantly smaller then either of the negative effects. Net reactivity feedback is *negative*.

In most fast reactor designs, large and small, radial expansion is estimated to be the largest negative feedback in the core (see Fig. 4.1). It is however notoriously difficult to accurately estimate the effect on the core geometry in larger systems, where hundreds of assemblies are bending and impacting on several axial levels. The larger the allowable movements are (i.e. the less *well defined* the core geometry), the more difficult the progression of radial expansion feedback is to estimate. Integrated codes such as ATLAS [97] and NUBOW-3D [98] have been developed aimed at solving the coupled neutron physics, thermo-hydraulics, core mechanics and structural analysis required to estimate the effects of radial expansion. A simple analytical model was developed by *Chang et. al. (1998)* for small fast cores [99]. It

appears similar in form to the method developed for axial fuel expansion analysis in Section 4.3 in this thesis. However, he *Chang et. al. (1998)* model neglects reactivity effects from bowing.

There are several real-world examples illustrating the difficulties in estimating and calculating radial expansion feedback. In 1989 and 1990, the 563 MWth PHENIX reactor in France experienced four extremely fast and highly oscillating transients in the signal from power range neutron chambers, an occurrence that triggered an automatic trip when the reactivity transient threshold was reached. Studies involving more than 200 men-year have been performed producing over 500 reports to find an explanation for these reactivity transients: Among all the analysed scenarios (chamber defects, neutron transport perturbation, control rod failure, oil or gas ingress, etc.), the most likely was determined to be the outward radial bending of fuel assemblies [100][101].

It is in part due to the great difficulty and uncertainty involved in estimating the highly complex radial expansion reactivity of large fast reactor cores that the development of new passive safety systems (see Chapter 6) was deemed necessary.

4.6 Coolant thermal expansion

The reactivity effect by a decrease in coolant density (caused by thermal expansion due to an increase in temperature) is highly spatially dependent and may be either positive or negative. As the atom density of coolant isotopes decrease in the core, the major effect is that neutron scattering on coolant isotopes decreases. This has two major impacts on reactivity: a hardening of the neutron spectrum and an increase in the neutron leakage probability out of the region where the density decrease occurs. An additional negative effect is the decrease in coolant neutron absorption, this effect is minor compared to the spectral and leakage effect in liquid metal coolants because of the low nominal coolant neutron absorption probability. If the density decrease occurs in a central region of the core, the spectral effect dominates. In the core periphery (both axially and radially), the increase in leakage dominates. Given a uniform coolant temperature increase in the core and reflector regions, the positive spectral component and negative leakage component compete to determine the sign and magnitude of the effect on reactivity. In large fast reactors with relatively low surface-to-volume ratio, the spectral effect tends to dominate and can result in a strong positive reactivity feedback. Much of the analysis of this thesis deals with the details of this problem and potential solutions, including Chapter 5, 6 and Section **??**.

4.7 Control rod drive-line expansion (CRDL)

The relative motion between the core and the control rods caused by a change in temperature of the control rod drivelines results in a partial insertion of the control rods in to the core. The drivelines are normally located in the coolant outlet, or hot, plenum, and respond to changes in core outlet temperature (see Fig. 4.2). The control rod drivelines are attached at the top to the core vessel. As the vessel heat up, its size increases, which in turn causes a withdrawal of the partially inserted control rods and a positive feedback. CRDL expansion is thus initially a negative feedback which may, with a significant time-delay, turn to a positive feedback. The magnitude of the CRDL expansion effect is directly correlated to the reactivity worth of the control systems of the core. Large breeder reactors typically have a minimal burnup reactivity swing and thus a minimized need for reactivity compensation control, making CRDL expansion a feedback of minor importance. A system to increase the negative feedback from CRDL expansion is presented an analysed in Section 5.8.

4.8 Quasi-static reactivity balance

4.8.1 Introduction

The quasi-static reactivity balance (QSRB) method was developed by *Wade et. al.* at Argonne National Laboratory (ANL) in the late 1980s. It is used to estimate the asymptotic core state after an unscrammed transient based on solving a reactivity balance equation that depends only on core flow, power and the ratios of three measurable integral reactivity parameters. The main principles of QSRB and safety criteria for a standard SFR system have been presented in a number of papers [70][102][103][104]. However, the derivation of the QSRB equations for different accident scenarios and the resulting derivations of safety criteria from QSRB principles are not available in literature. The QSRB equations have here been re-derived in order to generalize criteria for any accident scenario and quasi-static core response. This also enables the clear definition of assumptions made in derivations for each accident scenario. The derived QSRB equations are then used to show the non-conservatism of the assumptions that are conventionally made about metallic fuel axial expansion (see Section 4.3).

There are three ways in which the outside world can affect the state of a reactor core, giving a total of six scenarios to be analyzed:

1. Changes in primary system pumping
    a. Loss of flow (LOF)
    b. Pump overspeed
2. Control rod motion
    a. Injection
    b. Ejection (TOP)
3. Secondary cycle temperature & flow rate
    a. Loss of heat sink (LOHS)
    b. Chilled inlet temperature (CI)

The only information flowpaths across the reactor boundary are the primary flow rate (F) that is controlled by pumps, the coolant inlet temperature (T_{in}) and an externally introduced reactivity insertion (ρ_{ext}). The quasi-static method can accurately predict the asymptotic state of coolant temperatures for all the scenarios mentioned above. It is only in the first $\sim$10 seconds of a LOF transient that the analysis method is seriously in error, as temperatures can temporarily exceed those given by QSRB analysis. Dynamic analysis is needed for such transients. The quasi-static method is based on the principle that the core mixed mean coolant outlet temperature can be determined by three dimensionless ratios of measurable

integral parameters called A, B and C. Their definitions are given in the following sections. The quasi-static reactivity equation is given as:

$$0 = \Delta\rho = (P-1)\,A + (P/F-1)\,B + C\delta T_{\text{in}} + \rho_{\text{external}} \tag{4.128}$$

where,
ρ = Core reactivity
P = Normalized core power (P=1 is full power)
F = Normalized primary cycle flow (F=1 is forced-flow at full power)
P/F = Power-to-flow ratio (P/F=1 is standard full power operation)
δT_{in} is the change in the coolant inlet temperature.

In any accident or tranisent scenario, the power adjusts up or down through the power coefficient and the core will invariably return to a zero-reactivity state at some new power level. Re-arranging equation 4.128, the normalized power level can be expressed as:

$$P = 1 + \frac{B \times \left[\frac{F-1}{F}\right] - C\delta T_{\text{in}} - \delta\rho_{\text{ext}}}{A + B/F} \tag{4.129}$$

Solving instead for the normalized flow rate gives:

$$F = \frac{P \times B}{A + B - P \times A - C\delta T_{\text{in}} - \delta\rho_{\text{ext}}} \tag{4.130}$$

The coolant temperature rise across the core is a linear function of the power/flow ratio. It is given by:

$$\Delta T_{\text{coolant}} = \frac{P}{F}\Delta T_c \tag{4.131}$$

Where ΔT_c is the nominal coolant temperature rise. The coolant outlet temperature, using the preceding definitions, is given by:

$$T_{out} = T_{in} + \Delta T_c \tag{4.132}$$

The change in coolant outlet temperature is then:

$$\delta T_{\text{out}} = \delta T_{\text{in}} + \delta\Delta T = \delta T_{\text{in}} + \left(\frac{P}{F} - 1\right)\Delta T_c \tag{4.133}$$

The values of the components of the preceding equations are bounded by innate physical phenomena. The lowest flow-rate (F) is that given by free natural circulation. The maximum flow-rate is limited by the point where excessive cavitation limits the efficiency and possibly

damages the primary cycle coolant pumps. The lowest coolant temperature applicable to this type of analysis is the freezing temperature. The maximum external reactivity (ρ_{ext}) that can be introduced to the system is the total reactivity vested in the reactivity control systems (either absorbers or reflectors) inserted in to the core.

The definitions of the integral reactivity parameters A, B and C are given in the following sections.

4.8.2 A. Net power/flow reactivity decrement (¢)

A is the reactivity decrement of the fuel going from the average coolant temperature to the full-power average fuel temperature. It is dependent solely on core power. The definition of A is:

$$A\,(¢) = (\alpha_D + \alpha_l) \times \overline{\Delta T_f} \tag{4.134}$$

where α_D is the fuel Doppler coefficient of reactivity [$¢/K$],
α_l is the fuel axial expansion coefficient of reactivity [$¢/K$] and
$\overline{\Delta T_f}$ is the difference between the average fuel and average coolant operating temperatures [K]

As detailed in Section 4.3, the value of α_l is strongly dependent on the swelling state of the fuel, particularly when using metallic fuel. In the ANL QSRB analysis, α_l is assumed to be 0 when the fuel has swollen to mechanical contact with the clad [70][11] . The swollen, irradiated and high-temperature metallic fuel is assumed to be a very weak material (low elastic modulus). The actual strength of this material in this condition is not published in open literature and is potentially not well known experimentally. A is a parameter associated with the fuel temperature, and thus the assumption is that its expansion behavior (once swollen to mechanical contact with the clad) is governed entirely by the cladding expansion. The cladding expansion is furthermore assumed to be governed by coolant temperature rather than fuel temperature, and because of this the value of α_l is set by ANL as $\alpha_l = 0$ for clad-bounded metallic fuel. There are three primary reasons why this assumption is not accepted in this thesis:

1. It is not *always* conservative
As will be shown in the following sections, for some of the most serious accident scenarios, quasi-static passive safety is enhanced with a minimized value for A. This is true for both LOF and LOHS events. Thus, the conservative approach, at least for these transients, is to assume the maximum value for A given data uncertainty. In other transients such as TOP

[11]From ref. [70]: *Whether α_l goes in A or not depends on whether the fuel is free of the clad (fuel elongation depends on fuel temperature and α_l goes in A) or is linked to the clad (fuel elongation depends on clad i.e. coolant temperature and a does not go in A). For metal fuel, linkage to the clad occurs after several atom percent burnup.*

and CI where a large A-value is unfavorable, the ANL approach is indeed conservative and should be employed.

2. Fuel expansion (and thus α_l) is strictly given by force-balance
This argument is perhaps the most fundamental, and is described in great detail in Section 4.3. The axial expansion of the fuel, assuming it is mechanically bound to the cladding, is assumed to be governed by the thermal expansion of the cladding as a first approximation. The reason is the superior mechanical strength of the cladding. However, the actual physical expansion of the fuel/cladding-compound will be an expansion somewhere in-between that given by the individual expansion coefficients of fuel and cladding separately. The conservative approach, at least in analysing the quasi-static state following transients such as LOF and LOHS, is to estimate a realistic maximum value for the elastic modulus of the irradiated and swollen fuel and then solve the force-balance equation between the fuel and the cladding.

3. (Debatable) Is the clad temperature governed by the coolant or the fuel?
The argument of not including a value for α_l for swollen fuel in the A parameter (but including it in B and C) is that A is associated to fuel temperature rather than coolant temperature, and the cladding temperature (governing α_l) is determined primarily by the coolant temperature. It is not clear that this is the case. Heat transfer (conduction) between the swollen metallic fuel to the cladding steel is effective. The heat capacity per unit mass of fuel is $\sim$1/5th that of the cladding. Fuel mass per pin is >10 times that of cladding. The heat capacity of the thin cladding steel should not induce any significant time-lag to heat-up by the fuel on the time scales to quasi-static analysis. During the time-periods involved in the "slow" transients analysed with QSRB and given that a small value for A is sometimes non-conservative (point 1), it is potentially not valid to claim that cladding temperature is not at all governed by fuel temperature.

Conclusion: A new definition of the integral reactivity parameter *A*
In this thesis, a new conservative definition of A for metallic fuel is proposed that is transient-type-dependent rather than swelling-state-dependent. The new proposed complete definition of A is:

$$
\begin{aligned}
& a) \quad \text{For un-bounded fuel} \\
\mathrm{A}\,(\dot{\varphi}) \;&=\; (\alpha_D + \alpha_l) \times \overline{\Delta T_f} \\
& b) \quad \text{For clad-bounded fuel} \\
\mathrm{A}\,(\dot{\varphi}) \;&=\; (\alpha_D + \alpha_l) \times \overline{\Delta T_f} \quad \text{For LOF \& LOHS, } \alpha_l \text{ solved by force balance} \\
\mathrm{A}\,(\dot{\varphi}) \;&=\; (\alpha_D) \times \overline{\Delta T_f} \quad \text{For TOP \& Chilled inlet}
\end{aligned}
\tag{4.135}
$$

4.8.3 B. Power-to-Flow reactivity decrement (¢/100% P/F)

B is the reactivity decrement per 100% change in the power/flow ratio. Its definition is:

$$\mathrm{B}\,(¢) = (\alpha_D + \alpha_l + \alpha_c + 2\alpha_R) \times \frac{\Delta T_c}{2} \tag{4.136}$$

The coolant temperature rise through the core is directly dependent on the P/F ratio, with P/F=1 defining the nominal (design) core coolant temperature rise. B is thus the reactivity vested in a temperature rise of the coolant.

4.8.4 A+B. Power reactivity decrement (PRD) (¢)

A+B is the decrement in reactivity (¢) which occurs upon taking the core to full power and flow from an isothermal state at a set constant coolant inlet temperature. The values of A and B can be experimentally verified by two determinations of the power decrement (A+B). The power reactivity decrement is measured by establishing a constant 100% reactor flow rate, a constant reactor inlet temperature and then during the rise to full power measure reactivity as a function of power level. PRD-tests were performed in the EBR-II reactor which validated the use of the quasi-static method (as well as the calculation of reactivity coefficients). The results of a PRD-test (run 129) of the EBR-II reactor is given in Figure 4.28.

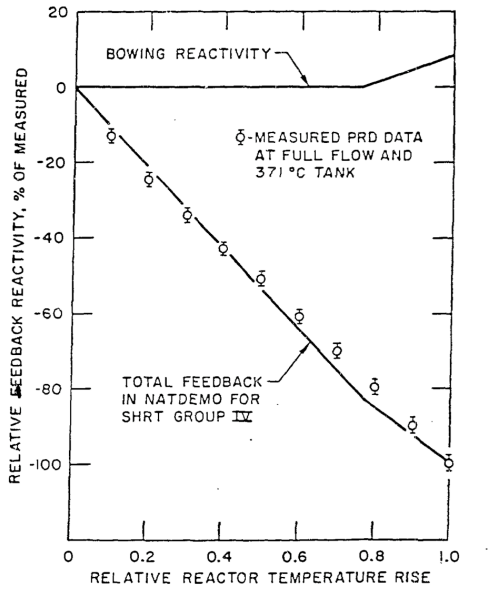

Figure 4.28: The result of a PRD-test in EBR-II (Run 129) [63]

4.8.5 C. Coolant inlet temperature coefficient (¢/ K)

C is the reactivity coefficient of the inlet coolant temperature. It is defined as:

$$\mathrm{C}\,(¢/\mathrm{K}) = \alpha_D + \alpha_l + \alpha_c + \alpha_R \tag{4.137}$$

The measurement of C can be done simply by speeding up the pumps in the secondary cycle (which lowers the coolant inlet temperature), and then measuring what the resulting power level is. Since A & B have been measured by the power reactivity decrement (where coolant inlet temperature stays constant), the value for C can be estimated by solving eq. 4.128. The parameter C can then be calculated as:

$$C = \frac{(P-1)\,A + \left(\frac{P}{F} - 1\right) B}{-\delta T_{\mathrm{in}}} \tag{4.138}$$

where P, F and δT_{in} are measured and A and B are calculated using two PRD-runs.

4.8.6 Accident scenarios

4.8.6.1 Loss of flow

In the unprotected loss of flow event, the primary system pumps are tripped and forced flow is lost without the actuation of the core SCRAM system. The primary pumps coast down eventually bringing flow levels down to natural circulation levels. The coolant inlet temperature is assumed to remain constant (i.e. $\delta T_{\mathrm{in}} = 0$). The accident progression is:

1. Primary system pumps are tripped
2. Power-to-flow ratio increases raising the core average temperature
3. The temperature rise introduces negative reactivity which lowers core power
4. A stable state of natural circulation flow is established at low power

In order to solve eq. 4.128 in a useful manner, some idealizations are necessary. In the ULOF scenario, it is the power/flow-ratio that determine the accident progression rather than the normalized power by itself. Thus the value for P coupled to the integral power reactivity parameter A can be set to zero for the asymptotic state. Letting P/F remain a variable, eq. 4.128 can be solved to show the quasi-static (long term) response:

$$0 = (0-1)A + \left(\frac{P}{F} - 1\right) B \rightarrow \left(\frac{P}{F} - 1\right) = \frac{A}{B} \tag{4.139}$$

A P/F ratio equal to one produces the nominal coolant temperature rise and thus $\delta T_{\mathrm{out}} = 0$. If it is larger than 1 the outlet temperature will rise. Given a constant coolant inlet temperature, the long-term coolant outlet temperature rise in the event of an unprotected loss of flow event is given by:

$$\delta T_{\text{out}} = \frac{A}{B}\Delta T_c \tag{4.140}$$

In the initial phase of the loss-of-flow transient, there is a significant risk that temperatures will exceed the temperatures of the quasi-static case. The state of the core during this dynamic phase cannot be predicted by the quasi-static method. During the first ∼10 seconds after a pump trip, the delayed-neutron holdback of the power decay may be longer than the pump coastdown time, thereby causing a transient overshoot in the power-to-flow ratio that causes the core outlet temperature to overshoot its asymptotic value [103]. In reality, power will not reach 0 since the core will transition to stable natural circulation coolant flow. The above equations can be refined to include a non-zero power level in the following way:

$$\frac{P}{F} = \frac{A+B}{AF+B} \tag{4.141}$$

$$\delta T_{\text{out}} = \frac{A\,(1-F)\,\Delta T_c}{AF+B} \tag{4.142}$$

The expected coolant outlet temperature behaviour during a ULOF event with pumps with low flow coastdown time constant (<14 s) is shown in Fig. 4.29.

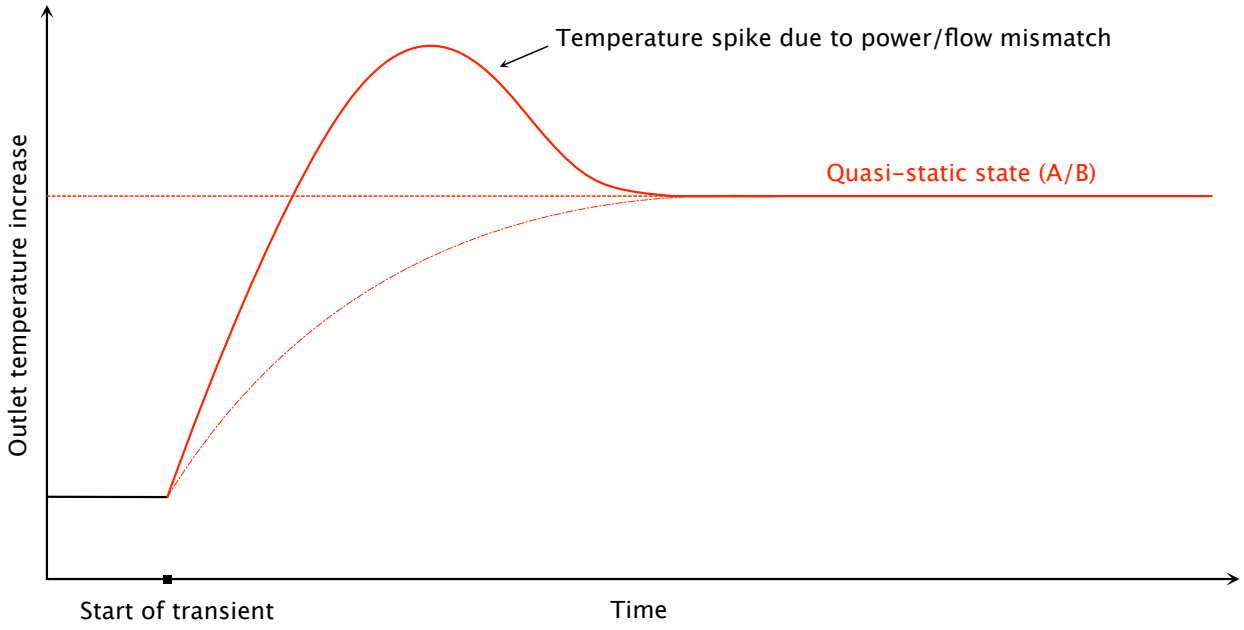

Figure 4.29: Coolant outlet temperature in a loss of flow accident with low pump coastdown time constant (<14 s)

4.8.6.2 Pump overspeed

The pump overspeed accident scenario is physically bounded by the power supply and cavitation limit of the pump. These effects limits the maximum perturbation to an estimated +15-20% (F=1.15-1.20) [105]. The pump over-speed scenario is the only pertubation where the quasi-static state is at a higher power than the nominal state. The power, keeping the flow rate as a variable (F), is:

$$P = 1 + \frac{\frac{B(F-1)}{F} - 0 - 0}{A + B/F} = 1 + \frac{B\,(F-1)}{F\,(A + B/F)} \tag{4.143}$$

Equation 4.143 can be re-written in terms of the A/B-ratio as:

$$P = \frac{1 + A/B}{1/F + A/B} \tag{4.144}$$

Since F $<$ 1 and A/B $>$ 0, this event always leads to an increase in core power. The maximum increase in power is exactly equal to the increase in normalized flow ($\delta P = \delta F$). The actual increase is limited by the non-zero ratio of A/B. In the "short" term, the coolant inlet temperature does not change and the coolant outlet temperature is perturbed as:

$$\delta T_{\text{out}} = \left(\frac{P}{F} - 1\right) \Delta T_c = \left(\frac{1 + A/B}{F \times (1/F + A/B)} - 1\right) \Delta T_c \tag{4.145}$$

Again, since F $<$ 1 and A/B $>$ 0, $\delta T_{\text{out}} < 0$. Thus, in the short term, the pump overspeed scenario decreases the coolant outlet temperatures and is thus not a constraining accident case. The biggest worry in this scenario is rather that pumps break and that the event transitions in to a loss-of-flow event. Eventually, coolant temperatures would rise because of the inability of the secondary cycle the remove the higher heat output. As temperatures in the primary cycle rise, negative reactivity will bring power back down.

4.8.6.3 Loss of heat sink

In an unprotected loss of heat sink event, heat rejection to the secondary system is lost. The heat rejection at all steam generators is lost, while primary and secondary pumps continue to operate. There is no change in the operation of the primary coolant system and the reactor is not scrammed. The assumption is that in the asymptotic state, the decay heat generation is within the capacity of the decay heat removal system. The progression of the accident scenario is:

1. Heat rejection from the primary system is lost
2. Coolant inlet temperature increases
3. Assuming a negative value for the integral reactivity parameter C, negative reactivity is introduced which lowers power

4. The power/flow ratio is reduced (primary system is still at full flow)
5. Decay heat generation exceeds passive decay heat removal capacity which heats all components in the primary tank
6. Core coolant temperatures stabilize at an equilibrium value as decay heat removal eventually match generation
7. Eventually the core is cooled to the point where it is again in a critical state at low power

As the transient is reaching its asymptotic state, the power level is adjusted to decay heat levels. The larger the primary coolant inventory heat capacity, the longer time it takes to reach the asymptotic state. Thus, a larger primary inventory reduces the capacity-requirement for the decay heat removal system. The final asymptotic stable state in the ULOHS scenario is reached when the positive reactivity introduced by bringing the power toward zero, (A+B), is balanced by the negative reactivity introduced by the rise in coolant temperature (at this point $T_{in} = T_{out}$, $\Delta T_c = 0$). This can be shown by solving eq. 4.128 for the ULOHS scenario as:

$$\begin{aligned} 0 &= (0-1)\,A + (0/F-1)\,B + \delta T_{in} C + 0 \\ \delta T_{in} C &= A + B \\ \delta T_{in} &= \frac{A+B}{C} \end{aligned} \tag{4.146}$$

The change in coolant outlet temperature is correspondingly:

$$\delta T_{\text{out}} = \frac{A+B}{C} - \Delta T_c \tag{4.147}$$

Thus, if the ratio (A+B)/C is equal to the nominal temperature increase in the core, the asymptotic core outlet temperature in this scenario is kept constant. Eq. 4.147 can be re-written in a way which facilitates the establishment of design guidelines for all transients as:

$$\delta T_{\text{out}} = \left(\frac{1 + A/B}{C\Delta T_c/B} - 1 \right) \Delta T_c \tag{4.148}$$

Eq. 4.148 is dependent on A/B (just like in a LOF event) as well as the ratio $C\Delta T_c/B$. Since the constraints for A/B is already set by the LOF analysis, the constraints for a LOHS event is primarily given by $C\Delta T_c/B$.

4.8.6.4 Chilled inlet

The chilled inlet scenario can be seen as the opposite scenario to the loss of heat sink event. In this scenario, the secondary coolant system is removing heat more efficiently than it was designed to. This can be caused by an increase of secondary pump speed, loss of feedwater heating, excessive turbine load or a reduction in the ultimate heat sink temperatures. The heat removal rate exceeds the heat generation rate until a new equilibrium state is established. Just as in the loss of heat sink event, the only way a chilled inlet event affects the core is through the coolant inlet temperature. The most severe type of postulated chilled inlet event is a blowdown of the steam generators. A blowdown occurs if the water side pressure boundary is breached, overcooling the intermediate (in Na-cooled cores) or primary (in lead or LBE-cooled cores) coolant loop. Such a chilled inlet event eventually turns in to a LOHS event as the continuous cooling capacity disappears. The primary coolant flow rate is assumed to remain at the rated level in this scenario (F=1), which simplifies eq. 4.129 to:

$$P = 1 - \frac{\delta T_{\text{in}} C}{A + B} \tag{4.149}$$

The maximum temperature change in the inlet coolant temperature is given by the physical constraint of the coolant freezing temperature. This can be expressed as:

$$| - \delta T_{\text{in}}| < (T_{\text{in}} - T_{\text{freeze}}) \tag{4.150}$$

For sodium, the maximum value of δT_{in} is given by freezing in the secondary (rather than the primary) coolant cycle. This gives a maximum δT_{in} of about ∼180-260°C. For coolants that do not have violent chemical reactions with water, only the primary cycle is considered. The maximum value of δT_{in} is ∼50-125°C for pure lead and for lead-bismuth eutectic it is ∼175-275°C. Given as a fraction of nominal core temperature rise, the values are ∼1.25-1.75×ΔT_c (sodium), ∼0.25-1×ΔT_c (lead) and ∼0.9-2.2×ΔT_c (LBE). The exact value is dependent on the design value for full power coolant inlet and outlet temperatures at standard operation. The change in outlet temperature is given by:

$$\delta T_{\text{out}} = \left(\frac{C \Delta T_c / B}{1 + A/B} - 1 \right) (-\delta T_{\text{in}}) \tag{4.151}$$

A detailed treatment of the steam-generator blowdown event impact on passive safety is given in *Vilim (1990)* [106].

4.8.6.5 Transient overpower

Transient overpower (TOP) scenarios involves the insertion of positive reactivity by the movement of a control or reflector component. The most analyzed scenario is the ejection

of a burnup reactivity compensation assembly out of the core. In this event, core operation continues at nominal rates (full flow and full power). Solving eq. 4.128 and setting the external reactivity insertion to $\Delta\rho_{\mathrm{TOP}}$ gives:

$$0 = (1-1)A + (1/1-1)B + C\delta T_{\mathrm{in}} + \Delta\rho_{\mathrm{TOP}} \rightarrow C\delta T_{\mathrm{in}} = -\Delta\rho_{\mathrm{TOP}} \tag{4.152}$$

$$\delta T_{\mathrm{in}} = -\frac{\Delta\rho_{\mathrm{TOP}}}{C} \tag{4.153}$$

As this event does not include a change in the power-to-flow ratio (P/F = 1), the coolant outlet temperature rise equals the coolant inlet temperature rise. In order to harmonize with the other constraints, 4.153 can be re-written as:

$$\delta T_{\mathrm{out}} = \left(\frac{\Delta\rho_{\mathrm{TOP}}/B}{-C\Delta T_c/B}\right)\Delta T_c \tag{4.154}$$

In this way, the ratio $\Delta\rho_{\mathrm{TOP}}/B$ is identified as the distinguishing constraint of the TOP scenario, as $C\Delta T_c/B$ is already defined by the LOHS and chilled inlet events. In the intermediate state, before a quasi-static state is reached, the inlet temperature remains unchanged. This is because the temperature increase is initiated in the core and is not communicated to the inlet temperature immediately. The power in the intermediate stage is given by solving eq 4.129 as:

$$P = 1 + \frac{\frac{B(1-1)}{1} - 0 - \Delta\rho_{\mathrm{TOP}}}{A + B/1} = 1 - \frac{\Delta\rho_{\mathrm{TOP}}}{A+B} \tag{4.155}$$

Since the primary cycle flow remains constant (F=1), the change in the coolant outlet temperature is simple given by:

$$\delta T_{\mathrm{out}} = (P-1)\,\Delta T_c \tag{4.156}$$

Plugging in the expressions yields:

$$\delta T_{\mathrm{out}} = -\left(\frac{\Delta\rho_{\mathrm{TOP}}}{A+B}\right)\Delta T_c = -\left(\frac{\Delta\rho_{\mathrm{TOP}}/B}{1+A/B}\right)\Delta T_c \tag{4.157}$$

4.8.7 Constraints

The quasi-static coolant outlet temperature rise resulting from each accident scenario can be expressed as a ratio of integral reactivity parameters multiplied by the nominal coolant temperature increase across the core. As detailed in the above section, there are three ratios that come in to play in the long-term evolution of these events. While more than one of these ratios appear in most of the accident scenarios, they are linked as follows:

- A/B for loss of flow

- C/B (or CΔT_c/B) for loss of heat sink and chilled inlet

- $\rho_{\mathrm{TOP}}/|B|$ for control rod ejection

To develop constraints for the ratios, a maximum coolant outlet temperature needs to be defined. To avoid structural damage at long term exposure to steel components in the core such as cladding and ducts, the maximum cladding temperature is set at 650 (°C. The following constraint on peak coolant outlet temperature is implemented (allowing for a 50°C difference between coolant outlet temp. and peak cladding temp) :

- Maximum $T_{\mathrm{out}} = 600$ (°C)

When a constraint for one ratio is set, the governing value for setting the constraint of the subsequent ratios is to use the value for the first constraint that gives the highest possible temperatures in other accident scenarios. The natural starting point is the loss-of-flow scenario, where the quasi-static state depends solely on the A/B ratio. Characteristic temperatures for liquid meal coolants are given in Table 4.9.

Table 4.9: Characteristic coolant temperatures

Coolant	Sodium	Lead	Lead-bismuth Eutectic
T_{in} (°C)	350	380	340
T_{out} (°C)	500	480	490
ΔT_c (°C)	150	100	150
Max. δT_{in} (CI) (°C)	225	165	215

The corresponding constraints on the A/B ratio are given in Table 4.10.

Table 4.10: A/B constraint by coolant

Constraint	Na	Pb	LBE
A/B	≤ 0.67	≤ 0.72	≤ 0.73

In the case of a loss of heat sink accident, a higher value for A/B gives higher quasi-static temperatures when all else is kept constant. Thus, to set a constraint for the C/B or CΔT_c/B ratios, the maximum allowed value of A/B from Table 4.10 is used. The resulting constraints are given in Table 4.11.

Table 4.11: C/B and CΔT_c/B constraint by coolant (for LOHS)

Constraint	Na	Pb	LBE
C/B	$\geq 6.68 \times 10^{-3}$	$\geq 7.82 \times 10^{-3}$	$\geq 6.65 \times 10^{-3}$
CΔT_c/B	≥ 1.00	≥ 0.782	≥ 0.998

The chilled inlet (CI) scenario is the inverse of the LOHS. For a CI event, the maximum temperatures are reached in the extreme case of A/B = 0. Given this and the reference values of Table 4.9, the constraints given by the CI event are summarized in Table 4.12.

Table 4.12: C/B and CΔT_c/B constraint by coolant (for CI)

Constraint	Na	Pb	LBE
C/B	≤ 0.0096	≤ 0.0172	≤ 0.0101
CΔT_c/B	≤ 1.44	≤ 1.72	≤ 1.51

The TOP analysis is determined primarily by the magnitude of the assumed reactivity insertion. If the event is meant to simulate a control rod ejection, this is determined by two factors:

- The burnup reactivity swing (for which control systems need to compensate)

- The number of control assemblies in the core

These factors determine the value of $\Delta\rho_{\text{top}}$. As an example, for a reactivity swing of 2% ($\sim$ 6\$) and 20 control assemblies, the average value for $\Delta\rho_{\text{top}}$ of a single rod assembly ejection is 30¢. The TOP-temperatures are most severe using the lowest allowable value for C/B, giving the specific constraint for the TOP-scenario as:

Table 4.13: $\Delta\rho_{\text{top}}/|B|$ constraint by coolant (for TOP)

Constraint	Na	Pb	LBE
$\Delta\rho_{\text{top}}/|B|$	≤ 0.67	≤ 0.94	≤ 0.73

To summarize, the constraints put upon the integral reactivity parameter ratios are given in Table 4.14.

Table 4.14: Integral parameter constraints by coolant (at $T_{\text{out}}(\text{max}) = 600°\text{C}$)

Constraint	Na	Pb	LBE
A/B	≤ 0.67	≤ 0.72	≤ 0.73
CΔT_c/B	$1.00 \leq \text{x} \leq 1.44$	$0.782 \leq \text{x} \leq 1.72$	$0.998 \leq \text{x} \leq 1.51$
$\Delta\rho_{\text{top}}/\lvert B\rvert$	≤ 0.67	≤ 0.94	≤ 0.73

4.8.8 Fuel/clad expansion effect on QSRB results

Section 4.3 details the specifics of the new methods and correlations developed in this thesis for the axial expansion of fuel rods with metallic fuels. The impact that these new methods have on the safety of a fast reactor core can be estimated using the quasi-static reactivity method. The average temperature of the fuel at standard operation can be expressed as:

$$T_F = T_{in} + \frac{\Delta T_c}{2} + \Delta T_F + \Delta T_{ccl} \tag{4.158}$$

where ΔT_F is the temperature gradient across the fuel and ΔT_{ccl} represents the temperature gradient from bulk coolant to the fuel outer radius. In calculations, ΔT_{ccl} is set, for simplicity, to 50°C. ΔT_F is given by:

$$\Delta T_f\,(K) = \frac{q'}{4\pi k} \tag{4.159}$$

ΔT_F does not depend on the diameter of the fuel but solely on linear power (q') and fuel thermal conductivity (k). Using characteristic fast reactor values of q'=35 kW/m and k = 18.3 W/(m×K) gives $\Delta T_F \approx 150$ K. The quasi-static average fuel temperature resulting from a transient that changes flow, inlet coolant temperature or power is given by:

$$T_f = (T_{\text{in}} + \delta T_{\text{in}}) + \frac{P}{F} \times \frac{\Delta T_c}{2} + P \times \Delta P_f + \Delta T_{ccl} \tag{4.160}$$

Representative values for reactivity coefficients of a metallic fuel reactor for use in this analysis are given in Table 4.15.

Table 4.15: IFR reactivity coefficients and temperatures [70]

Coefficient	α_D	α_E	α_{Na}	α_{cr}	α_r	T_{in}	ΔT_c	ΔT_f
Ref. unbound (¢/K)	-0.10	-0.12	+0.18	-0.05	-0.25	350	150	150
Ref. bound (¢/K)	-0.10	**-0.075**	+0.18	-0.05	-0.25	350	150	150
New. bound (¢/K)	-0.10	**-0.11**	+0.18	-0.05	-0.25	350	150	150

The resulting integral reactivity parameters A, B and C, and the ratio A/B are summarized in Table 4.15. The two bound states in the Table 4.15 refer to:

Ref. bound state 1
Axial expansion not included in parameter A, free expansion value in B and C

Ref. bound state 2
Axial expansion not included in parameter A, ref. bound expansion value in B and C

Ref. bound state 3
Axial expansion as controlled entirely by cladding included in all parameters

Table 4.16: Integral reactivity parameters

Fuel state	A	B	C	A/B
Fuel/clad unbound	-33	-44.25	-0.34	0.746
Fuel/clad bound ref. (1)	-15	-44.25	-0.34	0.339
Fuel/clad bound ref. (2)	-15	-40.87	-0.295	0.367
Fuel/clad bound ref. (3)	-26.3	-40.88	-0.295	0.642
Fuel/clad bound new.	-30	-42.76	-0.32	0.702

While the first reference bound state (row 2 of Table 4.16) makes no physical sense, it appears to be the version used in the data tables of all QSRB analysis found in literature. The second reference bound state corresponds to the physical interpretation as given in the various texts explaining the principles of QSRB [104][103]. The two first ref. states assume that the fuel/clad-expansion is controlled entirely by coolant temperature rather than fuel temperature, and thus the axial fuel expansion is not included in the A-parameter. The cladding of the fuel rod in this state can be seen as a thin metallic shell that is welded on the metallic fuel. The heat resistance between fuel and cladding is very low since thermal conductivity across the combined fuel/clad rod is high. It is therefore not obvious that the combined fuel/clad-system thermal expansion is governed only by changes in the coolant temperature, *even* with the assumption of a completely cladding-controlled combined expansion. The new analysis presented in this thesis takes in to account the real value of the combined expansion coefficient of fuel and cladding and assumes that the system reacts to changes in fuel temperature and is thus included in the A-parameter.

For a loss of flow event (as described in Section 4.8.6.1), the temperatures are calculated using eq. 4.141 and 4.142. The flow level as established in natural circulation is assumed to be 3% (F=0.03) of its nominal level. Maximum fuel temperatures were calculated assuming

an axial power peak factor of 1.3. The power level following a flow reduction from F=1 to a natural circulation flow level F is given by:

$$P = F \times \left(\frac{A + B}{AF + B} \right) \tag{4.161}$$

The effect on quasi-static system temperatures and power by the various methods of estimating integral reactivity parameters are summarized in Table 4.17.

Table 4.17: Quasi-static temperatures following an ULOF event

Fuel state	P	P/F	δT_{out}(°C)	T_{out}(°C)	$\bar{T}_f$(°C)	$T_f(max)$(°C)
Fuel/clad unbound	0.051	1.708	106	606	536	697
Fuel/clad bound ref. (1)	0.040	1.326	49	549	505	657
Fuel/clad bound ref. (2)	0.041	1.352	53	553	508	660
Fuel/clad bound ref. (3)	0.048	1.611	92	592	528	687
Fuel/clad bound new	0.050	1.667	100	600	533	692

Table 4.17 shows the non-conservative nature of the assumptions that have been made about the axial expansion of metallic fuel. Compared to the data and methodology developed in this thesis, reference methods underestimate peak fuel temperatures by up to 35°C. The established power level is off by up to 20% and coolant outlet temperature is underestimated by over 50°C.

In the quasi-static state following a ULOHS event, average component temperatures converge on a single value. The core state after a ULOHS is summarized in Table 4.18:

Table 4.18: Quasi-static temperatures following an ULOHS event

Fuel state	δT_{in}(°C)	δT_{out}(°C)	$T_{in} = T_{out} = \bar{T}_f$(°C)
Fuel/clad unbound	227	77	577
Fuel/clad bound ref. (1)	174	24	524
Fuel/clad bound ref. (2)	189	39	539
Fuel/clad bound ref. (3)	228	78	578
Fuel/clad bound new	227	77	577

Again, temperatures are underestimated by over 50°C by the assumptions made about fuel/clad axial expansion (bound ref. 1). The preceding analysis shows that a re-evaluation

of the assumptions surrounding the axial expansion reactivity feedback of metallic fuel is needed.

4.9 Feedback coefficient analysis for B&B cores

4.9.1 Core geometry

Two B&B reactor core designs at 3000 MWt and 1200 MWt were developed by *Heidet & Greenspan* (HG) in 2010 [38]. Specific core design parameters, including fuel pin, duct and assembly setup design of these cores was subsequently developed to enable the calculation of certain reactivity coefficients [40]. Based on the criteria of neutronic performance and technological maturity, the cores use sodium as primary coolant and metallic fuel with 6-10 wt.% zirconium. The general parameters of the two cores are summarized in Table 4.19. A plot of the 3000 MWt core layout and the assembly types (fuel, reflector & shielding) in the MCNP model for core analysis can be seen in Figure 4.30. The structural design and dimensions of the two cores is shown in Figure 4.31. Figure 4.32 gives the general axial geometrical design of the assemblies.

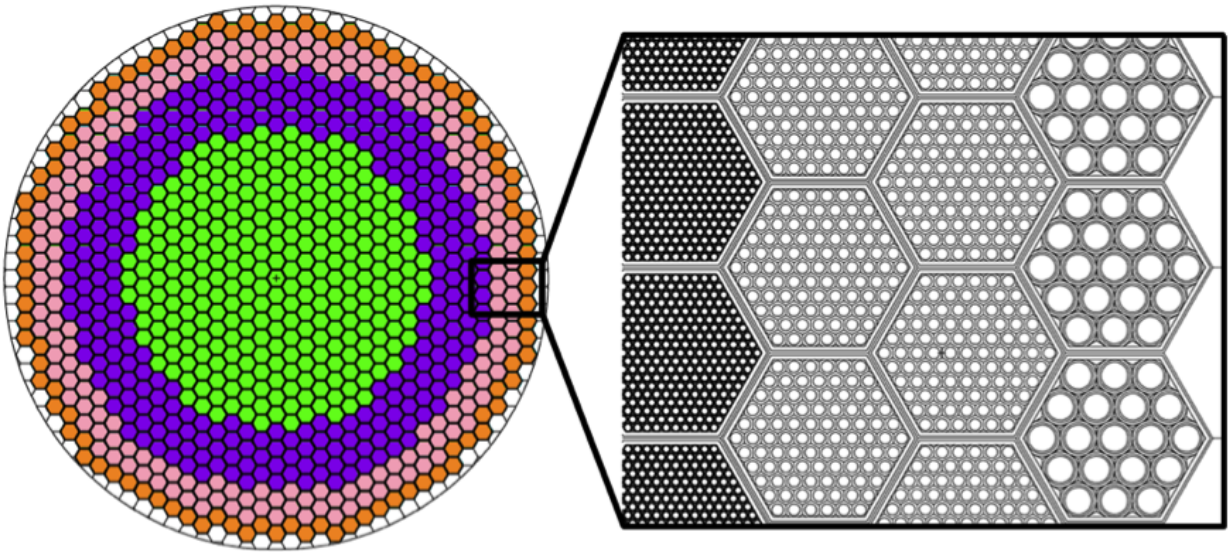

Figure 4.30: MCNP model of the *HG* B&B 3000MWth core, the cutout on the right side is showing fuel, reflector and shield assembly layouts.

Table 4.19: *Heidet and Greenspan* general B&B core design parameters [38]

Core parameters		
Thermal power (MW)	3000	1200
Core diameter (cm)	376.7	353.1
Core height (cm)	209.4	142.2
Core H/D	0.56	0.403
Fuel batches	8	16
Materials		
Fuel	U-10Zr	U-6Zr
Cladding	HT9	HT9
Coolant	Na	Na
Shield/Absorber	B_4C	B_4C
Volume fractions		
Fuel	37.5	34.1
Gap	12.5	11.4
Cladding	22.0	26.6
Coolant	28.0	28.0
Power density		
Peak power density (W/cm^3)	248	418
Specific power density (w/gHM)	21	22
Conversion ratio	1.15	1.11
Discharge burnup (MWd/kgHM)	541	410

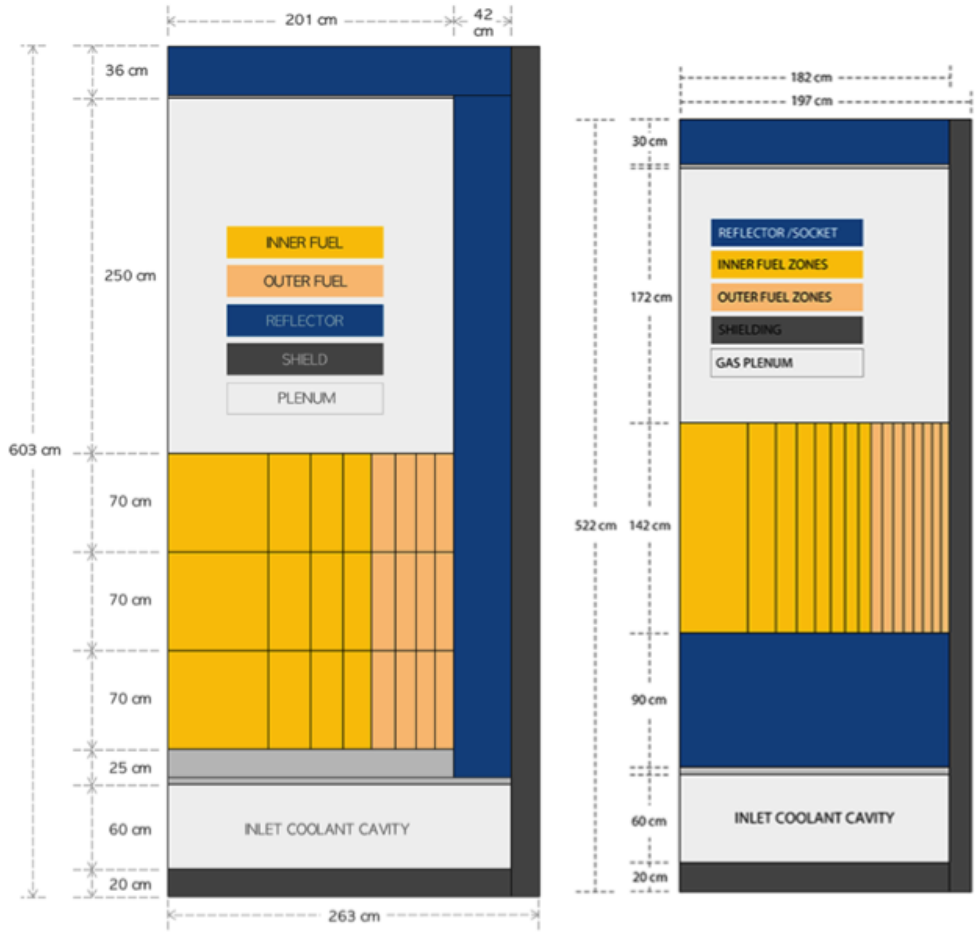

Figure 4.31: The 3000MWth (left) and 1200MWth (right) core structural design

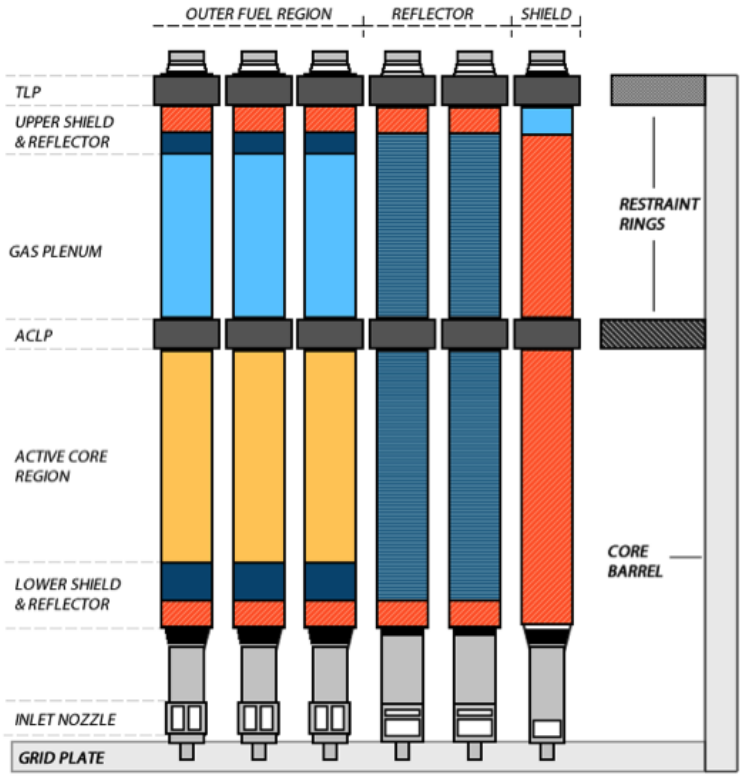

Figure 4.32: Fuel/reflector/shield assembly design for the outer radial zones. (ACLP: Above core load pad, TLP: Top load pad)

The (equilibrium) fuel cycle is based on an inwards radial shuffling scheme. Depleted uranium (DU) is loaded in the outer radial zone, then stepwise shuffled inwards until it is finally discharged from the inner radial zone. This process is shown in Figure 4.33.

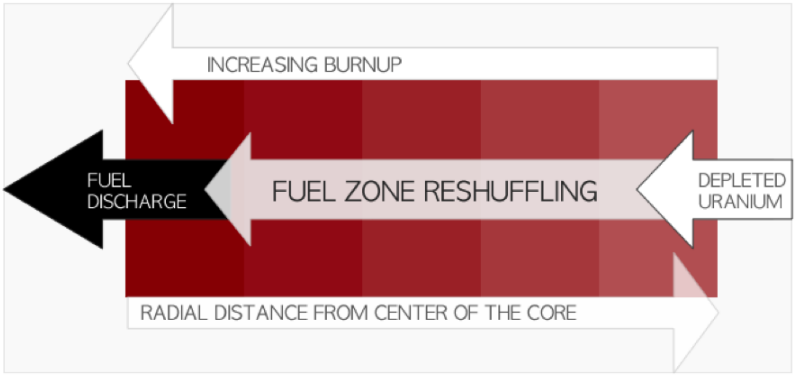

Figure 4.33: *HG* B&B core fuel zone shuffling scheme

The main burnup limitation of fast reactors is the radiation induced degradation of structural material in the core, most importantly the swelling and embrittlement of the cladding material. Based on experimental data availability and technological maturity, the ferritic-martensitic steel HT9 was selected as the cladding, wire-wrapping & duct material in the *HG* cores. The actual dose limits of this material have not been established, so current design limits are set either by attempts to estimate the actual limit, or (conservatively) using the available experimental data as the upper bound. In the *HG* B&B cores, the latter alternative was chosen and this provides one of the constraints for the fuel cycle. HT9 has been irradiated to a fast (E>0.1 MeV) neutron fluence of 3.9×10^{23} n/cm^2 in the Fast Flux Test Facility (FFTF) with negligible swelling and no pin breaches [107]. Consequently, a maximum fast fluence limit to HT9 of 4×10^{23} n/cm^2 was imposed in the *HG* B&B designs, necessitating multiple cladding replacements to reach high levels of fuel burnup.

A melt-refining processing scheme has been adopted for the *HG* B&B cores since it satisfies criteria for simplicity, cost and proliferation resistance. Once the core has reached the end of a cycle, the fuel assemblies are taken out of the core and the end-plugs, reflector and shield regions are removed from the fuel rods. The cladding, mechanically stuck with the fuel due to swelling, is then cut off and discarded. The fuel is heated up to melting in a ZrO_2-CaO crucible - volatile and gaseous fission products leave the fuel during this stage. Melt-refining allows for the removal of 100% of Br, Kr, Rb, Cd, I, Xe and Cs, as well as 95% of Sr, Y, Te, Ba, rare earth metals and americium. The fuel is then re-casted in to new U-TRU-Fs fuel rods with the addition of make-up DU, the fuel rods are re-plugged and then reloaded in to the reactor to their new positions. This general process was developed in the EBR-II project [108] and the method proposed for the UCB B&B cores is visualized in Figure 4.34.

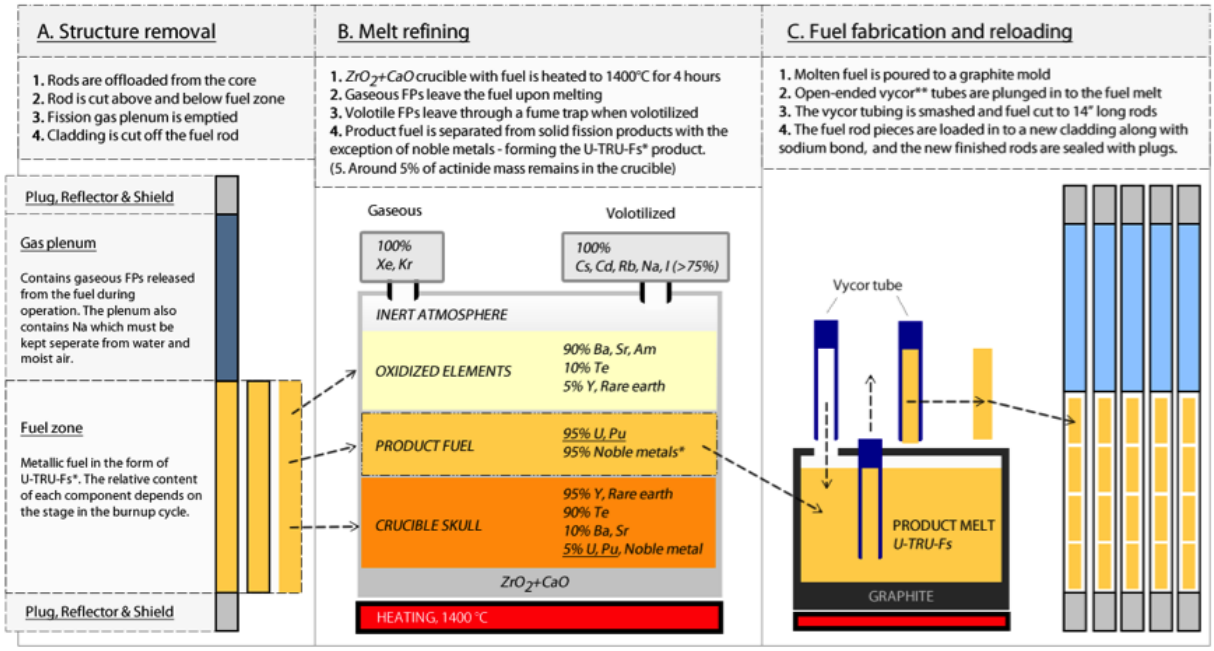

Figure 4.34: Simplified melt-refining process. Values from ref. [109]. *Fs (wt. %): 43.2% Mo, 33.2% Rt, 12.5% Tc, 5.9% Rh, 3.8% Pa, 1.3% Zr. **Vycor: A type of readily manufacturable glass made of 96% silica.

4.9.2 Reactivity coefficients

The calculated reactivity coefficients of the *HG* cores are summarized in Table 4.20.

Table 4.20: *HG* cores reactivity coefficient summary [39]

Reactivity coefficient (¢/K)	3000 MWt	1200 MWt
Fuel Doppler	-0.1	-0.1
Cladding Doppler	-0.01	-0.01
Coolant Doppler	∼0	∼0
Fuel axial expansion	-0.11	-0.12
Coolant density	+0.33	+0.22
Structural material dens.	+0.004	+0.003
Core radial expansion	-0.22	-0.33
Eff. delayed neuton frac (β_{eff})	0.0034	0.0034
Coolant void worth	12$	7$

The major difference between the 2 core designs are found in the leakage dependent reactivity coefficient terms of coolant density and radial core expansion. The calculated reactivity coefficients as bundled together in to QSRB bundled integral reactivity parameters are given in Table 4.21.

Table 4.21: Reactivity coefficient summary

Integral reactivity parameter	3000 MWt	1200 MWt
A (¢)	-33	-35
B (¢)	-25	-50
C (¢/K)	-0.10	-0.33

Because of the smaller size and lower height-to-diameter ratio of the smaller core, leakage is more important to reactivity in this core. Axial leakage is ∼6% in the smaller core, compared to ∼3.5% in the large core. A relative increase in leakage fraction due to a transient has a larger impact to the reactivity of the smaller core compared to the large core. The effect of this can be seen both in the larger (absolute) magnitude of core radial expansion coefficient and the smaller coolant density coefficient of the small core. Both of these effects have a positive impact on inherent safety characteristics. The adherence to QSRB inherent safety criteria for the cores is given in Table 4.22.

Table 4.22: QSRB parameter ratio criteria

Transient	Condition	3000 MWt	1200 MWt
ULOF	A/B < 0.67	1.33	0.7
ULOHS	$1 <$ CδT_c/B $<$1.44	0.61	1.01

The safety criteria of QSRB for both ULOF and ULOHS as defined in Table 4.14 are violated by both core designs, showing highly unfavorable reactivity feedback. These problems prompted the analysis and subsequent development of specific engineered passive safety systems.

Part II

Engineered safety systems

Chapter 5

Approaches for improving the safety of B&B cores

5.1 Introduction

Research in to the reactivity feedback and safety of fast reactors has been a subject of intense study and controverse since the inception of nuclear power technology in 1950s. Unlike properly designed under-moderated thermal spectrum reactors, fast reactors (even properly designed) can have positive temperature reactivity feedbacks that increases core power as temperatures rise. All else being equal, less moderation in a fast neutron core leads to an increase in core reactivity. The coolant density reactivity effect is dependent on core size and leakage probability and as described in Section 4.6. In large fast reactors where the relative importance of neutron leakage on core reactivity is small, core reactivity is generally increased by a decrease in coolant density. The extreme case of such an event is when coolant temperatures increase to the point where a coolant phase change occurs; the effect on reactivity of such an event is referred to as void worth. When mentioned in this thesis, void worth is the change in k_{eff} (measured in \$) by complete coolant voiding of the entire core, including the plenum and inlet cavity. While neutron leakage increases upon coolant voiding, the spectral hardening component dominates the reactivity feedback (changes in coolant absorption are irrelevant). Extensive studies on design approaches to minimize void worth have been carried out in the past (see *Okawa and Greenspan (2007)* [110]), but have primarily focused on smaller cores with higher nominal neutron leakage probability.

To solve the issue of positive coolant density and void worth feedback in a large core while inflicting a minimal impact on the core neutron economy in standard operation, a new system for improving the reactivity feedback and safety of large fast reactors (ARC) was invented and is presented in detail in Chapter 6. Before presenting the theory, function and operation of the ARC system, this chapter presents alternative competing solutions to the same problem. The main focus of this chapter are design alterations and on continuously operating engineered systems that automatically return to their initial state once a transient is over. For a complete overview of competing solutions, a state of the art review of self-actuated shutdown systems (SASS) are also included in this analysis.

5.2 Leakage based approach

The main focus of void worth reduction work worldwide has been devoted to leakage-based methods. This is because the main negative component of the reactivity effect of coolant voiding is the increase in neutron leakage from the core (as stated earlier, changes in coolant absorption rates can effectively be ignored). When the relative importance of neutron leakage in the core is increased, the leakage component of the void reactivity will increase and eventually dominate the positive spectral component, resulting in a negative total void worth. Ideally, a leakage-based void worth reducing design should feature low leakage during standard operation, while strongly increasing leakage in the voided state. However, such ideal (for neutron economy) designs have not been identified.

Leakage-based systems and designs for safety are in direct opposition to the operational requirements of efficient breeders and B&B systems. To enable a self-sustaining B&B cycle, nominal neutron leakage probability must be minimized. The efficiency of all safety systems and designs relying on a change in leakage are dependent on the nominal leakage probability. If the leakage impact on neutron economy during standard operation is small, the impact of a change in the neutron leakage probability will also be small. Conventional fast breeder reactors typically operate with an inner core of high fissile content surrounded by breeding blankets that are then removed and re-processed.[1] The neutron economy requirements for such a system is much more lenient than one where the fission processes is fully dependent on the breeding process (B&B systems). A conventional fast reactor operates with a neutron leakage probability of around ∼20%, a DU-fueled B&B core will not be self-sustaining at losses above ∼7-8%. Correspondingly, leakage-based safety approaches are highly efficient in leaky fast cores, and not at all efficient in more neutronically efficient core designs such as those needed for B&B systems. The specific advantages and disadvantages of known leakage-based safety approaches are examined in the following sections.

5.2.1 Large coolant plenum above active core

Most modern large fast reactor designs feature a large plenum of coolant above the active core region. This is an inherent feature of metallic-fueled cores because of the need for an upper fission gas plenum volume that is comparable to the fuel volume. Coolant voiding is likely to initiate in the upper part of the fueled region where the local boiling point is lowest (low pressure) and coolant temperature the highest. This boiling will quickly spread to the above core plenum region. Voiding of coolant outside of the active core region reduces neutron reflection back into the core and provides a way of reducing void worth without penalizing noticeably the neutron economy of the core in standard operation. In cores with

[1] Heterogeneous breeder reactors with fissile and fertile material interspersed have also been proposed. Whether heterogeneous or homogeneous, conventional fast reactors requires out-of-core reprocessing of the blanket assemblies to make use of the fertile material.

primarily below-core gas plena[2], adding an above core coolant plena is more effective than in above-core gas plena designs. This is due to that nearly all of the volume just above the active core of below-core gas-plena designs can be filled with coolant, compared to 30-50% in an above-core gas-plenum design. The corresponding impact on reactivity by the leakage increase stemming from a density decrease in the above core coolant can be up to 2-3 times larger for below-core gas-plena designs. This design feature plays a vital role in the safety design of the new Russian sodium fast reactor BN-800 [111]. The efficacy of the above-core coolant plenum is dependent on the change in neutron leakage probability between the nominal and voided plenum case. In a conventional fast reactor core like BN-800 with a fuel length of 75 cm, there is a significant axial neutron leakage probability. In such a core with oxide fuel, the nominal coolant void worth in the core region can be brought down to ∼2-3$, which can be effectively counteracted by an above-core coolant plenum with a length of >50% of the fuel length. For the BN-800 core, the in-core void worth is estimated to be 1.71$, with a combined core + above-core sodium cavity void worth of ∼0$. The addition of an absorption layer above the above-core coolant plenum further increases the void-worth reduction efficiency due to a decrease in back-scatter from upper reflectors in voided conditions. In a large B&B design, the effect of the plenum region on total void worth is, however, minor. As detailed in Chapter 2, the neutron economy requirements of a B&B cycle necessitates a minimized neutron loss fraction. Large, low-leakage fast reactor designs such as B&B cores feature long fuel lengths (typically ∼ 2 meters) with an axial neutron leakage probability of ∼1/5 that of smaller conventional fast reactors. In addition, the nominal in-core void worth of a large metallic-fueled sodium-cooled B&B is ∼5 times larger than in a small oxide-fueled SFR. Thus, introducing a coolant cavity above the active core is highly effective in small, high-leakage cores but only has a minor effect on larger reactors. In the large B&B-type of reactors developed in this thesis the above-core plenum contributes about -1$ to the total void worth. To summarize, an upper coolant plenum has the following characteristics:

- Advantages
    a. Reduces the coolant void worth (particularly for low H/D-cores)
    b. Minor impact on core cost and size
- Disadvantages
    a. Ineffective in low-leakage cores
    b. Removes only ∼1/10 of void worth in large B&B reactors

[2]Reactors relying on below-core gas plena typically also feature a shorter above-core plenum of 5-10 cm. For conventional metallic fuel designs, a liquid bond is needed to provide conductivity in the gap between fuel and cladding. Thus, for such designs, below-core gas plena designs are not possible. It is however possible to design metallic-fueled cores with below-core gas plena using the recently proposed annular metallic fuel form (see Section 4.3.10).

5.2.2 Height-to-diameter ratio

The main approach in the void worth reduction research has been focused on designing the core to have a large axial neutron leakage probability through reducing the height of the active core region. This is a very effective approach and was utilized successfully in, for example, versions of the Integral Fast Reactor (IFR) designs that aimed at negative void worth [112]. Reducing the H/D-ratio also increases the efficacy of the above-core coolant plenum (detailed in the preceding section), as it effectively increases the reactivity worth of the above-core coolant reflector. The H/D-approach to void worth reduction has led new core designs to be extremely "pan-cake" shaped. The Russian BN-1200 core design has an active core radius of 5.2 meters with an active core height of 84 cm, giving an H/D ratio of ∼0.16 [113]. The cost of the reactor increases much faster with an increase in the active diameter than with height, as all core components, including the containment vessel, needs to be scaled accordingly. An increase in core height has a much smaller impact on the core cost since it is not the main determining factor for the height of the vessel and does not in any significant way affect the sizing of other components. Thus, the H/D-reduction safety-design approach comes with a large economic penalty.

The safety improvements that the H/D-reduction bring in the form of lower void worth may lead to unwanted degradation of safety performance in other aspects. A high neutron leakage probability punishes the ability for in-core breeding, leading to a high burnup reactivity swing. As described in detail in Section 4.8.6.5, this has a detrimental effect on the safety performance in case of transient overpower scenarios. The worth of reactivity control systems increases as the reactivity needed to compensate the burnup swing increases. If the number of individual control rods/assemblies is not increased (at an additional punishment to core size or power density and therefore cost), the reactivity worth of an ejection of a control element is increased. The effects of H/D-ratio on coolant void worth and burnup reactivity swing from a study in the IFR core design program is illustrated in Fig. 5.1 [112]. Assuming a fixed number of burnup-compensation reactivity control elements in the IFR core study [112], the reactivity worth per element is ∼23 times higher for the H/D=0.192 core compared to the H/D=0.44 core. These differences in H/D, void worth and swing are similar to those between a large B&B core and a small conventional fast reactor. While the integral power/flow reactivity parameter (see definition in Section 4.8.3) is significantly larger for the low H/D-case, its increase is far smaller than the increase in the value of ρ_{TOP} given a set number of control elements. The result is significantly shorter cycle lengths and an increase in the number of control elements in the core, both incurring increasing costs and complexity and a decrease in the plant capacity factor.

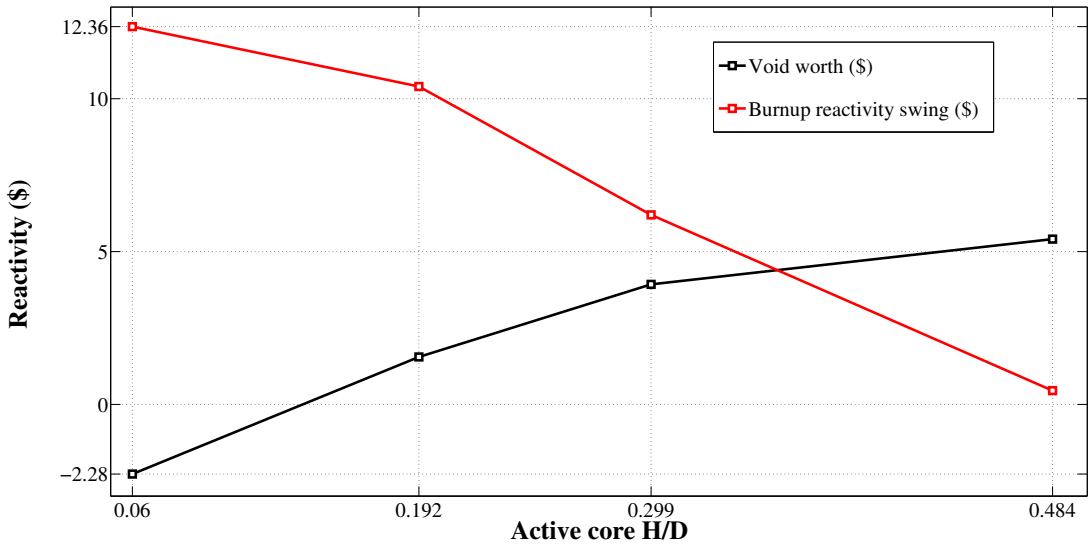

Figure 5.1: Void worth & burnup reactivity swing by H/D ratio (data from ref. [112])

While sodium void worth is reduced and the increased axial neutron leakage probability increases the magnitude of the radial core expansion reactivity feedback, a reduction in H/D-ratio also reduces the magnitude of the negative axial fuel expansion reactivity feedback. However, since the core-averaged fuel density varies as the square of the core radius, an increase in the core radius is twice as effective as a change in fuel height at reducing reactivity. At H/D=1, the reactivity effect of expansions in either direction are roughly equal, meaning that the reactivity decrease from a 2% increase in fuel length corresponds to a 1% increase in core radius. A reduction in core H/D has the following effect on reactivity feedback:

- Increase in the (negative) leakage component of coolant density reactivity feedback due to an increased total neutron leakage probability
- Increase in the radial core expansion reactivity feedback due to an increase in axial neutron leakage probability
- Decrease in the axial fuel expansion reactivity feedback due to a decreased radial neutron leakage probability

The past trends of reactor power versus the height and diameter of the core can be identified by the data available from previous reactor designs. For this study, the data from 34 liquid metal cooled fast reactor concepts (17 of which were built and operated) was collected. The result is plotted in Figure 5.2[55].

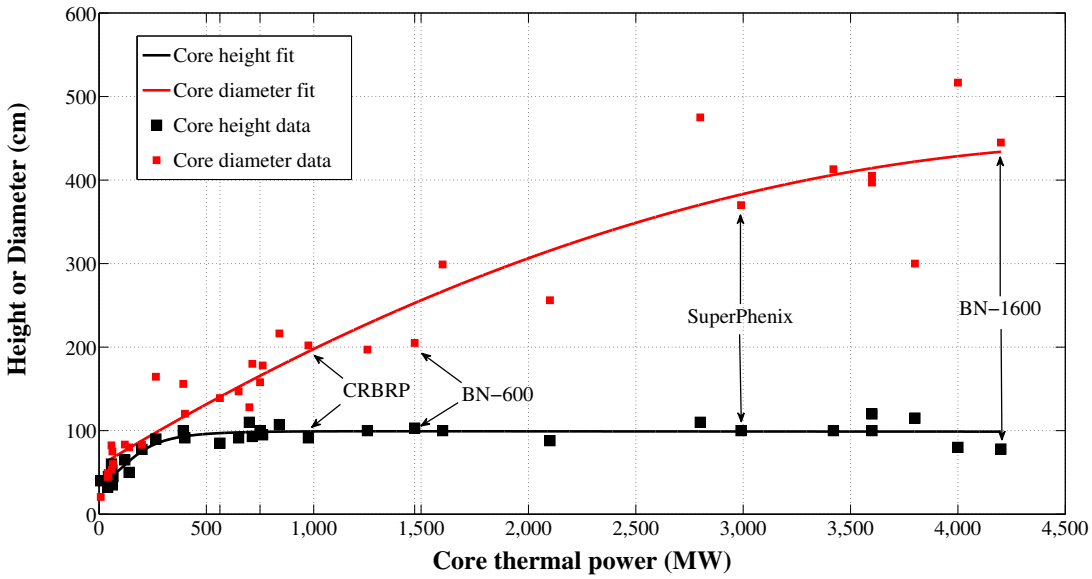

Figure 5.2: Height and diameter vs. power for 34 major fast reactor concepts (data from ref.)

The expected height-to-diameter ratio of a liquid metal reactor (valid in the range $50 \leq$ P $\leq$ 4200 MWt) can be expressed as:

$$\frac{\text{HEIGHT}}{\text{DIAMETER}}\,(\text{MWt}) = \frac{p_1 P^3 + p_2 P^2 + p_3 P + p_4}{\left(P^3 + q_1 P^2 + q_2 P + q_3\right)\left(w_1 P^2 + w_2 P + w_3\right)} \tag{5.1}$$

From eq. 5.1, the values for core height, diameter and H/D ratio can all be estimated from past reactor design experience. Table 5.1 summarizes the expected values at 5 different values of core thermal power:

Table 5.1: Expected core geometry as given by eq. 5.1

Thermal power (MW)	Height (cm)	Diameter	H/D	Power density (W/cm^3)
250	82.6	95.53	0.86	422
500	96.0	131.6	0.73	383
1000	99.1	197.8	0.50	329
1500	99.2	256.0	0.39	294
2000	99.1	306.4	0.32	274
2500	99.0	348.8	0.28	264
3000	98.9	383.3	0.26	263
B&B 3000	200	400	0.50	120

For B&B cores, H/D-reduction is not a viable approach primarily due the detrimental effects it has on neutron economy. As seen in Table 5.1, large B&B cores are derated and require H/D ratios of ∼0.5. A core with negative or even small positive void worth due to reduced H/D alone cannot sustain the B&B mode of operation. In summary, H/D-reduction (also known as "geometric spoiling" or "pancaking") has the following characteristics:

- Advantages
    a. Highly effective in reducing the coolant void worth
    b. Increases the efficacy of an upper coolant plenum for negative feedback
    c. Increases the magnitude of the core radial expansion reactivity coefficient
- Disadvantages
    a. Detrimental to the core neutron economy (precluding its use in B&B core design)
    b. Increases the core diameter at great capital cost
    c. Makes burnup reactivity control requirements more severe
    d. Decreases the magnitude of the fuel axial expansion reactivity coefficient (for a given core volume)

5.2.3 Heterogeneous core design

It has been shown that carefully designed strongly heterogeneous cores with different fuel heights and fuel diameters in different parts of the core can reduce the void worth without significantly damaging neutron economy. Concepts such as the diabolo design with an axially shorter central core region show great promise [114][115][116][117]. Voiding is likely to initiate in the upper fueled region of the central zone. As the void reaches the central above-core region, both axial leakage from the central core zone as well as radial leakage from peripheral zones provide a strong negative reactivity feedback. In the french SFR design program, the standard "pancake"-type core (see 5.2.2) called SFRv2b has a coolant void effect of 5.1$. The core was redesigned in a highly heterogeneous way, with a shorter average fuel height, the addition of fuel regions with different heights, fertile/fissile axial fuel zoning and an absorber region above the upper coolant plenum. The shift in core design is shown (simplified) in Fig. 5.3. The performance of the redesigned CVF core is inferior to the original design in several ways, but the coolant void effect is reduced to -0.5$. The addition of axial fertile/fissile fuel zoning resulted in a reduction of -3$ to the void worth, the absorber region above the upper coolant plenum added -0.5$. The "diabolo" core shape with a shorter central fuel region adds an additional -1.5$, giving a sum of new components of -5$. When analysed together, these individual effects enhance each-other to produce the -5.6$ total void worth reduction. As compared to the reference core (SFRv2B), the CVF core requires a higher enrichment (20-23.5% vs. 13.9-17.6%), a doubled burnup reactivity swing (!), an increase in the core diameter (340 vs. 326 cm) and a reduction in the cycle length (360 vs. 390 days).

Unfortunately, the total nominal leakage probability needed for these design changes to have such a large impact is prohibitively high for B&B cores. Moreover, fuel shuffling in the B&B cores requires uniform fuel assemblies throughout the core. In a standard self-sustaining[3] SWR B&B (as opposed to a TWR B&B), each fuel assembly will spend some time of its cycle in each region of the core. This requires a single uniform fuel assembly design across the core and precludes the use of "diabolo" methods for the core design. Using fertile/fissile axial fuel zoning was shown to have the largest effect of all individual design changes in the SFRv2→CFV core re-design. In the equilibrium cycle of a SWR B&B, the feed fuel is primarily fertile material. A B&B system makes the most sense, both from an economic and a resource-utilization point of view, if the feed fuel has a fissile content at or below that of natural uranium. This fact leaves little room for fissile/fertile axial zoning [4] The burnup progression of a freshly loaded fuel batch in the B&B system quickly eliminates

[3]This is the case for the "pure" B&B systems analyzed in this thesis, where the only feed fuel in the equilibrium cycle is fertile fuel. B&B type cores operating a dual shuffling scheme with a fissile seed and a fertile (B&B) blanket are also possible [118]. In such cores, there is indeed a theoretical possibility for 2 or more different type of assembly designs.

[4]The maximum fissile-content difference in feed fuel is ∼0.71%, assuming a zoning between ^{232}Th and natural uranium.

all effects of a potential initital feed-fuel zoning. Indeed, the level of fissile content in the feed fuel has a very small impact on the neutronics of the system (see Section 2.7.4).

Thus, void worth reduction through increasingly heterogeneous designs is not applicable ("diabolo") or completely ineffective (axial zoning) for B&B cores. The only applicable design implementation from the SFRv2→CFV re-design is the addition of an absorbing layer above the upper coolant plenum zone. However, the impact is dependent on the axial leakage probability, so this implementation has a near-negligible effect on void worth in a B&B core. The addition of an additional absorber layer does however increase the cost, complexity and most important of all; the pressure drop through the core. In summary, none of the heterogeneous core re-design strategies for void worth reduction are recommended for use in B&B core design. The advantages and disadvantages are summarized as follows:

- Advantages
    a. Highly effective in reducing the coolant void worth
    b. Smaller negative impact on core neutronics than H/D reduction
- Disadvantages
    a. Significant core complexity and cost increase
    b. Complicates fuel shuffling
    c. Not applicable for B&B cores

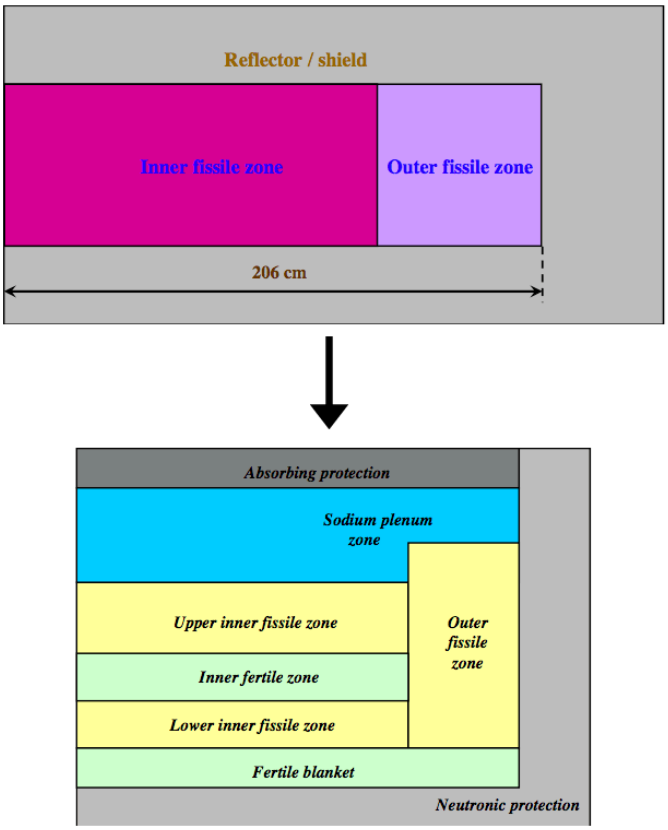

Figure 5.3: SFRv2B (top) and CFV heterogeneous void-worth reduction core (bottom) [115]

5.2.4 Gas expansion modules (GEM)

The first system specifically designed to reduce reactivity through leakage in accident scenarios is the GEM system developed at FFTF in the 1980s. GEMs are empty assemblies located between the outer fuel assembly row and the reflectors. They are sealed at the top but open at the bottom and filled in their upper part with a pressurized gas. During standard operation, coolant flow provides upward pressure inside the GEM that compresses the gas so that it stays above the active core region. When flow decreases in a loss of flow (LOF) accident, the gas expands into the core region and thereby reduces the neutron reflection and hence, the core reactivity. The operation of the system is shown in Fig. 5.4. While GEMs are conceptually both simple and brilliant and worked well in the FFTF, they are effective only if the neutron importance in the outer core region is sufficiently high. This is not the case in large B&B cores in which depleted uranium fuel is loaded at the core periphery. In addition, GEMs only respond to one accident scenario (LOF), and concerns have been raised about the potential response of the core to gas leakage from the GEMs. If a GEM system

fails and gas is leaked, it has the potential for a positive reactivity insertion. For large B&B cores, the radial neutron leakage is minimal (1-3%), so GEMs do not have a significant effect on reactivity and are thus not a viable option.

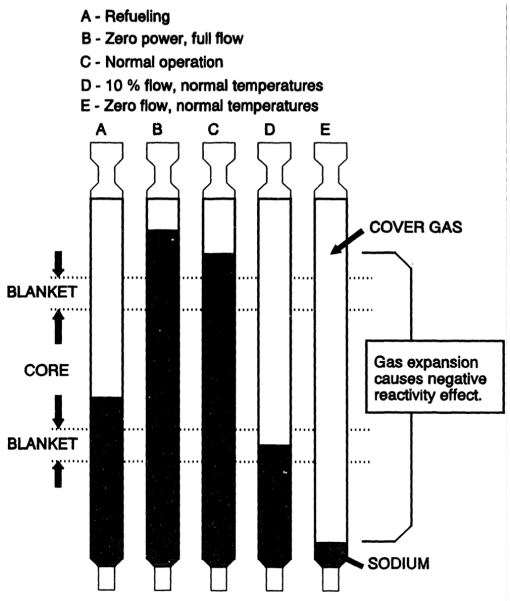

Figure 5.4: Gas Expansion Module (GEM) principle of operation [119]

- Advantages
    a. Passive and continuously operating
    b. Very simple and cheap system to install and test
    c. Minimal impact on core neutron economy
    d. Does not degrade with or burnup
- Disadvantages
    a. Only responds to loss-of-flow accidents
    b. Only effective in small cores with large radial leakage probability
    c. If failed, they can add positive reactivity
    d. Complicates start-up and shutdown procedures

5.3 Moderation based approach

The positive reactivity component of coolant voiding is due, primarily, to the fact that the fission/capture probability in the fuel actinides and the number of neutrons produced per fission (ν) rise sharply with increased neutron energy. At above 1 MeV, this rise is near-exponential. In addition, non-actinide absorption cross-sections decrease and the fertile actinide isotopes that have energy thresholds for fission see sharply increased fission rates upon hardening of an already hard spectrum. If the neutron spectrum can be kept soft enough upon coolant voiding, the void worth can be greatly reduced. This is incidentally one argument for choosing oxide fuel over metallic fuel in certain fast reactor designs. Because of this, core designers have proposed incorporating solid moderating material such as BeO or ZrH in fast reactor cores. However, it is vital for the neutron economy of B&B cores to both maximize the fuel volume fraction and maintain the hardest possible neutron spectrum during standard operation. Therefore, the addition of solid moderator material is not a viable option for B&B cores.

- Advantages
    a. No failure probability and does not degrade over time
    b. Reduces void worth
- Disadvantages
    a. Large negative impact on neutron economy

5.4 Solid absorber based approach

The use of permanent solid neutron absorbers that preferentially absorb high-energy neutrons (such as Ca_3Na_2) can reduce the positive reactivity during core voiding. Calcium isotopes have many high-energy neutron absorption resonances and an increasing one-group absorption cross-section as the spectrum of a fast reactor hardens. The absorption cross-section of ^{40}Ca in the energy range of 10 keV to 1 MeV is shown in Fig. 5.5. The problem, as with moderation-based approaches, is that the absorbers are present and active during standard operation as well. To have an appreciatively large effect on coolant voiding reactivity, the absorbers will strongly impair the neutron economy at standard operation. Therefore, permanent solid absorbers of any type are not a viable option for B&B cores.

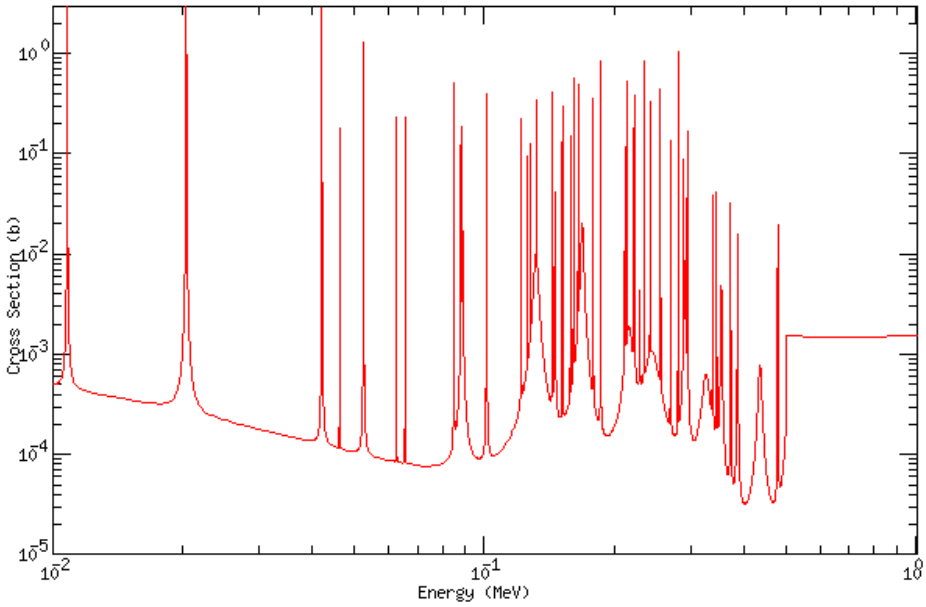

Figure 5.5: The high-energy neutron absorption cross-section of ^{40}Ca (log/log scale) [57]

- Advantages
    a. No failure probability
    b. Reduces void worth
- Disadvantages
    a. Large negative impact on neutron economy
    b. System effectiveness is a function of burnup (degrades over time)

5.5 Liquid absorber based approach

Liquid absorbers have the potential to move continuously as temperatures in the core change, poisoning the core when needed and retracting from the active core region as temperatures decrease. While conceptually highly promising, the challenge has been to find a viable engineering implementation for a liquid-based absorber system. Two methods have been devised to date, presented below. A new system (for which this chapter is an introduction) is presented in Chapter 6.

5.5.1 TWR thermo-stating modules

The use of ^{6}Li for reactivity control was introduced along with the original B&B travelling wave reactor design by *Teller et. al* in 1996 [15]. Lithium has several unique properties that make it suitable for reactivity control. Natural lithium consists of 92.5% ^{7}Li and 7.5% ^{6}Li. ^{7}Li is neutronically benign while ^{6}Li is a very potent neutron poison with a high absorption cross-section also at high neutron energies. Isotopic separation of the lithium isotopes is relatively inexpensive, and lithium stays liquid throughout sodium-cooled reactor operating temperature regimes. Because of this, lithium has been the focus of at least two innovative passive reactivity control systems. The system devised by *Teller et. al.* for the traveling wave reactor consists of two connected metallic compartments, one filled with ^{6}Li and the other with ^{7}Li, fed by capillary tubes. The ^{7}Li, which is permanently located within a compartment in the fuel region, expands upon a temperature increase, which in turn actuates a piston that injects ^{6}Li into a separate compartment located inside a coolant channel. When temperatures decrease, the ^{6}Li retracts down a tube and leaves the in-core compartment. In this way, a passive thermostating reactivity control system with negligible impact on core neutronics during standard operation was devised. The system is shown in Fig. 5.6.

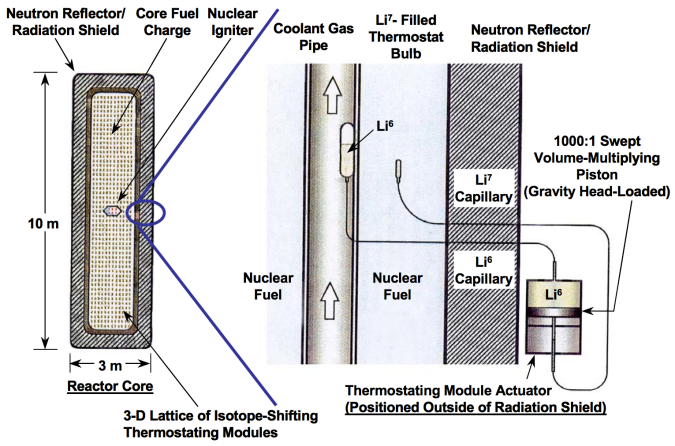

Figure 5.6: The TWR ^{6}Li thermo-stating control system [15]

The system characteristics are precisely what is needed for a large breeder or breed & burn core, however the proposed specific engineering implementation does not work in a shuffled system. Also, the system function cannot be said to *inherently safe* in the strictest sense. It relies upon the the function of thousands[5] of moving mechanical parts (pistons) with an assigned failure probability, rather than simply on natural laws and phenomena.

- Advantages
    a. Large negative insertion of reactivity during transients
    b. Minimal impact on neutron economy
    c. Does not significantly degrade in efficiency with burnup
- Disadvantages
    a. Involves moving mechanical parts with failure probabilities
    b. Makes fuel shuffling operations impossible

5.5.2 Lithium expansion modules

In 1998, Kambe et. al developed the Lithium Expansion Module (LEM) system for reactivity control for the RAPID cores [120]. LEMs consist of one or more large reservoirs of ^{6}Li located above the core, with close ended tubes leading down through the active core region. During standard operation, the ^{6}Li in the tubes is suspended above the active core by argon gas. When temperatures increase, the ^{6}Li inside the reservoir expands. This pushes ^{6}Li down the tube and into the core region while compressing the argon gas. Lithium-expansion systems can provide large amounts of negative reactivity, operate passively and do not affect core neutronics noticeably during standard operation. In addition, LEM-devices do not have any moving mechanical parts with associated failure probability. Both conceptual and detailed analyses of lithium-based control systems were carried out within the scope of the work in this thesis. Several different new systems based on the passive injection of ^{6}Li that integrate seamlessly into conventional fast reactor fuel assemblies were developed in this work specifically for use in shuffled B&B cores (see Chapter 6 on ARC). The inspiration for the ARC-systems came from the LEM and TWR thermo-stating systems. The actuation characteristics with temperature of a LEM-device is shown in Fig. 5.7. A proposed installation of the system in a fast breeder reactor is shown in Fig. 5.8.

[5]Ref. [15] proposes the need of 1000 thermostating modules per 1 GWe of core output.

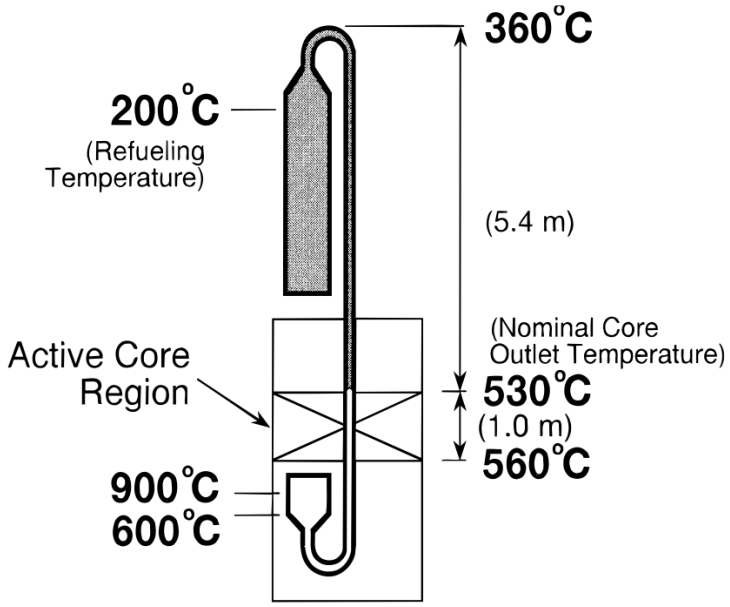

Figure 5.7: LEM-device system actuation (gray component is ^{6}Li) [120]

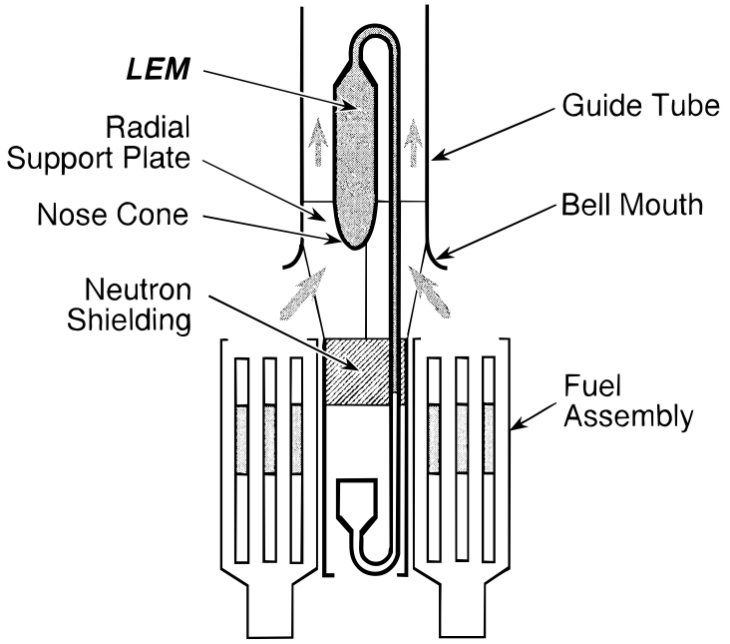

Figure 5.8: LEM-device system installation [120]

While LEM-systems are the most promising existing option analyzed, they have a number of drawbacks that are not immediately obvious. The installation approach as given in Fig. 5.8 effectively makes conventional shuffling operations difficult. The proposed method is to remove the entire LEM-system from the core and hang it from a support in the upper internal structure as the fuel is being shuffled or added/removed from the core. While this is conceivable, it may be a quite difficult operation in the opaque environment of a liquid metal cooled reactor. The LEMs are located axially above the core in a position with low neutron flux. However, the rather massive reservoirs of highly enriched lithium will inevitably see a continuous finite flux, causing (primarily) the following reaction[6] :

$$^{6}\mathrm{Li} + n \rightarrow {}^{4}\mathrm{He} + {}^{3}\mathrm{H} \tag{5.2}$$

While accident-scenario-actuations can reasonably be assumed to occur seldom enough to have a negligible impact on the material composition of the LEM reservoir, the same cannot be said for continuous finite flux over decades of operation. While not mentioned in the reports, it is conceivable that He-translucent apartures in the LEM-reservoir could vent helium to the coolant and depressurize the system[7]. The fate of the non-negligible amount of solid LiH produced in the LEM reservoirs is also not addressed, putting a questionmark next to the A6 criteria of Table 5.2. The main issue with LEM-systems however is that of criteria A2 (the risk of positive reactivity insertion). If the gas/liquid interface breaks during full actuation of the system, gas bubbles will travel axially upwards through the highest worth regions of the core, producing a positive reactivity insertion. Uncertainties in the stability of the gas/liquid interface and the potential of positive reactivity insertions make the licenseability of the systems questionable (failing criteria E5).

5.5.3 Flow levitated absorbers

Flow levitated absorbers (FLAs) consists of balls or plates held in a separate assembly at or just above the axial level of the top of the active core by the coolant flow. As the coolant flow decreases in a loss-of-flow event, the absorbers drop in to the core causing a negative reactivity insertion [121][122]. FLAs, just as GEMs (see Section 5.2.4), only responds to loss-of-flow accident scenarios, and thus a direct comparison between the two is justified. The FLA actuation is similar to the way the gas pocket of a GEM-assembly operates, but FLAs function through absorption as opposed to leakage. Compared to GEMs, this has two major advantages and one major drawback. Since FLAs are absorption-based, they can be placed anywhere in the core and are highly effective even in low-leakage systems such as B&B cores. Additionally, the systems have no obvious way of adding reactivity during a loss-of-flow event, but are just as complicating to start-up procedures as GEMs. On the other hand, continuous neutron absorption in the finite neutron flux above the core means the system degrades in worth over time (not a problem for GEMs). The design of an FLA

[6]Note that it is the same reaction that provides negative reactivity in the event of an actuation.

[7]Such an implementation was in fact proposed for the TWR thermostating module [15].

system utilizing small spherical absorbers balls is given in Fig. 5.9. A cylinder based FLA system developed mainly for gas cooled reactors is shown in Fig. 5.10

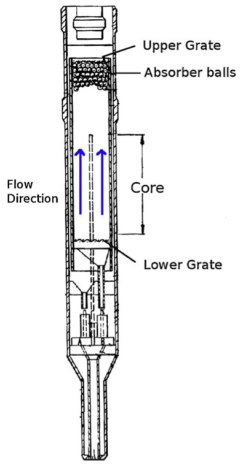

Figure 5.9: Ball-based FLA system [121]

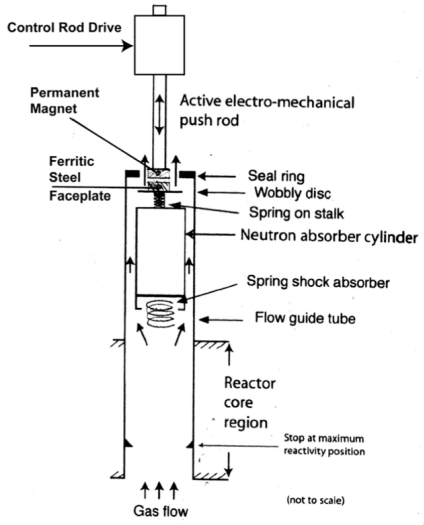

Figure 5.10: Cylinder FLA system [122]

- Advantages
    a. Large negative insertion of reactivity during transients
    b. Minor impact on neutron economy
- Disadvantages
    a. Only responds to loss-of-flow accidents
    b. Can only actuate once and will not return to its initial state
    c. Complicates start-up and shutdown of the core

5.6 Curie-Point actuated systems

The curie-point is the temperature at which a permanent magnetic material loses its magnetic properties. At this temperature, the aligned magnetic spins of electrons in a ferromagnetic material change in to a disordered paramagnetic state. Any device (for example a control rod or neutron poison) that is held against gravity by a magnetic force of a permanent magnet will automatically drop as the temperature of the magnet goes above its curie point. If the magnet material is carefully selected to have a curie-point tailored to an appropriate emergency-shutdown temperature of a reactor core, such a device can be used to passively provide emergency shutdown capability. Since such a system operates only by laws of nature (gravity and magnetic properties), it has the potential to qualify as inherently safe. SCRAM

operations of any type in a fast reactor are events that should, if possible, be avoided. The resulting thermal shocks may damage and/or reduce the lifetime of core-components. Thus, the applicability of a curie-point system is more the replacement of conventional SCRAM systems than an added inherent safety design feature. The operation, function, advantages and disadvantages of curie-point shutdown rods are fairly straightforward. The main issue is that there is a significant potential for time-lag and/or misfire as the magnet needs to be heated to a specific average temperature by the outlet coolant in order to demagnetize. Choosing a material with too high curie-point and the device will not actuate in time, too low and it may shut down the core from a minor temperature perturbation. The proper function of the system relies on the efficiency of the heat transfer of the outlet coolant through the control assembly duct to the magnet. The schematic of a curie-point device is given in Fig. 5.11. Such a system has been successfully tested in the JOYO reactor in Japan [123]. Curie-point rods can be retracted after use (also proven in the tests of ref. [123]), and are thus not, like most other SASS designs, single-actuation systems.

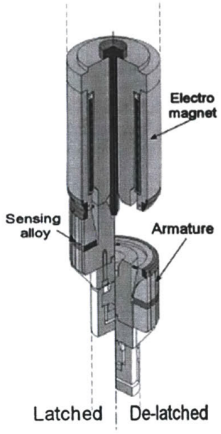

Figure 5.11: Curie-point control rod in latched and de-latched state [124]

- Advantages
    a. Large negative insertion of reactivity during transients
    b. Minor impact on neutron economy
- Disadvantages
    a. Discontinuous SCRAM-type of actuation
    b. Can either time-lag or misfire unless calibration is optimal

5.7 Melting point and seal-rupture actuated systems

A number of SASS-systems actuated by the rupture of an interface between a neutron absorber and the active core have been proposed. In these systems, an absorbing material, either liquid or solid, is placed in a compartment above the active core. As temperatures and/or pressure rise above some set margin, the seals break (or melts), leaving the absorbing material to fall by gravity in to the core and terminate the fission process. The Lithium Injection Module (LIM), shown in Fig. 5.12, scrams the reactor by the rupture of a seal that allows ^{6}Li to flow in to the active core [125]. Another concept uses an aluminium seal that melt to release solid spherical absorber balls in to the active core [126]. This type of SCRAM systems operative passively but can only be actuated once and cannot be brought back, even manually, to the original state. While they can be placed anywhere in the reactor and function well in B&B cores, the discontinuous (SCRAM) behavior and single-actuation nature of actuation are big disadvantages. In addition, the fact that the systems that are installed in the core cannot be tested may prove an insurmountable licensing hurdle.

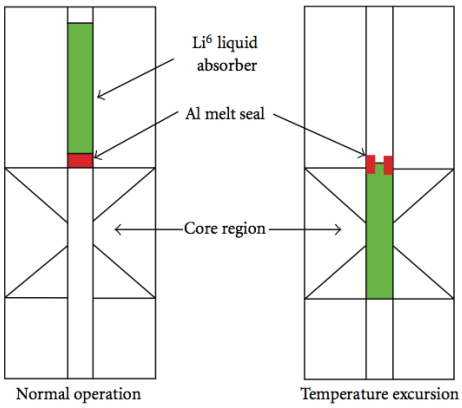

Figure 5.12: ^{6}Li injection module (LIM) [125]

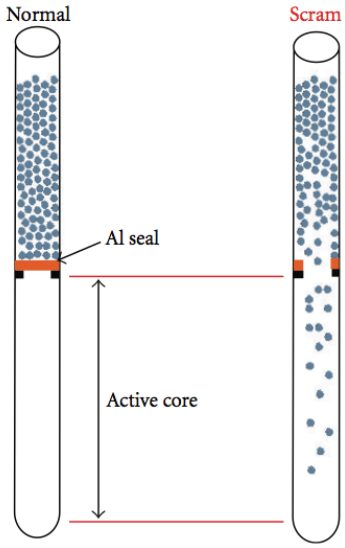

Figure 5.13: Al melt-seal absorber concept [126]

- Advantages
    a. Large negative insertion of reactivity during transients
    b. Minor impact on neutron economy
- Disadvantages
    a. Cannot be tested

b. Discontinuous SCRAM-type of actuation

c. Can only actuate once and will not return to its initial state

5.8 Enhanced CRDL thermal-expansion systems

Efforts have been made to design passive systems that increase the expansion of standard reactor control rods in to the core upon coolant temperature increases. The *ATHENa* design, shown in Fig. 5.14, uses the expansion of sodium located in a compartment with an upper part consisting of expandable metal bellows, to push the control rods in to the core. The design operates passively but is rather complicated by passive-safety-system standards. The "weak" point of the system may be the uncertainty related to the long-term reliability of the metallic bellows. It may be preferential to have control rods operate separately to fulfill their function (burnup reactivity control, SCRAM etc.) and have safety systems operate independently as to not interfere with these operations.

- Advantages
  a. Large negative insertion of reactivity during transients
  b. Minor impact on neutron economy
- Disadvantages
  a. Complicated mechanical design
  b. Long-term operation uncertainty
  c. Requires high control-rod-worth to be efficient

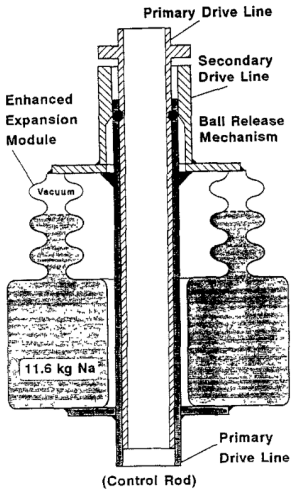

Figure 5.14: The ATHENa module [127]

5.9 Additional systems

Far from all of the systems that have been proposed for inherent safety and SASS-operation have been explicitly evaluated here. Other options, as mentioned in ref. [122], include (with main disadvantages in parenthesis): fusible link-latches on control rods (slow acting and single-actuation), alkali-vapor pressure driven devices (slow acting), pressure activated control rod scram systems (there are better SCRAM options), cartesian-diver type actuation (slow acting). These devices are mostly in early stages of development. As they mature or more is published on their design and function, they will be analyzed in more detail and compared with the newly developed ARC-system of this thesis (Chapter 6).

5.10 System evaluation criteria

The evaluation criteria for systems and design-approaches to improve the inherent safety performance of large fast breeder and breed & burn system are summarized in Table 5.2. Initially, an attempt was made to assign relative weighing factors to each category of Table 5.2 in order to be able to quantify differences between systems. As analysis progressed it was realized however that it is more efficient to treat the criteria in a binary fashion: If any of the criteria of Table 5.2 are outright violated, the system is not applicable for B&B designs. In the event that more than one system meets all criteria (this is not the case), a more detailed comparison would be performed. Assigning numerical values to the different categories of evaluation criteria (which is the norm) does not work, as a system could score a high overall value (and thus be ranked high) but have a single drawback that still precludes its use. These criteria have been developed specifically with radially shuffled B&B cores in mind.

SASS-systems complicate the evaluation as all of them by definition violate the A5 criteria (continuous operation). While other systems and design approaches impact the physical behavior of the core itself, SASS-systems are essentially SCRAM systems that are actuated passively. The approach regarding continuously operating designs and SASS-systems adopted in the B&B core design strategies developed in this study are the following:

1. All cores are equipped with some form of SCRAM system actuated by a wide variety of automated triggers from measurements of temperatures, neutron flux, flow rates etc.

2. The SCRAM system can either be a dual-purpose (conventional actuation + passive actuation) combined SASS-system, or a conventional SCRAM system can be backed up by additional SASS-system for extra redundant safety.

3. If SCRAM systems fail, continuously operating passive/inherent systems or design characteristics should ensure that the reactor remains in a safe state and temperatures remain below constraints set by safety margins.

Ideally, the core should avoid the SCRAM-events entirely, even for extreme-situation shutdown by proper design of continuously operating systems or by the design of the core itself. Since the inclusion of SCRAM systems in the core design is likely to be unavoidable from a licensing standpoint, SASS-type systems should act as a backup to the primary SCRAM-system.

Table 5.2: Binary evaluation criteria for FBR/B&B safety systems/designs

Designation	**Description**
A.	System operational efficiency
A1.	Significantly improves system response to transients
A2.	Has no credible failure mode that introduces positive reactivity
A3.	Operates passively/inherently
A4.	Has no moving mechanical parts
A5.	Operates continuously
A6.	Is not significantly degraded by time and/or burnup/fluence
A7.	Sufficient speed of negative reactivity insertion/actuation
A8.	General accident scenario applicability
A9.	Seismic stability
B.	System impact on standard op. neutron economy
B1.	Spectral degration
B2.	Leakage impact
B3.	Absorption impact
C.	System impact on core operation
C1.	Does not interfere with shuffling operations
C2.	Does not complicate start-up and shutdown
D.	System impact on core/reactor cost
D1.	Core size/shape cost impact
D2.	System component costs
E.	System complexity & predictability
E1.	Non-nuclear testability
E2.	Modeling complexity
E3.	Operational uncertainty
E4.	Single-system redundancy
E5.	Licenseability in current frameworks
E6.	Possibility of jamming and/or non-zero failure prob.

5.11 Summary systems evaluation

The evaluation of the systems analysed for improving inherent safety of large breeder and breed & burn reactors are summarized in Table 5.3. A *direct violation* means that the criteria of Table 5.2 is outright violated, while a *conditional violation* means that the systems does have a noticeable negative impact on the specific performance criteria but it is a minor effect.

Table 5.3: Safety systems/designs violations of evaluation critera

Method	**Direct violation**	**Conditional violation**
Large above-core plenum	-	A1, D1
H/D-ratio adjustment	B2, D1	E2*
Heterogeneous core	C1, D1	B2
Gas Expansion Module	A1, A2, A8, C2	-
Added moderator	B1	B3
Solid absorbers	A6, B3	A1, B1
Liquid absorber (TWR-type)	A4, C1, E5, E6	A6
Liquid absorber (LEM-type)	A2	A6, A7, A9, C1, D1, E5
Flow-levitated abs. SASS	A8, C2, E3, E5, E6	A6
Curie-point SASS	A5, E6	A7, A9
Melting point and seal-rupture SASS	A5, E1, E3, E5	A6, A7, A9, E6
Enhanced CRDL expansion	A4, E3, E5	A7, E6

* Specifically referring to the complexity of modeling radial expansion bowing of large cores

As seen in Table 5.3, only the large above-core coolant plena design-approach has no direct violation of criteria, and is thus recommended for implementation. As has been described, the effectiveness of the plenum approach is highly dependent on the H/D-ratio adjustment (more pancaked type of core), which does directly violate two criteria. In large cores with a high value for H/D (>0.5), a large above-core coolant plenum does not add much in terms of safety performance and thus conditionally violates criteria A1. The best SASS-system from this evaluation are clearly those actuated by Curie-point temperature. One problem with the Curie-point systems is that they will always violate criteria E6 (and, of course, A5), since they cannot be constructed with a liquid absorber (which would preclude the possibility of jamming).

Chapter 6

The Assembly Reactivity Control (ARC) systems

6.1 Introduction and development

The main motivation that inspired the creation of the ARC-systems was the need for improving the reactivity feedback of large B&B cores without damaging the neutron economy. Initially, all systems studied and evaluated in Chapter 5 were considered for implementation in B&B cores. The liquid-absorber based *Lithium Expansion Module* (LEM) was identified as the best currently available option. This introductory section details the evolution from the LEM to the ARC-systems, via the intermediate AILEM-systems, and reviews the steps taken and insights gained in the process.

Severe limitations of the LEM-systems (detailed in Section 5.5.2) prompted the development work of other systems based on the same principle. The basic principle, shared between the TWR thermostating modules (See section 5.5.1), LEM and ARC-systems is to passively inject the liquid neutron poison ^{6}Li in to the core during temperature excursions. The key to this idea is the relatively high neutron absorption cross-section of ^{6}Li in the high-energy range. The total absorption cross-section between 10 keV and 1 MeV of ^{6}Li and ^{238}U are given in Fig. 6.1.

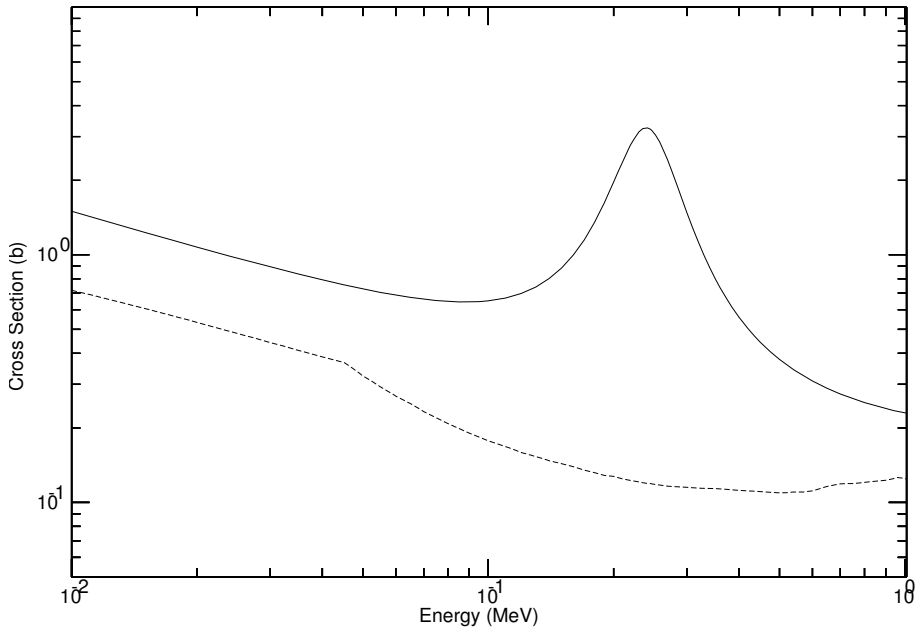

Figure 6.1: Total abs. cross-section of ^{6}Li (solid) and ^{238}U (dotted)

6.1.1 Re-designing the LEM-system to the AILEM-systems (the first step towards ARC)

The challenge of liquid-absorber based systems is primarily the engineering implementation and installation of the system in the core. This includes deciding on ways to both *actuate* and *deliver* the liquid absorber to the core. Many new systems with the basic *actuation* principle of the LEM-type system were developed before they were abandoned for the ARC systems. During this work, optimal *delivery* systems, generally applicable for liquid-absorber based systems, were identified. Initial strategies were all based on attempting to re-design the LEM-system to better fit a shuffled B&B core, while adhering to as many as possible of the criteria of Table 5.2. *Delivery* system studies included:

1. Conventional LEM-system
2. Diversified conventional LEM-system
3. ^{7}Li/^{6}Li piston-pin system
4. AILEM-IA, Inter-assembly gap installation
5. AILEM-HD, Hollowed-out duct wall installation
6. AILEM-P, Replaced fuel-pin installation
7. AILEM-C, Dedicated assembly corner installation (w. capillary-type tubes)

No feasible engineering solution was found to approaches 1-5 for a shuffled B&B core that would not violate several of the performance criteria of Table 5.2. Some limitations are briefly covered in Section 6.1.1.1. However, approaches 6 and 7 proved to have major advantages over the currently available competing designs. Their design and operation is covered in Sections 6.1.1.2 and 6.1.1.3 respectively. By putting the delivery system inside of individual fuel assemblies rather than in separate dedicated assemblies, concerns about fuel shuffling and redundancy are resolved. As an integral part of the assembly, the systems will not interfere with operations such as fuel load/offload and shuffling. Since a larger fast reactor core has several hundred assemblies and each installed system operates independently from the rest, there is an extreme level of redundancy.[1]

6.1.1.1 The AILEM-IA and AILEM-HD systems

The initial strive in developing the AILEM systems was to achieve a design improving the feedback with no negative impact on the core neutron economy whatsoever. The only conceptual design conceived (to date) which could achieve this is converting parts (or all) of the inter-assembly regions of the core to an actuation volume for a passive control system.

[1] In contrast, a conventional LEM-system consists of a handful of dedicated assemblies for a large reactor [120].

The inter-assembly region takes up 2-3% of the active core volume and is typically non-essential to the cooling of the fuel. The reactivity worth of filling the inter-assembly gap with ^{6}Li is estimated from neutron transport calculations to be about 30-40$ in large fast reactor cores. Thus, only a small part of this volume would be needed to install a highly effective control system. Unfortunately, no functioning engineering implementation of the AILEM-IA (IA = InterAssembly) system using this principle was found nor is likely to ever be found. The next idea was to utilize the duct walls themselves as the vessel for lithium-injection. By making the duct walls a bit thicker (and simultaneously reducing the inter-assembly gap), a lithium injection system can be accommodated inside the duct wall in a hollowed-out compartment. This is the AILEM-HD (HD = Hollow duct) idea, shown for a fast reactor fuel assembly in Fig. 6.2.

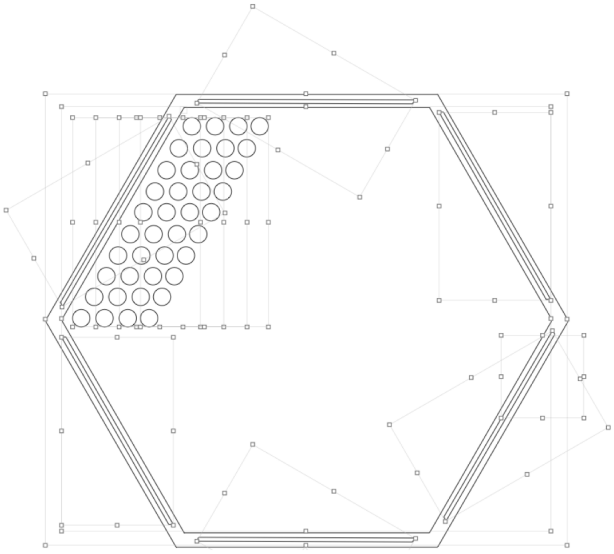

Figure 6.2: Engineering drawing of an AILEM-HD fuel assembly

Two major problems halted the development of the AILEM-HD idea:

1. The thickening of the duct wall caused a considerable (surprisingly large) negative impact on core neutron economy

2. Concerns that the swelling and creep of the duct walls would change the system characteristics (such as actuation speed and reactivity worth) as high levels of fast fluence are reached.

Both of these arguments were serious enough to completely halt the AILEM-HD project. The far superior AILEM-P (and later AILEM-C) system solved these problems and replaced AILEM-IA & HD.

6.1.1.2 The AILEM-P system

In the AILEM-P (p=pin) system, a reservoir of ^{6}Li is installed in the fuel assembly above the upper gas plenum. The reservoir is large enough to provide liquid volume-expansion for a full insertion of ^{6}Li in to the core over a predetermined temperature range (100-200°C). This reservoir is connected to 3 of the pins at the top of the upper gas plenum. These pins are of the same outer dimensions as the other fuel pins in the assembly, but in the active core region the fuel is replaced by argon gas. During standard full power operation, the argon gas in the core suspends liquid ^{6}Li to a position of low reactivity worth above the active core. When temperatures increase in the core, this is communicated to the coolant, which flows upward and heats the ^{6}Li reservoir. The ^{6}Li in the reservoir will thermally expand, and since it is enclosed by a steel container, the expansion will be directed down through the AILEM-P tubes in to the core region, compressing the argon gas. The volume of the reservoir needed for the system is given by:

$$V_{\text{reservoir}} = \frac{V_{\text{l6c}} - V_{\text{l6p}} \times (\alpha_{\Delta T} - 1)}{\alpha_{\Delta T} - 1} \tag{6.1}$$

where,
V_{l6c} is the volume of ^{6}Li needed in the core,
V_{l6p} is the volume of ^{6}Li present in the piping system at normal operation,
$\alpha_{\Delta T}$ is the volumetric expansion of Li between operating and full-actuation temperature.

The values of V_{l6c} and V_{l6p} are dependent on the nominal coolant void worth and coolant density reactivity coefficient. The most aggressive implementation of a passive liquid absorber injection system is one that provides a negative reactivity state at full coolant void when fully actuated. As a rough estimate, the reactivity state of a fully voided large fast reactor core is negative if ∼0.5-0.7% of the core volume is filled with ^{6}Li. The margin between coolant outlet temperature and voiding in a standard SFR is ∼350°C. To allow for a significant time-lag in the actuation of the control system, a full-actuation temperature (ΔT) of 150°C can be set. The volumetric change of lithium going from 500 to 650°C is 2.54% ($\alpha_{\Delta T} = 1.0254$) [128][129]. As a calculation example, a core with a volume of 10 m^3 requiring a 0.5% volume-injection of ^{6}Li for a negative voided state is used. In this example, the fission gas plenum is of the same height as the fuel length, giving $V_{\text{l6p}} \approx V_{\text{l6c}}$.

Approximate values for this core example are as follows:
$V_{\text{l6c}} = 0.05$ m^3
$V_{\text{l6p}} = 0.05$ m^3
$\alpha_{\Delta T} = 150$°C
$V_{\text{reservoir}} = 1.94$ m^3

The length of the reservoir addition on top of the fuel assembly (H_{AILEM}) can be calcu-

lated by the following equation:

$$H_{\text{AILEM}} = \frac{2 \times V_{reservoir}}{R_{\text{eff}} \times 3\sqrt{3}S_{\text{id}}^2 \times \text{Assemblies}} \tag{6.2}$$

where,
S_{id} is the inner side-length of the fuel assembly hexagon,
Assemblies is the total number of fuel assemblies in the core,
R_{eff} is a reservoir *efficiency factor*, describing the cross-sectional area-fraction of reservoir in the assembly.

S_{id} is ∼10 cm for a typical fast reactor fuel assembly, giving ∼262 assemblies in a core with height/diameter-ratio of 0.5 and a volume of 10 m^3. Active coolant typically makes up ∼30-40% of the volume of a fast reactor fuel assembly. If the coolant volume fraction is maintained through the reservoir region, the value of R_{eff} is ≈0.6-0.7. The resulting height addition to the assembly is 40 cm (R_{eff}=0.7) to 50 cm (R_{eff}=0.6). The total assembly length of a core of this size is approximately 4-5 meters, giving a relative height addition by the AILEM-reservoir of ∼10%. Based on this, the total increase in pressure drop through the assembly by the installation of the AILEM-P system is estimated to be around 5-10%, but depends on the specifics of the internal reservoir design. The massive improvement in core reactivity feedback and safety margins by installation of this system justifies this minor negative impact (a slight increase in pumping power), but uncertainties about the gas/liquid interface remains. The stability of the interface is achieved by ensuring a balance between surface tension of the liquid and the buoyancy force of the trapped gas. The following analysis is based on the methodology outlined in *Kambe et. al (1998)* [120]. Inside a cylinder such as a fuel pin or thin tube, the gas/liquid interface will form a half-sphere geometry. The buoyancy force in such a system is given by:

$$B = n\frac{\pi D^3 \rho(T) G}{12} \quad \text{[N]} \tag{6.3}$$

where,
n is the ground acceleration multiplier (n=1 for standard gravity),
G is the gravitational acceleration constant,
D is the interfacial diameter (unit of meters),
ρ(T) is the density of lithium (kg/m^3)

The surface tension is given by:

$$S = \pi D \sigma \quad \text{[N]} \tag{6.4}$$

where, σ is the surface tension per unit length (N/m).

If the buoyancy force exceeds the surface tension, the gas/liquid interface will brake. The

maximum allowable diameter is given by:

$$D = \sqrt{\frac{12\sigma}{n\rho(T)G}} \quad [m] \tag{6.5}$$

During the Iwate-Miyagi Nairiku earthquake in Japan in 2008, a peak ground acceleration (PGA) of 4.36g (n=5.36) was recorded, which is the highest value ever recorded [130][2]. Since this was far from the largest magnitude earthquake ever recorded (at 7.2 on the Richter scale), it is conceivable that a very shallow larger earthquake could cause even larger ground acceleration. The diameters required for different stability criteria (including the estimated *safety limit* of D<10.30 mm) are summarized in Fig. 6.3.

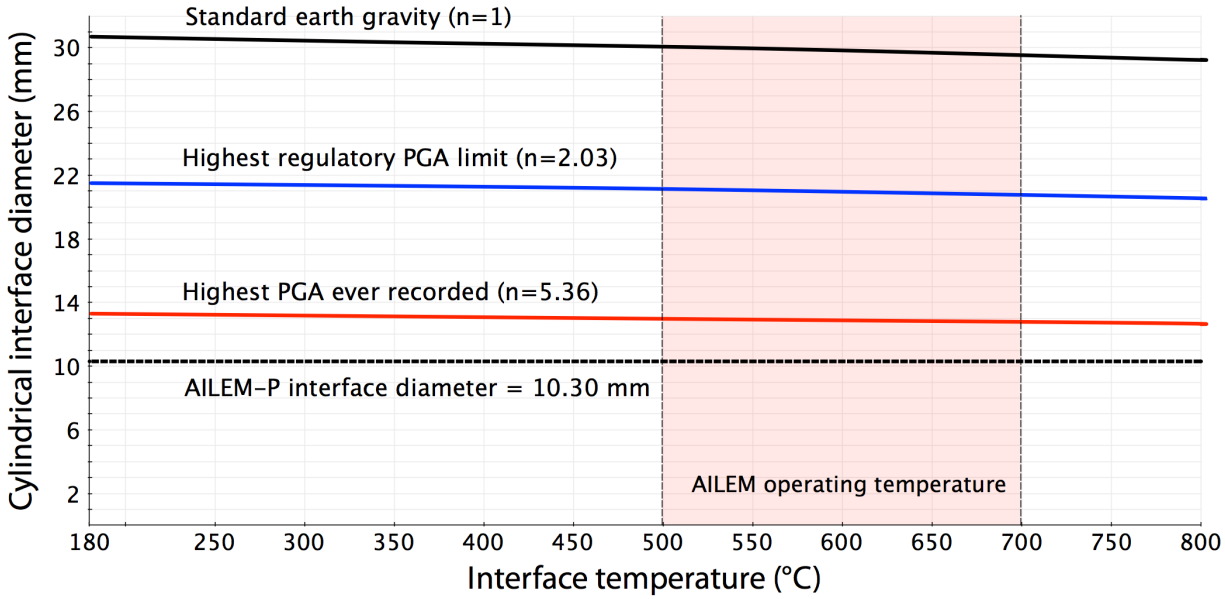

Figure 6.3: Stability limit of a lithium-argon gas/liquid interface

Experiments conducted in Japan have confirmed stability for up to 12 mm diameter of cylindrical lithium/argon-interface [132]. However, the experiments only allowed for a few mm of axial travel of the interface. While the system is stable in theory, it needs to be validated with further experimental data. Especially to ensure the stability of the interface during its movement up and down the cylinder, and to establish if there are maximum allowable travel velocities for reliable operation. A small experimental station for proof-of-concept and the establishment of operational characteristics was proposed during the AILEM-P development work, but was never constructed. A sketch of this experimental setup can be seen in Fig. 6.4.

[2]The massive Tohoku Earthquake in march of 2011 had a recorded PGA of 2.99 (n=3.99) [131]

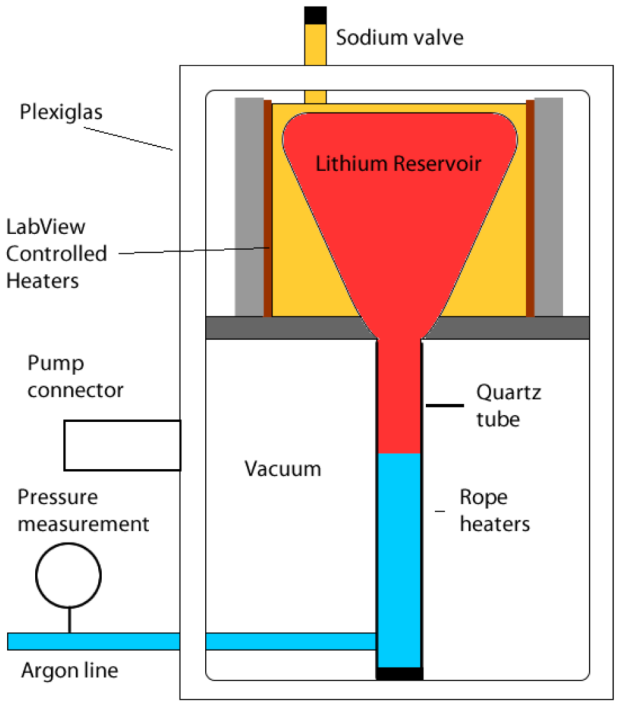

Figure 6.4: Proposed non-nuclear experimental setup to test the AILEM-P system

To fully ensure that there is no uncertainty in the stability of the gas/liquid interface, another concept called the AILEM-C was conceived using a large number of very thin diameter pipes.

6.1.1.3 The AILEM-C system

As described in the previous section, a LEM or AILEM-system consists of a liquid (^{6}Li) floating atop a pocket of gas. As temperatures go up, the liquid expands and compresses the gas. The main concern with the actuation of the LEM-system is the stability of the gas/liquid interface that is maintained by the surface tension. Analysis in the preceding section showed that great stability can be achieved (at least statically) for cylindrical tubes at diameters as large as 1 centimeter. However, since a break of the gas/liquid interface causes a positive reactivity insertion in an actuated system, extreme care should be taken and large margins should be applied. The AILEM-C (C=Capillary) is a modified version of the AILEM-P system that utilizes a large number of very small diameter tubes inside a specialized compartment at one of the corners of the fuel assembly. This necessitates the removal of 1-2 more fuel pins per assembly for the same reactivity worth. However, it also makes it possible to install a high-reactivity delivery system that removes the concerns about the stability of the gas/liquid-interface. The equations presented in Section 6.1.1.2 are directly applicable to the AILEM-C concept as well. However, the capillary-tube idea

involves a considerable amount of extra engineering. A top-view of an AILEM-C cartridge installed in a corner of a fuel assembly is given in Fig. 6.5.

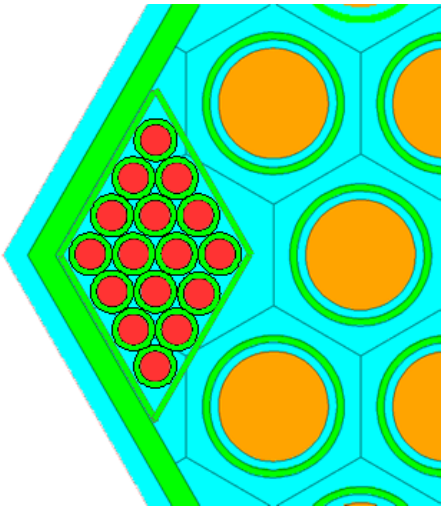

Figure 6.5: Top view of an AILEMC cartridge (red = ^{6}Li, yellow = fuel, green = cladding/duct, blue = coolant/bond)

Going back to the performance criteria of Table 5.2, the AILEM-C design eliminates the conditional violations of A9 and C1, adding redundancy, flexibility and stability to the system. The risk of a positive reactivity insertion during failure (A2) is arguably eliminated if there is no risk of failure, so this has been moved to the category of conditional violations. The criteria-adherence of the AILEM-C system is summarized in Table 6.1.

Table 6.1: Safety systems/designs violations of evaluation critera

Method	**Direct violation**	**Conditional violation**
AILEM-C	-	A2, A6, A7

While the AILEM-C represents an improvement over other comparable systems, some serious issues remain. In the design of the TWR thermostating module, steps were taken to minimize the amount of ^{6}Li in the system for a number of reasons. Since the actuation of a LEM-type system is driven completely by the ^{6}Li itself, a large reservoir volume exposed to a continuous finite neutron flux is needed. This lead to a significant production of tritium and helium gas, potentially having an impact on the long-term performance of the system. The remaining issues with the AILEM-C system prompted the creation of the entirely new ARC-systems, presented in Section 6.2.

6.1.2 AILEM systems summary

The AILEM systems were developed based on the innovative ideas of Japanese researchers *Mitsure Kambe and colleagues* and the Lithium Expansion Systems= (LEM). The envisioned system designs and their operational states are shown in Fig. 6.6. The figure shows the systems actuated (left assembly) and at standard operation (right assembly).

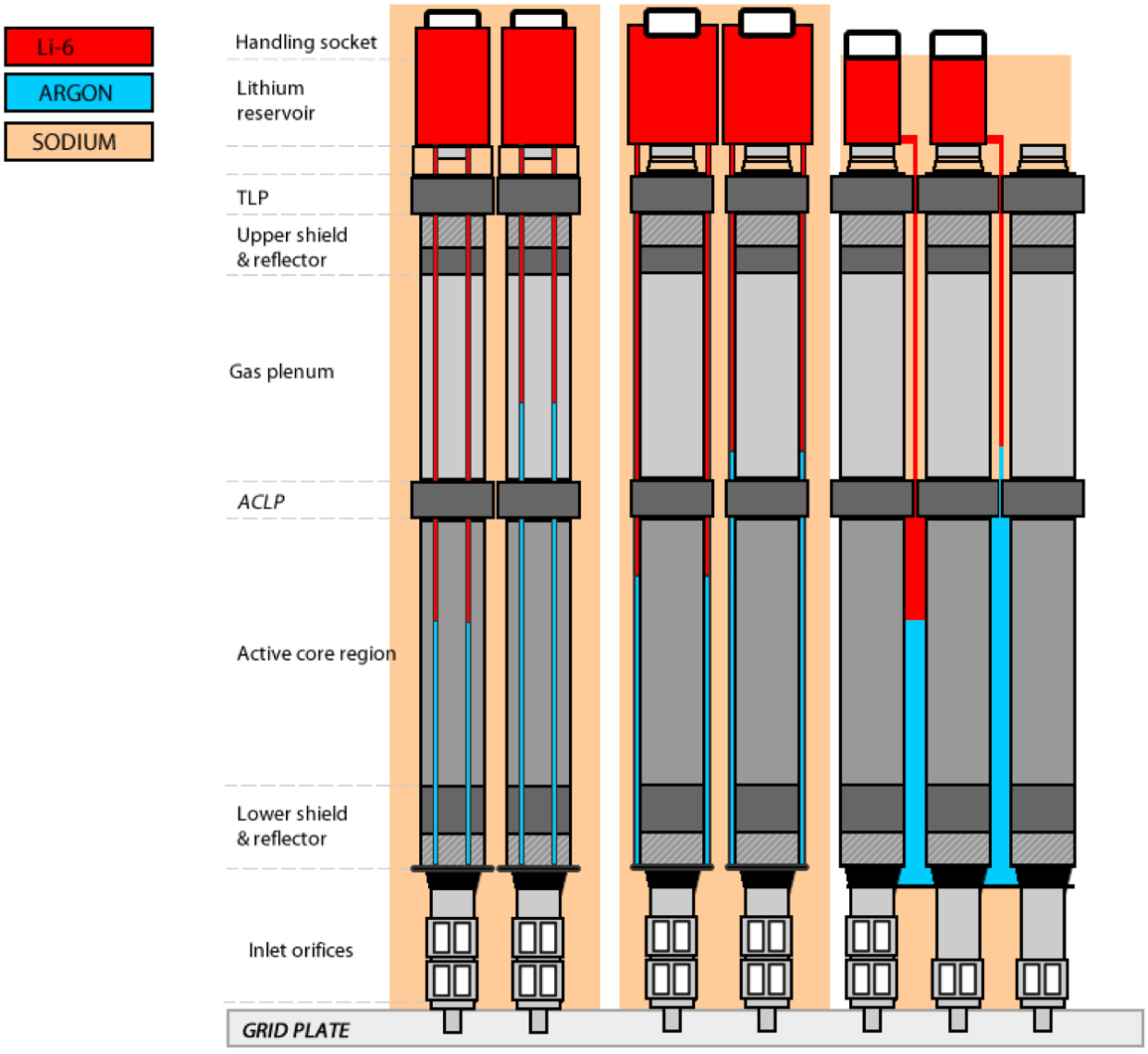

Figure 6.6: Left: AILEM-P & AILEM-C, Center: AILEM-HD, Right: AILEM-IA

The AILEM-system eventually evolved in to the new ARC-systems, detailed in the following section.

6.2 The ARC-LL (Liquid/Liquid) system

6.2.1 Design and operation

The ARC-LL system is based on the idea of having a separate liquid push neutron-absorbing ^{6}Li in to the core in the event of an accident, rather than having ^{6}Li expand itself in to the core as in the LEM and AILEM systems. The injection should be through one or more emptied out fuel rods, which requires a minimal change to a conventional fuel assembly design. If this can be achieved, the system would have numerous vital advantages over LEM and AILEM systems:

- No reliance on a gas/liquid interface
- Minimized inventory of ^{6}Li
- Faster, more reliable and more efficient actuation
- Increased system stability
- Reduced costs

The idea is based on having an upper liquid reservoir at the top of the fuel assembly filled with a neutronically transparent liquid that is immiscible with lithium. As temperatures rise from some reference operating state, a small pipe inside a larger pipe communicates the volumetric expansion of the upper liquid (henceforth: the *expansion liquid*) to a compartment below the core. The lower compartment contains a dual-layer of liquids, with ^{6}Li floating on top of the expansion liquid. Axially above the dual-layered liquids (in the axial region of the active core) is an inert gas such as argon. As the liquid in the reservoir expands, the upper axial level of the ^{6}Li rises (while compressing the gas) and enters in to the volume between the inner and outer pipe and is injected in to the axial region of the active core from below. When temperatures drop again, the system will re-equilibriate (in a similar manner to a LEM or AILEM system) to its initial state. In such a way, the system avoids the use of a gas/liquid interface and only needs a small amount of ^{6}Li. The system and its components, as installed in a conventional fast reactor fuel assembly, is shown in Fig. 6.7. Details of the upper ARC-reservoir compartment is shown in Fig. 6.8. The lower compartment is shown in Fig. 6.9. The area ratio between the inner and outer ARC-tubes determine both the reactivity worth and the relative speed of actuation of the ARC-pin. This makes it possible to design a sequential system with fast acting low-worth pins and slower acting high-worth pins. A top-view of the ARC-LL fuel assembly design of such a system is given in Fig. 6.10.

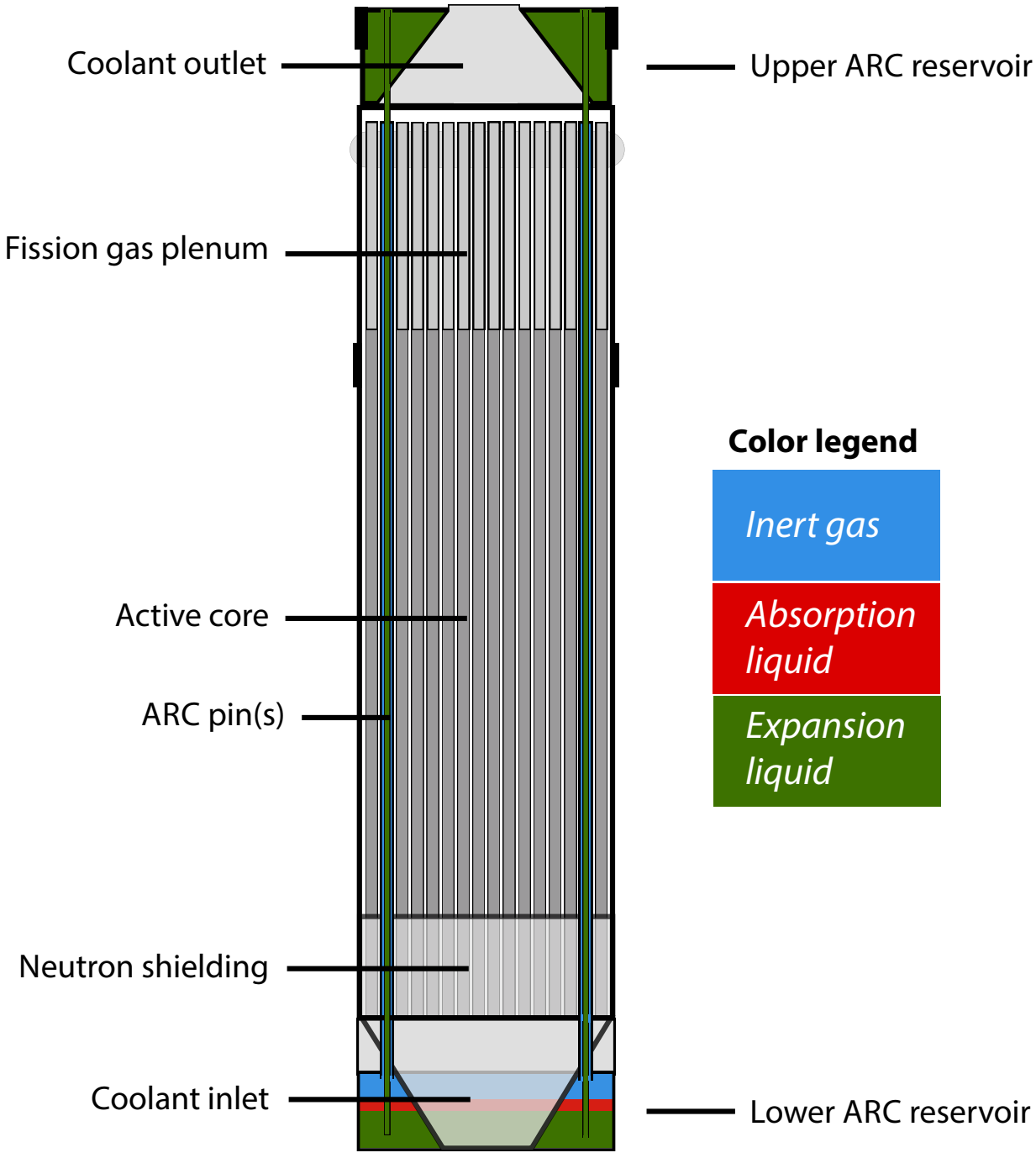

Figure 6.7: The ARC-LL fuel assembly system design

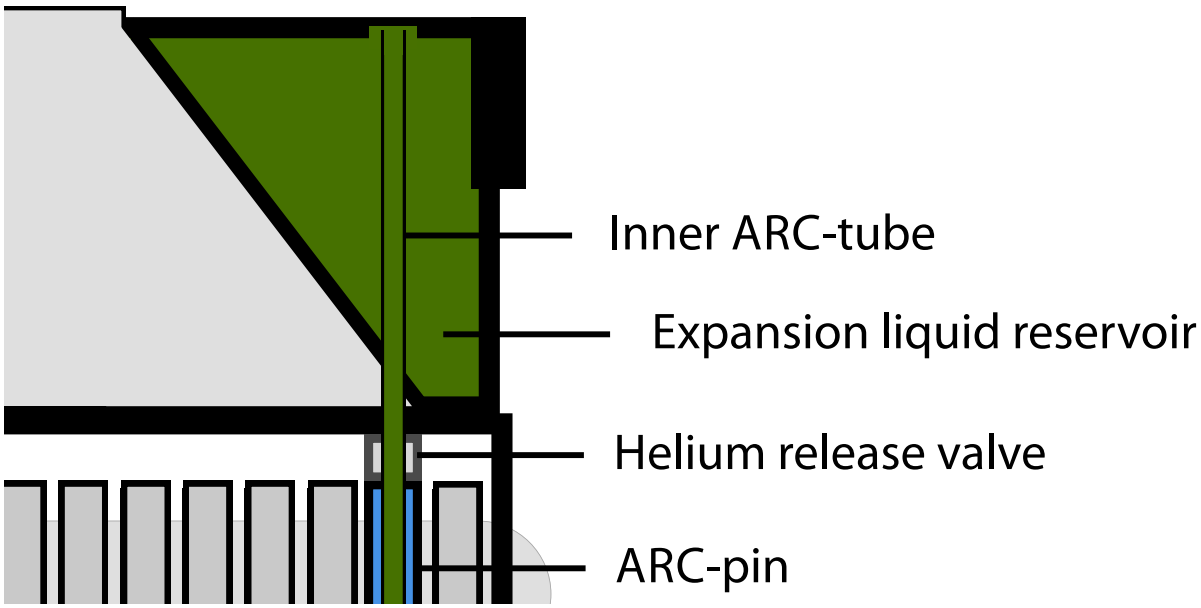

Figure 6.8: The ARC-LL upper reservoir system design

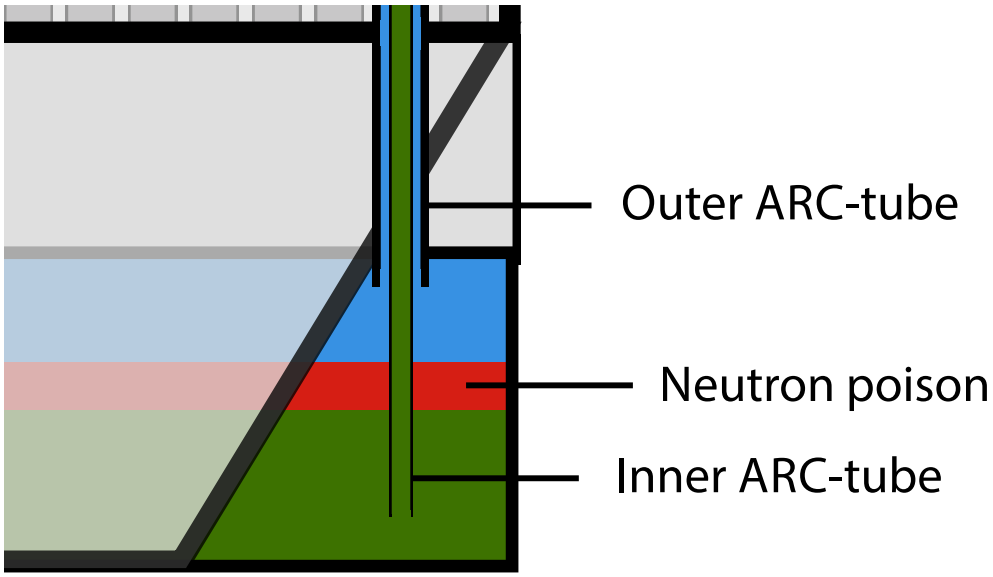

Figure 6.9: The ARC-LL lower reservoir system design

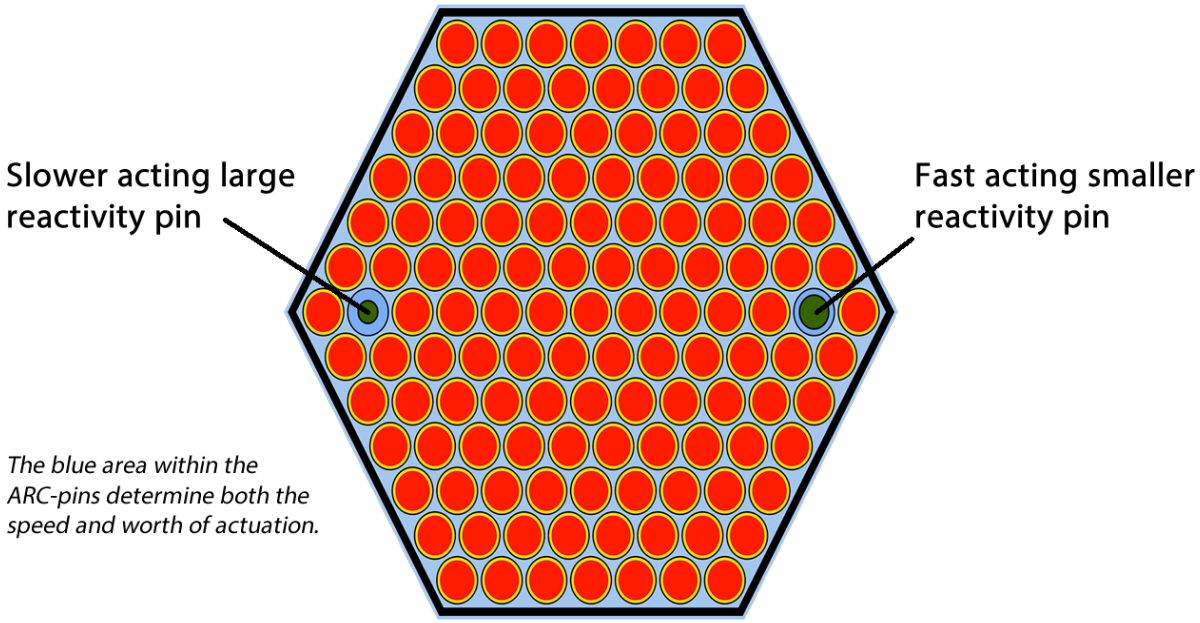

Figure 6.10: Top view of the ARC-LL fuel assembly system design (red = fuel, green = expansion liquid, yellow = bond, light blue = coolant, dark blue (within ARC-pin) = inert gas, black = structure)

6.2.2 Identifying a suitable expansion liquid

At the time the idea of the ARC-LL system was conceived, it was not known if a material fulfilling the requirements of the *expansion liquid* existed. An extensive search was undertaken, with a detailed analysis of over 40 elements, compounds and alloys. The requirements for the expansion liquid are summarized in Table 6.2. These requirements are ordered in two categories by importance, with A denoting strict requirements and B offering criteria to select between material options that adhere to the requirements of A1-A7.

Table 6.2: ARC-LL expansion liquid criteria

A1	Liquid range of at least 200°C $\leq$ T $\leq$ 650 °C
A2	Very low solubility or (preferably) completely immiscible with lithium
A3	Non-corrosive
A4	Low neutron absorption cross-section
A5	Not prohibitively expensive
A6	Chemically stable under irradiation
A7	Chemically compatible with liquid metal coolants
B1	Large thermal expansion coefficient
B2	Limited volume change upon phase change
B3	High boiling point ($T_{\text{boil}} \geq 700$ °C)

A material meeting the requirements of Table 6.2 is not trivial to find. The search yielded a total of 4 alternatives that could possibly work as the expansion liquid. The relevant data to assess the viability of the different options are summarized in Table 6.3. A 50°C margin to phase-change (boiling) was imposed on the temperature ranges for calculating volumetric expansion. Production, reserve and cost data in Table 6.3 are from reports published in 2010.

Table 6.3: Properties of ARC-LL expansion liquid alternatives

Material	Cesium	Indium	Potassium	Rubidium
T_{melt}	28°C	157°C	63°C	39°C
T_{boil}	671°C	2072°C	759°C	688°C
Corrosivity	Acceptable [133]	Low [134]	Very low [135]	Low [136]
Li solubility	None [137]	1 at% [138]	<4 wt. ppm [139]	None [140]
Neutron abs. xs [57]	High	Very high	Very low	Low
Price/kg	47800$ [141]	571$ [142]	∼20$ [143]	52300$ [144]
Production / year (MT)	n/a	640 [145]	>30000 [143]	n/a
World reserves (MT)	>7000 [146]	6000 [147]	$> 8 \times 10^9$ [143]	n/a
Exp. temp-range	500-620°C	500-700°C	500-700°C	500-630°C
% vol. exp. in range	4.5 [148]	2.30 [149]	6.9 [150]	4.9 [151]

All the 4 elements have liquid lithium solubility low enough to ensure stable stratification. Based on the low boiling temperature and general material unavailability, Cesium and Rubidium were not chosen for detailed study. Indium is available commercially in large quantities and has the most favorable temperature range of possible single-phase operation. The much higher relative volumetric expansion coefficient of potassium, lower cost and most significantly; lower neutron absorption cross-section (by 3 orders of magnitude!), make it a far superior option. In summary, **potassium** is the current choice for the expansion liquid for ARC-LL system. The criteria-adherence for the candidate materials are given in Table 6.4.

Table 6.4: Candidate material ARC-LL criteria evaluation

Material	Cesium	Indium	Potassium	Rubidium
A1	Pass	Pass	Pass	Pass
A2	Pass	(Barely) Pass	Pass	Pass
A3	(Barely) Pass	Pass	Pass	Pass
A4	Fail	Fail	Pass	(Barely) Pass
A5	Fail	Pass	Pass	Fail
A6	Pass	Pass	Pass	Pass
A7	Pass	Pass	Pass	Pass
B1	Pass	Fail	Pass	Pass
B2	Pass	Pass	Pass	Pass
B3	Fail	Pass	(Barely) Pass	Fail
Sum fails	3	2	**0**	2

Note. There may very well be alloys between the elements of Table 6.3, or between elements of Table 6.3 and other elements, that form superior performing materials. This is a topic of further investigation.

6.2.3 Determining the system response

There are essentially three rational design approaches for the neutronic response and worth of an ARC-system that fundamentally impacts its design characteristics. The reactivity response strategies for an ARC-system can be summarized as:

1. A system response-speed and worth that ensures that temperatures stay below safety margins during severe unprotected accident scenarios such as ULOF, ULOHS and UTOP.

2. A system worth that matches the positive single-phase coolant temperature reactivity feedback

3. A system worth that gives a negative core reactivity state at full coolant voiding

The requirements for total size and worth of the ARC-systems increases dramatically going from strategy 1 to 3. Valid arguments can be made for the adopting either of these strategies.

Arguments for strategy 1.

Analyzing and finding the ARC-design corresponding to strategy-1 is preferable, as it gives the minimal possible intrusion to the standard fuel assembly design and is therefore optimal for both neutron and financial economy. A reliable and licensable assessment of a system corresponding to strategy 1 is however very complicated and requires the use of a transient systems code such as SASSYS/SAS4A [85] or SSC-K [77].

Arguments for strategy 2.
Strategy-2 is a simpler but less precise method, simply matching in both time and worth the only[3] positive reactivity feedback in the core to make sure that power and temperatures are always kept within safe bounds. Formally, such an assessment cannot be made confidently without in fact running a transient code, which arguably mutes the arguments for adopting strategy-2. If reactor designs are of a conceptual or scoping nature, or if access to transient codes is not available, strategy-2 represents the best option. In general (again, this is not formally a certainty), designs that follow strategy-2 will achieve the goals of strategy-1 with some margin.

Arguments for strategy 3.
For pool-type reactors, the third strategy only applies to sodium-cooled reactors. Total coolant voiding by boiling in lead and LBE-cooled cores occurs at temperatures far higher than the melting point of the structural material in the core. A sodium cooled core with an average coolant temperature of 450°C looses about 12% of its density as a single-phase liquid going to the boiling temperature. The remaining ∼88% is lost in the phase-transition. Correspondingly, there is a large discontinuity in the temperature reactivity feedback of the coolant when boiling occurs. During voiding by boiling, ∼9x as much reactivity is added as during the ∼400°C rise of the single-phase coolant temperature needed to reach boiling. This is the reason for the strong focus of sodium fast reactor research to avoid voiding events. Strategy-3 aims to take this one step further than usual, and the ARC-system has unique advantages making this possible. If the full actuation-worth of the ARC-system matches that of the positive reactivity insertion of complete coolant voiding and reaches this state at a time and temperature before boiling occurs, such a system could provide a type of "ultimate" safety. In any real anticipated situation, such a system would completely shut off the fission process in the core long before there is a chance to reach the state which it is meant to save the core from. A strategy-3 type ARC design can potentially tackle a situation that can be referred to as an *"unknown unknown"*[4]. Even if there is no known way for the core to reach a specific state (complete coolant voiding), or even a known unknown/uncertainty that may lead to such a state, there may still be an unknown unknown/uncertainty that leads to a sequence of events that does. In SFR safety analysis, it may not be necessary

[3]Reactivity effects such as cladding radial thermal expansion and the radial expansion of fuel at low burnup are positive, but so small that they are of no importance to reactor safety.

[4]While this phrase is commonly used in risk and reliability analysis, it is most famous for being part of a 2002 speech made by US Secretary of Defense Donald Rumsfeld when addressing the absence of evidence linking the government of Iraq with the supply of weapons of mass destruction to terrorist groups.

to go that far, as there are known but improbable scenarios that could lead to partial or complete coolant voiding even in cores with nominally very strong negative feedback. For instance, a simultaneous and instantaneous complete failure of primary coolant pumps, failure of primary and secondary SCRAM systems combined with a control-rod withdrawal of any rods in the core would produce a very serious accident progression in any reactor design. Such events however have a probability and thus frequency far below what is required for analysis by any regulator. If a passively operating safety system can add enough negative reactivity *quickly enough* to give a negative reactivity state at full core voiding, *even these events* are of little concern for safety. The ARC-systems are uniquely equipped to be able to provide such a response primarily due to three reasons:

- The potential worth of the system is large enough to match complete coolant voiding without excessively damaging the standard operation neutron economy
- The distributed nature of the system (one in each assembly) means it will react locally where sodium boiling is *initiated*. This localized actuation will hinder the spread of boiling across the core and limit the accident scenario.
- The system can be designed with variable actuation speeds. A system of 3 ARC-pins per assembly can have a very fast acting / low-worth pin, a medium-worth / medium-speed pin and a large-worth / slow-speed pin. Such a multi-tier system is much more effective in shutting down transients than a single-speed system. This is a unique feature of the ARC system that is not possible in any other known passive safety system. The speed and worth is simply set by adjusting the diameter of the inner tube of the ARC-pins.

6.2.4 Performance assessment

In order to test the performance of the conceptual ARC-designs, an extensive calculation module was implemented in the ADOPT code (see Chapter 7). The module calculates the geometry of the upper and lower reservoirs and the diameter of the inner ARC-tubes. The output is in the form of Serpent code input files at specific core states corresponding to increases in the average core coolant outlet temperature. Four modes of simulation are possible:

1. ARC-system only
2. ARC-system and coolant density reactivity effect
3. ARC-system assuming a complete coolant void
4. ARC-systems and coolant density reactivity effects + voiding effects

Because of the rather small impact of single-phase coolant density reactivity compared to that of the ARC-system, mode-2 simulations look similar to mode-1. Mode-4 is the most powerful analysis tool and was developed in order to analyze the entire reactivity progression in a realistic way. A sodium-cooled, metallic-fueled core model with a diameter of 4 meters and a active core height of 2 meters was used to evalutate the ARC-system performance. The core uses a uniform fuel composition and has a nominal void worth (+10$). In this simulation, the actual core response of both ARC-systems and coolant density is modeled, including coolant boiling at the boiling temperature. 4 ARC-pins are installed in the 271 pin assembly (267 fuel pins). The resulting core reactivity state, given in the unit of $, is shown in Fig. 6.11.

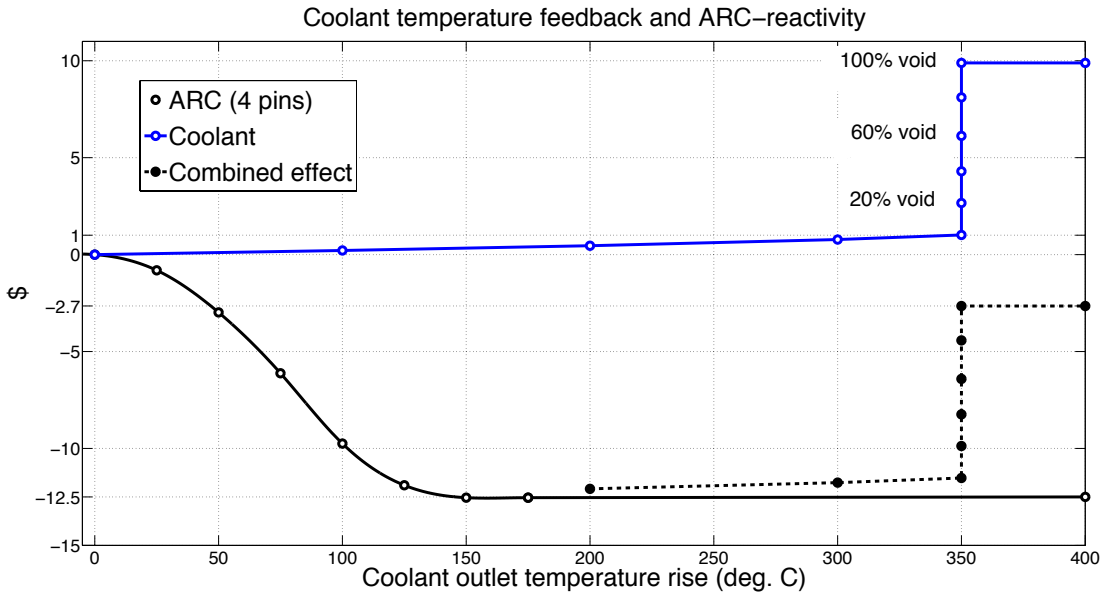

Figure 6.11: ARC-LL mode 4 multiplication response curve (total pins per assembly: 271)

The nominal reactivity loss by installing the 4-pin system in the core is about 800 pcm (or 2.2$). The gain in safety performance by this minor negative impact on the neutron economy is larger than could be argued necessary. The core state at complete coolant void is negative once the ARC-reservoir has been heated up 100°C, or two-thirds of its complete actuation. This gives a temperature margin of over 300°C before any general (not confined locally) coolant boiling could occur. An ARC-system of 4-pins operates on 4 different time scales (see 6.10 for a visualization of a 2-pin system). The theory is that the negative reactivity added by the fast reaction low worth pins will delay the coolant temperature rise so that the slower operating high-worth pins can fully actuate before boiling temperatures are reached. This remains to be proven in a detailed transient thermal-hydraulic/neutronic analysis code.

6.2.5 Failure mode analysis

The analysis of failures modes of any passive safety system is paramount to assessing its performance. The LEM and GEM systems (see Section 5.5.2 and 5.2.4) are simple, passive and ingenious passive safety solutions. However, their most important disadvantage is the potential for failure modes that lead to a more severe accident condition. Systems with such a potential are likely to be difficult to license. To represent a significant improvement over the existing solutions, the requirements for ARC-system are threefold:

1. No credible failure modes
2. If the system fails, no rapid introduction of positive reactivity
3. The total system still fulfills its purpose even with several subsystems in a failed state

The ARC-system operates at low pressures and relies only on physical phenomena that do not have a probability of failure. Three physical phenomena underlie the single-phase operation of the system: Thermal expansion, miscibility and gravity/pressure. The fill pressure of the argon-gas in the ARC-tube at standard operation must match the weight of the potassium that flows up and down the inner tube as the reservoir liquid expands in order to re-equilibriate after an actuation. This mass is on the order of $\sim$100 grams, and the resulting pressures inside the tube is therefore significantly lower than that exerted on the outer tube by the coolant. It is conceivable that such a pressure differential could lead to buckling and failure/leakage of the ARC-tubes. This situation is easily avoided by installing internal support structures at a number of axial locations inside the ARC-tube. The operation of the ARC-system would not be noticeably affected by the installation of axial supports.[5] Proper axial support design and sufficiently thick ARC-tubes can eliminate any *credibility* of the only failure mode that has been postulated for the system. If some currently unknown event could force the rupture of the outer ARC-tube, the initial reactivity response will likely be either *none* or *negative*. The theoretically possible failure-modes are here analyzed one by one in the following sections. To follow the discussion in these sections, it is recommended to have Figures 6.7-6.10 at hand or in fresh memory.

6.2.5.1 Outer ARC-tube break in the gas-region

The most probable of the failure-modes for the ARC-system is a break or a leak in the low-pressure gas region of the outer ARC-tube at an axial level above the liquid absorber. At this point, the pressure differential across the tube is at its largest. If the tube breaks in the gas region above the liquid poison, no rapid reactivity events (either positive or negative) are expected. Since the system is liquid-filled from the axial level of the liquid poison and downward, there is no possibility of any positive reactivity insertion from this failure event.

[5] In contrast, the gas/liquid interface of a LEM or AILEM system would likely brake as the interface traverses the supports.

If the tube is filled with coolant above the poison, the system cannot actuate and introduce negative reactivity to the core. Thus, this accident scenario deactivates the function of the ARC-tube, but it does not introduce any positive reactivity.

6.2.5.2 Outer ARC-tube break in the liquid region

For uniformity and simplicity, the outer ARC-tube in the reference design is of the same thickness as the fuel rod cladding (regardless of the specifics of the assembly and rod design). The stresses induced in the fuel rod cladding by fuel/cladding mechanical interactions and fission gases is an environment many orders of magnitude harsher than what is experienced by the outer ARC-tube. Consequently, the same relation holds for the probabilities of failure. If the outer ARC-tube were to fail in the lower axial region of the tube that is filled with liquid, the coolant liquid will push in to the tube as it at higher pressure and there is a free-gas volume available inside the pin. Regardless of where the leak/break is axially, the coolant will bring the liquid absorber up through the core. This will introduce negative reactivity to the core for a short while until the tube is filled with liquid and the actuation of the system is stopped. If the leak occurs in a fully actuated system, no reactivity effect at all is expected. Since the pressure of the coolant is higher than the pressure inside the tube, only a slow leaching-type outward leakage can occur. If the liquid absorber is slowly leached in to the coolant loop, it is diluted in the entire loop rather than being confined in the core, and thus its total negative reactivity impact is reduced. This effect is too small and too slow to have any noticeable effect on an accident scenario.

6.2.5.3 Inner ARC-tube break

While a break of the outer ARC-tube is an exceedingly improbable but definitely possible event, a break of a properly manufactured inner ARC-tube requires a truly exceptional event to occur. However, manufacturing errors such as faulty welding needs to be taken in to account. The inner ARC-tube is completely separated from the reactor environment, and is thus simply a metal tube filled with a non-corrosive liquid at low pressure. The inner ARC-tube is welded in place at two axial locations in the assembly - one at the top of the rod and one connecting it to the upper reservoir. In the reference ARC-design, all structural materials (including ARC-tubes and reservoirs) of the assembly are made of the same type of steel. This minimizes the risks of differential thermal expansion that induces stress that may break components. However, the axial temperature distribution of the core will induce thermal stresses in the assembly even during standard operation. Improper welds and thermal stress may lead to cracks in the inner tube. A crack at the weld location connecting the inner ARC-tube to the upper ARC-reservoir would cause a gravitational flooding of the inner tube and fully actuate the system, introducing the full negative reactivity worth of the tube in to the core. A break in the weld connecting the inner ARC-tube and the outer ARC-tube at the top of the rod would likely deactivate the tube from further actuation. Bubbles of the gas between the inner and outer tube may however enter the upper reservoir and in this way

actuate the system and introduce negative reactivity. This event cannot introduce positive reactivity.

6.2.5.4 Upper ARC-reservoir break

A break in the upper ARC-reservoir at anywhere but the top surface would cause a coolant intrusion in to the reservoir. This coolant intrusion pushes the reservoir liquid down the inner tube and actuates the system, introducing negative reactivity. If the top "lid" of the upper ARC reservoir breaks, the expansion liquid could escape the reservoir from the top and thus de-actuate the system. This is the *only* scenario where the potential for a positive reactivity insertion has been identified. The top lid size of the upper ARC-reservoir has no impact on the core performance or design, and could thus be made "arbitrarily" thick, to completely avoid even the discussion of such a failure scenario.

6.2.5.5 Lower ARC-reservoir break

A break in the lower ARC-reservoir would cause a coolant intrusion in to the reservoir. If the break occurs below the axial level of the absorber liquid, it will push the absorber upwards in to the core and introduce negative reactivity. If the break occurs when the system is not actuated and the location of the break is above the absorber liquid level, coolant will fill the ARC-system and hinder the actuation. There is no event where positive reactivity is added.

6.2.6 Summary

In conclusion, no credible failure mode of any ARC-component that introduces positive reactivity to the core has been identified. The individual failure probabilities of ARC-tubes and reservoirs are small, but the systems are extremely redundant. A large fast breeder core has ∼400-500 ARC-systems with ∼1200-2200 ARC-tubes, all operating independently.

6.2.7 Theoretical operation characteristics

6.2.7.1 Worth of a single ARC-system actuation

The time-independent neutron diffusion equation for the flux distribution and eigenvalue in a fissionable system can be written as:

$$\vec{\nabla} \cdot D\vec{\nabla}\phi + \frac{1}{k}\nu\Sigma_f\phi - \Sigma_a\phi = 0 \tag{6.6}$$

Adding an absorber such as the ^{6}Li of the ARC-system introduces an additional absorption term $\delta\Sigma_a$, changing eq. 6.6 to:

$$\vec{\nabla} \cdot D\vec{\nabla}\phi' + \frac{1}{k'}\nu\Sigma_f\phi' - (\Sigma_a + \delta\Sigma_a)\,\phi' = 0 \tag{6.7}$$

The primed quantities k' and ϕ' refer to the multiplication factor and and flux as perturbed by the addition of the ARC-absorber. Multiplying eq. 6.7 by the original (unperturbed) flux level ϕ and integrating over the entire core volume V yields:

$$D \int \phi \vec{\nabla}^2 \cdot D \vec{\nabla} \phi' \mathrm{dV} + \frac{1}{k'} \int \phi \nu \Sigma_f \phi' \mathrm{dV} - \int \phi \left(\Sigma_a + \delta \Sigma_a \right) \phi' \mathrm{dV} = 0 \tag{6.8}$$

Multiplying the original (unperturbed) diffusion equation (eq. 6.6) by the perturbed flux ϕ' and integrating over the core volume V similarly yields:

$$D \int \phi' \vec{\nabla}^2 \cdot D \vec{\nabla} \phi \mathrm{dV} + \frac{1}{k'} \int \phi' \nu \Sigma_f \phi \mathrm{dV} - \int \phi' \left(\Sigma_a + \delta \Sigma_a \right) \phi \mathrm{dV} = 0 \tag{6.9}$$

The difference between the eq. 6.7 and eq. 6.9 then becomes:

$$D \int \left(\phi \vec{\nabla}^2 \phi' - \phi' \nabla^2 \phi \right) \mathrm{dV} + \left(\frac{1}{k'} - \frac{1}{k} \right) \int \phi' \nu \Sigma_f \phi \mathrm{dV} - \int \phi \left(\delta \Sigma_a \right) \phi' \mathrm{dV} = 0 \tag{6.10}$$

With this the nominal absorption term Σ_a has been eliminated, leaving the change in absorption from the actuation of the ARC-system ($\delta \Sigma_a$). The first integral on the left side of eq. 6.10 can be eliminated through the use of the vector calculus divergence theorem. Noting the following mathematical relations:

$$\vec{\nabla} \left(\phi \vec{\nabla} \phi' \right) = \phi \nabla^2 \phi' + \left(\vec{\nabla} \phi \right) \cdot \left(\vec{\nabla} \phi' \right) \tag{6.11}$$

$$\vec{\nabla} \left(\phi' \vec{\nabla} \phi \right) = \phi' \nabla^2 \phi + \left(\vec{\nabla} \phi' \right) \cdot \left(\vec{\nabla} \phi \right) \tag{6.12}$$

Re-writing eq. 6.11 and 6.12 in the form used in eq. 6.10 yields:

$$\phi \nabla^2 \phi' = \vec{\nabla} \left(\phi \vec{\nabla} \phi' \right) - \left(\vec{\nabla} \phi \right) \cdot \left(\vec{\nabla} \phi' \right) \tag{6.13}$$

$$\phi' \nabla^2 \phi = \vec{\nabla} \left(\phi' \vec{\nabla} \phi \right) - \left(\vec{\nabla} \phi' \right) \cdot \left(\vec{\nabla} \phi \right) \tag{6.14}$$

We can then substitute eq. 6.13 and 6.14 in to the first integral of eq. 6.10, which yields:

$$\begin{aligned} \int \left(\phi \nabla^2 \phi' - \phi' \nabla^2 \phi \right) \mathrm{dV} &= \\ \int \left[\vec{\nabla} \left(\phi \nabla \phi' \right) - \vec{\nabla} \left(\phi' \nabla \phi \right) + \left(\vec{\nabla} \phi' \right) \cdot \left(\vec{\nabla} \phi \right) - \left(\vec{\nabla} \phi \right) \cdot \left(\vec{\nabla} \phi' \right) \right] \mathrm{dV} &= \\ \int \vec{\nabla} \left[\phi \vec{\nabla} \phi' - \phi' \vec{\nabla} \phi \right] \mathrm{dV} & \end{aligned} \tag{6.15}$$

The divergence theorem states that a volume integral can be converted to a closed surface integral over the entire volume. Formally, its definition is:

$$\iiint_V \left(\nabla \cdot \mathrm{F} \right) \mathrm{dV} = \oiint_S \left(\mathrm{F} \cdot \mathrm{n} \right) \mathrm{dS} \tag{6.16}$$

Applying the eq. 6.16 theorem to eq. 6.15 yields:

$$\int \vec{\nabla} \left(\phi \vec{\nabla} \phi' - \phi' \vec{\nabla} \phi \right) \mathrm{dV} = \int \hat{n} \left(\phi \vec{\nabla} \phi' - \phi' \vec{\nabla} \phi \right) \mathrm{dA} \tag{6.17}$$

Since by definition both perturbed and unperturbed flux must vanish at the extrapolated surface A, the surface integral vanishes. The original difference-equation (eq. 6.10) then simplifies to:

$$\left(\frac{1}{k} - \frac{1}{k'} \right) \int \phi \nu \Sigma_f \phi' \mathrm{dV} = \int \phi \delta \Sigma_a \phi' \mathrm{dV} \tag{6.18}$$

The ARC-system responds to an increase in the outlet coolant temperature. Using the assumption that the core is in a critical state (k=1) when the ARC-actuation begins (certainly not true at for example TOP accidents), the reactivity following the insertion of the ARC-system (neglecting other reactivity effects) is:

$$\rho = \frac{k' - 1}{k'} \tag{6.19}$$

This assumption further simplifies eq. 6.18 to:

$$\rho = - \frac{\int \phi \delta \Sigma_a \phi' \mathrm{dV}}{\int \phi \nu \Sigma_f \phi' \mathrm{dV}} \tag{6.20}$$

Assuming that the added absorption from the ARC-actuation is uniform across the core, the one-group core-averaged cross-sections can be put outside of the integrals, simplifying eq. 6.20 further to:

$$\rho = - \frac{\delta \Sigma_a}{\nu \Sigma_f} \tag{6.21}$$

Noting also the definition of the infinite multiplication factor:

$$k_\infty = \frac{\nu \Sigma_f}{\Sigma_a} \tag{6.22}$$

Eq. 6.21 can be re-written as:

$$\rho = - \frac{1}{k_\infty} \frac{\delta \Sigma_a}{\Sigma_a} \tag{6.23}$$

The perturbed flux can be expressed as:

$$\phi' = \phi + \delta \phi \tag{6.24}$$

Inserting eq. 6.24 in to eq. 6.20 yields:

$$\rho = - \frac{\int (\delta \Sigma_a \phi^2 + \phi \delta \Sigma_a \delta \phi) \mathrm{dV}}{\int (\nu \Sigma_f \phi^2 + \phi \nu \Sigma_f \delta \phi) \mathrm{dV}} \tag{6.25}$$

If the flux pertubation is small compared to the value of total flux, the value of $\delta\phi$ can be ignored relative to ϕ. This approximation yields the first order perturbation approximation for an absorption insertion. Defining the change in absorption probability as $\delta\Sigma_a = \Sigma_{\text{ARC}}$, the resulting reactivity is:

$$\rho = -\frac{\int \Sigma_{\text{ARC}}\phi^2 \text{dV}}{\int \nu\Sigma_f\phi^2 \text{dV}} \tag{6.26}$$

6.2.7.2 Partial actuation of a single ARC-system

It is unlikely that the any single ARC-system in a well-designed core will ever be fully actuated and introduce its entire reactivity worth to the core, as the addition of negative reactivity will shut off the fission process long before the temperature needed for this to happen is reached. ARC-systems can be split up in to fast acting rods with a smaller total worth that may fully actuate in a severe accident and slower acting rods with a large reactivity worth which are not likely to every fully actuate. For simplicity, this analysis will assume a single average value for the actuation of the ARC assembly and disregard the effects of slow and fast components. The reactivity effect of a partial insertion of a single ARC-system ^{6}Li neutron poison can be expressed by transforming eq. 6.26 in to a spatially dependent equation. Since most reactors are cylindrical, the volume differential can be transformed to cylindrical coordinates as:

$$\text{dV} = rdrd\omega dz \tag{6.27}$$

where r is the radius, ω the azimuthal angle and z the axial elevation. Defining the core radial center as r=0, the axial mid-core level as H=0 and the starting azimuthal angle as ω=0, eq. 6.26 can be re-written as:

$$\rho = -\int_{-\tilde{H}/2}^{\tilde{H}/2}\int_{0}^{2\pi}\int_{0}^{\tilde{R}} \delta\Sigma_a\phi^2 rdrd\omega dz \Big/ \int\int\int \nu\Sigma_f\phi^2 \text{dV} \tag{6.28}$$

where $\tilde{H}$ and $\tilde{R}$ are the extrapolated height and radius of the core (where flux is equal to zero). In the volume covered by the ARC system (now for simplicity assuming a 1-tier type ARC system without faster and slower acting components), the change in absorption is again denoted as:

$$\delta\Sigma_a = \Sigma_{\text{ARC}} \tag{6.29}$$

There is no change in the absorption outside of the volume occupied by the ^{6}Li of the ARC-system and this can be set to 0. Assuming a cylindrically symmetrical core, the flux does not depend on the azimuthal angle ω. The ARC-system that is being analyzed is located at a distance r from the radial center of the core and a distance x from the bottom of the core (since the ARC actuation comes from underneath the core). The cross-sectional area of the actuation of a single ARC-system (A_{arc}) is tiny compared to the total area of the core. The variation in r over the width of the ARC-system (now a single assembly) is small

enough ($r_{arc}/R_{core} < 0.05$) that the variation of flux over its diameter can be ignored. These definitions lead to the following expression for reactivity:

$$\rho\left(r,x\right) = -A_{arc}\Sigma_{ARC}\int\limits_{-\tilde{H}/2}^{x-\tilde{H}/2}\phi^2\left(r,z\right)dz \Bigg/ \int\int\int \nu\Sigma_f\phi^2\left(r,z\right)\mathrm{dV} \tag{6.30}$$

As is well known from basic reactor theory, the flux distribution of a bare finite cylindrical core can be described by[6] :

$$\phi\left(r,z\right) = CJ_0\left(\frac{2.405r}{\tilde{R}}\right)\cos\left(\pi z/\tilde{H}\right) \tag{6.31}$$

where C is a constant proportional to the power of the core, J_0 is a bessel function of the 0th-order, r is the radial position as previously defined and $\tilde{R}$ and $\tilde{H}$ are the extrapolated radius and height of the full core respectively.

Plugging this flux distribution in to eq. 6.30 yields:

$$\rho\left(r,x\right) = -A_{\mathrm{ARC}}\Sigma_{\mathrm{ARC}}\frac{C^2J_0^2\left(\frac{2.405r}{\tilde{R}}\right)}{\int\nu\Sigma_f\phi^2\left(r,z\right)\mathrm{dV}}\int\limits_{-\tilde{H}/2}^{x-\tilde{H}/2}\cos^2\left(\frac{\pi z}{\tilde{H}}\right)dz \tag{6.32}$$

The integral evaluates to:

$$\int\limits_{-\tilde{H}/2}^{x-\tilde{H}/2}\cos^2\left(\frac{\pi z}{\tilde{H}}\right)dz = -\frac{1}{2}\frac{\sin\left(\frac{\pi x}{\tilde{H}}\right)\cos\left(\frac{\pi x}{\tilde{H}}\right)\tilde{H}-\pi x}{\pi} \tag{6.33}$$

The reactivity worth of a partial insertion of the ARC-system to the level x from the bottom of the core can be evaluated by expressing it as a fraction of the total worth of a complete ARC-insertion across the entire active core height. The normalized reactivity introduced by a partial insertion of the rod is given by:

$$\rho\left(r,x\right) = \frac{\int\limits_{-\tilde{H}/2}^{x-\tilde{H}/2}\cos^2\left(\frac{\pi z}{\tilde{H}}\right)dz}{\int\limits_{-\tilde{H}/2}^{\tilde{H}/2}\cos^2\left(\frac{\pi z}{\tilde{H}}\right)dz}\times\rho\left(r,x=H\right) \tag{6.34}$$

[6]The flux shape as described in eq. 6.31 is useful for illustrative purposes but does not hold in practice for a core of non-uniform composition such as a breed and burn system.

The denominator is simply:

$$\int_{-\tilde{H}/2}^{\tilde{H}/2} \cos^2\left(\frac{\pi z}{\tilde{H}}\right) dz = \frac{\tilde{H}}{2} \tag{6.35}$$

Given eq. 6.35 and 6.33, equation 6.34 becomes:

$$\rho\left(r,x\right) = -\left(\frac{\sin\left(\frac{\pi x}{\tilde{H}}\right)\cos\left(\frac{\pi x}{\tilde{H}}\right)\tilde{H} - \pi x}{\pi H}\right) \times \rho\left(r, x = H\right) \tag{6.36}$$

The worth of the ARC-system actuation also varies along with the flux distribution radially in the core. The worth is distributed radially as:

$$\rho\left(r\right) \propto J_0^2\left(\frac{2.405r}{\tilde{R}}\right) \tag{6.37}$$

Equation 6.36, giving the relative reactivity worth of a single ARC-system insertion (corresponding to, for instance, a flow blockage event in a single assembly) is plotted in Figure 6.12 for ARC-systems actuated at three different radial positions in the core. For example, r=0.25R means that in a 100-cm extrapolated-radius core, the ARC-system is located at a radial position 100*0.25=25 cm from the core radial center.

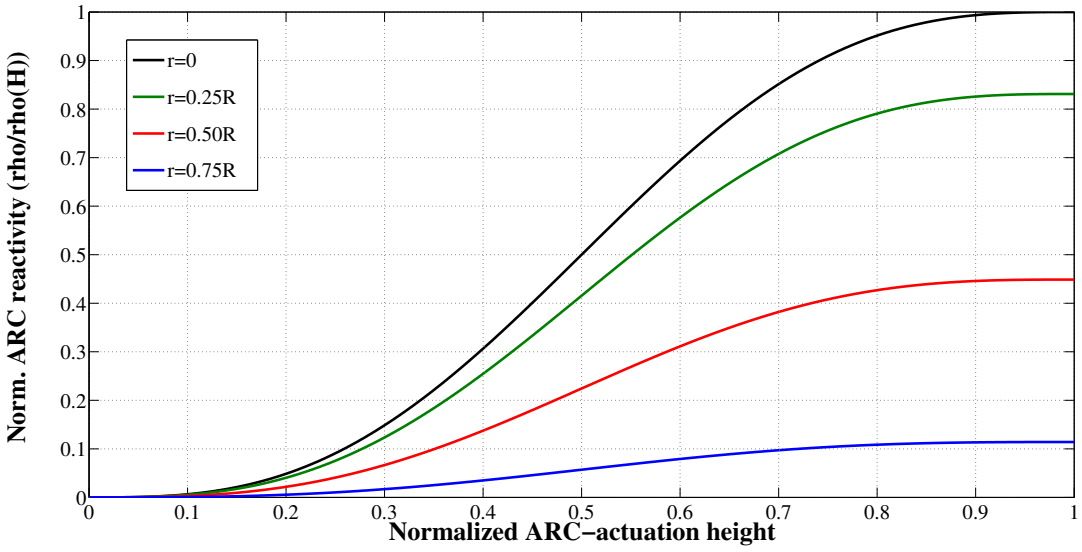

Figure 6.12: The relative reactivity effect of a single ARC-assembly actuation by height at four different radial positions in the core.

If an ARC-system is designed to match a nominal void worth of +7$ in a core with 500 assemblies, the average worth of a single ARC system is 1.4¢. Assuming a radial distribution of the shape given by eq. 6.37, the maximum ARC-system worth is 2.96¢. Thus, for such a core, Figure 6.12 can be turned from relative to absolute values by multiplying all values by 2.96¢.

6.3 The ARC-GL (Gas/Liquid) system

6.3.1 Concept description

The idea for the ARC-Gas/Liquid is to replace the liquid reservoir of the reference ARC-LL with a gas. The system operation principle could be described with an analogy to a person drinking a liquid from a container through a straw. If the straw is inserted in the liquid and the person exhales in to the straw, the pressure exerted on the liquid inside the straw will force it out of the straw and subsequently raise the liquid level of the soda in the container. If the person exhaling is replaced by a gas-filled upper ARC-reservoir, the straw is an ARC-tube and the liquid is ^{6}Li, this analogy describes the function of the ARC-GL system. Any gas undergoes a much larger volumetric expansion upon an increase in temperature than any liquid. In addition, the heat capacity of the gas is much lower, meaning that the ARC-GL system could potentially be significantly more responsive than the ARC-LL system. Figure 6.13 shows a design for the ARC-tube in a ARC-GL system and 6.14 show (highly simplified) the concept of the ARC-GL system as installed in a large fast reactor design with a lower fission gas plenum.

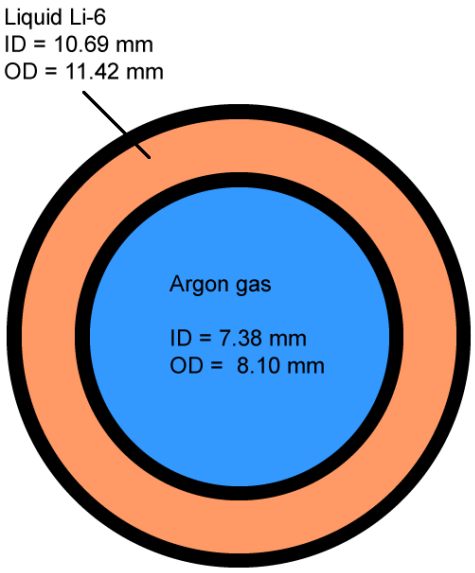

Figure 6.13: View from the top of a horizontal cut of a ARC-GL tube design

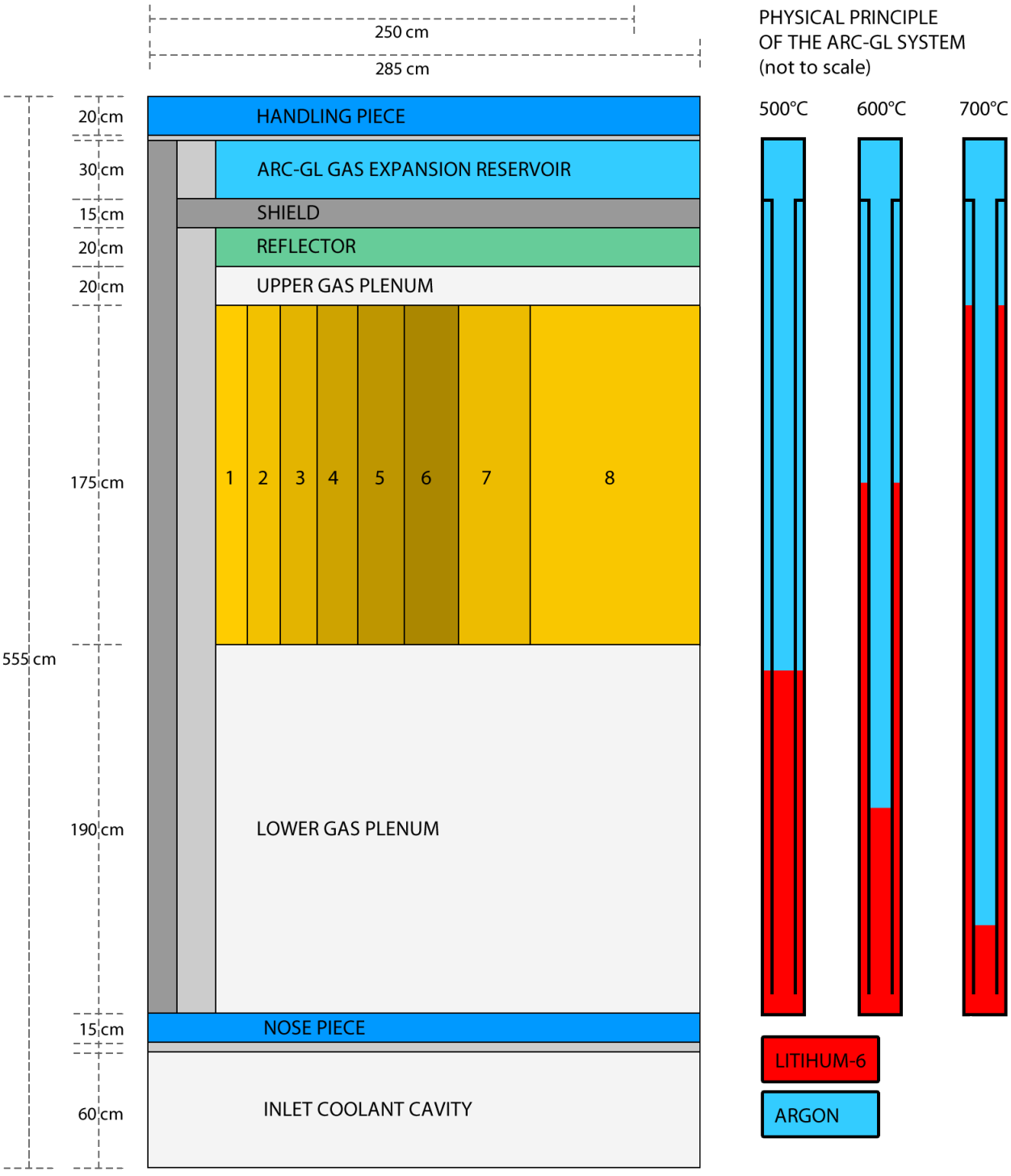

Figure 6.14: The concept of the ARC-GL system as installed in a large fast reactor with a lower fission gas plenum

Both ARC-concepts (Liquid/Liquid and Gas/Liquid) operate inherently, passively and have no moving mechanical parts with failure probabilities. The difference in performance is the potential speed of actuation and the neutronic efficiency. For the same sized upper reservoir, the response-time of ARG-GL can greatly outperform the ARC-LL system. However, the versatility of the ARC-tube designs that is possible with the LL-systems is not available when utilizing a gas as the expansion actuator. During all temperatures of interest, the expansion-gas of the GL system needs to remain within the inner ARC-tube. If it escapes down the bottom of the inner tube, a severe positive reactivity insertion event occurs, very similar to what happens in a LEM or AILEM system at a break of the gas/liquid interface. To avoid this eventuality, there is an extremely limited design space when determining the inner and outer ARC-tube diameter ratio. The sequential actuation of the ARC-LL system, as shown in Fig. 6.10, is thus not possible in the GL-system. However, due to the superior speed of actuation, this may not be needed. The inner tube diameter requirements makes the reactivity worth a single ARC-GL-tube smaller than the average worth of an ARC-LL-tube. This means more tubes are needed per assembly for the same total reactivity worth and thus the impact on core neutronic is more severe. Depending on the specific characteristics of the sequential actuation of the ARC-LL system, an ARC-GL system requires an estimated 30-40% more tubes per assembly for the same total reactivity worth (for instance 4 instead of 3 pins in a 271 pin assembly). Conceptually the ARG-GL system is highly promising, but engineering the system is challenging. The main difficulty is determining the operating characteristics of the system at all relevant temperature levels in the core: refueling, operation and transient. In principle, the system needs to accommodate the expansion between the melting temperature of lithium (180°C) and the standard operating coolant outlet temperature of the core ($\sim$500°C). The volumetric expansion of any gas in this temperature range is significant and presents an unexpected engineering problem for the lower ARC-reservoir. In a core with a lower gas plenum, this can be accommodated by a precise adjustment of the diameter of the inner ARC-tube in the region below the core. For a core with an upper gas plenum (as is the standard for all metallic fueled cores due to the need for a liquid bond), the problem is quite complex. A numerical solver routine was written and implemented in the MATLAB code to find a lower ARC-GL-reservoir and tube geometry that would provide the necessary operating characteristics in the full temperature range from solid lithium at 125°C to a severe sodium boiling transient at 1000°C. The quite complex resulting geometry is shown in Fig, 6.15. With this design, a lower reservoir for the ARC-GL system could take up as little as 15 cm below the core, which is similar to what is needed for the ARC-LL system.

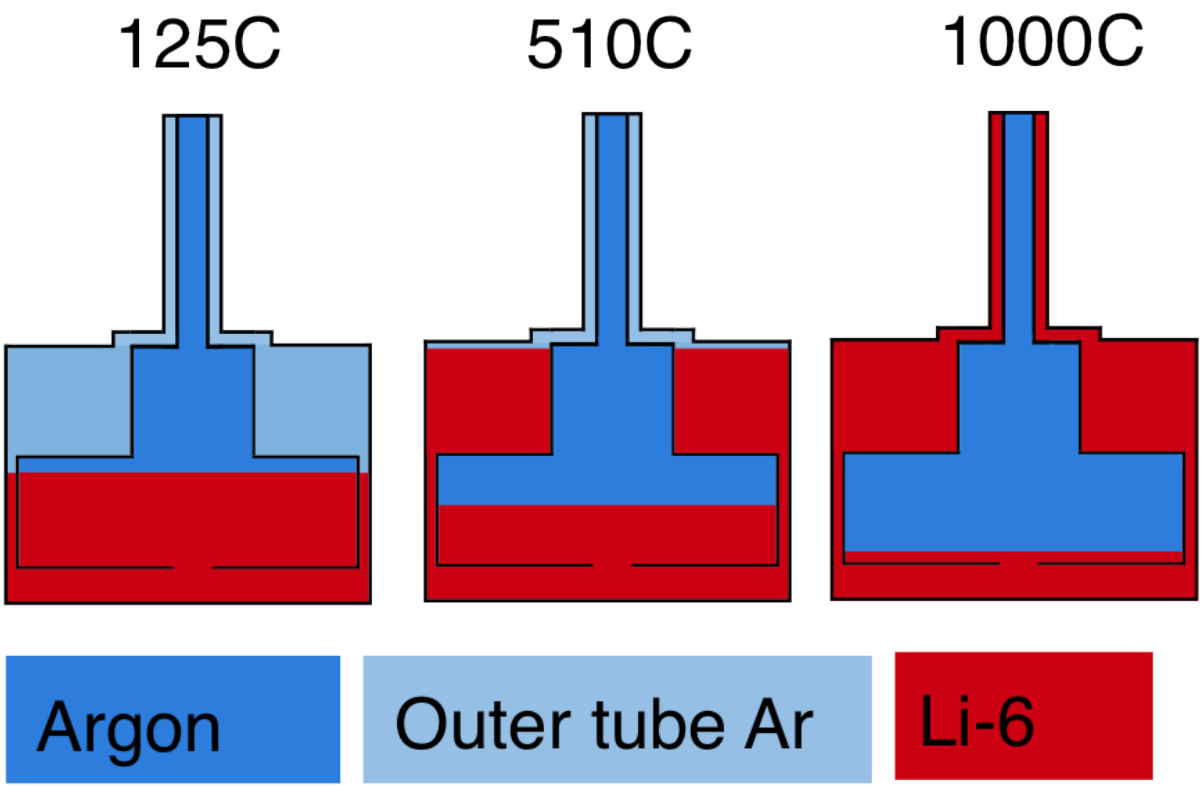

Figure 6.15: Compact lower ARC-GL reservoir for fast reactors with an upper fission gas plenum

As is obvious from Fig. 6.15, the engineering implementation of the ARG-GL system, particularly for upper gas plenum cores, is considerably more challenging than for the the ARC-LL system. Nevertheless, the system shows great promise as a faster acting alternative and will continue to be developed.

6.4 Summary of ARC-system evaluation criteria

The summary of the adherence of the new ARC-systems to the initial evaluation criteria as defined in Table 5.2 are given in Table 6.5. The ARC-LL system has a possible conditional violating regarding actuation speed. While the actuation speed of an ARC-LL system is a design variable, and could by design be set to any value needed, the relationship between actuation speed, reactivity worth and reservoir size need to be quantified and proven in a full systems code such as SASSYS/SAS4A before this possible conditional violation can be removed with certainty. The ARC-GL system is a complex system to model and thus conditionally violates criteria E2. By design, any scenario that would introduce positive reactivity in the ARG-GL system can be made exceedingly improbable, but it remains a physical possibility, which justifies a conditonal violation of the A2 criteria. As is clearly seen by comparing Table 5.3 (the evaluation of existing designs) and Table 6.5, the ARC-systems represents a vast improvement over currently available systems. The ARC-systems are protected intellectual property [152].

Table 6.5: ARC-system evaluation by critera from Table 5.2

Method	**Direct violation**	**Conditional violation**
ARC-LL	-	Possibly A7
ARC-GL	-	E2, Possibly A2

Part III

Fast reactor core design

Chapter 7

Assembly Design and Optimization code (ADOPT)

7.1 Introduction

The Assembly Design and OPTimization code (ADOPT) is a comprehensive computer code written to automate the process of designing and analyzing fast reactor fuel assemblies and cores. The default version of the code finds a fuel assembly design that maximizes the fuel volume fraction in the core while adhering to set constraints for all component temperatures, pressure drop, coolant velocity and structural integrity limits, subjected to a specified assembly peak power level. When provided with power peaking factors, ADOPT can be used very effectively as the first step in the design process of fast reactor cores that offer the maximum possible breeding ratio, which is proportional to the fuel volume fraction. To design fast reactor cores with different objectives, one can start with a neutronic analysis to find material volume fractions that provide the sought core performance. ADOPT can then reverse-engineer a fuel assembly design with the desired volume fractions that abide by all the thermal-hydraulic and structural constraints.

The code consists of a collection of coupled modules that perform separate calculational tasks. These modules are a mix of new solvers & methods developed specifically for this purpose and modules using methods that are already well established and widely published. New models were developed to calculate fuel rod dimensions & pitch, cladding thickness, optimized fuel rod locations within a fuel assembly, assembly duct wall thickness & inter-assembly gap and optimal coolant chemistry (for certain coolants). The code then provides the necessary input files of the produced geometry for a full core model to neutron transport codes such as MCNP [153] and Serpent [47] at a user-defined level of heterogeneity.

The design of a fast nuclear reactor core requires detailed analysis of many interdependent phenomena, spanning different disciplines of engineering and physics. At the most basic level, designing a fast reactor core is an iterative process between reactor physics (neutronics), thermal-hydraulics, structural mechanics and economics. Whereas in water-cooled thermal reactors (and, in particular, in boiling water reactors) there is a strong coupling between the core neutronics and thermal-hydraulics (as the water functions as both the moderator and coolant, the water density has a strong axial variation as well as axial power dependence and the neutron mean-free-path is small), in liquid-metal (and gas) cooled fast reactors the coupling between neutronics and thermal-hydraulics (T-H) is weak. This fact simplifies the core design process for certain types of fast reactors such as reactors designed to maximize the breeding ratio. The core offering the highest breeding ratio (henceforth defined as optimal) is that which has the maximal fuel volume fraction, given the same core constituents and core dimensions. The realization of these facts led to the development efforts that eventually resulted in the ADOPT code. If a decent initial guess for core power peaking factors is provided, a convergent solution between the results from neutron transport and the thermal-hydraulics & structural mechanics of ADOPT is reached within 3 iterations. While initially developed specifically for liquid-metal cooled breeder reactors, the ADOPT code has been expanded into a general-purpose fast reactor fuel assembly design code that

can be applied to any type of single-phase-coolant fast reactor core. ADOPT has a built-in library of properties for a large number of materials for coolant, structure, duct, bond and fuel. Material properties are supplied in external files to the ADOPT calculation framework, and users are free to add other material options without making changes inside the code. The presently available built-in library allows for 15000 material combinations, which covers much of the known design space for fast reactors.

7.2 ADOPT fast reactor core design process

The first step of the design process is to define the design objectives: what is the purpose of the system. The next step is to make overarching design & technology selections applicable for the specific reactor objective. These decisions include the selection of a coolant technology, general material selections, power level and core dimensions. Once these parameters are defined, the actual core design process can begin. Perhaps the most popular approach for a third step is to guess an approximate reactor core design from experience and coarse calculations and then iteratively improve on this design. A number of excellent tools for fuel assembly thermal-hydraulic analysis exists, but all these tools require a baseline design to be improved upon. If a good guess for a core design is made, iteratively utilizing these tools to improve the core design can quickly lead to optimized solutions. If the initial guess is far from the optimal, this type of design process tends to be inefficient. A highly simplified version of such a design process is shown in Figure 7.1.

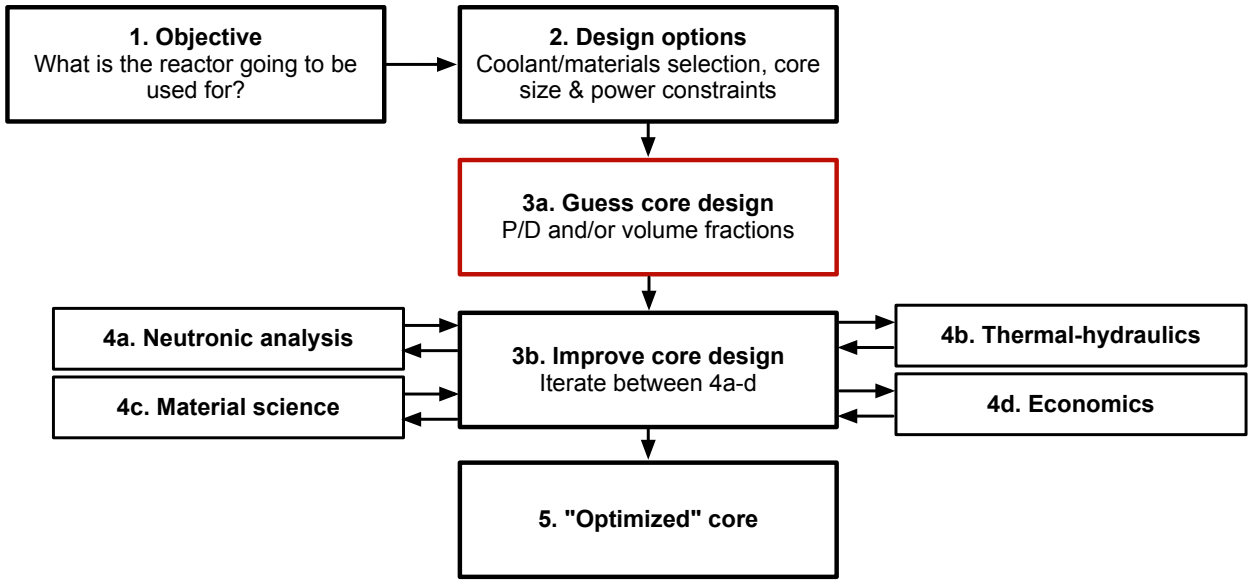

Figure 7.1: Conventional fast reactor core design process

The ADOPT code was developed to replace steps 3a and 4b-d with a single automated

code. For some applications such as high breeding-ratio cores, the ADOPT solver can find a converged optimized core design within 2-3 iterations with a neutron transport code. For other applications, such as low conversion ratio burner reactors, the design process is not as straightforward. For such cores, it is advantageous to first reach a neutronically optimal solution using as variables the material volume fractions. This is a commonly used approach for the neutronic analysis of fast reactor cores; it is made possible by the fact that the neutron mean free path in such cores is larger than the dimensions of individual material layers, such as fuel pins. ADOPT can then be used to reverse-engineer an actual fuel assembly and core design that matches the volume fractions found optimal from the neutronic analysis; it is found to be a powerful tool for this purpose. If no constraints are violated, this method can reach a fully optimized and complete core design in a single iteration.The design process equivalent to that presented in Figure 7.1 with the use of ADOPT is given in Figure 7.2 (for burner cores, 3 and 4 change places in the Fig. 7.2).

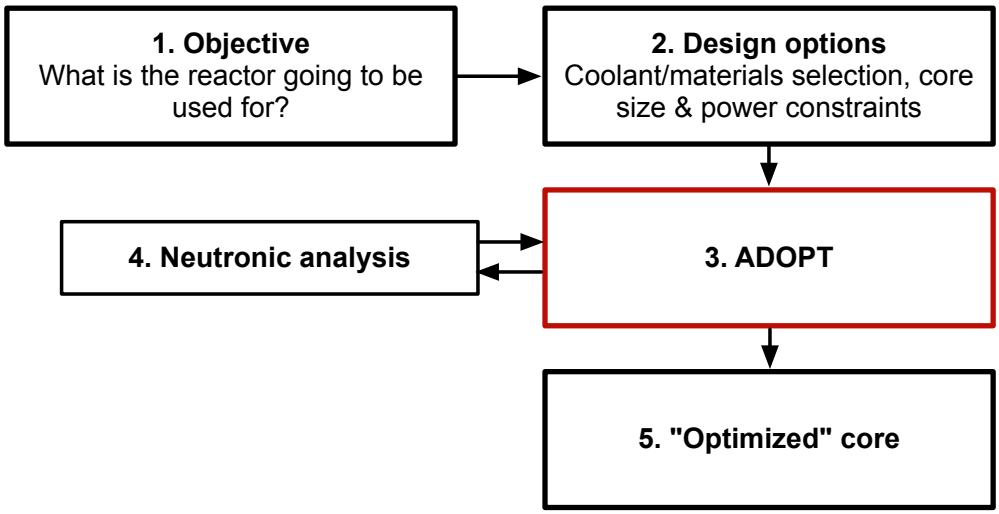

Figure 7.2: Fast reactor core design process using ADOPT

The ADOPT approach also enables the design of highly unconventional cores, as any materials for which there are relevant thermo-physical properties may be used for any component in the core. A major advantage is that the entire design is developed in one coherent open-source framework using a single set of assumptions, empirical correlations, material properties and solver techniques that are all documented in one user manual.

7.3 Structure, input & modes of operation

ADOPT consists of a collection of coupled modules each of which performs a different design-related task. Most of these modules use methods that were worked out decades ago and are well established and widely published. Examples are the heat transfer module that calculates all component temperatures and the pressure drop module. Both of these modules are primarily based on methods presented in *Todreas & Kazimi (1990)* [154]. Several modules are based on new methodology developed for ADOPT. These include modules to calculate pin geometry & pitch, cladding thickness, flow distribution, duct wall thickness & inter-assembly gap and optimal coolant chemistry (for certain coolants); the methodology these modules use will be described in detail in the following sections. The general structure of the ADOPT code is given in Figure 7.3.

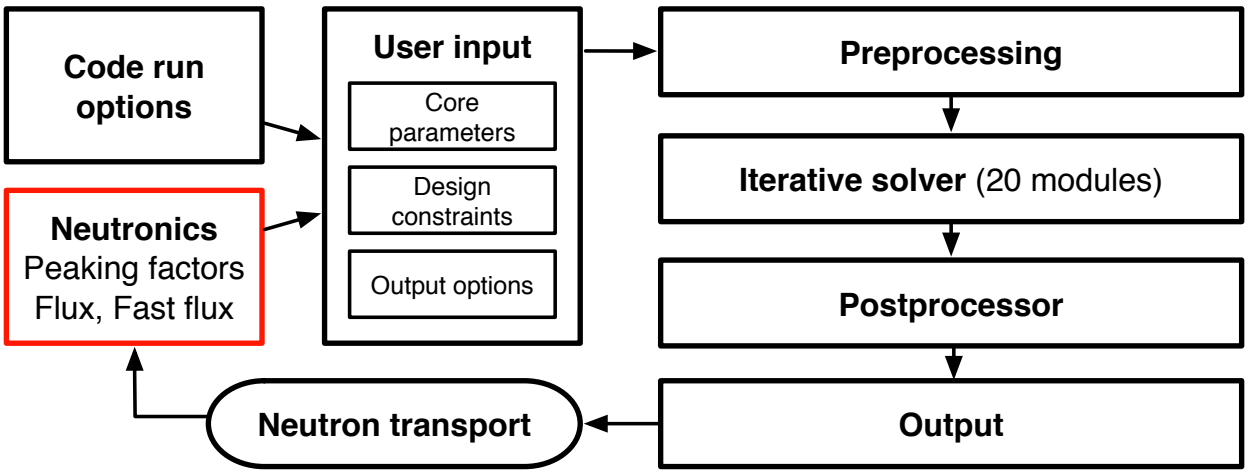

Figure 7.3: The over-arching structure of the ADOPT code

The main input file for ADOPT is a list of ∼50 parameters, 2/3 of which are needed for any problem. Specification of the other 1/3 of the input parameters is required if the code is to produce full core geometry (including axial and radial shields and reflectors etc.) input files for neutron transport codes such as MCNP and Serpent. A separate input file defines the constraints that are imposed on the specific core design optimization. Figure 7.4 shows the inter-connection of different ADOPT modules.

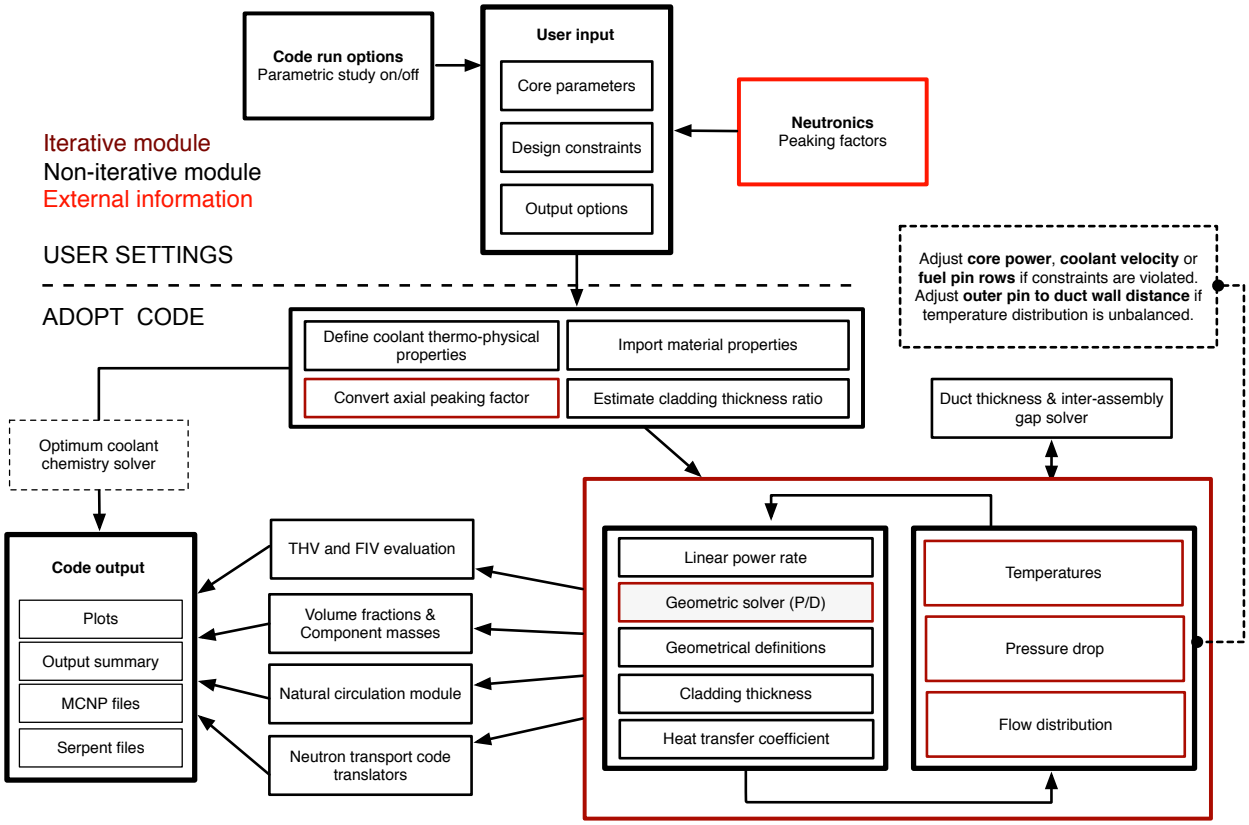

Figure 7.4: ADOPT internal module configuration

The constraints ADOPT can consider are summarized in Table 7.1.

Table 7.1: ADOPT code constraints

Constraint	Reason	Typical value
Coolant velocity	Mechanical vibrations (Na) Erosion-corrosion (HLM)	Na: 12 m/s HLM (conventional): 2.0 m/s HLM (new materials): 6.0 m/s
Fuel max. T	Avoiding fuel melting in transients	Metal: <800°C Oxide <2200°C Carbide <2050°C Nitride <2200°C
Clad. inner wall T.	Structural strength, Avoiding clad-fuel eutectic (metal fuel)	Na bond: <650°C HLM bond: <570°C He bond: <700°C
Clad. outer wall T.	Structural strength, Corrosion (HLMs)	Na coolant: <650°C HLM coolant: <550°C Gas coolant: <700°C
Min clad. and duct thickness	Manufacturability, strength	> 0.4 mm
Cladding strain	Flow area, structural integrity	0.2-2%
Duct strain	Withdrawal forces, flow areas	No duct-duct contact at EOC
Pressure drop	Pump limitations, Enabling nat. circulation	3 kPa - 2 MPa

The dimensional parameters of the fuel assembly solved for by ADOPT are defined in Figure 7.5. The user must specify the axial and radial power peaking factors of the core, which cannot be known with certainty until a neutronic analysis has been performed. Additionally, for accurate calculation of cladding and duct creep strain and swelling, the flux level and the fast flux (E>0.1 MeV) fraction can be defined in the input file.

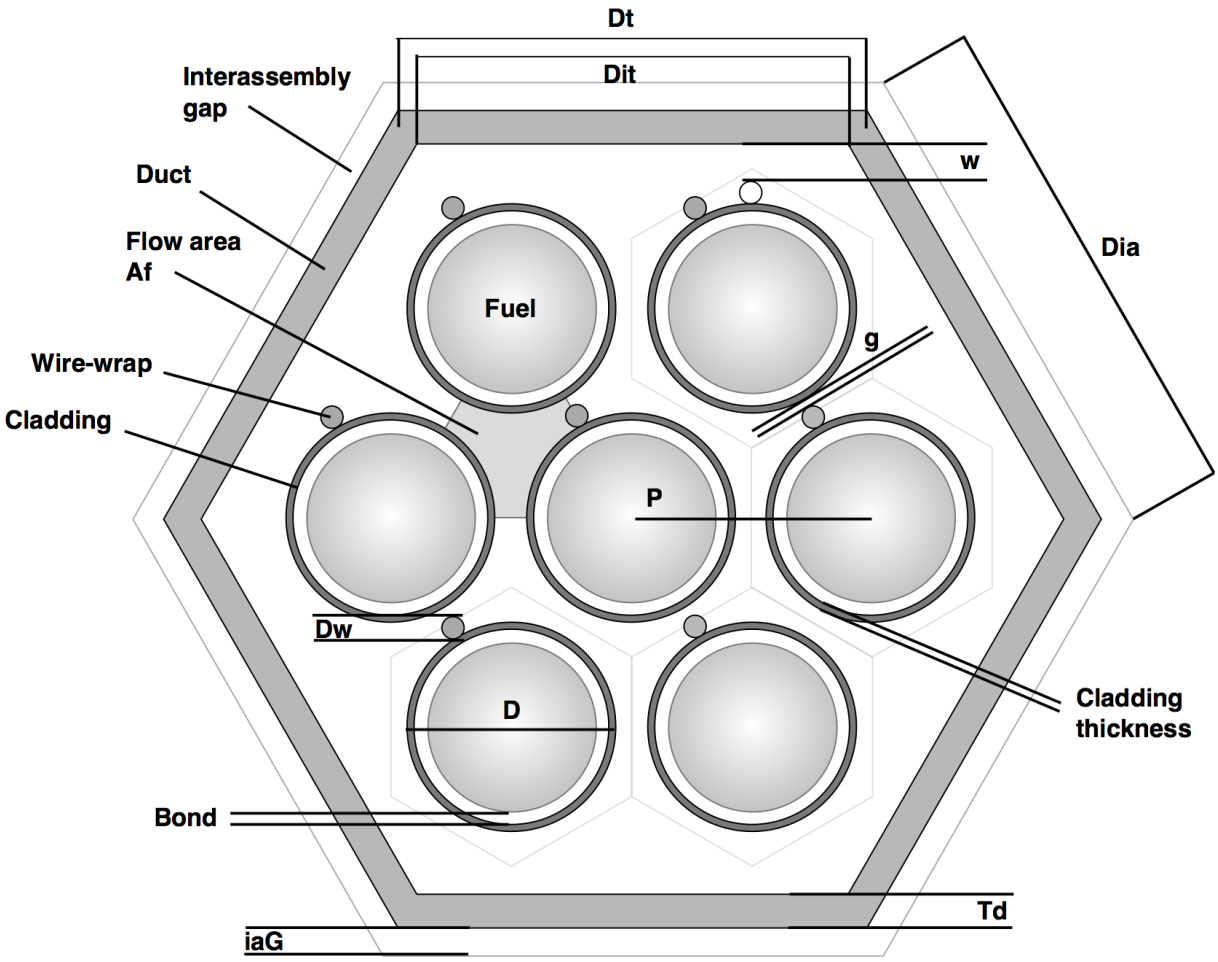

Figure 7.5: Assembly geometry parameters calculated by ADOPT

By default, ADOPT is run in the *optimization*-mode. This mode finds a single solution for a given set of input parameters and constraints. The *parametric*-mode option of the ADOPT code facilitates design trade-off studies. If the code is run in this mode, the value of any parameter specified as input can be varied at a user defined number of datapoints between a given minimum and maximum. All core parameters (as well as neutron transport code input files, if selected) of the optimal solution are given as output at each datapoint and stored as vectors ready for plotting. The utility of the parametric run-mode can be illustrated for the analysis of the wire-wrap spacer pitch length in a sodium-cooled breeder core. The pitch length is defined as the axial length of one 360° revolution of the wire around a fuel pin divided by the pin outer diameter (H/D). A larger value of H/D means a smaller pressure drop along the fuel bundle, which enables a more efficient (higher fuel volume fraction) assembly design. Running ADOPT in the optimization mode would yield the optimal solution to be the largest allowable value for H/D (set as H/D=50, which is

the upper limit of experimental data [155]). The result of a parametric mode study of this problem, for a sodium-cooled core with a total bundle channel-length of 3.8 meters, P/D=1.08 and wire diameter of 1.22 mm, is given in Figure 7.6.

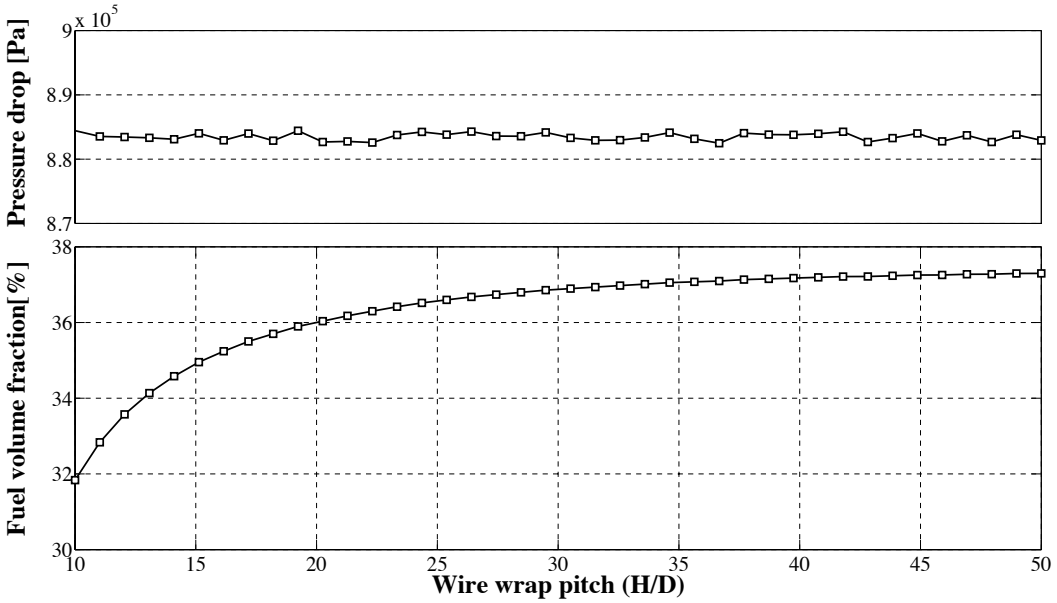

Figure 7.6: Effect of wire wrap pitch factor on attainable fuel volume fraction for a fixed pressure drop constraint.

Although H/D=50 gives the highest fuel volume fraction (as already confirmed by the optimization calculation), the relative gain going from H/D=30 up to 50 is negligible. As seen at the top of the figure, the total core pressure drop remains constant as the solution is pushed to this constraint at every datapoint. Since H/D=30 provides nearly twice as many contact points between the pins than H/D=50, it was the chosen value for this core design. If the two modes (optimization and parametric) of ADOPT are effectively combined in this way it can be used to highlight otherwise unknown aspects of core design.

7.4 New methodologies developed for ADOPT

The analysis methodologies used for most of the modules of ADOPT are based on well-known approaches that are documented in literature. They are described in the 165-page manual of the ADOPT code [156]. This section describes some of the new methodologies developed for the ADOPT modules that are set to calculate: cladding thickness, coolant chemistry and assembly flow distribution. New general correlations for the density of elemental zirconium and U-Zr nuclear fuels, developed specifically for ADOPT, are also presented.

7.4.1 Cladding thickness calculation

It is not possible to decouple the calculation of the optimal fuel rod cladding thickness from the calculations of cladding temperature and of the fuel rod outer diameter - since the hoop stress in the cladding is linearly dependent on its diameter. When the ADOPT code is applied to determine the optimal fuel assembly design, the designer does not know a priori how many fuel rods the assembly will contain and of what diameter. To find a solution, the ADOPT code uses the *cladding thickness ratio* (C_t) as the design variable; it is defined as the ratio between the cladding thickness and the outer diameter of the rod. For a given cladding material, the thickness ratio depends on:

(a) Pressure of gases inside the fuel rod

(b) Stress induced by fuel/cladding mechanical interaction (FCMI)

(c) Cladding temperature and thermal stresses

(d) Pressure of the outside coolant

(e) Inside/Outside corrosion attacks

The fission gas pressure is often the most important design parameter, FCMI-stresses are important for certain types of fuel, while parameters c-e often have a minimal effect on the solution. The fission gas pressure depends on the fraction of the gaseous fission products that migrate out from the fuel into the fission gas plenum, as well as on the volume of the fission gas plenum. However, since absolute volumes cannot be calculated before the fuel rod design is determined, ADOPT also introduces the *fuel/plenum volume ratio* (V_r) as the design variable. This method is partly based on the discussion of cladding thickness calculations in *Waltar et. al (2012)* [55]. Since the gas plena (subscript p) and fuel (subscript f) are contained within the same cladding, a volume & length relation can be defined as:

$$\frac{L_f}{L_p} = \frac{V_f}{f_{\mathrm{SD}} \times V_p} \tag{7.1}$$

where L is the axial length, V is the volume and f_{SD} is the fuel smear density. The volume ratio is defined from this relation as:

$$V_r \equiv \frac{V_f}{V_p} = \frac{f_{\mathrm{SD}} \times L_f}{L_p} \tag{7.2}$$

The volume of fission gas released to the plenum per m^3 of fuel at standard temperature and pressure is given by:

$$\alpha_o = \frac{FnRT_o}{P_o} \tag{7.3}$$

where F is the fission gas release fraction from the fuel - a fuel specific quantity depending on burnup and temperature. A correlation for this value is given for each fuel type in the

code material property database. R is the universal gas constant = 8314 J/kg-mol-K and n is the kg-mol of fission gas produced per m^3 of fuel.

The value of n can be estimated for each fuel type from the discharge burnup as:

$$n = B \times \frac{N_{\text{fm}}}{N_{\text{kg}}} \times \rho_f \times \alpha_f \times g_f \quad \left[\frac{10^3 \times \text{mol}}{m^3}\right] \tag{7.4}$$

where,
B is the average fuel discharge burnup in MWd/kg-actinide (given as input),
N_{fm} is the number of fission events per MWd,
N_{kg} is the number of molecules per kg-mol = $N_{\text{avogadro}} \times 1000 = 6.023 \times 10^{26}$,
ρ_f is the fuel density in kg/m^3,
α_f is the mass fraction of actinides in the fuel (calculated directly from user input),
g_f is the average number of gas atoms produced per fission event

The value of N_{fm} is obtained by estimating the energy produced in each fission event compared to the energy of one MWd. The average total heat energy generated by a fission event can be set by the ADOPT user (default is 200 MeV) and an MWd corresponds to 5.3927×10^{23} MeV of energy. Given these values, the default value used for N_{fm} is 2.6963×10^{21} fissions/MWd. The fraction of gaseous fission products generated per fission event depends on both the fuel isotopic composition and the neutron energy spectrum of the specific system. A default value of g_f=0.27 is set for the average gaseous fission products generated per fission event (either directly or by decay from other fission products) [55]. The user is free to supply a custom value in the user input file if more detailed information is available. Plugging in values, Equation 7.4 becomes:

$$n = 1.0287 \times 10^{-6} \times \alpha_f \times \rho_f \times B \tag{7.5}$$

The resulting pressure due to fission gases in the plenum, using the ideal gas law, is given by:

$$P_p = \alpha_o P_o V_r \times \frac{T_p}{273} \tag{7.6}$$

where T_p is the average temperature in the plenum. Plugging in all the values derived above gives:

$$P_p = 0.01005 \times \alpha_o \times \rho_f \times T_p \times V_r \times B \times F \quad \text{[Pa]} \tag{7.7}$$

The maximum pressure allowed by the industry safety standard (ASME) for pressurized tubes is [157]:

$$P_{\max} = \frac{\sigma_{max} \times \delta_{\text{clad}}}{0.5 D_{\text{clad}} - 0.4 \delta_{\text{clad}}} \quad \text{[MPa]} \tag{7.8}$$

where D_{clad} is the inside diameter of the cladding in mm, δ_{clad} is the cladding thickness and $\sigma_{\max}$ is the maximum allowable stress in MPa. The maximum allowable stress level is given

conservatively as [158]:

$$\sigma_{\max} = \min\left(\frac{\sigma_{\text{uts}}}{3.0}, \frac{\sigma_y}{1.5}\right) \tag{7.9}$$

Where σ_{uts} is the ultimate tensile strength and σ_y is the yield stress of the cladding. Solving equation 7.8 for C_t and setting $P_{\max} = P_p$ finally yields the thickness ratio of the cladding (based on fission gas pressure alone) as:

$$C_t = \frac{2.5P_p}{5\sigma_{\max} + 2P_p} \tag{7.10}$$

A good initial guess for the cladding thickness ratio is made automatically by the code using this methodology, with the only initial approximations being the temperatures of the cladding and plenum. The code then quickly converges on the final design. If a cladding creep strain limit is set as a constraint, the resulting cladding thickness (as calculated by the *CladStrain* module) may be larger than the value given by Equation 7.10, if this value is found to be insufficient.

7.4.2 Heavy liquid metal chemistry optimization

Design constraints imposed by coolant chemistry effects are determined in the *chemistry* module of ADOPT for both pure lead (Pb) and lead-bismuth eutectic (LBE) coolant loops. The methodology developed is illustrated in this section for the LBE coolant. Lead and lead-based alloys are highly corrosive at high temperatures to structural materials such as steel. Therefore, the protection of the steel by an oxide layer is a necessity in any system with flow and a temperature gradient such as the primary coolant system of a nuclear reactor. This is accomplished by incorporating a small amount of oxygen in the coolant. The solubility of oxygen in LBE is given by [159]:

$$C_s(O) = 10^{1.2-3400/T} \quad [wt.\%] \tag{7.11}$$

In a standard coolant loop temperature span of 300-500°C, the solubility is 0.2-6 ppm. If the oxygen concentration exceeds this value, lead oxide (PbO) particles will form in the coolant. This can lead to clogs in the primary coolant loop, which will reduce the efficiency of heat removal and may lead to severe accidents. The first soviet submarine using LBE coolant suffered a partial core melt and a large release of fission products due to flow path clogging by PbO [8]. Because of this, a strict upper limit, given (with some margin) by equation 7.11, evaluated at the lowest temperature in the coolant loop must be imposed. The thermodynamically least stable oxide of relevance gives the lower limit of oxygen concentration in the melt. In standard steels, this is usually the iron oxide magnetite (Fe_3O_4). If chromium-rich steels are used, the more stable iron-chromium spinel layer ($Fe_{3-x}Cr_xO_4$) effectively provides the main corrosion protection, and the magnetite layer is of lesser importance. Setting the lower limit of oxygen content to form magnetite for such steels (such as HT-9 and T-91) is still valid (dual layers will form) and conservative. For steels developed specifically for

Pb/LBE use, such as FeCrAl-coated or high-silicon content steels (such as EP-823), the oxygen content can safely be kept significantly lower than what is needed to form magnetite. However, since these steels are rarely used throughout the entire primary system, their use as cladding material may not change the solution for optimal oxygen content in the coolant of the full loop. The chemical reaction for the formation of magnetite is:

$$\frac{3}{4}\mathrm{Fe} + \mathrm{PbO} \longrightarrow \frac{1}{4}\mathrm{Fe_3O_4} + \mathrm{Pb} \tag{7.12}$$

The standard free enthalphy of this reaction is [159]:

$$\Delta_r G^o = -544.13 - 0.1712 \times T \quad \left[\frac{\mathrm{kJ}}{\mathrm{mol}}\right] \tag{7.13}$$

The Pb activity (α_{Pb}) in an LBE solution is given by [160]:

$$\ln\left(\alpha_{\mathrm{Pb}}\right) = -\frac{135.21}{T} - 0.8589 \tag{7.14}$$

The solubility of iron in LBE is [159]:

$$C_s(\mathrm{Fe}) = 10^{2.01-4380/T} \quad [wt.\%] \tag{7.15}$$

The oxygen and iron activity ratios α_O and α_{Fe} are defined as:

$$\alpha_O = \frac{C(O)}{C_s(O)} \tag{7.16}$$

$$\alpha_{\mathrm{Fe}} = \frac{C(\mathrm{Fe})}{C_s(\mathrm{Fe})} \tag{7.17}$$

The activity product of magnetite formation in LBE can be written as:

$$\alpha_O \times \alpha_{\mathrm{fe}}^{3/4} = \exp\left(\frac{\Delta_r G^o}{\mathrm{RT}}\right) \tag{7.18}$$

Plugging in all the known relations and solving Equation 7.18 for oxygen concentration yields:

$$C_{O_{\min}} = \frac{40.3 \times \exp\left(-\frac{6878.76}{T}\right) \times 10^{-3400/T}}{\left(\frac{C(\mathrm{Fe})}{10^{-4380/T}}\right)^{3/4}} \quad [wt.\%] \tag{7.19}$$

This is the minimum allowable oxygen content in LBE that ensures magnetite formation on the surface of the steel. Thus, the range of acceptable oxygen content in LBE is:

$$C_{O_{\min}} = \frac{40.3 \times \exp\left(-\frac{6878.76}{T}\right) \times 10^{-3400/T}}{\left(\frac{C(\mathrm{Fe})}{10^{-4380/T}}\right)^{3/4}} \leq C_O \leq 10^{-3400/T} \quad [wt.\%] \tag{7.20}$$

The minimum oxygen concentration is a function depending on both temperature and the amount of iron that is dissolved in the coolant. It is set by solving equation 7.18 at the highest temperature expected anywhere in the primary loop (= the cladding hotspot). In a non-isothermal flow system such as a reactor coolant loop, the iron content will not be at saturation (meaning α_{Fe} <1.0). Iron will dissolve in to the coolant in the hot leg (from the cladding steel) and precipitate in the cold leg (cold part of primary loop heat exchanger). Unfortunately it is difficult to measure iron content and currently impossible to monitor it on-line. The lower detection limit by chemical analysis is currently 5 ppm, which is higher than the iron saturation value for most of the temperature range of LBE reactor operation [159]. Figure 7.7 shows the minimum oxygen concentration for magnetite formation at different iron activity ratios.

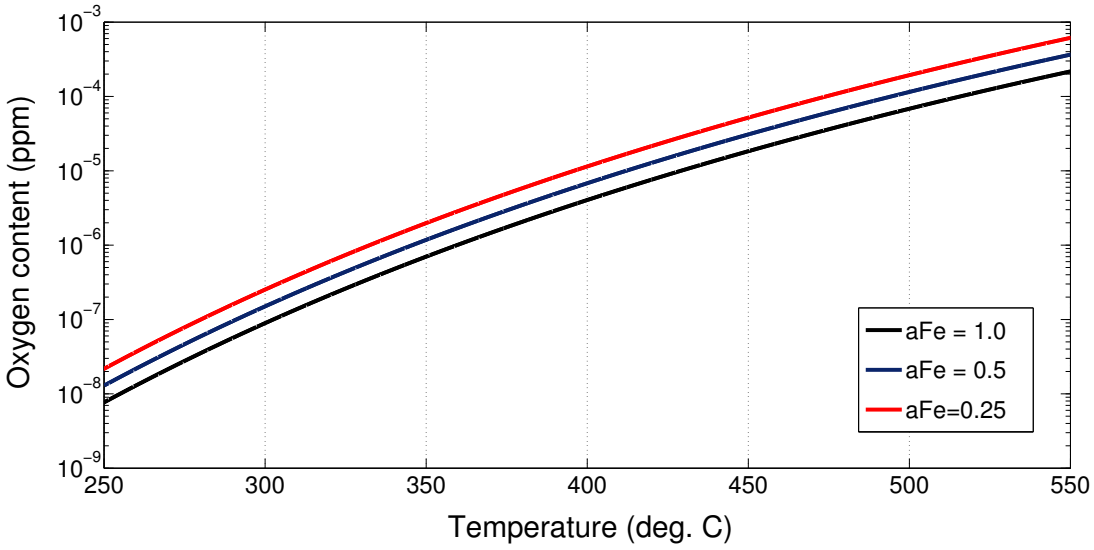

Figure 7.7: Minimum oxygen concentration for magnetite formation in LBE at different iron activity ratios

The full range can be seen in Figure 7.8, for a melt with saturated iron ($\alpha_{\mathrm{Fe}} = 1.0$) content. Since more oxygen is needed with less iron in the coolant, and the iron concentration is more or less unknown, the recommended strategy is to use the maximum oxygen concentration allowed. As will be shown later, employing this strategy also provides the optimal coolant temperature range.

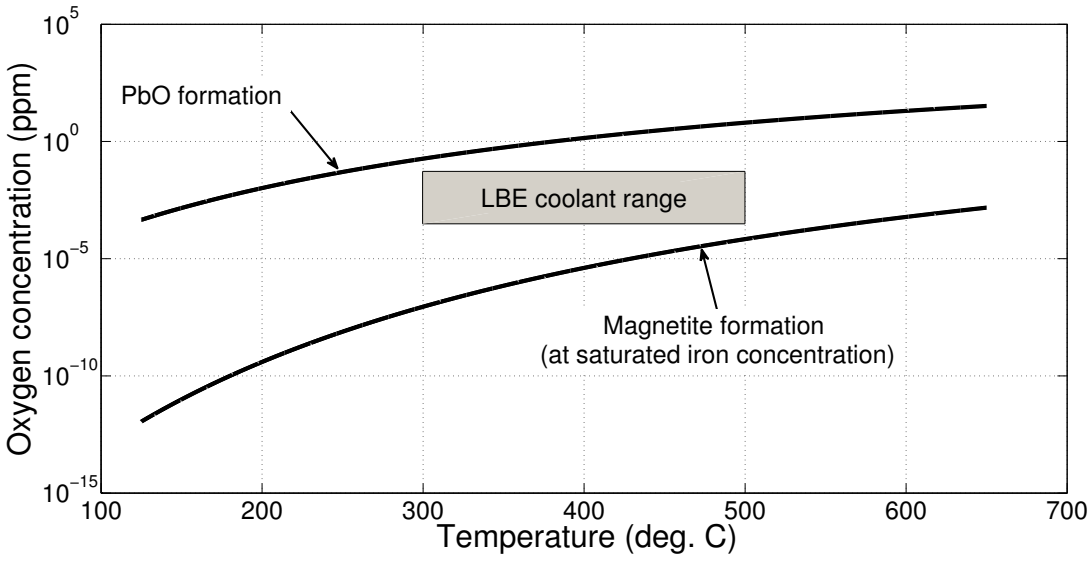

Figure 7.8: Acceptable oxygen-concentration range estimate for LBE cooled cores

While informative, eq. 7.20 is only a range and from it one cannot define the optimal oxygen concentration in the loop. Oxygen control is only done in one part of the primary cycle, and the oxygen potential is dependent on temperature and is thus different throughout the loop. The chemical reaction for the formation of lead oxide is:

$$\mathrm{Pb} + \frac{1}{2}\mathrm{O_2} \rightarrow \mathrm{PbO} \tag{7.21}$$

The standard free enthalpy for this reaction is [159]:

$$\begin{aligned} \Delta_r G^0 &= -439.87 + 0.1988 \times T \quad T < 732K \\ &= -437.61 + 0.1991 \times T \quad T \geq 732K \quad [\mathrm{kJ/mol}] \end{aligned}$$

The reaction for the formation of solid bismuth oxides in the LBE melt is:

$$\frac{4}{3}\mathrm{Bi} + O_2 = \frac{2}{3}\mathrm{Bi_2}O_3 \tag{7.22}$$

The free enthalpy of this reaction is [159]:

$$\Delta_r G^o = -389.14 + 192.6 \times T \quad \left[\frac{\mathrm{kJ}}{\mathrm{mol}}\right] \tag{7.23}$$

Since the values of equation 7.23 are larger than those of equation 7.23 throughout the applicable temperature range, the formation of bismuth oxide can effectively be ignored. Apart

from magnetite, two other reactions compete for iron atoms: Fe_2O_3 (rust) and FeO (wustite). The energy of formation of rust remains above that of magnetite so this reaction will not occur. The energy of formation of wustite drops below that of magnetite at 620°C. For temperatures above ~570°C, this reaction competes effectively with the magnetite formation, as the reaction free energies are near identical. Wustite is a structurally weak material that easily spalls off and thus both increases corrosion rates and the risk of clogging coolant paths. Because of this, an upper temperature limit of 570°C is imposed on steels exposed to LBE. The unsaturated oxygen potential in LBE has been determined experimentally as [161]:

$$RT \ln\left(p_{O_2}/\mathrm{P}^\circ\right) = -58.59 \times T - 2.510 \times 10^5 + 38.29 \times T \times \log\left(10^6 \times C_O\right) \tag{7.24}$$

where,
R is the gas constant (here, 8.314 J/(mol × K)),
p_{O_2} is the oxygen partial pressure,
P^0 is atmospheric pressure (101300 Pa),
C_O is the oxygen concentration in weight ppm.

The energy of formation of lead-oxide, magnetite and wustite as well as the unsaturated oxygen potential in LBE gives the relevant Ellingham diagram as seen in Figure 7.9.

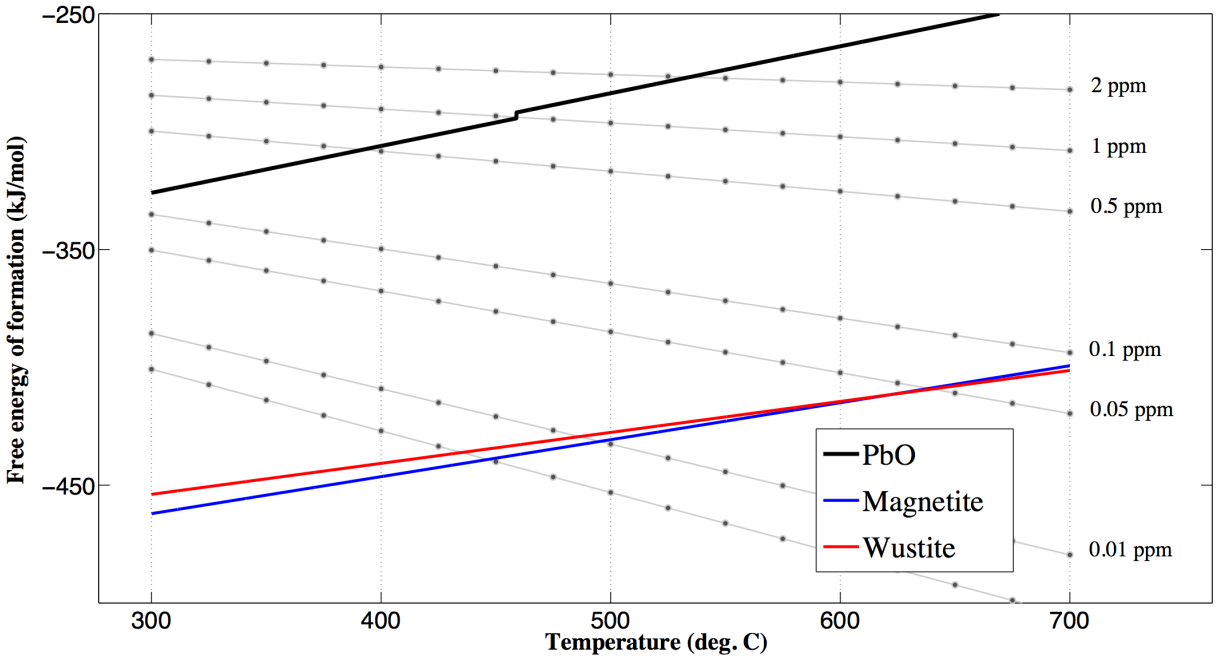

Figure 7.9: Ellingham diagram for the relevant reactions of an LBE coolant loop (grey lines represent the oxygen concentration)

It is clear from Figure 7.9 that there exists an optimum oxygen concentration for any given coolant loop. This optimum is defined as the oxygen concentration that enables the

formation of magnetite, does not enable the formation of lead oxides and provides corrosion protection in such a way over the largest possible span in temperature. The optimum is found by setting equation 7.24 equal to 7.22 and solving for C_O at the lowest temperature present in the coolant loop. The solution is given as:

$$C_{\mathrm{O}} = 5.2738 \times 10^{6} \times \exp\left(\frac{-11357.8}{T_{\min}}\right) \quad [\text{w. ppm}] \tag{7.25}$$

Accounting for uncertainties in both experimental data and oxygen sensor measurements, a more realistic optimum includes a 20% reduction in the oxygen concentration from the theoretical optimum:

$$C_{\mathrm{O}}\,(\text{conservative}) = 4.2190 \times 10^{6} \times \exp\left(\frac{-11357.8}{T_{\min}}\right) \quad [\text{w. ppm}] \tag{7.26}$$

This is the optimal oxygen concentration to ensure corrosion protection for any non-isothermal loop of LBE (nuclear or otherwise). While highly useful, this result does not directly affect the core design process. However, it has an important indirect effect on core design by setting the maximum allowable temperature in the coolant loop. This can be calculated by setting equation 7.24 equal to equation 7.13 and solving for temperature. Plugging in the optimal oxygen concentration (equation 7.25), the expression giving the theoretically highest allowable temperature in the coolant loop is:

$$T_{\max} = \frac{301}{0.2155 - \frac{0.0383 \times \ln\left[\exp\left(\frac{-11357.78}{T_{\min}} + 15.478\right)\right]}{\ln(10)}} \quad [K] \tag{7.27}$$

Implementing the 20% safety margin (equation 7.26 plus an additional 20% margin at the high temperature end), gives the following expression for the highest allowable temperature in the loop:

$$T_{\max} = \frac{240.79}{0.2155 - \frac{0.0383 \times \ln\left[4.219 \times 10^{6} \times \exp\left(\frac{-11357.78}{T_{\min}}\right)\right]}{\ln(10)}} \quad [K] \tag{7.28}$$

The results are summarized in Table 7.2. In the Table, *margin* refers to the 20/20% margin as described above.

Table 7.2: LBE temperature constraints

$T_{\min}$	C_O ppm	C_O ppm	$T_{\max}$ (°C)	$\Delta T_{\max}$ (°C)
-	Theory	Margin	Theory/Margin	Theory/Margin
150	1.151×10^{-5}	0.921×10^{-5}	471/317	321/167
200	0.000197	0.000157	569/394	369/194
250	0.00195	0.00156	570/473	320/223
300	0.0129	0.0104	570/553	270/253
350	0.0637	0.0510	570/570	220/220
400	0.247	0.197	570/570	170/170

Notably, maximum temperature restrictions lower than the 570°C constraint are activated for coolant loops with inlet (lowest) temperatures below 310°C. The maximum temperature span that any LBE coolant loop can run at is the 260°C span between 310°C and 570°C, which is illustrated in Figure 7.10.

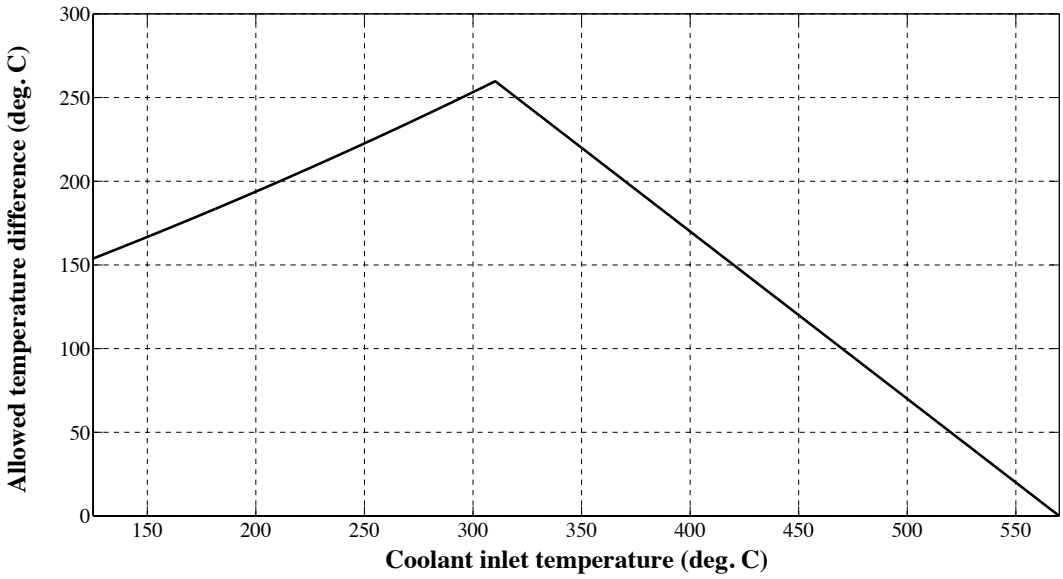

Figure 7.10: The allowed coolant loop temperature difference for LBE as a function of inlet (or minimum) temperature

The temperature span has a profound effect on the assembly design as well as the natural circulation characteristics of the system. These solvers are implemented in the ADOPT code

and will produce warnings if the coolant inlet & outlet temperatures are outside of the valid range.

7.4.3 Metallic fuel density correlations

Typical metallic fuel for fast reactors is an actinide or combinations of actinides alloyed with zirconium. The minimum required amount of zirconium depends on metallurgical considerations and, presently, is not well defined. Hence, there is interest in designing optimal cores using metallic fuel that has different amount of zirconium, thereby determining the sensitivity of the core performance to zirconium weight percent (see Section 2.7.2). No correlation of the metallic alloy fuel density dependence on the zirconium concentration could be found in the open literature. Therefore, a correlation for uranium-zirconium fuel, valid for the Zr-range 0-100 wt.% in the temperature range 50-900°C was developed for ADOPT. The density of zirconium at standard conditions is reported as 6.511 g/cm^3 [162] (original source: [163]). Ref. [162] also reports a density-temperature correlation for zirconium, without specifying the data-source or the temperature range of validity. The density change of elemental zirconium, from room temperature (293K) up to the ($\alpha \rightarrow \beta$) phase-transition at 1135 K can be represented by a second-order curve-fit based on the thermal-expansion data available in *Touloukian et. al. (2003)* [164]. The expansion data of ref. [164] was developed in to an expansion correlation and then converted to a density correlation through the following relation:

$$\rho = \left[1 + \frac{1 - \left(1 + \frac{\Delta L}{L_o}\right)^3}{\left(1 + \frac{\Delta L}{L_o}\right)^3}\right] \rho_o \tag{7.29}$$

Defining ρ_o as 6.511 g/cm^3, based on ref. [163], a new proposed density correlation for alpha-phase zirconium is:

$$\rho_{\mathrm{Zr}}(\alpha) = 6.541 - 9.08 \times 10^{-5} - 3.655 \times 10^{-8} T^2 \quad \left[\frac{g}{cm^3}\right] \quad (293K \leq T \leq 1135K) \tag{7.30}$$

Zirconium undergoes a density-increasing phase transition ($\alpha \rightarrow \beta$) at 1135K. The density correlation for β-phase Zr between 1135K and 1800K is given by:

$$\rho_{\mathrm{Zr}}(\alpha) = 6.569 - 9.825 \times 10^{-5} T - 3.046 \times 10^{-8} T^2 \quad \left[\frac{g}{cm^3}\right] \quad (1135K \leq T \leq 1800K) \tag{7.31}$$

The comparison of the new correlations, the experimental data and the correlation from ref. [162] is given in figure 7.11. Notably, the correlation given in *IAEA 2008* (ref. [162]) does not match the density at room temperature given in the same report.

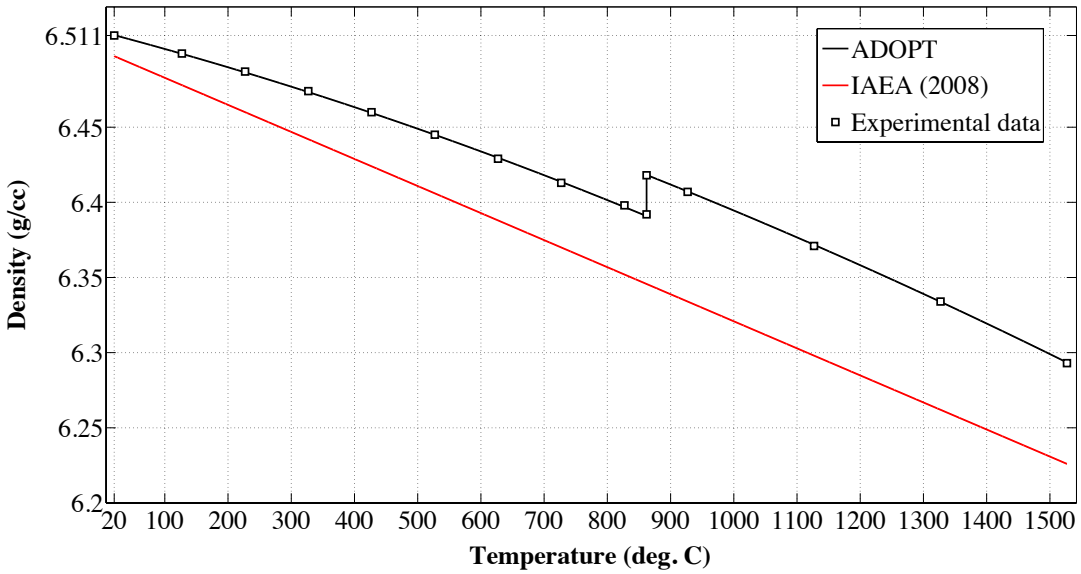

Figure 7.11: Data and correlations for the density of elemental zirconium

The density of U-Zr at room temperature for the full range of mixtures (0-100%) is given in Figure 36 of ref. [165]. While no correlation or raw data is given apart from the figure, it is clear from the figure itself (and is mentioned in the text) that the U-Zr alloy closely follows the law of mixtures. Thus, a correlation for the density of U-Zr can be developed from density correlations of U and Zr separately. Uranium undergoes two solid-state phase transitions: $(\alpha \rightarrow \beta)$ at 942K and $(\beta \rightarrow \gamma)$ at 1049K. The density of elemental uranium is given by the following correlations [162]:

$$\rho_U(\alpha) = 19.36 - 0.00103347 \times T \quad \left[\frac{g}{cm^3}\right] \quad (273K \leq T \leq 942K) \tag{7.32}$$

$$\rho_U(\beta) = 19.092 - 0.0009707 \times T \quad \left[\frac{g}{cm^3}\right] \quad (942K \leq T \leq 1049K) \tag{7.33}$$

$$\rho_U(\gamma) = 18.447 - 0.0005166 \times T \quad \left[\frac{g}{cm^3}\right] \quad (1049K \leq T \leq 1405K) \tag{7.34}$$

The atom fraction of Zr in U-Zr, A_{Zr}, is correlated to the its weight fraction, W_{Zr}, by the following equation:

$$A_{\mathrm{Zr}} = \frac{W_{Zr}}{0.61675 \times W_{Zr} + 0.3832} \tag{7.35}$$

The uranium atom fraction is:

$$A_U = 1 - A_{\mathrm{Zr}} \tag{7.36}$$

As a rough estimate, the combined density of the U-Zr system can be given by:

$$\rho_{\mathrm{UZr}} = \rho_U V_U + \rho_{\mathrm{Zr}} V_{\mathrm{Zr}} \approx \rho_U A_U + \rho_{\mathrm{Zr}} A_{\mathrm{Zr}} \tag{7.37}$$

Where V is the volume fraction of each component. Equation 7.37 represent a significant simplification that is only strictly correct if and when U and Zr have matching crystal structure and thus atom fractions correlate directly to volume fractions. The phase diagram of the U-Zr system is well defined and phase-transitions are different from the individual transitions of Zr and U. The density of the U-Zr is also dependent on the way the alloys are cast. A comparison of the results at room temperature from the correlation developed for ADOPT and the experimental data from ref. [165] is given in Figure 7.12.

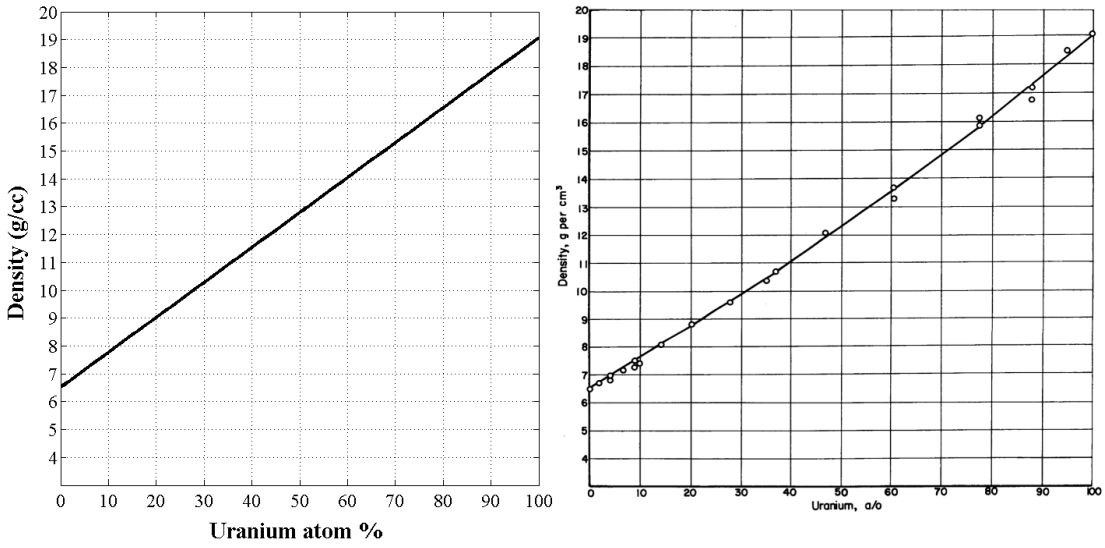

Figure 7.12: ADOPT correlation (left) and experimental data from [165] (right) for U-Zr density at 20°C

There are no discernible differences between the results. The ADOPT correlation was developed independent of the data in [165], which gives validity to the use of Equation 7.37 for low temperatures. Experimental density data at higher temperatures for different U-Zr alloys is needed for further validation. *Basak et. al. (2009)* [93] measured thermo-physical data, including thermal expansion, for pure U and U-Zr alloys at 2, 5, 7 and 10 w.% Zr. *Kaity et. al (2012)* reported the same data for the U-6Zr (w.%) alloy [92]. The thermal expansion data reported in ref. [93] and [92] can be converted to density correlations using Equation 7.29 and the room-temperature density values from the ADOPT correlation (which, as seen in 7.12, match those of ref. [165]). Comparison of the results are given in Figure 7.13 for the 0-10 w.% Zr range that is of interest in breeder reactor designs. Results from the ADOPT correlation and the data from ref. [93] match to within 2% with the exception of one datapoint (5%-difference at 10 wt.% Zr, 900°C). Where data by Source 2 and 3 of Figure 7.13 is available, they represent the recommended values. Lacking specific

experimental data apart from those reported in ref [93], and given the excellent agreement between the correlation and this data, Equations 7.30-7.37 provides a good general estimate of U-Zr fuel density.

Zr wt. %	Source	Temperature (°C)								
		25	100	400	500	550	600	700	800	900
0	1	19.1	19.0	18.7	18.6	18.5	18.5	18.1	17.9	17.8
	2		18.9	18.7	18.6	18.5	18.5		17.9	17.8
1	1	18.7	18.7	18.4	18.3	18.2	18.1	17.8	17.6	17.5
2	1	18.4	18.3	18.0	17.9	17.9	17.8	17.5	17.3	17.3
	2		18.3	18.0	17.9	17.8	17.8		17.2	17.1
3	1	18.1	18.0	17.8	17.7	17.6	17.6	17.3	17.0	17.0
4	1	17.8	17.8	17.5	17.4	17.3	17.3	17.0	16.8	16.7
5	1	17.5	17.5	17.2	17.1	17.1	17.0	16.7	16.5	16.5
	2		17.5	17.2	17.0	17.0	16.9		16.3	16.2
6	1	17.3	17.2	16.9	16.8	16.8	16.7	16.5	16.3	16.2
	3	17.3	17.2	17.0	16.8	16.7	16.7		16.2	16.1
7	1	17.0	16.9	16.7	16.6	16.5	16.5	16.2	16.0	16.0
	2		16.9	16.7	16.5	16.5	16.4		15.8	15.7
8	1	16.7	16.7	16.4	16.3	16.3	16.2	16.0	15.8	15.7
9	1	16.5	16.4	16.2	16.1	16.0	16.0	15.7	15.5	15.5
10	1	16.2	16.2	15.9	15.8	15.8	15.8	15.5	15.3	15.3
	2		16.2	15.9	15.8	15.7	15.6		15.0	14.5

Figure 7.13: Density of U-Zr fuel (g/cc)

Source 1. ADOPT correlation
Source 2. Data from ref. [93] converted by Equation 7.29 with ρ_o given by the ADOPT correlation
Source 3. Data from ref. [92] converted by Equation 7.29 with ρ_o given by the ADOPT correlation

7.5 Benchmarking and validation

Benchmarking of the ADOPT code and its modules and methods is being carried out in collaboration with Argonne National Laboratory (ANL). Initial comparisons have been made against the Small Modular Fast Reactor (SMFR) design [171]. The geometric results of reproducing the SMFR fuel assembly from the volume fractions given in ref. [171] are given in Table 7.10. In ref. [171], values for duct wall thickness, inter-assembly gap and cladding thickness were set to given values rather than calculated. For the comparison in

Table 7.10, the same values were set for these 3 parameters as input in ADOPT. In the table, [C] denotes a calculated parameter and [I] an input parameter in the ADOPT code.

Table 7.3: Fuel assembly reverse-engineering by ADOPT for given volume fractions

Parameter	ADOPT	SMFR design report [171]	Difference (%)
P/D	1.064 [C]	1.064	0
Pins/Assembly	127 [I]	127	n/a
Pin diameter (cm)	1.750 [C]	1.750	0
Pin pitch	1.861 [C]	1.861	0
Assembly pitch (cm)	22.17 [I]	22.17	n/a
Fuel slug diameter (cm)	1.429 [C]	1.429	0
Bundle pressure drop* (kPa)	65 [C]	58	+12
Core actinide mass (kg)	13741 [C]	13849	-0.77

*It is here assumed that bundle means the full length of the rod

Full benchmarking of the new methods developed for ADOPT will require further study and comparison against other, preferably breeder-type, core designs. Further benchmarking that includes more detailed analysis of the components of pressure-drop, flow distribution and temperatures in different components are being carried out.

7.6 Parametric studies for B&B cores design

To show the power of the *parametric* mode of the ADOPT code, a number of examples relating to B&B core designs are presented in the following sections.

7.6.1 Reference core for parametric study

A set of reference SWR core properties have been defined in Table 7.3 to form the base input for calculations in ADOPT to enable parametric studies.

Table 7.4: SWR B&B Reference Reactor Parameters

Parameter	Value
Power (thermal)	3000 MW
Active fuel length	200 cm
Fuel rod length	275 cm
Active core diameter	400 cm
Radial power peak factor	2.2
Coolant inlet/outlet T	355/510°C (Na) 300/480°C (LBE)
Assembly inner flat-to-flat distance	20.15 cm
Pressure drop in core / total pressure drop	65%
Assembly geometry type	Hexagonal lattice
Fuel type	U-10Zr (w.%)
Fuel smear density	75%
Wire-wrap pitch	30 x Fuel diameter
Fission gas plenum type	Vent-to-coolant (50 cm height)

7.6.2 Varying the pressure drop constraint

For B&B reactors, the core volume fractions will primarily be defined by the limit that is set for pressure drop in the primary coolant cycle. The pressure drop limitation limits the coolant flow velocity, which determines the spacing between the fuel pins for a given coolant temperature rise. To show the impact of the pressure drop constraint, the constraints of Table 7.1 are applied to a reference B&B core geometry as defined in Table 7.3, while allowing the pressure drop constraint to vary. The resulting achievable core volume fractions, as calculated by ADOPT for a set 169 pins per assembly, are given in Fig. 7.14.

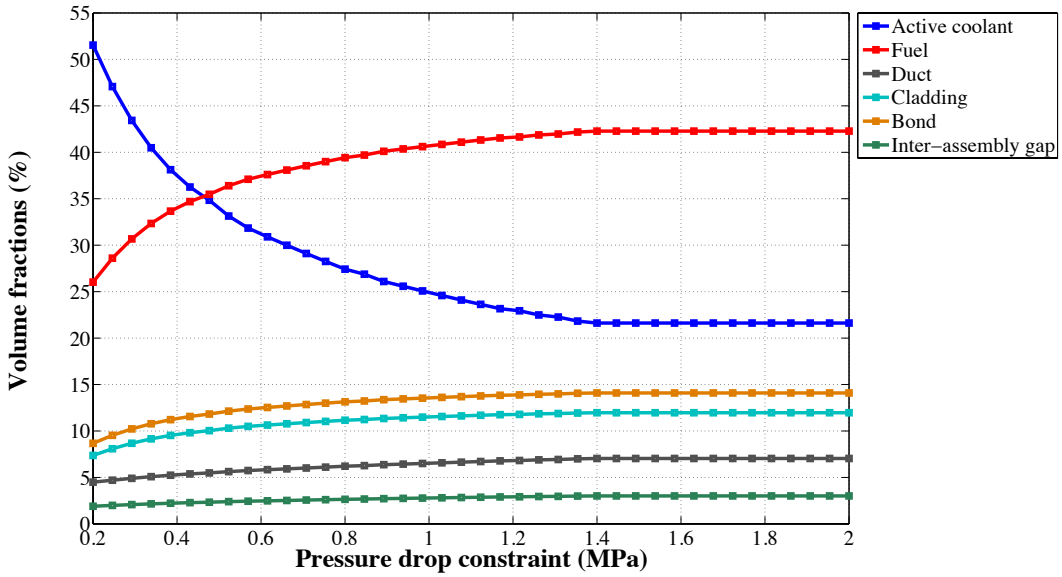

Figure 7.14: B&B core volume fractions by pressure drop constraint

The fuel assembly designs as produced by ADOPT for 4 selected values of pressure drop constraints are shown in Fig. 7.15. Asymptotic values are reached at pressure drops above ∼1.4 MPa, at which point the 12 m/s velocity constraint of Table 7.1, stemming from concerns of mechanical vibrations and wear, is activated. A known limitation of single-stage impeller pumps is a head of about 170 meters of sodium [166]. At 480°C, this corresponds to about 1.38 MPa, conveniently matching the value for 12 m/s sodium flow through an hexagonal assembly with 2.75 meter long wire-wrapped rods at 150°C coolant temperature rise. A primary cycle pressure drop constraint of 1.38 MPa imposed on a sodium-cooled B&B reactor of the type defined by Table 7.3 results in a fuel lattice with 169 pins per assembly and a pitch-to-diameter ratio (P/D) of 1.080. Increasing the pressure drop through the assembly leads to an increase in the pressure difference across the duct wall. The resulting stress increases the creep and deflection of the duct walls leading to thicker duct walls and a larger inter-assembly gap (as can be seen in Fig. 7.15). The combined width of the duct wall and inter-assembly gap is 3.39 mm for the top assembly in Fig. 7.15; this value is increased to 5.48 mm for the assembly design at the bottom.

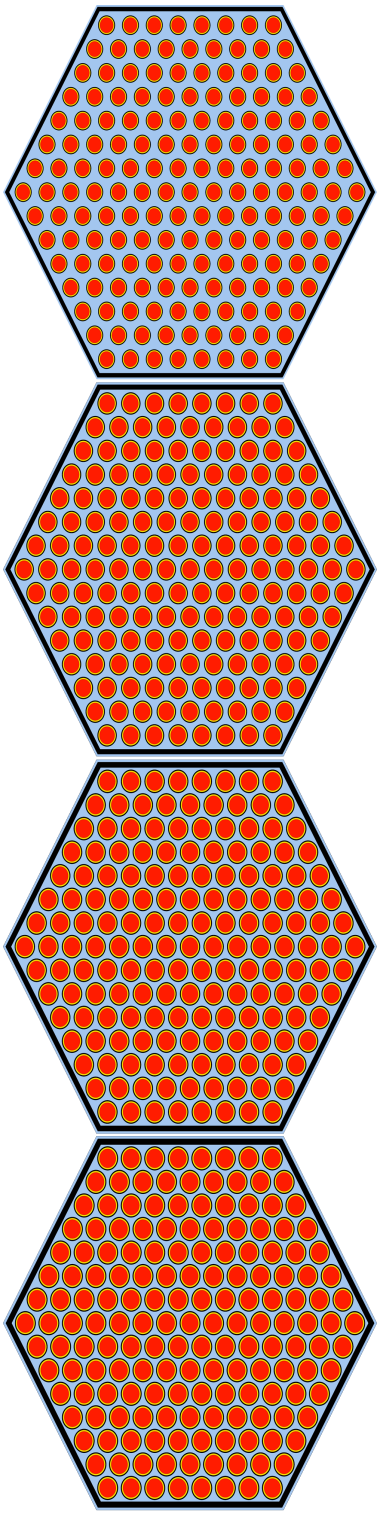

Figure 7.15: Fuel assembly designs for primary loop pressure drop constraints of (from top to bottom): 0.2, 0.4, 0.6 and 0.8 MPa. Black is structure (cladding & duct), blue is coolant, red is fuel and yellow is the bond filling the fuel/cladding gap.

7.6.3 Assembly flow distribution

If the same distance is kept between the outside row of pins and the duct wall as the distance between interior pins, the edge and corner coolant channels will be significantly overcooled compared to the internal channels. An optimal assembly design can be found where the distance between the outer row of pins and the duct wall produces the same coolant temperature increase across the core in both the edge and the interior coolant channels. The ADOPT user has the option to activate an automated calculation to find the optimal pin-to-duct-wall distance (parameter w in Fig. 7.5). A simplified flow-chart of the calculational approach is given in Fig. 7.16.

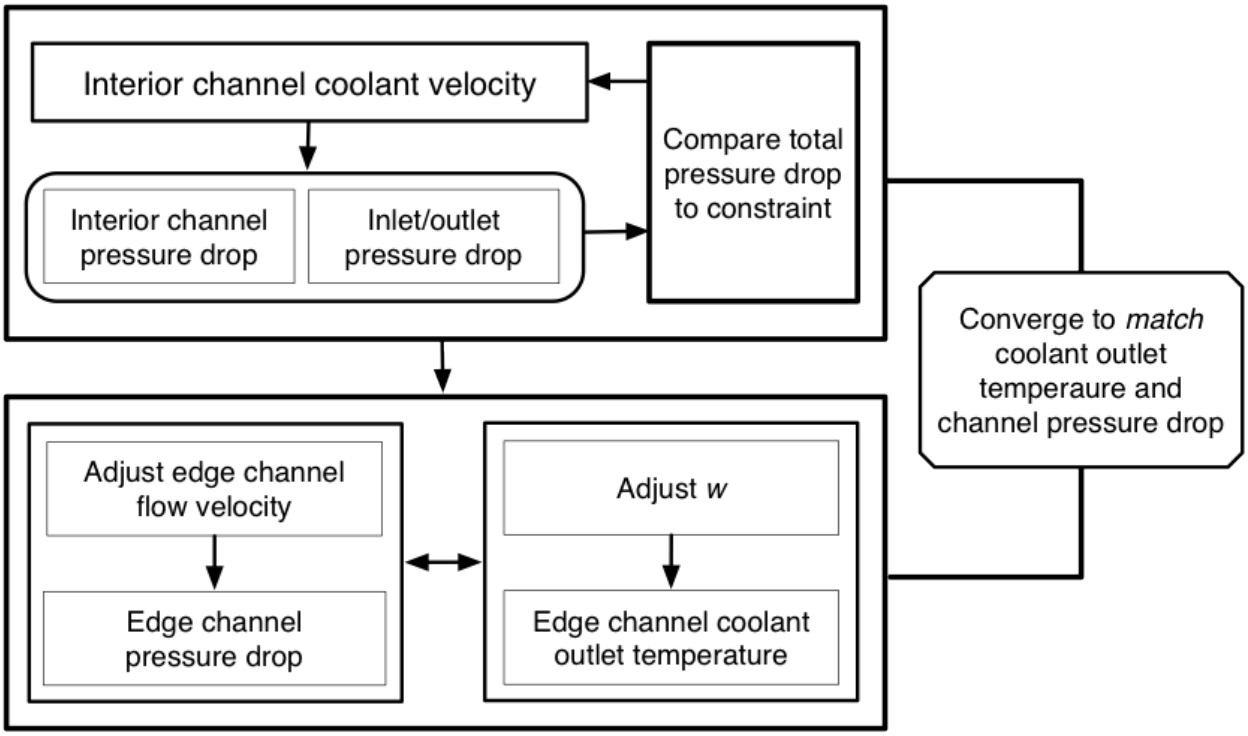

Figure 7.16: ADOPT flow optimization scheme

Such an optimization can increase the fuel volume fraction in the assembly by as much as 1%, giving a noticeable boost to the neutron economy of a SWR B&B core. An example of the effect of varying the parameter w for an LBE-cooled SWR B&B assembly with 127 pins is shown in Fig. 7.17.

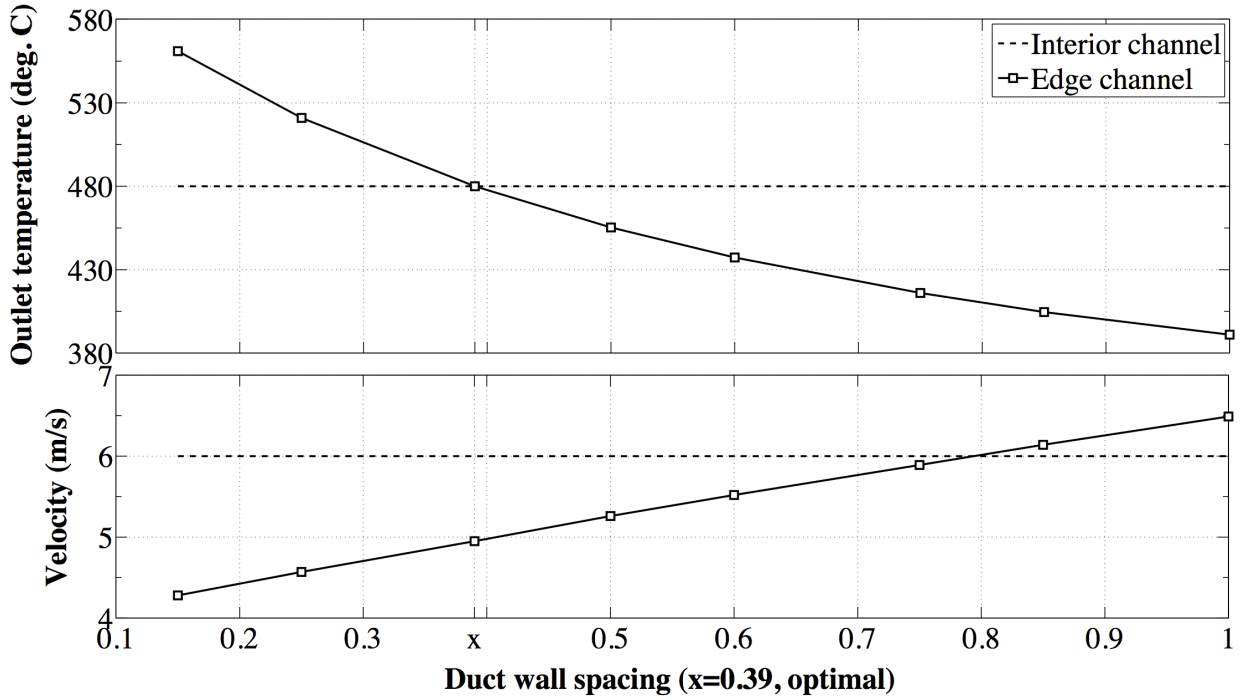

Figure 7.17: Duct wall spacing optimization study for an LBE-cooled SWR B&B assembly with 127 pins.

Here w is defined as the distance between the outer row pins and the duct wall relative to the distance between the pins. A w-value equal to one gives a duct-wall distance equal to the fuel rod pitch minus the fuel rod diameter, w=0 means no spacing at all. In this example, to achieve a uniform outlet temperature (excluding corner channels, which remain overcooled), the distance between the outer row of pins and the duct wall was found to be less than half the distance between pins ($w_{\text{optimal}} = 0.39$).

7.6.4 Power density

By varying the total thermal power and keeping the active core geometry as defined by Table 7.3 - 2 x 4 m (~25 m^3), the impact of core power density on the assembly design of a sodium-cooled reactor can be assessed. The ADOPT solution is based on the peak power density, which is the average value multiplied by the radial power peak factor (R_{pp}). The achievable fuel volume fractions in the core for two different values of R_{pp} are given in Fig. 7.18. ~50.5% fuel volume fraction corresponds to P/D=1.0 for this geometry, which is the theoretical minimum. This is the reason for the plateau seen at low power densities for R_{pp} = 1.5 in Fig. 7.18.

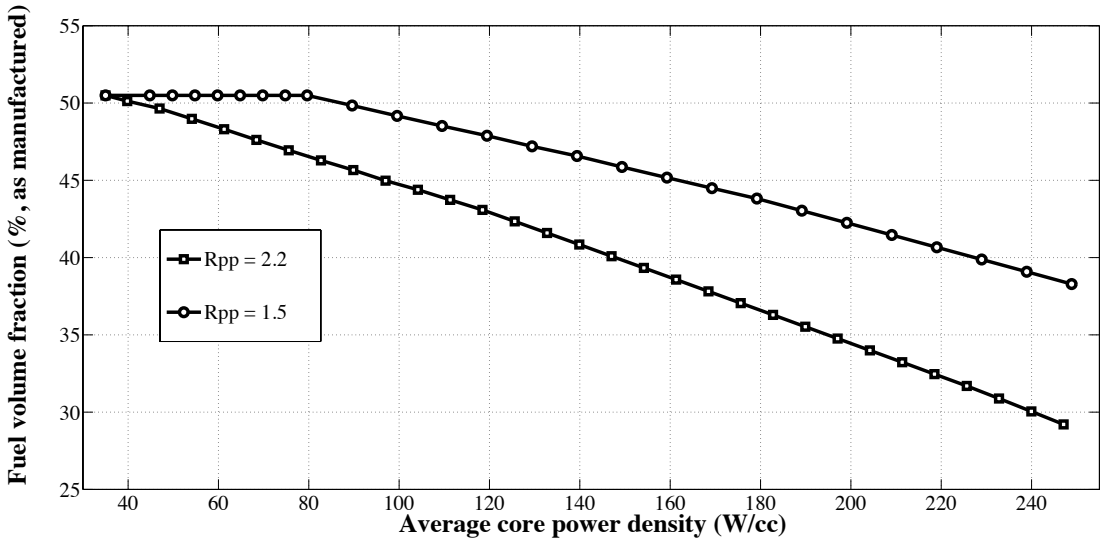

Figure 7.18: Impact of average core power density on the fuel volume fraction of a sodium-cooled SWR B&B core

7.7 Defining the optimum B&B core shape

Using the full capabilities of the ADOPT code coupled to the FAST-BEAU equilibrium cycle code [167], it is possible to estimate the optimum breed and burn core height and diameter (i.e. the core shape) and the impact that the power density has on core performance. Uniquely, B&B equilibrium cores require a minimum level of average discharge burnup in the fuel to sustain the breed & burn mode of operation. The major limiting factor for breed and burn cores is the material damage (as measured in displacements per atom dpa) associated with this minimum fuel burnup level. The peak structural material dpa damage level is a function of time-integrated flux (fluence) and the flux energy spectrum. The spectrum remains fairly constant with changes in the core shape, so in this study the relative dpa damage level can be estimated directly from burnup. For simplicity, the optimum B&B core shape is defined here as:

The shape that gives the minimum required equilibrium cycle average discharge burnup at a given volumetric power density.

Any core that is designated as optimal with this definition has the core shape that gives the best neutron economy. The existence of an optimum shape is easily realized from basic reactor physics. If the active core height is really low (i.e. pancake core), the axial neutron leakage probability will be prohibitively high for a good neutron economy. For really tall cores, axial neutron leakage probability is small but the friction pressure drop at a given coolant velocity is high. Given a set pressure drop constraint, tall cores need a more open pin lattice configuration which causes a decrease in the fuel volume fraction for a given total core volume. Somewhere in-between these two extremes, there is a core shape with the optimal balance between total neutron leakage probability (axial and radial) and core actinide density. The only physically accurate way to find such an optimum is to develop full core designs for a wide variety of shapes and calculate the equilibrium cycle performance parameters (i.e. min. req. burnup). The neutron balance method is not sufficiently accurate for this type of study, since it cannot properly account for leakage phenomena. The development of the ADOPT and FAST-BEAU codes makes it possible to perform such a study in an automated way. The FAST-BEAU code [167] couples neutron transport codes such as Serpent or MCNP with the depletion code ORIGEN [168] and automates the process of finding an equilibrium core composition given a shuffling scheme. In order to make a fair comparison between various core shapes, some parameters were set and were not allowed to vary between the different designs. Most important for the shape, the total active core volume was kept constant at 20 m^3. A uniform outer assembly size as well as duct wall thickness and inter-assembly gap was used for all cores, while the number of assemblies varies with the core diameter. The set parameters for the study are summarized in Table 7.4. A graphical side-view (to scale) of the core shapes that were studied is given in Fig. 7.19.

Figure 7.19: View from the side of some of the core-shapes studied (to scale)

Table 7.5: Set parameters for all core designs

Core volume	20 m^3
Coolant	Sodium
Feed fuel	DU-6Zr (wt.%)
Fuel smear density	75%*
Duct/Cladding/Reflector	HT9
Fission gas plenum	Gas venting through 50 cm above-core plenum
# of batches	16
Shuffling scheme	See Fig. 7.20
Primary cycle pressure drop	1.36 MPa
Core pressure drop	0.90 MPa
Max. clad temperature	600°C
Max. fuel temperature	800°C
Coolant inlet/outlet temperature	355/510°C
Assembly pitch	21.05 cm
Duct wall thickness	3.5 mm
Inter-assembly gap	3.5 mm
Cladding thickness	0.50 mm
Duct-wall spacing	P-D (uniform assembly)**
Wire-wrap pitch	30 x Rod Diameter
Radial reflectors	2 assembly rows (∼42 cm) + 1 shield row
Axial reflectors	30 cm below core, 30 cm above gas plenum
Reflector composition	HT9 steel (radial refl. vol. frac: 70% HT9, 30% sodium)

* This study was done with a set smear density of 75%. However, to enable peak burnup as high as 30% FIMA, the smear density may have to be reduced to 70% to ensure cladding integrity in future studies. The effect of changing the fuel smear density from 75 → 70% in this model is physically the same as reducing the fuel volume fraction and correspondingly increasing the bond volume fraction. This effect can be quantified using the extended neutron balance method as described in Section 2.6.

** This value refers to the spacing between the outer (edge) pin row and the inner duct wall. In a uniform conventional assembly, this is equal to the spacing between the inner rods. In the ADOPT code, a more optimized solution can be found automatically where this spacing is decreased until a uniform coolant outlet temperature is reached. For simplicity in this study, uniform assembly geometries were used.

The same 16-batch shuffling scheme was used for all core designs and is shown in Fig. 7.20. This shuffling scheme provides a minimized radial peaking factor while still ensuring a good neutron economy in the equilibrium cycle.

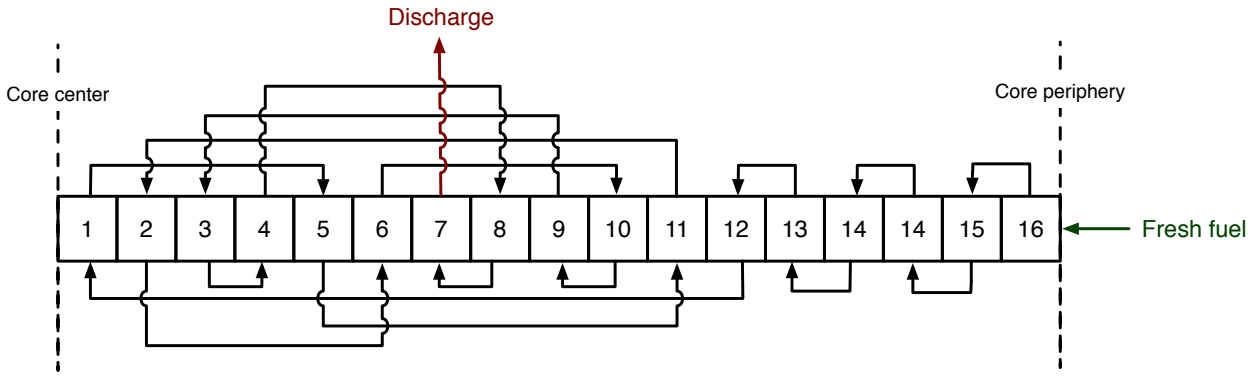

Figure 7.20: 16-batch radial shuffling scheme

To estimate the effect of power density on the core performance, and see whether power density by itself has an impact on the optimum core shape, design were developed for 4 different power-density levels. Within a reasonable span, the magnitude of the flux level of these cores has a small effect on the neutron economy. A lower power density allows for a smaller active coolant volume fraction and a higher actinide density loading, which gives a better neutron economy. The relative degradation in neutronic performance from an increase in power density will then have to be weighed against the potential economic benefit of a higher power output. This is outside the scope of the present study.

While the core volume is kept constant, the core fuel mass loading varies significantly between the different core designs. In a conventional fast core design study, this would have to be taken in to account explicitly when attempting to find and define an optimum. In a B&B

core however, feed fuel for the equilibrium cycle (such as depleted uranium) is available for very low cost (or even free or at negative cost) and the fuel manufacturing cost constitutes only a small fraction of the total plant cost. Therefore, the specific power density (kW/kg-actinide) has not been taken in to accound in determining the optimum core shape.

The design parameters of the 40 different cores that were developed for this study are given in Tables 7.6-7.9 for 175-250 W/cm^3 axially averaged volumetric power density at the peak radial power position respectively at the end of this report. The shuffling scheme as shown in Fig. 7.20 gives a maximum radial power peaking factor of about 2.0, nearly independent on the specifics of the core design. The achievable core-averaged volumetric power density corresponding to the values of Tables 7.6- is thus 87.5, 100, 112.5 and 125 W/cm^3 respectively. This corresponds to a total core thermal power level of 1.75-2.5 GW. The average linear power is conserved as the core shape changes, since there was no need to adjust the number of pins per assembly within the design space that was analyzed. However, at 250 W/cm^3, the number of pins per assembly was increased from 127 to 169 to increase heat transfer efficiency to keep temperatures below the set constraints. The values related to power density are summarized in Table 7.5.

Table 7.6: Core power density parameters

Core total thermal power (MW)	1750	2000	2250	2500
Max. (ax. average) batch power density (W/cm^3)	175	200	225	250
Core-averaged power density (W/cm^3)	87.5	100	112.5	125
Max. (ax. average) batch linear power (kW/m)	40	45	51	57
Core-averaged (ax. average) linear power (kW/m)	20	22.5	25.5	28.5

In order to obtain results without an unreasonable computational burden, equilibrium cycle performance for all core designs were obtained for a single value of average discharge burnup (16.5%). For any low-burnup B&B-core, reactivity increases from BOEC to EOEC[1]. The constraining case is thus generally to find an average discharge burnup level for which the specific core design is critical at BOEC. The optimum core-shape was effectively defined as the one with the highest value of BOEC multiplication factor (k_{eff}). If the value at BOEC is above 1.01 (critical with a 1% margin for error), it is possible that the specific core design could run a B&B cycle at or even slightly below 16.5% FIMA average discharge burnup.

The structural steel dpa-damage per unit of fast fluence and burnup remains relatively constant within a limited design space of varying core constituent volume fractions in metallic fueled sodium reactors. These trends are shown in Figure 7.21.

[1]BOEC/EOEC: Beginning/End of Equilibrium Cycle

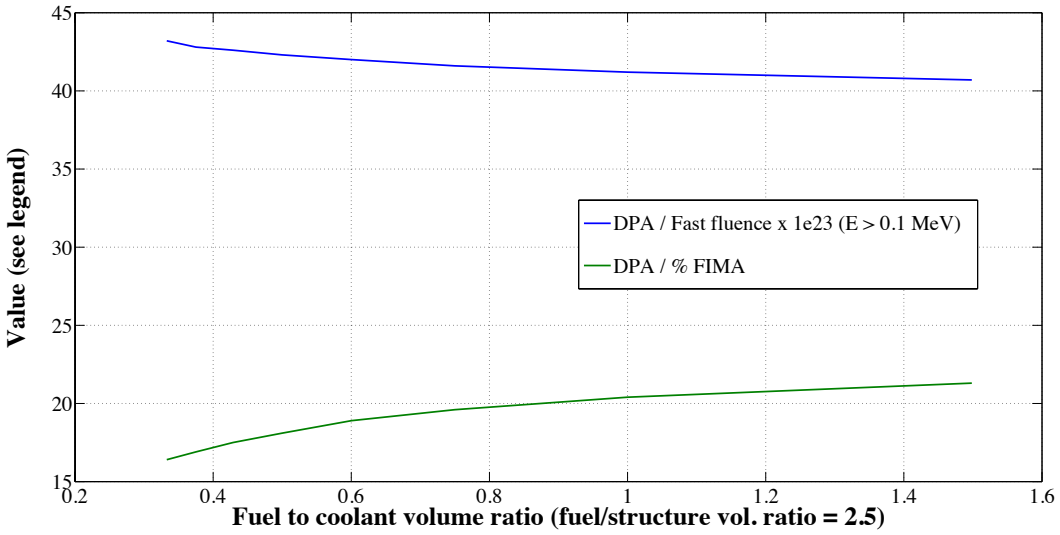

Figure 7.21: Relation between HT9/T91-steel dpa and fluence/burnup in a sodium-cooled U-10Zr fueled system (adapted from data in ref. [169])

In a 16.5% FIMA average discharge burnup system, the peak axial burnup is ∼1.75 times the average burnup level, which means the peak discharge burnup is ∼29%. In a design using 6% Zr fuel and a fuel volume fraction of ∼40%, this corresponds to a time-integrated total peak cladding damage of ∼580 dpa, above which it is highly unlikely any presently available structural material for cladding and duct could be qualified. TerraPower LLC believes that their improved versions of the HT9 steel will eventually be qualified for use up to 600 dpa [34], but so far this type of steel has only been tested to a maximum of 208 dpa [170]. This means that even if higher power densities than those listed in Table 7.5 may be of interest to make the core more economically viable, the degradation of core performance will lead to unrealistic material performance requirements *even if* the improved HT9 steel works as advertised. Thus, if a core-design cannot achieve BOEC criticality at 16.5% FIMA average discharge burnup, it is not a viable design option unless completely new and dramatically improved steels for cladding and duct are developed and tested. From these considerations, it is justified to assess the equilibrium cycle performance of all core-shapes and power densities at this single value of average discharge burnup rather than going through the very computationally expensive process of finding the specific burnup level at which each specific core design can run a B&B cycle.

7.7.1 Core-specific results

Core shapes for 20 m^3-volume active cores with height-to-diameter (H/D) ratios in the span 0.26-1.30 were analysed in this study. The optimum balance between neutron leakage

probability and core actinide density was found for cores with H/D ≈ 0.50. For a 20 m^3 core volume, this means an optimal fuel height and core diameter of 185 and 370 cm respectively. Core performance is significantly degraded with increasing power density, but there is no noticeable change in the optimal core shape. The maximum batch power density at which a 20 m^3-volume B&B core is able to operate an equilibrium cycle on depleted uranium fuel with a peak cladding damage below 600 dpa is estimated at ∼260 W/cm^3. With a radial power peaking level of 2.0, this corresponds to a core-averaged volumetric power density of 130 W/cm^3 and a total thermal power level of 2600 MW. If the core volume is increased, a higher power density will be possible due to decreasing leakage. The core volume effect on achievable power density has not been explicitly analysed, and should be a focus of continued study. The results relating core performance and fuel height are shown in Figure 7.22. For a 20 m^3 active volume core, the optimum leakage design of H/D=1 means a core height and diameter of 294 cm. Thermal hydraulic considerations push this optimum down toward the height span of 170-200 cm, or an active H/D ratio of 0.44-0.52.

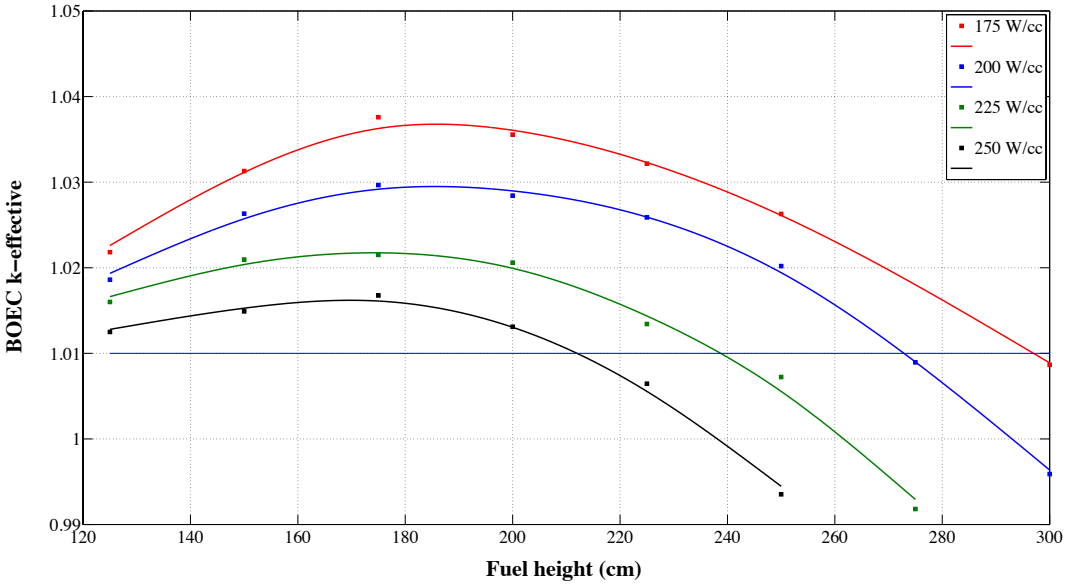

Figure 7.22: BOEC k_{eff} at 16.5% FIMA burnup with varying core shape and power density

At the optimum core-shape (H/D=0.5), an increase in the peak radial power density of 25 W/cm^3 causes a reduction in the fuel volume fraction of ∼1.5%. When going from 175 W/cm^3 to 200 W/cm^3, this corresponds to an opening of the fuel pin lattice from P/D=1.061 to 1.077. The corresponding *increase* in the minimum required burnup by this increase in power density is ∼0.3% FIMA. At 175 W/cm^3, an equilibrium B&B cycle can run at an estimated 15.7% FIMA of average discharge burnup, at 200 W/cm^3, this value is increased to 16.0% FIMA. The geometric effects are non-linear across the different core shapes, so no

accurate and simple generalized correlation can be given between power density and minimum required burnup. However, the only interesting case is that of the optimum core shape, for which the effect is approximately linear, with an increase of 0.01% FIMA required burnup per 1 W/cm^3 increase in peak batch volumetric power density. The materials limit, defined either as <600 dpa or 30% peak burnup is reached at 260 W/cm^3 radial peak power density for an optimally shaped core.

It is very clear from this study that the core performance is highly sensitive to the core shape. Any B&B core designed with a height-to-diameter ratio that is not within the range 0.4-0.6 will have a significantly degraded performance and may not be viable at all.

7.7.2 Generalization of results

The values presented in the preceding section are only strictly valid for one specific type of core design with a specific set of values for variables such as Zr-content in fuel, fissile loading in feed fuel, structure/coolant ratio etc. Varying any of these parameters may significantly change the absolute values of the minimum required burnup. It is also reasonable to assume that there will be some change in the local optima for core shape as these design parameters are varied. Preliminary results indicate that the change in optimal core shape is rather small, and the optima remain within the general H/D ratio range of 0.40-0.65.

Using a recently developed *extended neutron balance method* (ENB) based on the neutron balance principle [38], the impact of core design variables of the B&B design space have been identified. This method is presented in Section 2.6. With it, it is possible to develop expressions for the relative change in minimum required discharge burnup at a given level of neutron loss (leakage + loss to control elements) for any set core design parameter. At this point, such expressions have been developed for the following variables:

- Zr-content in metallic fuel
- Feed fuel ^{235}U-fraction
- Fuel/Active coolant volume fraction ratio (and equivalently, P/D-ratio)
- Power density (this study)
- Structure/Coolant volume fraction ratio

The results of these studies (apart from Structure/Coolant volume fraction) is shown for 6% total level of neutron loss in Figure 7.23.

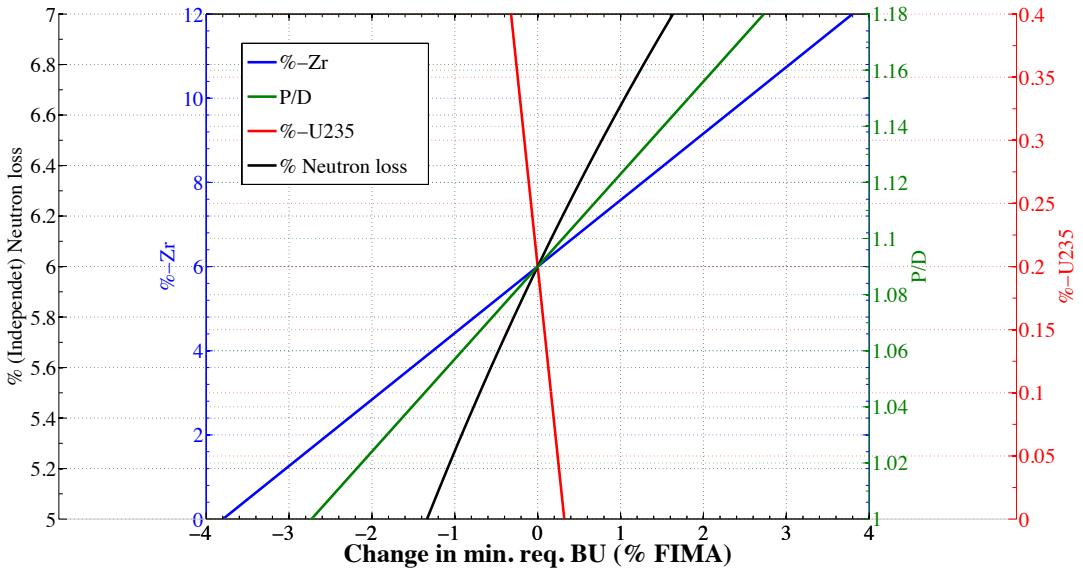

Figure 7.23: The B&B reactor design space at 6% total neutron loss

The total neutron leakage of the optimum core designs as presented in the preceding section are ∼5%. Using the *ENB* method, the results of the preceding section can be generalized. For instance, the reference core design with an axially averaged radial peak power density of 175 W/cm^3 requires an average discharge burnup of 15.7% FIMA to operate on a DU-fed B&B cycle. If the Zr-content in the fuel is increased from 6 wt.% to the more conventional 10 wt.%, the resulting required average discharge burnup is increased to 18.2% FIMA burnup. The higher average discharge burnup flattens the axial burnup distribution as compared to the reference scenario, and the resulting peak discharge burnup increases from 29% to ∼31.2% FIMA. The Zr-content in the fuel is at this point the only real design *variable*, since P/D (and thus fuel volume fraction) is determined by core power density. Once the fuel/active-coolant volume ratio is defined, there is a very limited design space with regards to the structure/coolant volume ratio. As is seen in Fig. 7.23, the performance can also be slightly improved (on the order of 0.2% FIMA) by selecting depleted uranium feed fuel with an average ^{235}U content of 0.4% rather than 0.2%. The impact on minimum required discharge burnup by the relevant design parameters on a B&B core with 5% neutron loss are approximately:

- 0.54% FIMA increase per wt. % increase of Zr-fraction in fuel
- 0.10% FIMA decrease per 0.1% (absolute) increase in ^{235}U content in feed fuel (ex. 0.2% to 0.3%)
- 0.01% FIMA increase per 1 W/cm^3 increase in peak batch axially averaged volumetric power density

The full range of these design perturbations is limited by physical constraints. Concerns of low melting point and dimensional stability limits the Zr-content to a lower level of 6 wt.%. Zr-based fuel is known to have excellent performance at 10 wt.%-Zr, so there is no reason to go above this value. In the full applicable range of Zr-contents (6-10%), minimum required burnup can vary by ∼2.16% FIMA. P/D-ratio is directly correlated to core shape and power density, so it does not make sense to present it as an independent variable. The effect of power density on min. req. burnup at the optimal core shape is of much greater importance. There is no physical constraint that gives a lower limit for power density, but in reality this is constrained by considerations of the return on investment for purchasing and running a power plant. No explicit economical study has been done within the scope of this study. The upper limit is known (as discussed in the previous section) to be ∼260 W/cm^3 (axially-averaged, radial peak) for a 20 m^3 core to remain within material damage constraints. If a lower limit is set at the lower bound of validity in this study – 175 W/cm^3 (87.5 W/cm^3 core-averaged), the total range of impact of varying power density on the B&B average discharge burnup is approximately 0.8% FIMA, corresponding to a peak cladding & duct damage difference of ∼30 dpa.[2]

[2]As the coolant volume fraction is increased at higher power density, the spectrum is slightly softened. This reduces the dpa/fluence-rate, giving a smaller difference in relative peak dpa than relative peak burnup.

Table 7.7: 20 m^3 175 W/cm^3 radial peak pow. dens. B&B core parameters

Core geometry										
Height (cm)	125	150	175	200	225	250	275	300	325	350
Diameter (cm)	451	412	382	357	336	319	304	291	280	270
# of assemblies	556	463	398	347	309	278	253	231	214	199
H/D	0.28	0.36	0.46	0.56	0.67	0.78	0.90	1.03	1.16	1.30
Pin geometry (cm)										
Pin diameter	1.704	1.675	1.646	1.613	1.581	1.548	1.511	1.474	1.434	1.391
Pin pitch	1.751	1.749	1.747	1.744	1.742	1.739	1.736	1.733	1.730	1.726
Flug slug diameter	1.389	1.364	1.339	1.311	1.283	1.253	1.222	1.189	1.155	1.118
P/D	1.028	1.044	1.061	1.081	1.101	1.124	1.149	1.176	1.206	1.241
Masses (MT)										
Actinide mass	210.7	202.9	196.2	187.3	179.8	171.3	163.1	154.0	145.9	136.9
Fuel mass	224.1	215.9	208.7	199.3	191.3	182.2	173.6	163.9	155.2	145.6
Structure mass	42.9	40.4	38.7	37.1	35.9	35.7	33.8	32.8	32.1	31.3
Coolant mass	5.7	6.2	6.7	7.3	7.9	8.5	9.2	9.8	10.5	11.2
Mass fractions (%)										
Fuel	82.17	82.23	82.12	81.79	81.38	80.83	80.14	79.38	78.47	77.40
Structure	15.73	15.39	15.22	15.21	15.26	15.40	15.62	15.89	16.22	16.64
Coolant	2.10	2.37	2.65	3.00	3.36	3.77	4.23	4.73	5.30	5.96
Vol. fractions (%)										
Fuel	50.16	48.34	46.59	44.65	42.87	40.84	38.79	36.78	34.69	32.51
Bond (gap)	16.72	16.11	15.53	14.88	14.26	13.61	12.93	12.26	11.56	10.84
Cladding	8.61	8.45	8.31	8.14	7.97	7.79	7.60	7.41	7.20	6.98
Active coolant	14.78	17.37	19.84	22.61	25.26	28.03	30.96	33.83	36.82	39.95
Duct	6.43	6.43	6.43	6.43	6.43	6.43	6.43	6.43	6.43	6.43
IA-gap coolant	3.30	3.30	3.30	3.30	3.30	3.30	3.30	3.30	3.30	6.43
Max. temp (°C)										
Outer clad wall	519	516	515	515	514	514	514	514	514	514
Inner clad wall	540	537	536	536	536	537	537	538	538	539
Fuel rim	560	558	557	557	557	557	558	558	559	560
Fuel center	726	724	723	723	723	724	724	725	725	725
Spec. power (kW/kg)	16.61	17.25	17.84	18.68	19.46	20.43	21.45	22.71	24.00	25.57
16.5% BU cycle (d)	565	544	526	502	482	461	438	413	391	367
Residence time (y)	24.8	23.8	23.1	22.0	21.1	20.2	19.2	18.1	17.1	16.0

Table 7.8: 20 m^3 200 W/cm^3 radial peak pow. dens. B&B core parameters

Core geometry										
Height (cm)	125	150	175	200	225	250	275	300	325	350
Diameter (cm)	451	412	382	357	336	319	304	291	280	270
# of assemblies	556	463	398	347	309	278	253	231	214	199
H/D	0.28	0.36	0.46	0.56	0.67	0.78	0.90	1.03	1.16	1.30
Pin geometry (cm)										
Pin diameter	1.687	1.654	1.619	1.582	1.546	1.503	1.459	1.416	1.369	1.318
Pin pitch	1.750	1.747	1.745	1.742	1.739	1.735	1.732	1.728	1.724	1.720
Flug slug diameter	1.375	1.346	1.316	1.284	1.252	1.215	1.177	1.139	1.099	1.054
P/D	1.037	1.056	1.077	1.101	1.125	1.154	1.187	1.221	1.260	1.306
Masses (MT)										
Actinide mass	206.0	197.5	189.3	179.5	171.0	161.1	151.3	141.2	131.8	121.5
Fuel mass	219.2	210.1	201.4	191.0	182.0	171.4	161.0	150.2	140.2	129.3
Structure mass	42.6	40.1	38.3	36.6	35.4	34.2	33.2	32.1	31.3	30.4
Coolant mass	6.2	6.8	7.4	8.1	8.7	9.5	10.2	10.9	11.7	12.6
Mass fractions (%)										
Fuel	81.78	81.75	81.49	81.04	80.48	79.69	78.76	77.74	76.52	75.06
Structure	15.91	15.61	15.51	15.55	15.66	15.91	16.23	16.61	17.08	17.65
Coolant	2.31	2.63	3.00	3.42	3.85	4.40	5.01	5.65	6.40	7.29
Vol. fractions (%)										
Fuel	49.11	47.09	45.00	42.82	40.73	38.38	36.01	33.74	31.37	28.90
Bond (gap)	16.37	15.70	15.00	14.27	13.58	12.79	12.00	11.21	10.46	9.63
Cladding	8.52	8.35	8.17	7.97	7.78	7.56	7.33	7.11	6.86	6.60
Active coolant	16.27	19.14	22.10	25.20	28.19	31.54	34.92	38.18	41.59	45.14
Duct	6.43	6.43	6.43	6.43	6.43	6.43	6.43	6.43	6.43	6.43
IA-gap coolant	3.30	3.30	3.30	3.30	3.30	3.30	3.30	3.30	3.30	3.30
Max. Temp. (°C)										
Outer clad wall	519	517	516	515	515	514	515	515	515	515
Inner clad wall	542	541	540	540	541	541	542	543	544	545
Fuel rim	566	564	564	564	564	565	565	567	567	569
Fuel center	752	751	750	751	750	751	751	753	753	754
Spec. power (kW/kg)	19.41	20.25	21.13	22.28	23.39	24.83	26.43	28.33	30.36	32.91
16.5% BU cycle (d)	484	463	444	421	401	378	355	331	309	285
Residence time (y)	21.2	20.3	19.5	18.5	17.6	16.6	15.6	14.5	13.5	12.5

Table 7.9: 20 m^3 225 W/cm^3 radial peak pow. dens. B&B core parameters

Core geometry										
Height (cm)	125	150	175	200	225	250	275	300	325	350
Diameter (cm)	451	412	382	357	336	319	304	291	280	270
# of assemblies	556	463	398	347	309	278	253	231	214	199
H/D	0.28	0.36	0.46	0.56	0.67	0.78	0.90	1.03	1.16	1.30
Pin geometry (cm)										
Pin diameter	1.669	1.630	1.591	1.548	1.506	1.458	1.407	1.356	1.301	1.241
Pin pitch	1.749	1.745	1.742	1.739	1.735	1.732	1.727	1.723	1.719	1.714
Flug slug diameter	1.359	1.325	1.291	1.254	1.218	1.176	1.132	1.088	1.040	0.988
P/D	1.047	1.071	1.095	1.123	1.152	1.188	1.228	1.271	1.321	1.382
Masses (MT)										
Actinide mass	201.3	191.2	182.0	171.2	161.7	150.7	139.8	128.6	117.9	106.5
Fuel mass	214.2	203.4	193.7	182.1	172.0	160.3	148.7	136.8	125.5	113.3
Structure mass	42.4	39.8	37.9	36.2	34.9	33.6	32.5	31.4	30.4	29.5
Coolant mass	6.7	7.4	8.1	8.8	9.6	10.4	11.3	12.1	13.0	13.9
Mass fractions (%)										
Fuel	81.36	81.18	80.79	80.18	79.46	78.44	77.24	75.91	74.30	72.33
Structure	16.10	15.87	15.82	15.93	16.12	16.46	16.90	17.40	18.03	18.81
Coolant	2.54	2.95	3.38	3.89	4.42	5.10	5.86	6.69	7.67	8.86
Vol. fractions (%)										
Fuel	48.01	45.64	43.42	40.89	38.55	35.93	33.29	30.75	28.11	25.35
Bond (gap)	16.00	15.21	14.44	13.63	12.85	11.98	11.10	10.25	9.37	8.45
Cladding	8.43	8.22	8.02	7.80	7.58	7.33	7.06	6.80	6.51	6.19
Active coolant	17.83	21.20	24.50	27.96	31.29	35.04	38.82	42.47	46.28	50.27
Duct	6.43	6.43	6.43	6.43	6.43	6.43	6.43	6.43	6.43	6.43
IA-gap coolant	3.30	3.30	3.30	3.30	3.30	3.30	3.30	3.30	3.30	3.30
Max. Temp. (°C)										
Outer clad wall	519	517	516	516	515	515	515	515	515	516
Inner clad wall	546	544	544	545	545	546	547	549	550	552
Fuel rim	572	571	571	571	572	573	574	576	577	579
Fuel center	778	777	776	777	777	778	779	781	782	783
Spec. power (kW/kg)	22.35	23.53	24.72	26.28	27.82	29.87	32.20	35.00	38.16	42.25
16.5% BU cycle (d)	420	399	380	357	337	314	292	268	246	222
Residence time (y)	18.8	17.5	16.7	15.6	14.8	13.8	12.8	11.7	10.8	9.7

Table 7.10: 20 m^3 250 W/cm^3 radial peak pow. dens. B&B core parameters

Core geometry										
Height (cm)	125	150	175	200	225	250	275	300	325	350
Diameter (cm)	451	412	382	357	336	319	304	291	280	270
# of assemblies	556	463	398	347	309	278	253	231	214	199
H/D	0.28	0.36	0.46	0.56	0.67	0.78	0.90	1.03	1.16	1.30
Pin geometry (cm)										
Pin diameter	1.428	1.389	1.350	1.308	1.262	1.213	1.161	1.108	1.050	0.985
Pin pitch	1.517	1.514	1.512	1.509	1.505	1.502	1.498	1.494	1.490	1.486
Flug slug diameter	1.150	1.117	1.083	1.046	1.007	0.964	0.918	0.873	0.822	0.767
P/D	1.062	1.090	1.119	1.153	1.193	1.238	1.291	1.349	1.420	1.508
Masses (MT)										
Actinide mass	192.2	181.0	170.6	158.8	147.2	134.8	122.6	110.2	98.3	85.5
Fuel mass	204.4	192.5	181.6	168.9	156.6	143.4	130.4	117.3	104.5	90.9
Structure mass	45.6	42.6	40.5	38.5	36.9	35.4	34.0	32.6	31.4	30.1
Coolant mass	7.3	8.1	8.9	9.7	10.6	11.6	12.6	13.5	14.5	15.6
Mass fractions (%)										
Fuel	79.45	79.15	78.61	77.79	76.70	75.32	73.67	71.80	69.48	66.57
Structure	17.71	17.53	17.55	17.74	18.09	18.59	19.23	19.96	20.88	22.05
Coolant	2.83	3.32	3.85	4.47	5.21	6.09	7.11	8.24	9.63	11.38
Vol. fractions (%)										
Fuel	45.76	43.13	40.56	37.87	35.04	32.12	29.17	26.34	23.39	20.32
Bond (gap)	15.25	14.38	13.52	12.62	11.68	10.71	9.72	8.78	7.80	6.77
Cladding	9.54	9.28	9.01	8.71	8.39	8.05	7.69	7.32	6.92	6.48
Active coolant	19.72	23.49	27.19	31.07	35.15	39.40	43.69	47.83	52.16	56.70
Duct	6.43	6.43	6.43	6.43	6.43	6.43	6.43	6.43	6.43	6.43
IA-gap coolant	3.30	3.30	3.30	3.30	3.30	3.30	3.30	3.30	3.30	3.30
Max. Temp. (°C)										
Outer clad wall	516	515	514	514	514	514	514	514	515	515
Inner clad wall	542	542	542	543	544	545	547	549	551	554
Fuel rim	564	564	564	565	566	568	569	571	573	576
Fuel center	740	740	740	742	742	743	744	747	748	750
Spec. power (kW/kg)	26.02	27.63	29.30	31.49	33.97	37.08	40.78	45.36	50.89	58.49
16.5% BU cycle (d)	368	349	330	306	287	264	241	216	193	172
Residence time (y)	16.1	15.3	14.5	13.4	12.6	11.6	10.6	9.5	8.5	7.5

7.8 Output and code coupling

Output from the ADOPT code is available in five different forms:

- Plots of selected outputs (temperatures, volume fractions etc.)
- Text-file summarizing main output (80 parameters in total)
- MCNP & Serpent input files for assembly level plotting
- MCNP & Serpent input files for full core neutronic analysis
- MCNP & Serpent input files for full core equilibrium cycle analysis (using the Fast-BEAU code [17])

If the code is run in parametric mode, the geometric model at every datapoint is stored as output in MATLAB vectors that can be plotted at will. By default, ADOPT will plot the volume fractions of all constituents of the active core as a function of the parameter that is being varied (see illustration in Figure 14).

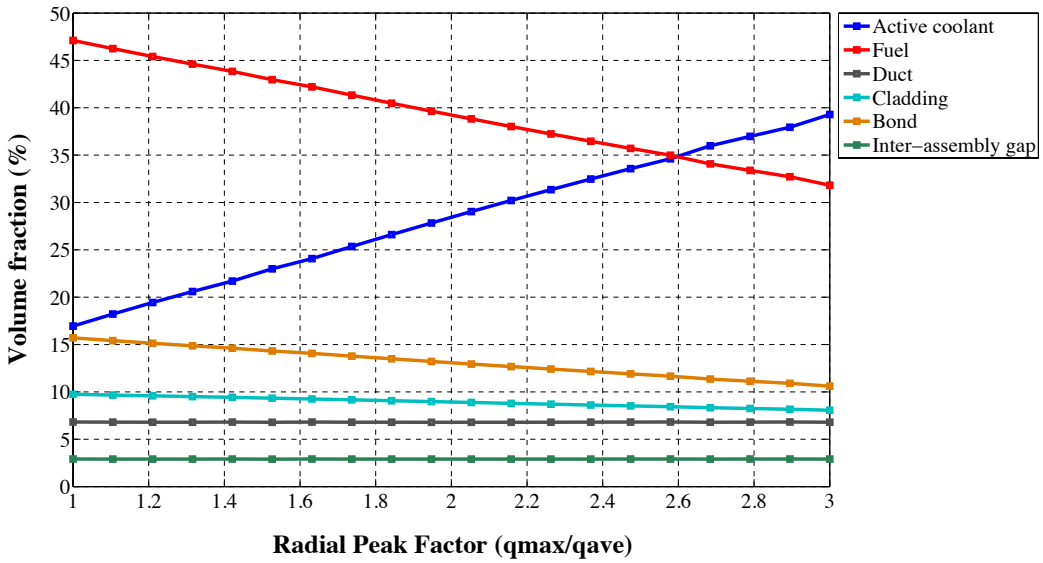

Figure 7.24: Volume fraction output plot of a parametric study in ADOPT

The ADOPT code has no built-in function for plotting the geometry of the fuel assembly designs it produces. Instead it utilizes the plotting functions built-in to the neutron transport codes Serpent [47] and MCNP [153]. One output option is to create a Serpent/MCNP input file of a single fuel assembly in full geometric detail. Horizontal cuts through fuel assembly

designs, including Assembly Reactivity Control (ARC) system pins in blue, for sodium and LBE-coolants produced by ADOPT and plotted by Serpent are shown in Figure 7.25.

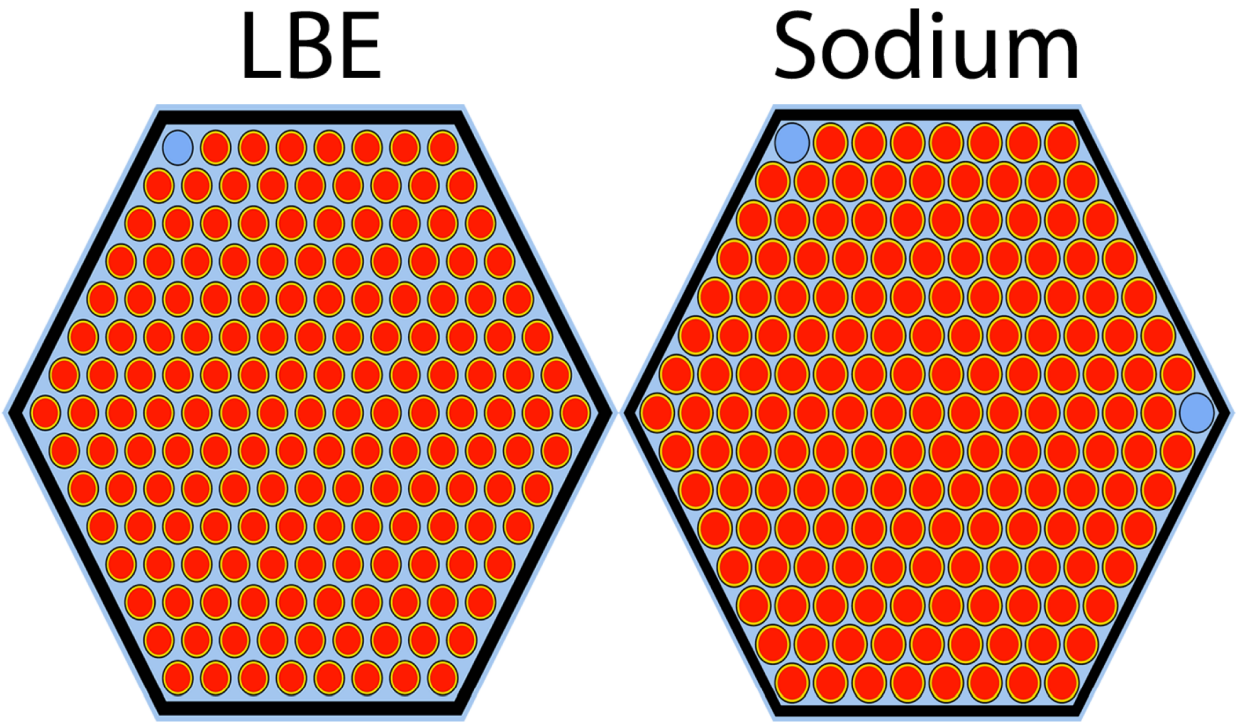

Figure 7.25: Fuel assembly designs produced by ADOPT and plotted by Serpent

Another output option is the creation of full core models for Serpent/MCNP with an arbitrary (user defined) number of homogenized cells. If more than one axial zone is defined, the temperature of each constituent at the axial center of each zone is used to define the atom densities for the neutronic model.

7.9 Calculation accuracy

Accuracy settings in ADOPT refer to the accuracy of the optimization process. A perfectly accurate solution is pushed exactly up to at least one of the set constraints (pressure drop, temperature etc.). If the solution as found by ADOPT does not equal the constraint, this is referred to as an in-accuracy (or a non-optimal solution). The difference between the set constraint and the solution is referred to as the error. To show the effect of calculation accuracy settings, a parametric run was set up to violate the core pressure drop constraint by increasing the length of the fuel. This requires a reduction in the coolant flow velocity and a subsequent opening of the assembly (increasing P/D ratio). This calculation is run for 100 datapoints for fuel lengths between 0.25-5 meters. The total primary loop pressure

drop constraint, set at 1.38 MPa, is violated by the maximum allowable coolant velocity of 12.2 m/s at a fuel length of 1.4 m. The same study was run with the parametric study calculational accuracy setting (CAS_P) set to 0.99, 0.995 and 0.999 respectively. As can be seen in Fig. 7.26, CAS_P=0.99 introduces an error in the form of a non-optimized result, on the order of ∼2.4% (the pressure drop is, at its lowest value, only 97.6% of the allowed value). In Fig. 7.27, CAS_P has been raised to 0.995 and the error reduced to half its previous value: ∼1.2%. At $CAS_P = 0.999$, the "*optimization error*" has fallen below 0.3%. Thus, for precise results, a value of $CAS_P \sim 0.999$ is recommended. These calculations were performed on a MacBook Pro laptop, with 16GB 1600 MHz DDR3 RAM and a Intel Core i7 CPU with a clock frequency of 2.6 GHz. As constraints are violated and parameters are being adjusted, the calculations are using ∼4 GB of the available RAM. The calculational time per datapoint is given in Fig. 7.29. The total time of the calculation is summarized in Table 7.11. With every added decimal 9, as in going from 0.99 to 0.999, the calculational time increases 10 times, the optimization error is reduced by the same amount.

Table 7.11: Parametric study calculation time versus accuracy comparison

CAS_P	Max. optimization error	Time (seconds)
0.990	∼2.4%	275
0.995	∼1.2%	504
0.999	∼0.2%	2744

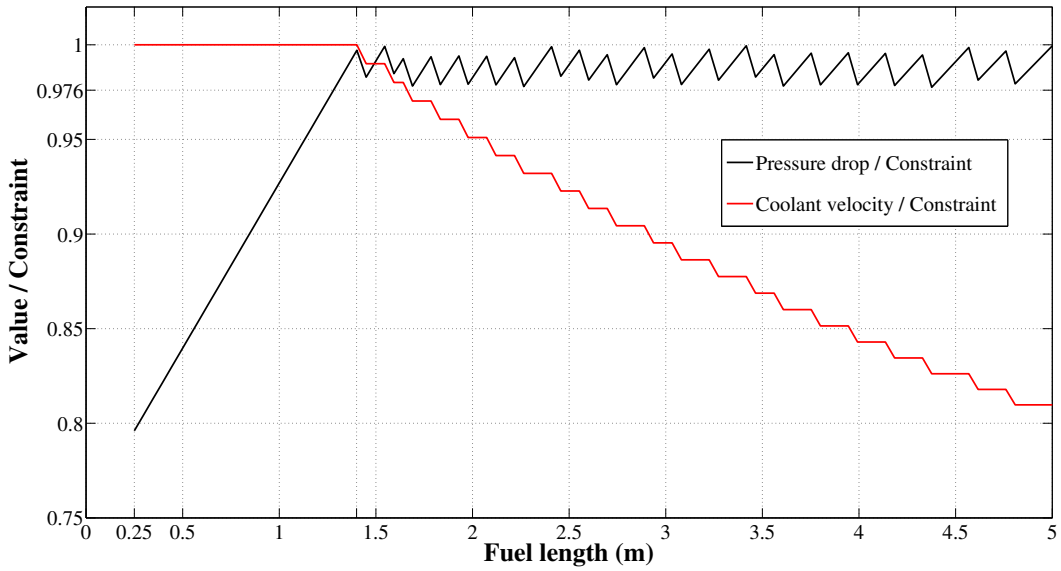

Figure 7.26: Pressure drop constraint violation and coolant velocity adjustment at $C_P = 0.99$

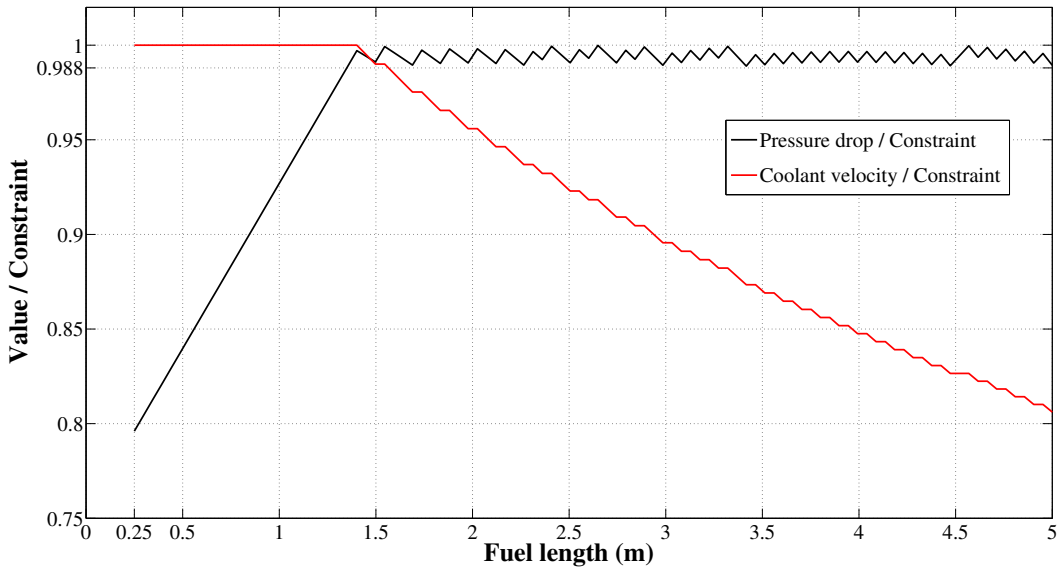

Figure 7.27: Pressure drop constraint violation and coolant velocity adjustment at $C_P = 0.995$

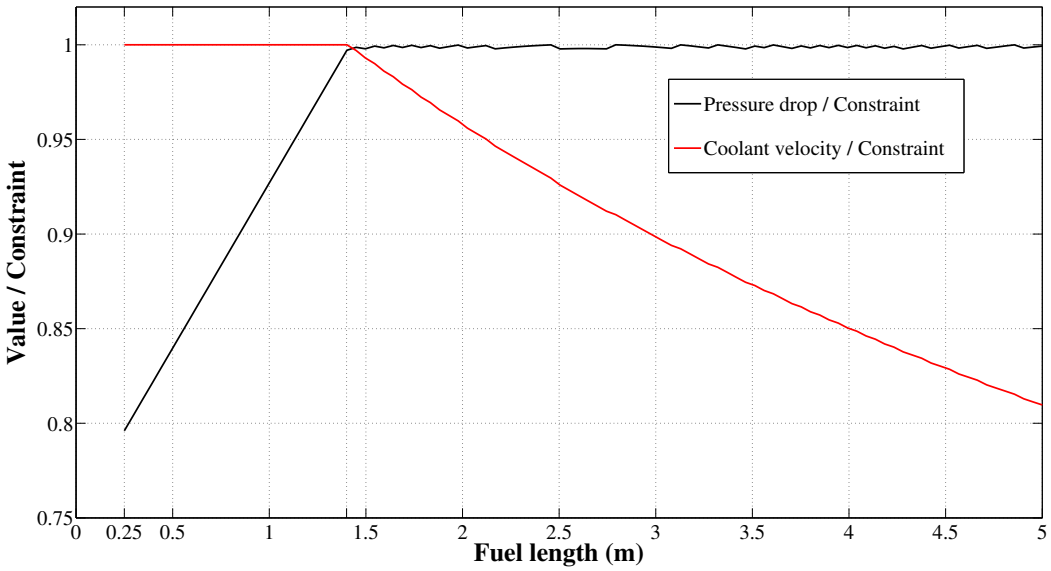

Figure 7.28: Pressure drop constraint violation and coolant velocity adjustment at $C_P = 0.999$

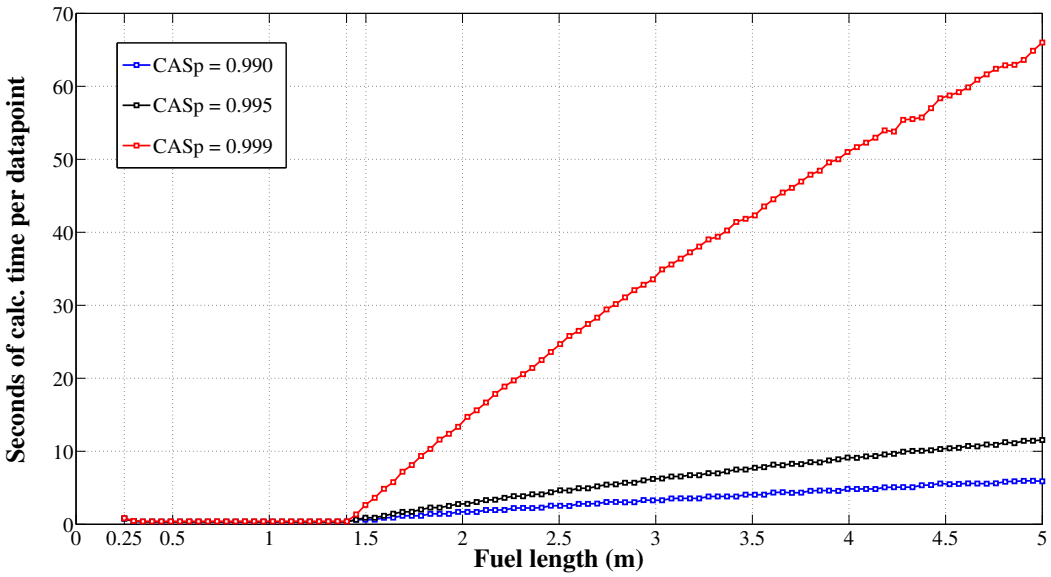

Figure 7.29: Seconds of calculational time per datapoint at different values for CAS_p

7.10 Development plans

Most of the planned development work will focus on improvement of the physics rather than the creation of additional design modules. Near-term emphasis is given to further benchmarking and validating the existing framework. The following improvements are being worked on:

1. More complete physical model for duct wall & inter-assembly gap calculations
2. Oxide layer growth models and their effect on heat transfer
3. Full primary cycle modelling including heat exchangers
4. Explicit calculation of the stresses induced by FCMI
5. Economics module

To increase the utility of ADOPT for core analysis, focus is also being directed to the coupling with neutronic codes, with the greatest emphasis on the Serpent neutron transport code. Reactivity coefficients impact core design choices and cannot be estimated from within ADOPT. Currently, neutron transport code input files for the automatic calculation of the reactivity effect of the actuations of ARC systems and the effect of coolant density can be generated. The following capabilities are being added:

1. Fuel temperature (Doppler) coefficient
2. Axial fuel expansion (using new hybrid calc. model)
3. Radial core expansion (using new hybrid calc. model)

Work done to assist the ADOPT project by mathematician V. Mahadeo of New York University at Stony Brook identified the mathematical solution to the problem of how to distribute an arbitrary number of connected hexagons in a cylindrical-type shape [to be published]. Solutions given by this method are shown in Figure 7.30, clearly showing how an increasing number of appropriately connected hexagons can accurately approximate a cylindrical geometry. Future work will implement this solution in ADOPT to automatically create optimal full-core geometries for neutron transport codes at the assembly-level.

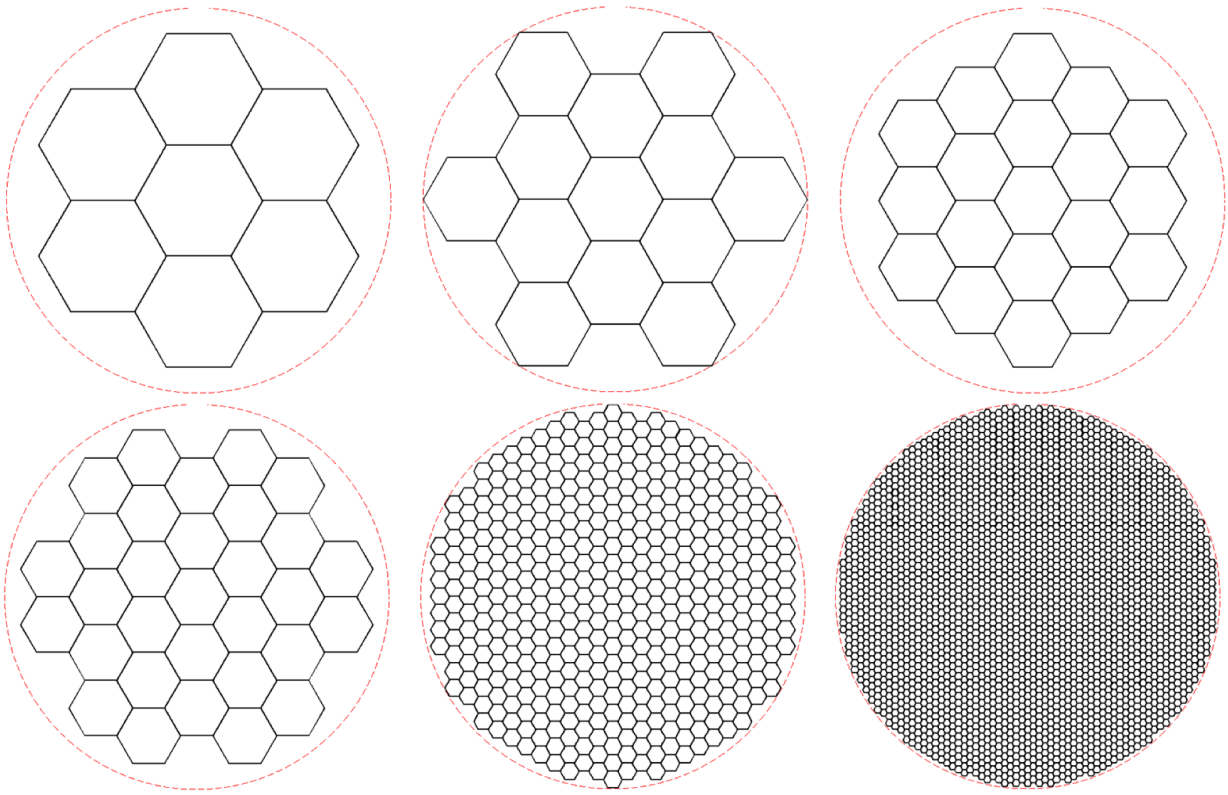

Figure 7.30: ADOPT cylinder representation by connected hexagons

Part IV

The ICE-II experiment

Chapter 8

The Irradiation and Corrosion Experiment II (ICE-II)

8.1 Introduction

Research and development of lead and lead-bismuth eutectic (LBE) cooled nuclear technology is currently pursued worldwide under the framework of generation-IV nuclear programs or spallation neutron source development. As a nuclear reactor coolant, lead and LBE offer significant advantages over other available alternatives. They have no explosive chemical reactions with air, water and steam, very high boiling points (>1600°C) and excellent natural circulation cooling capability compared to alternatives such as sodium-based coolants. Lead-based coolants are especially attractive for use in accelerator-driven systems (ADS) as they can be used as a combined spallation neutron source and coolant. Material research facilities such as the proposed material test stand (MTS) at Los Alamos National Laboratory also utilize LBE as a coolant [172]. The main alternatives for fast reactor coolants are sodium-based liquid metal systems or the use of gaseous coolants. Sodium emerged as the main fast reactor coolant technology and has been the coolant choice for all commercial fast reactors that have been constructed so far worldwide. The major technological hurdles for the widespread adoption of lead-cooled fast reactor (LFR) technology was and continues to be the problem of high temperature corrosion of structural materials [173], liquid metal embrittlement (LME) [174] and liquid metal enhanced creep (LMC) [175]. Discoveries in the Russian lead reactor development program found that careful control of the oxygen content inside a Pb/ LBE melt enables the creation of stable protective oxide layers on steel surfaces, which ignited worldwide interest in conceptual and commercial design of lead/LBE cooled reactor concepts [176]. Major LFR projects currently under development are summarized in Table 8.1.

Table 8.1: Lead and LBE-cooled nuclear concept characteristics.

Region	Concept	Power (MWe)	Clad	Coolant	Clad T.
US	ENHS [177]	50	HT9	LBE	650
	Gen4M [178]	25	HT9	LBE	600
	SSTAR [179]	20-400	Si-FM	Pb	650
	MABR/ABRT [180]	300	HT9	LBE/Pb	600
EU	ELSY [181]	600	T91 (GESA)	Pb	550
	MYRRHA/XT-ADS [182]	20-35	T91	LBE	550
	EFIT [183]	135	T91	LBE	550
	ALFRED [181]	120	12R72 (GESA)	Pb	550
	ELFR [181]	600	T91 (GESA)	Pb	550
Russia	SVBR [184]	75/100	EP823	LBE	650
	BREST [185]	300-1200	Cr12MoVNbB	Pb	650
Japan	CANDLE [186]	Variable	HT9	LBE/Pb	528
	PBWFR [187]	150	N/A	LBE	620
	LSPR [188]	53	HT9	LBE	<700
S. Korea	PEACER [189]	300	HT9	LBE	<700
	BORIS [190]	10	HT9	Pb	600
	PASCAR [191]	35	Fe-Cr-alloy	LBE	<700
Sweden	ELECTRA [192]	0.5 (th)	D9 (GESA)	Pb	480
India	CHTR [193]	0.1 (th)	Graphite	LBE	1000

Experiments testing the corrosion behavior in steels at various temperatures, oxygen contents and flow-rates have been set up at a number of institutions worldwide and the corrosion knowledge base for a number of steels is substantial [173]. However, no experimental setup so far has been designed to test the combined effect of corrosion and irradiation in a high temperature environment under chemistry control. Such tests are necessary in the process of building the experimental database for licensing of any steel for use in a LBE cooled nuclear system. Ideally, experiments would be performed in a fast flux region of an existing nuclear test reactor, a high-flux spallation source or in a materials testing Pb/LBE research reactor. These options, however, present major hurdles both in the form of costs and availability. The first irradiation and corrosion experiment (ICE-I) [194] was an initial attempt at obtaining such data without the use of nuclear reactors or a spallation source, and it utilized a proton particle beam from a conventional ion accelerator as the irradiation

source. The ICE-I experiment operated at a temperature of 300°C, well below the nominal design temperature expected in a commercial nuclear reactor. Also it did not feature oxygen content control and had shielding that limited the beam current to less than 500 nA with concomitant limitation on the dose rate. While the ICE-I experiment did not produce meaningful experimental results, it did form the conceptual basis and outline for the design of the ICE-II station reported here [195].

8.2 Degradation phenomena on candidate nuclear materials by lead-based coolants

All of the major elements present in candidate steels for nuclear applications (iron, chromium, and nickel) have significant solubility in Pb and LBE [196]. While this is not a significant issue in isothermal systems due to the eventual saturation of the elements in the melt, it can lead to significant issues in non-isothermal systems such as reactor coolant loops. In such sys- tems, the dissolution of elements in the hot area (cladding) is continuous, as corrosion products precipitate out of the system at cold areas (heat exchanger) due to their reduced solubility at lower temperatures. This brings fresh unsaturated LBE back to the hot area where further dissolution can take place. This process leads to a reduction of wall thickness on the fuel cladding and hot area piping which can result in the subsequent mechanical failure of the components, as well as a clogging of the flow path inside the pipe in the cold section (heat exchanger) because of deposition. Therefore in order to safely operate coolant loops for extended time periods using lead or LBE, the rates of dissolution and deposition need to be minimized.

When oxygen is present in the coolant medium, oxides will form on the steel surfaces of the reactor internal structures because of the fact that the steel constituent oxides (Fe_3O_4, Cr_2O_3, NiO, etc.) have lower Gibbs free energy than the oxides of the melt (PbO, Bi_2O_3, etc.). The oxide layer prevents direct contact between the steel surface and liquid metal, which helps to mitigate the problems of corrosion, LME and LMC mentioned above. The diffusion rate of the alloying elements and the oxygen through the passivation oxide layer is several orders of magnitude lower than in the bulk steel. Since the surface of the steel is not in contact with the corrosion medium if an oxide layer is present, the corrosion process can be slowed down significantly [197]. It has been found that oxidation of steel in LBE is significantly faster than in air at the same temperature, which seems to be based on a combination of leaching and oxidation. Small pore channels enhancing mass transport through the passivation films were discovered, which explain these issues [198]. To form a stable, dense and adherent passivation layer, careful continuous control of the oxygen activity throughout the coolant loop is a necessity. If the oxygen concentration is kept at saturation, the formation of solid lead oxides may lead to clogging of the coolant flow paths. Such an event led to the failure of one of the first soviet LBE cooled nuclear submarine reactors [199]. In addition,

high oxygen concentrations will lead to thicker oxide scales, which reduces the structural integrity and the heat transport efficiency and significantly increases the probability of spalling off the oxide layer in the flow. Too low oxygen concentrations may leave bare metal exposed to dissolution in the corrosive medium.

The optimal concentration is a function of temperature in the loop as well as the specific types of the steels being used. Steels with sufficient amounts of strong oxide formers (e.g. aluminum or silicon) will easily form very thin, dense and strong oxide layers, which are excellent diffusion barriers. It has been shown that the Russian martensitic alloy EP823 (containing 1.5 wt% Si) behaves better than similar materials without Si [200] and materials containing 5.5 wt% Al do not show any significant sign of corrosion attack [201]. Surface alloying using the Gepulste Elektronen-strahl Anlage (GESA) process, with protection based on a thin layer of FeCrAlY welded to the surface by an intense electron beam, has been shown to provide excellent corrosion resistance to all steels subjected to the treatment [202].

8.3 The effect of irradiation on liquid metal corrosion

The main objective of the ICE-II station is to investigate the effects that irradiation induced damage has on the corrosion behavior of steels exposed to high temperature liquid metals. Incoming high-energy particles create primary knock-on atoms (PKA) leading to displacement cascades and creating point defects (interstitials and vacancies) within the material. The interstitials diffuse fast and are absorbed in the grain boundaries and interfaces, leaving behind net vacancies in the material. The increased steady state vacancy concentration is known to lead to radiation enhanced creep and diffusion, which in some materials can lead to the formation of new phases or grain boundary segregation. Increased vacancy and interstitial density within the oxide layer enhances ion transport from the bulk steel through the oxide layer. Since successful protection against corrosion is based on the decrease in diffusion rates through in-situ grown oxide films, irradiation is expected to be detrimental to corrosion protection.
Candidate materials in LBE environments often form multi-layer oxide structures with various phases depending on the material. It has been found that the main structure formed in ferritic/martensitic steels (such as HT9) is a duplex layer consisting of an inner ironchromium spinel $(Fe_xCr_{1-x})_3O_4$ and outer layer of magnetite (Fe_3O_4) [173]. While the magnetite layer adds corrosion protection to the steel, it can be structurally weak and if it grows too thick it can easily spall off, especially in high flow-velocity Pb/LBE loops. The stronger inner spinel layer provides the main protective function. Irradiation induced defects in the steel enhance the diffusion of chromium to the steel surface. The faster chromium segregation to the surface induced by the irradiation damage may lead to the formation of a more protective scale. At present, there is no experimental data concerning the effects of irradiation damage on high temperature liquid metal corrosion of ironchromium based steels. The initial experimental campaigns of the ICE-II station will determine if the effect of radiation damage is

helpful, hurtful or insignificant for corrosion protection, and help quantify the importance of the processes involved. Future work will investigate the possible effects of the irradiation damage rate on corrosion by comparing results from campaigns using different beam current densities.

8.4 ICE-II design constraints and objectives

The four principal design requirements for the ICE-II experiments were:

8.4.1 Function

Exposure of a sample surface to chemistry controlled liquid metal at temperatures up to 550°C with simultaneous proton beam irradiation in the energy range 36 MeV at a current density up to 0.35 μA/mm^2, with continuous operation during a minimum of 150 h.

8.4.2 Flexibility

Ability to change the corrosion medium and sample type. Ability to control temperature and oxygen content, and the ability to achieve high vacuum (10^{-8} Torr) in the ion beam characterization part of the station.

8.4.3 Safety

To safely achieve high levels of irradiation damage in the sample, the ICE-II station has to been designed with sufficient shielding and the ability for completely remote operation.

8.4.4 Control

Experimental control of temperatures, of the chemical environment and of the energy, current, and spot size of the incoming ion beam. The ICE-II station does not enable continuous flow of the corrosive medium. Ideally, a flowing setup would be more desirable since it is closer to a real application in a spallation source or reactor environment. Instead, LBE in the corrosion chamber was refreshed approximately every 8 h during the four-day experiment.

8.5 ICE-II station components and design

The ICE-II beam end station consists of two main components: the beam and vacuum control system and the corrosion medium handling system. A particle beam enters one side of the ICE-II station and goes through a set of beam characterization equipment that measures the size, position and current of the beam. The beam then hits the sample, which constitutes the interface between the beam system and the corrosion system in the station.

One side of the sample is subjected to high vacuum and is hit by the beam, while the other side of the sample is in contact with the high-temperature corrosion medium. The charged particle beam interacts with the sample and causes irradiation damage in the surface of the sample that is subjected to the corrosion medium, enabling the investigation of the combined effect of irradiation damage and corrosion at the sample surface. The conceptual design of the ICE-II corrosion medium handling system can be seen in Fig. 8.1, and the beam and vacuum control systems are shown in Fig. 8.2. These major components are built up of a set of eight interconnected subsystems, summarized in the following section.

8.6 ICE-II subsystems

8.6.1 Beam characterization

A remotely actuated Faraday cup and a beam profile measurement system ensures that the particle beam, controlled by the slits and focusing lenses of the beam-line, is indeed providing the required beam to the sample. Inside the spherical vacuum chamber, a scintillator detector system is located adjacent to the sample. A microscope camera is centered on the back of the sample to monitor the scintillator output. If the beam is misaligned by more than 1 mm, it hits the scintillator, and is picked up by the camera.

8.6.2 Vacuum control

A roughing pump coupled to a large capacity turbo pump provides vacuum control in the system. Three separate pressure measurements are continuously taken in the system. Two convectron pressure sensors are installed, one on the sphere and one between the roughing pump and the turbo pump. An ion gauge pressure sensor is installed on the sphere to provide measurements of low pressures. This ion gauge is interlock to control the separation valve between the main accelerator and the ICE-II beamline in case of the thin disk sample failure during the irradiation.

8.6.3 Temperature control

A heater-controller unit with eight independent controllers is utilized to provide power and control to all heaters in the system. J-type thermocouples connected to the heater tapes give feedback to the controller unit.

8.6.4 Oxygen content control

A 4% H2, 96% Ar gas cylinder connected to the oxygen control crucible enables the control of oxygen content in the corrosion medium melt. For LBE, pressurization of the crucible to 10 psi with this atmosphere brings the oxygen content down from a saturated level to sub-ppm levels in about 5 h.

8.6.5 Corrosion medium handling

The corrosion medium handling system consists of three separate crucibles. Transport of the medium is done by gravity alone. The general setup of the system can be seen in Fig. 8.1. The top crucible is used for oxygen content control, and provides a conditioned melt to the sample chamber where the experiment is being performed. The volume of corrosion medium present in the sample chamber is deliberately minimized, to reduce the consequences of a potential failure of the sample/vacuum interface. The movement of corrosion medium through the system is facilitated by two pneumatically actuated valves, which allow the flow of corrosion medium when the pipes are heated above the medium melting temperature.

8.6.6 Control panel

A centralized control panel gives control of all system temperatures, gas flows, valves and pressures. The control panel has been placed upstream of the beam-line, to minimize the potential radiation dose to an operator at that location. The pressure control system is shown in Fig. 8.4.

8.6.7 Data collection

A 16-channel data acquisition system is connected to the thermocouples and oxygen sensor voltage outputs of the system. All system data is real-time monitored and stored on a laptop located at the control panel.

8.6.8 Shielding

A shielding system consisting of 4 in. of mixed borated and un-borated polyethylene moderates and absorbs neutrons to reduce the dose from (p,n) reactions in the sample down to acceptable levels. 1-inch thick lead blankets attenuates the gamma dose.

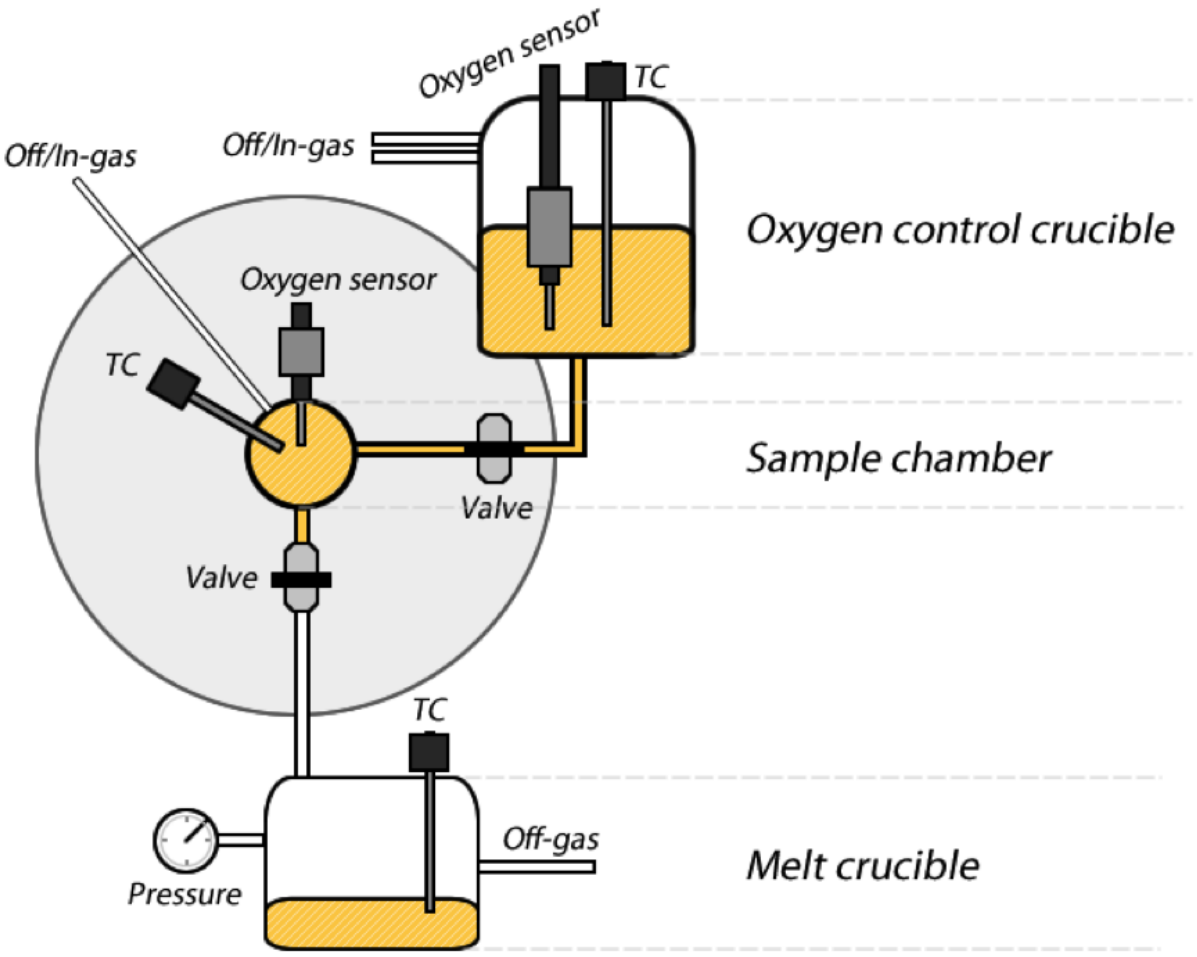

Figure 8.1: Corrosion medium handling system seen from the back, facing the incoming beam line.

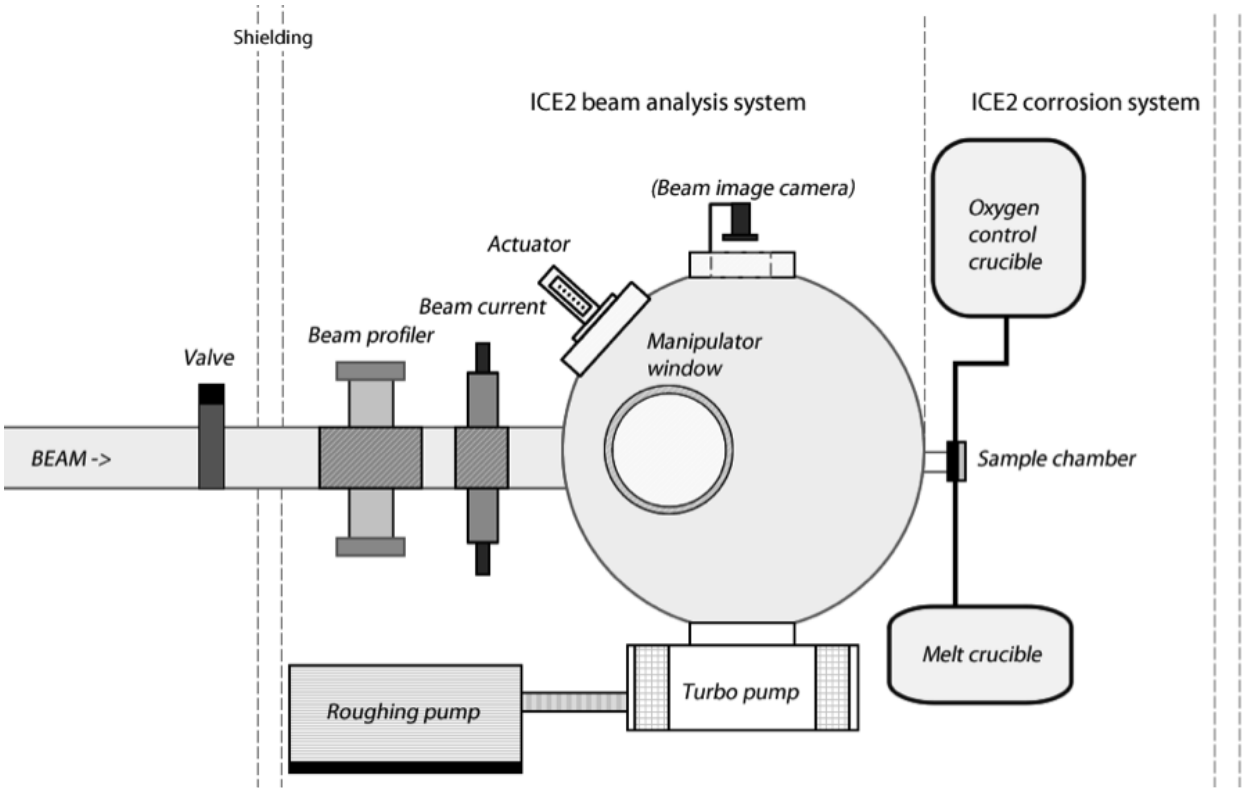

Figure 8.2: Conceptual side view of the ICE-II station.

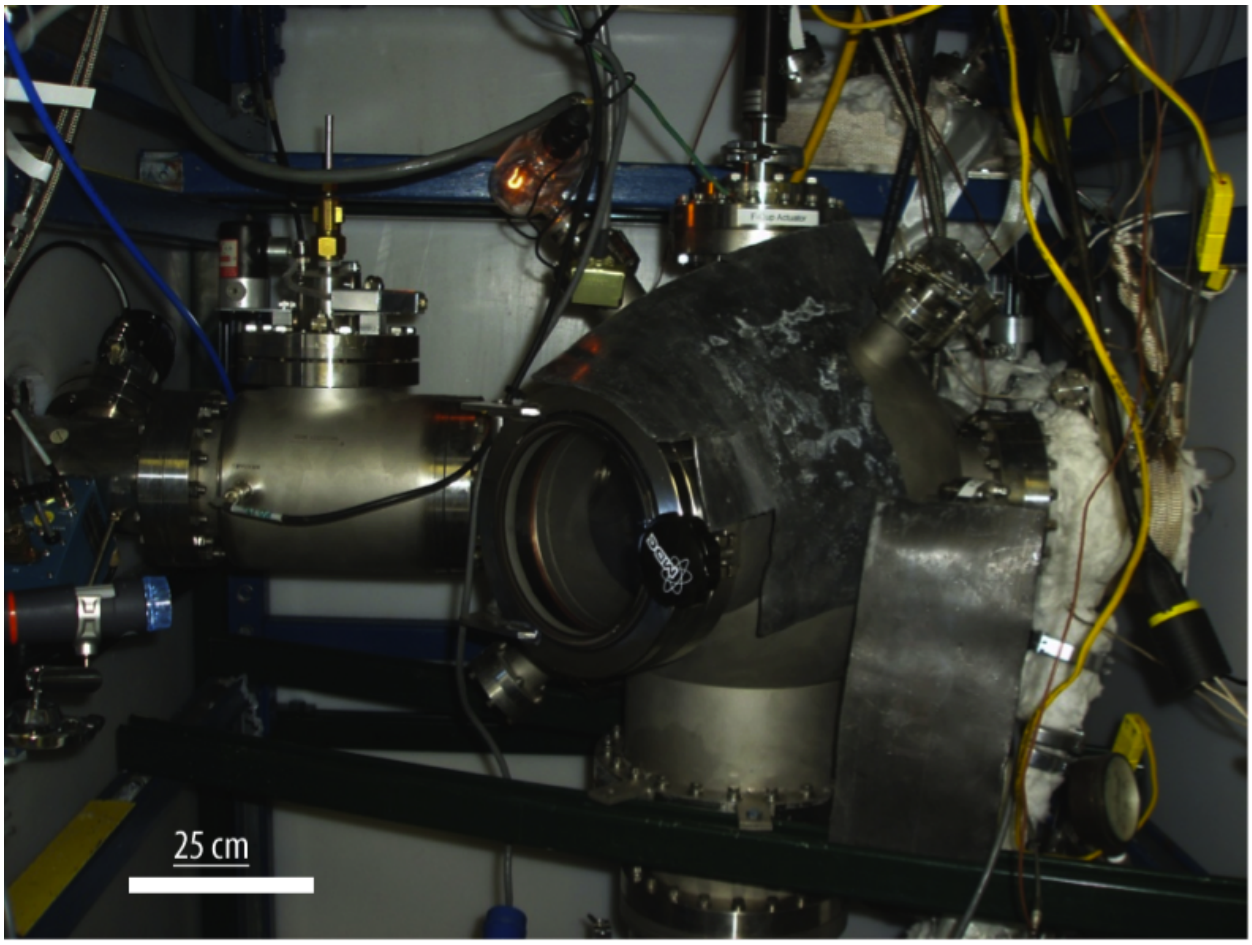

Figure 8.3: Side view of the ICE-II station.

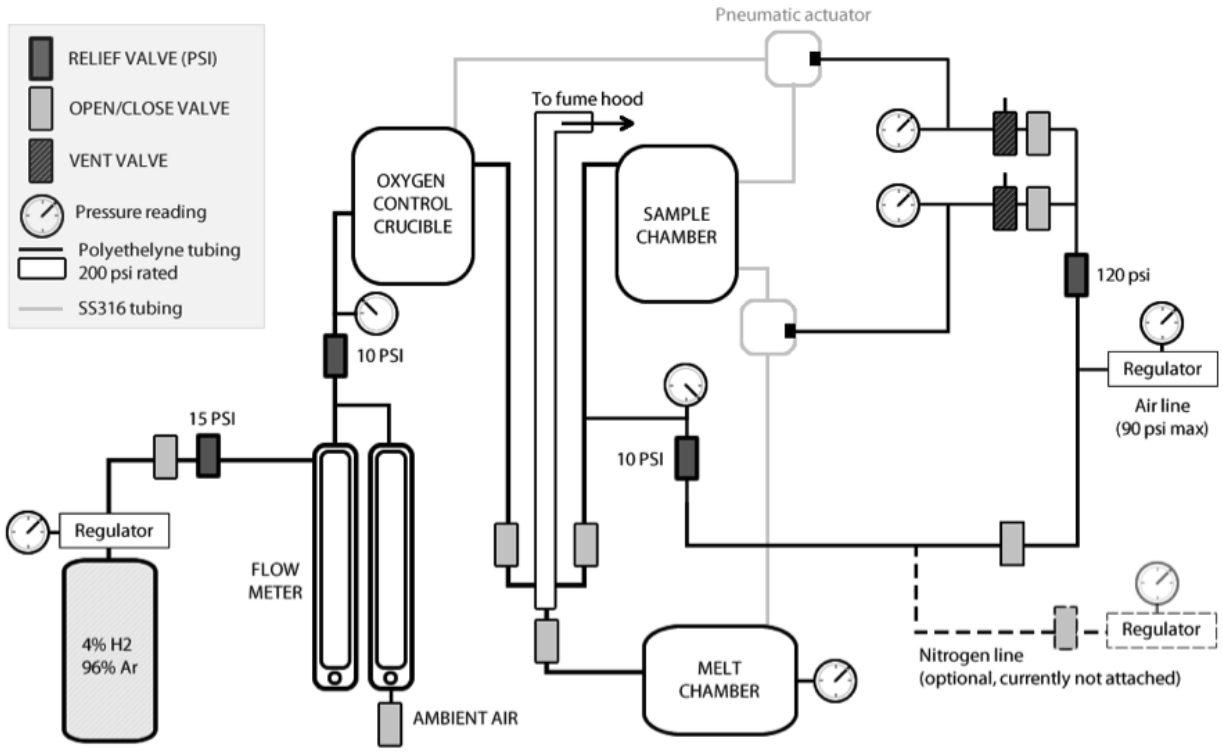

Figure 8.4: Pressure safety system of the ICE-II station.

8.7 Sample design and dose calculation methodology

The samples in ICE-II are subjected to a wide range of radiation damage in the sample surface in each experimental campaign when using charged particle beams. This is made possible by shaping the sample in the form of a concave lens facing the incoming particle beam, as illustrated in Fig. 8.5. The incident angle of the incoming particle beam relative to the curved sample surface is accounted for in the calculations.

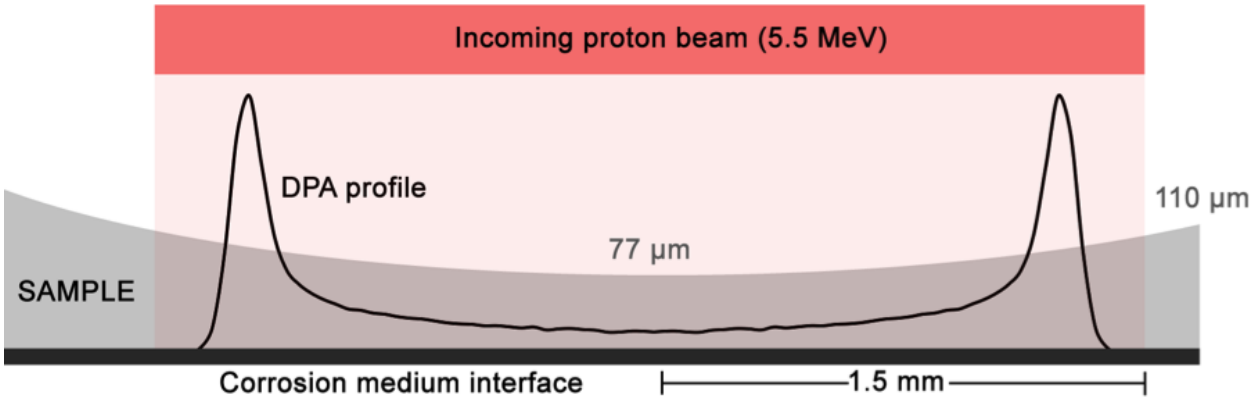

Figure 8.5: Sample design and damage profile.

Determining the optimal shape of the sample requires knowledge and consideration of the following parameters:

- Ion beam type and energy
- Stopping power and ion range in sample material
- Maximum operating current of the irradiation source
- Average grain size of the sample material
- Minimum machinable sample thickness and measurement accuracy
- Dose rate restrictions
- Minimum required sample surface damage (in dpa) for the specific experiment
- Pressure and temperature in the sample chamber
- Yield strength and thermal expansion coefficient of the sample material

The stress induced by the pressure difference between the vacuum and corrosion medium sides must be well below the yield strength of the material. In addition, the differences in thermal expansion between the sample and sampler holder must not induce excessive stress in order to maintain the vacuum seal and sample integrity. These conditions are met with a wide margin in this experiment but may need extra attention if other types of sample materials are used. To maximize the range of irradiation damage in each run, the thickness of the sample needs to be optimized so that the surface of the sample exposed to the corrosion medium receives a wide range of doses, including the full width of the Bragg peak. The penetration depth to the center of the Bragg peak is a function of ion type and energy as well as sample composition and density. The following discussion will focus specifically on

HT9 steel that is used for the demonstration campaign, but the principles apply to any type of steel sample. The ferritic/martensitic steel HT9 (also known as 12Cr1MoVW), developed by the Sandvik Steel Corporation in Sweden, is the reference US fast nuclear reactor cladding steel. As seen in Table 1, HT9 steel has been chosen as cladding material for more than half of the major lead and LBE cooled reactor programs world- wide. It has been in use in several US sodium-cooled test reactors and is currently the only steel that has been brought to levels of fast neutron fluence, corresponding to over 200 dpa while main- taining acceptable material properties (no excessive swelling or embrittlement). The elemental composition of the steel is given in Table 8.2.

Table 8.2: Nominal composition of Sandvik HT9 ferritic/martensitic steel (wt. %).

Fe	Cr	Mo	V	W	C	Si	Mn	Si
84.5	12	1	0.3	0.5	0.2	0.4	0.6	0.5

HT9 has been extensively tested in both flowing and static LBE loops in the US and worldwide, but no combined irradiation and LBE corrosion experiment has previously been performed.

Fig. 8.6 presents SRIM [203] based dose calculations (>500000 particle histories) for different proton energies in HT9 steel.

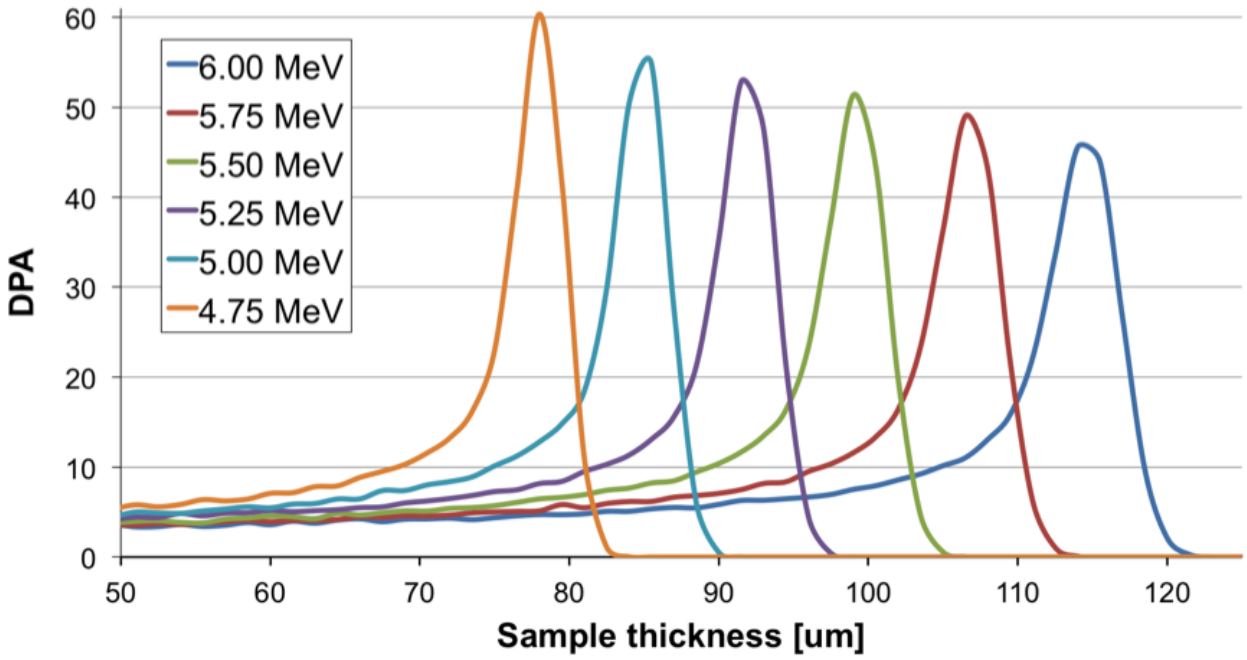

Figure 8.6: Displacements per atoms produced by 3.0 μA H^+ irradiation for 100 h in HT9 steel using a 3 x 3 mm beam-spot.

In the energy range of interest (4.756 MeV) a linear fit to the position of the Bragg peak vs. ion energy gave the following expression:

$$x_{\text{bragg}}(\mu m) = 28.6E - 57.6 \tag{8.1}$$

where x_{bragg} is the penetration depth in micrometers to the Bragg peak, E is the H^+ energy in MeV and the constants are fitting parameters. The actual range of H^+ ions extends 5 micrometers beyond the Bragg peak maximum in HT9, nearly independent of the incoming particle energy in the stated energy range. Theoretically, the full range of irradiation damage from the maximum at the Bragg peak down to zero dose could be achieved by varying the sample thickness exposed to the beam-spot as:

$$x_{\text{bragg}} \leq x_{\text{HT9}} \leq (x_{\text{bragg}} + 5\mu\text{m}) \tag{8.2}$$

where x_{HT9} is the thickness of the HT9 sample in micrometers. If extremely precise machining and measurement equipment are available, this is in fact the optimal thickness variation within the sample exposed to the beam-spot. In practice, machining and measuring a sample with the accuracy needed for such a design is difficult using simple machine-shop tools. Dimple setups similar to what is known for TEM sample preparation and as used in ICE-I [194] or chemical processing (jet polishing) can improve the sample manufacture but are time consuming, specific to each alloy tested, and difficult to conduct. Instead, the approach

used in the ICE-II sample design is to utilize the variation in irradiation damage at lower thicknesses prior to the Bragg peak (see Fig. 8.6), leading to a more relaxed (although still challenging) sample-machining process. This also leads to a significant relaxation of the requirements for beam positioning and beam spatial stability. During the SRIM study it was found that if the sample thickness is reduced by 20 μm from the thickness at the Bragg peak, the damage rates are reduced to approximately 10% of maximum damage at the peak in the energy range of interest (4.75-6.0 MeV). Thus, to achieve the damage range of 10100% across the beam spot in the central part of the beam-spot, as well as the previously mentioned 0100% at the rim, the sample thickness variation needed is given by:

$$(x_{\text{bragg}} - 20\mu\text{m}) \leq x_{\text{HT9}} \leq (x_{\text{bragg}} + 5\mu\text{m}) \tag{8.3}$$

The concave sample design with thickness range in the beam spot mentioned above eases beam positioning, sample machinability and post irradiation examination (PIE). The optimal range of sample thickness for this experimental design is summarized in Table 8.3.

Table 8.3: Optimized HT9 sample beam-spot thickness range.

H^+ Energy (Mev)	4.75	5.0	5.25	5.50	5.75	6.0	10.0
Thickness range (μm)	59-82	66-90	73-97	80-104	87-111	94-118	208-232

Since we operate at high temperature but low pressure, and given that the experience gained in ICE-I [194] based on sample pressure testing leads to concerns about LBE leakage into the accelerator beamline, a limit was imposed for the minimum sample thickness. This limit was set at 30 μm for FM steels, which leads to a minimum ion beam energy of 4 MeV.

To produce a given amount of material damage (dpa), a balance needs to be achieved between irradiation time, current and the size of the beam-spot. The current limit is set by accelerator operation and involves both the technical limitations of the accelerator ion source and beam line as well as the dose rate limits in the facility. Since the dose rate per unit area decreases linearly with beam spot size, the beam-spot should be kept at the practical minimum for efficient operation. For the initial ICE-II experimental campaign, considering beam alignment, focusing and post irradiation examination (PIE) work, the minimum desired beam-spot size was determined to be 3 x 3 mm. The initial experimental campaign of the ICE-II experi- ment aimed at producing a maximum local damage of at least 10 dpa in the sample surface exposed to the LBE. The damage caused by a charged ion beam is inversely related to the particle energy, which means lower particle energies enable more efficient operation. The Pelletron tandem accelerator in use for ICE-II produces a maximum H energy of 6.0 MeV. Machining of the sample for the first ICE-II campaign produced a 77 μm sample at the thinnest point, optimized for a 5.5 MeV particle energy. The damage rate versus thickness/radius is summarized for the initial- campaign ICE-II sample design is seen in Fig. 8.7.

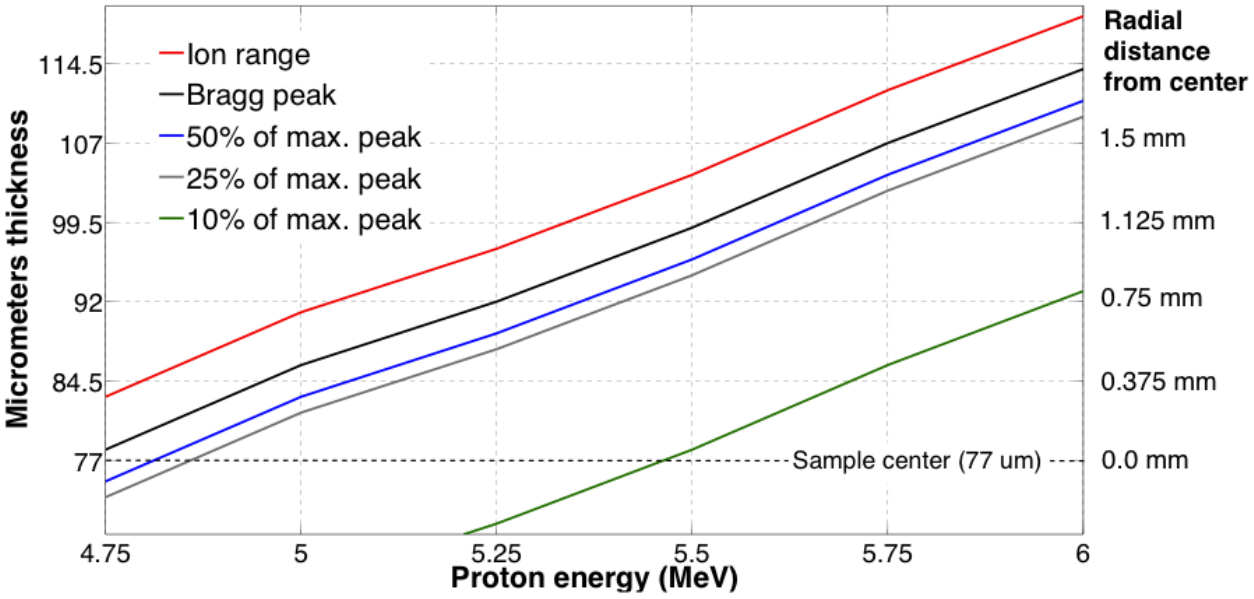

Figure 8.7: HT9 irradiation damage as a function of proton energy and sample thickness.

The final sample design for the initial run of the ICE-II station is shown in Fig. 8.5. The damage profile in Fig. 8.5 was produced by SRIM [203] calculations of 5.5 MeV neutrons on an HT9 target, and shows that the full damage range is present (from zero up to the maximum at the Bragg peak) within the sample surface exposed to the beam.

8.8 Ion beam effects on corrosion medium chemistry

In the central part of the sample, which is designed to be thinner than the ion stopping length, most of the particles of the beam pass through the sample and deposits in the corrosion medium. The chemistry of the corrosion medium can be affected by H-deposition and can form compounds with the dissolved oxygen. An initial estimate of this effect can be made using the following assumptions:

1. All the particles in the beam deposit in the corrosion medium
2. All of the deposited hydrogen eventually reacts with oxygen to form H_2O molecules.

In this model, the amount of hydrogen deposited in the corrosion medium is given by:

$$N_c(s^{-1}) = I_c \times C \tag{8.4}$$

where I_c is the current in amperes and C is the number of elementary charges corresponding to one Coulomb (6.2415×10^{18}). With a particle current of 3.0 μA, the maximum theoretical deposition rate is about 1.9×10^{13} H/s. If all the incoming particles react with the dissolved

oxygen to eventually form H_2O, the oxygen atom depletion rate in the LBE is $9.6 \times 10^{12} s^{-1}$. Considering the LBE atomic density of 2.935×10^{23} atoms/cm^3 at 450°C [204], it is estimated that 0.33 ppb/s oxygen are reacting to form H_2O in a volume of 1 cm^3. For ICE-II with a total LBE volume of 29 cm^3, 0.011 ppb oxygen per second is removed. While this does not seem high, it has to be mentioned that an oxygen concentration of 0.1 ppm in LBE would have its oxygen completely consumed in 3h. Since continuously refreshing the LBE in the experimental chamber would make the experiment significantly more complicated and LBE exchanges every 8-10 h are more reasonable from a practical operations point of view, the oxygen content in fresh LBE should be kept higher than 0.3 ppm.

8.9 First experimental campaign of the ICE-II station

The demonstration run for the ICE-II station used an HT9 steel sample subjected to 450°C LBE at an average oxygen concentration of 2 wt. ppm. The details of the irradiation and corrosion campaign are summarized in Table 8.4.

Table 8.4: ICE-II station first experimental campaign parameters.

Parameter	Value
Sample temperature	450°C
LBE (bulk) temperature	420°C
Particle energy	5.5 MeV
Particle current (average)	2.0 μA
Beam spot-size	3x3 mm
LBE oxygen content	2.0 ppm
Cumulative irradiation time	58 h
Cumulative LBE-melt contact time	80 h
Maximum sample surface dpa	22.1 dpa

The final damage deposition achieved in this experimental campaign, calculated using SRIM with the available current and temperature data, is given in Fig. 8.8. Fig. 8.9 shows the sample from both beam-side (left) and corrosion side (right) after the first campaign, with the effect of irradiation clearly visible on the surface of the center of the sample.

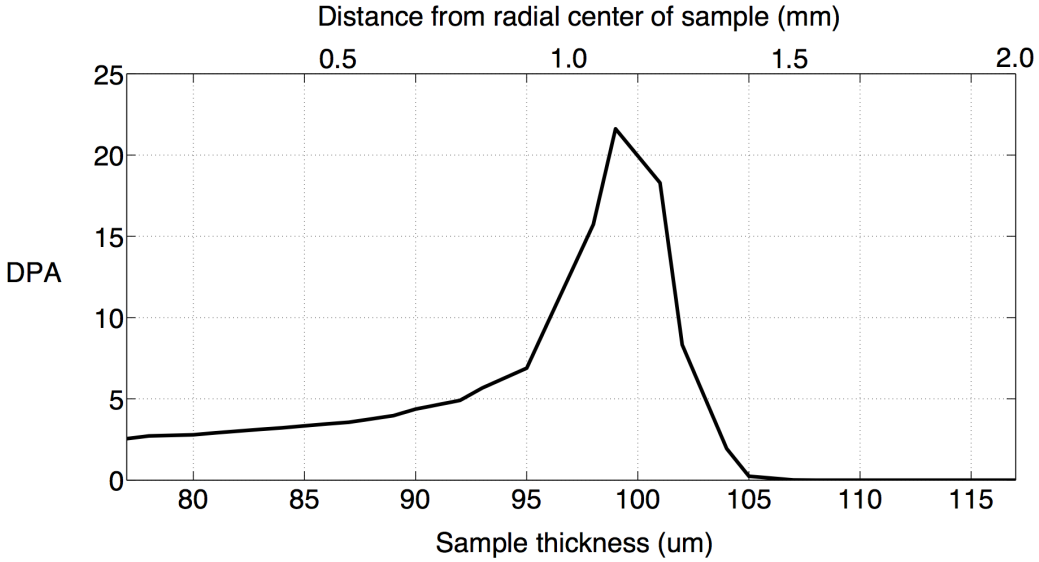

Figure 8.8: SRIM calculation of displacements per atom in the HT9 sample using data from the first ICE-II campaign.

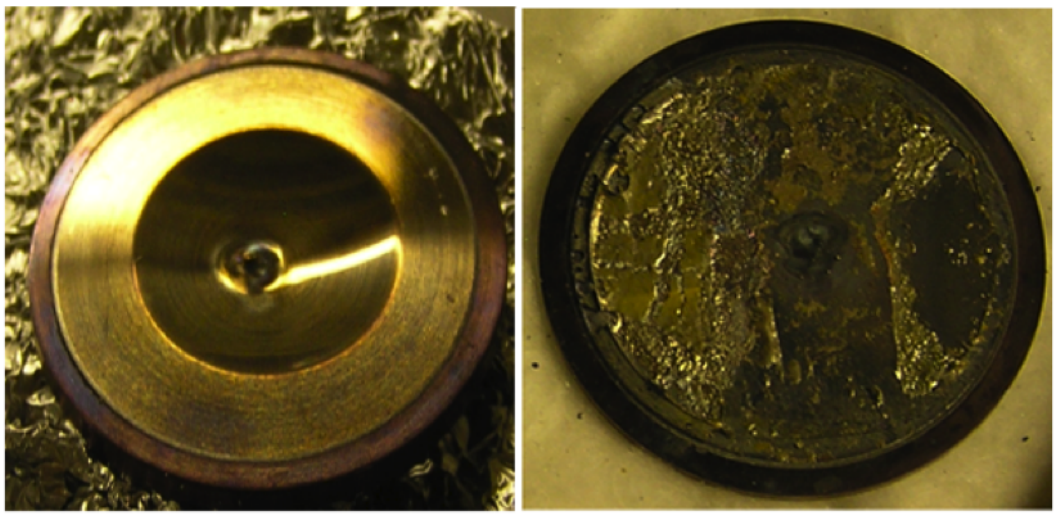

Figure 8.9: HT9 sample after the initial ICE-II experimental campaign (left: beam-side and right: LBE-side)

The shielding material and thickness (4 in. high density poly-ethylene and 1 in. lead blanket) was chosen based on initial MCNPX calculations [205]. The shielded ICE-II station kept the activation level below 1.5 mR/h at 30 cm distance from the station during the entire campaign. Neutrons produced by (p,n) reactions in elements of the steel were the

major dose contributors during the operation. Measurements of sample activation after the experimental campaign showed a combined β and γ-radiation at the sample surface of 15 mR/h. The main isotopes contributing to this dose were, in order of importance: ^{58}Co, ^{56}Co and ^{54}Mn (as seen in Fig. 8.10). The activity was measured again seven days after the end of the experiment. The results indicate a summed average radioactive half-life of the activation products in the steel of 5±0.2 h.

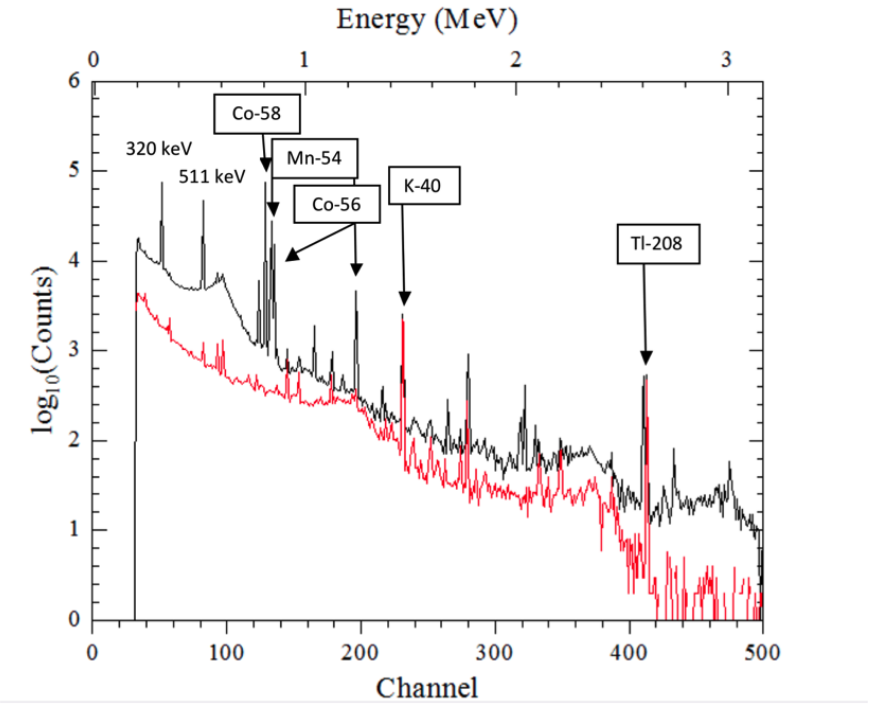

Figure 8.10: ICE-II sample surface gamma activity at the end of the experimental campaign (lower line is background and upper line is with the sample).

8.10 Conclusions and future work

The ICE-II station was designed and built with the purpose of gathering data on the combined effects of irradiation and corrosion on candidate materials for use in liquid metal environments. A first experimental campaign that ended in February of 2012 subjected an HT9 steel sample to a range of irradiation damage between 4 and 22 dpa while in contact with 450°C oxygen controlled liquid lead-bismuth eutectic for nearly 60 h. The data obtained in this and other ICE-II experimental campaigns will form the base for an understanding of the mechanisms that affect corrosion during irradiation and their relative importance. Post irradiation examination is still ongoing, using scanning electron microscopy (SEM) and transmission electron microscopy (TEM) with Energy Dispersive X-ray Spectroscopy (EDS)

to identify and analyze differences in the sample oxide layers at positions exposed to varying amounts of irradiation damage.

8.11 Acknowledgements

The work on ICE-II was carried out under the supervision of Professor Peter Hosemann, with important contributions by Alan Michael Bolind of JAEA and Yongqiang Wang, Joseph Tesmer, Magdalena Serrano De Caro and Mark Bourke of LANL. John Balog of LANL helped with design, construction, and installation of beamline and target chamber shielding unit, and John Blix helped with MCNPX dose calculations. Engang Fu and Carol Haertling assisted during the first irradiation campaign. Antonio Maestas and Rebekkah Aguilar (RP-1) helped with radiation monitoring. The sample was provided by Stuart Maloy. This work was supported by a Los Alamos National Laboratory LDRD fund.

Part V

Conclusions and summary

Chapter 9

Conclusions and summary

9.1 Study objectives

The primary objectives of this study was to find ways of improving the safety, design and performance of large liquid-metal cooled cores, with a specific focus on the breed & burn (B&B) type of reactor systems. B&B systems potentially offer the highest level of uranium utilization of any known type of critical nuclear system without the need for extensive chemical reprocessing in the fuel cycle. The following sections summarize the contributions and findings that were presented in this dissertation.

9.2 Reactivity feedback of large B&B-type liquid-metal cooled reactors

In order to operate on the B&B principle, cores have to maintain a very hard neutron spectrum with a minimized neutron leakage probability. Such core designs were shown to have significant disadvantages in safety performance compared to smaller more conventional fast reactor cores. An extensive analysis of the reactivity feedback mechanisms and the methodology to calculate feedback was performed. The analysis showed that the leakage-based negative feedback components of large fast reactors are significantly smaller than in conventional fast reactor cores. When the nominal leakage probability is small, dimensional changes (such as core axial and radial expansion) that cause an increase in the relative leakage probability has a small impact on core reactivity. In addition, the negative leakage-based component of the coolant density reactivity effect is relatively small, yielding a larger total positive reactivity feedback from an increase in coolant temperature since the positive spectral component is still present. The quasi-static reactivity balance method (QSRB) was used to estimate the impact these effects have on core safety. The analysis showed an unacceptable response of large B&B systems to unprotected transients such as loss of flow and loss of heat sink.

The reactivity feedback analysis led to a new methodology for the calculation of axial fuel expansion reactivity for metallic fuels. As metallic fuel reaches ∼2% burnup, it has swollen radially to make physical contact with the cladding steel of the fuel rod. In current reactivity feedback analysis, the axial expansion of the combined fuel-cladding system is assumed to be controlled entirely by the expansion of the cladding. This assumption is based on the assumption that metallic fuel, once it has swollen by 25-33%, is so porous and mechanically weak that its impact on the combined system can effectively be ignored. Using measurement data on U-Zr alloys from the late 1950s, new correlations for the elastic modulus of metallic fuels were developed. Rather than being so weak it can effectively be ignored, this study showed that the mechanical strength of the fuel is ∼40% that of the cladding steel. At an average operating temperature of 585°C and a porosity of 33%, the estimated elastic modulus of the U-10Zr alloy is ∼67 GPa. For a conventional fuel rod geometry (with a cladding thickness at 5% of the total rod diameter) the conventionally assumed clad-driven expansion assumption is shown to introduce an error of up to 45% in the calculation of the axial expansion coefficient (and the corresponding reactivity effect) of the fuel-clad system.

9.3 Safety systems for large liquid metal cooled reactors

An extensive review of currently available safety systems and design approaches for improved large fast reactor safety was performed. The study concluded that no currently available system or approach meet all performance criteria for implementation in a B&B-type of system. Two completely new systems for inherent fast reactor safety (the ARC systems) are were developed and analysed. The ARC-systems operate passively based only on the laws of nature, have no moving mechanical parts and offer a high level of redundancy. In the event of a temperature excursion, the systems inject a neutron poison (^{6}Li) in to the core and quickly shuts off the neutron chain reaction. As the analysis in this dissertation shows, such systems are necessary to enable the safe and efficient operation of breed & burn type cores. While they are a necessity in breed and burn systems, ARC-systems can be used to improve the safety and economics of any type of fast reactor core.

9.4 Design parameter impact on B&B reactor performance

The *extended neutron balance method* (ENB) was developed based on the neutron balance principle [38]. Using ENB, the impacts of core design variables on the available B&B design space were defined. Uniquely, B&B equilibrium cores require a minimum level of average discharge burnup in the fuel to sustain the breed & burn mode of operation. The major

limiting factor for breed and burn cores is the material damage (as measured in displacements per atom - dpa) associated with this minimum fuel burnup level. With the ENB method, it is possible to develop expressions for the relative change in minimum required discharge burnup at a given level of neutron loss (leakage + loss to control elements) for any set core design parameter. Such expressions were developed for the following variables:

- Fuel type (Oxide, Carbide, Nitride, Metallic)
- Zr-content in metallic fuel
- Feed fuel ^{235}U-fraction
- Fuel/Active coolant volume fraction ratio (and equivalently, P/D-ratio)
- Power density
- Flux level
- Structure/Coolant volume fraction ratio

The effects of varying some of these design parameters in sodium cooled B&B reactors, starting from a reference design of P/D=1.09, ^{235}U in feed fuel of 0.2%, Zr-content in fuel of 6% and a total neutron loss level of 6% is shown in Figure 9.1.

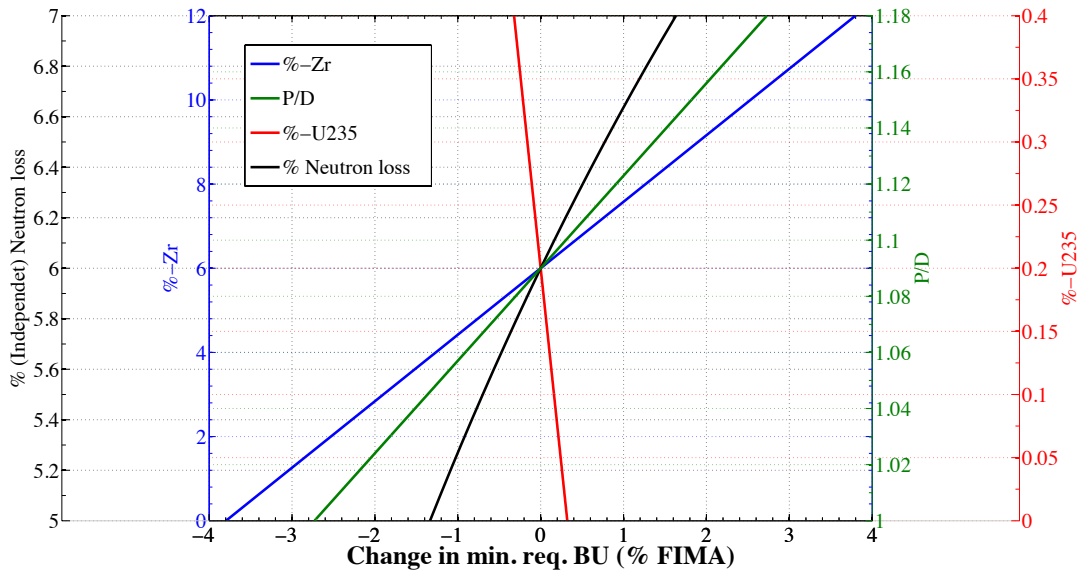

Figure 9.1: The effects of design parameter variation in a sodium-cooled B&B reactor at 6% nominal neutron loss

Once the fuel/active-coolant volume ratio is defined, there is a very limited design space with regards to the structure/coolant volume ratio. The fuel/coolant-volume ratio is effectively defined by the thermal-hydraulic constraints relating to power density. The change in the minimum required burnup for a metallic-fueled sodium-cooled B&B core at 5% total neutron loss can be summarized as:

- $\sim$ 0.54% FIMA increase per wt.% increase of Zr-fraction in fuel
- $\sim$ 0.10% FIMA decrease per 0.1% (absolute) increase in ^{235}U content in feed fuel (ex. 0.2% to 0.3%)
- $\sim$ 0.01% FIMA increase per 1 W/cm^3 increase in peak batch axially averaged volumetric power density

9.5 New fast reactor core design methods

The Assembly Design and OPTimization code (ADOPT) is a comprehensive computer code written to automate the process of designing and analyzing fast reactor fuel assemblies and cores. The default version of the code finds a fuel assembly design that maximizes the fuel volume fraction in the core while adhering to set constraints for all component temperatures, pressure drop, coolant velocity and structural integrity limits, subjected to a specified assembly peak power level. When provided with power peaking factors, ADOPT can be used very effectively as the first step in the design process of fast reactor cores that offer the maximum possible breeding ratio, which is proportional to the fuel volume fraction. To design fast reactor cores with different objectives, one can start with a neutronic analysis to find material volume fractions that provide the sought core performance. ADOPT can then reverse-engineer a fuel assembly design with the desired volume fractions that abide by all the thermal-hydraulic and structural constraints.
The code consists of a collection of coupled modules that perform separate calculational tasks. These modules are a mix of new solvers & methods developed specifically for this purpose and modules using methods that are already well established and widely published. New models were developed to calculate fuel rod dimensions & pitch, cladding thickness, optimized fuel rod locations within a fuel assembly, assembly duct wall thickness & inter-assembly gap and optimal coolant chemistry (for certain coolants). The code then provides the necessary input files of the produced geometry for a full core model to neutron transport codes such as MCNP [153] and Serpent [47] at a user-defined level of heterogeneity.

9.6 B&B limits of performance and the optimum core shape

Using the full capabilities of the ADOPT code coupled to the FAST-BEAU equilibrium cycle code [167], the optimum breed and burn core height and diameter (i.e. the core shape) and the impact that the power density has on core performance was estimated. In order to make a fair comparison between various core shapes, some parameters were set and were not allowed to vary between the different designs. Most important for the shape, the total active core volume was kept constant at 20 m^3. A uniform outer assembly size as well as duct wall thickness and inter-assembly gap was used for all cores, while the number of assemblies varies with the core diameter. Core shapes with height-to-diameter (H/D) ratios in the span 0.26-1.30 were analysed in this study. The optimum balance between neutron leakage probability and core actinide density was found for cores with H/D $\approx$ 0.50. For a 20 m^3 core volume, this means an optimal fuel height and core diameter of 185 and 370 cm respectively.

Core performance is significantly degraded with increasing power density, but there is no noticeable change in the optimal core shape. The maximum batch power density at which a 20 m^3-volume B&B core is able to operate an equilibrium cycle on depleted uranium fuel with a peak cladding damage below 600 dpa is estimated at $\sim$260 W/cm^3. With a radial power peaking level of 2.0, this corresponds to a core-averaged volumetric power density of 130 W/cm^3 and a total thermal power level of 2600 MW. If the core volume is increased, a higher power density may be possible due to decreasing leakage.

9.7 The effect of irradiation on corrosion protection of steel exposed to heavy liquid metals

The second Irradiation and Corrosion Experiment (ICE-II) was designed and built with the main objective to investigate the effects that irradiation induced damage has on the corrosion behavior of steels exposed to high temperature liquid metals. A first experimental campaign that ended in February of 2012 subjected an HT9 steel sample to a range of irradiation damage between 4 and 22 dpa while in contact with 450°C oxygen controlled liquid lead-bismuth eutectic for nearly 60 h. The data obtained in this and other ICE-II experimental campaigns will form the base for an understanding of the mechanisms that affect corrosion during irradiation and their relative importance. Post irradiation examination is still ongoing, using scanning electron microscopy (SEM) and transmission electron microscopy (TEM) with Energy Dispersive X-ray Spectroscopy (EDS) to identify and analyze differences in the sample oxide layers at positions exposed to varying amounts of irradiation damage.

9.8 Summary conclusions and future directions

The studies presented in this dissertation have attempted to tackle some of the major challenges present in large liquid-metal cooled reactor design. The ARC-systems are a highly promising new type of safety system, but requires extensive further study and experimental verification before their real potential can be confidently determined. The ADOPT code was developed to automate the fast reactor core design process. While it is a highly useful utility in its current state, further development of both the existing models and the scope of its capabilities are needed. Most importantly, an extensive validation and benchmarking campaign of the code must be conducted with external partners. The ICE-II experimental station makes it possible to examine the effects of irradiation on the corrosion protection of steel exposed to liquid metals. Post-irradiation examination needs to be performed to quantify the effects seen on the sample from the first experimental run of the station.

Bibliography

[1] US Energy Information Administration. *International Energy Outlook 2011*. Tech. rep. EIA, 2011.

[2] Clean Air Taskforce. *The Toll from Coal*. Tech. rep. CATF, 2010.

[3] The Health and Environment Alliance. *THE UNPAID HEALTH BILL, How coal power plants make us sick*. Tech. rep. HEAL, 2013.

[4] P. BOWRING. *Nuclear or Coal?* Tech. rep. The New York Times, 2011.

[5] T. PLAFKER. *Chinese coal industry in need of a helping hand*. Tech. rep. The New York Times, 2007.

[6] E. SHUSTER. *Tracking New Coal-Fired Power Plants*. Tech. rep. National Energy Technology Laboratory, 2012.

[7] T. K. KIM and T. A. TAIWO. *Systematic Evaluation of Uranium Utilization in Nuclear Systems*. Tech. rep. Argonne National Laboratory, 2010.

[8] S. M. FEINBERG and E.P. KUNEGIN. "Discussion comment". In: *Proceedings of the International Conference on the Peaceful Uses for Atomic Energy* 9.2 (1958), p. 447.

[9] E. GREENSPAN. "The encapsulated nuclear heat source reactor for low-waste proliferation-resistant nuclear energy". In: *Progress in Nuclear Energy* 40.3-4 (2002), pp. 431–439.

[10] H. SEKIMOTO and A. NAGATA. "Performance optimization of the CANDLE reactor for nuclear energy sustainability". In: *Energy Conversion and Management* 51.9 (2010), pp. 1788–1791.

[11] E. GREENSPAN. "A Phased Development of Breed-and-Burn Reactors for Enhanced Nuclear Energy Sustainability". In: *Sustainability* 4.10 (2012), pp. 2745–2764.

[12] L. P. FEOKTISTOV. *Analysis of a Concept of Reactor Physical Safety*. Tech. rep. Kurchatov Institute for Atomic Energy, 1988.

[13] L. P. FEOKTISTOV. "Neutron-induced fission wave". In: *Soviet Physics Doklady* (1989).

[14] V. Y. GOLDIN and D. Y. ANISTRATOV. "Fast reactor in a self-regulated neutron-nuclear regime". In: *Mat. Modelir* (1995).

[15] E. TELLER, M. ISHIKAWA, and L. WOOD. "Completely automated nuclear reactors for long-term operation". In: *International Conference on Emerging Nuclear Energy Systems, Obninsk, Russia* (1996).

[16] S. HATTORI, A. MINATO, and N. HANDA. "Present Design Features of the Super Safe, Small and Simple Reactor". In: *Potential of Small Nuclear Reactors for Future Clean and Safe Energy Sources* (1992), pp. 225–234.

[17] H. SEKIMOTO, K. RYU, and Y. YOSHIKANE. "CANDLE: The New Burnup Strategy". In: *Nuclear Science and Engineering* 139.3 (2001).

[18] N. UEDA et al. "Design Study of Sodium Cooled Small Fast Reactor". In: *GENES4/ANP2003, Sep. 15-19, 2003, Kyoto, JAPAN* ().

[19] H. CHOI, R. W. SCHLEICHER, and P. GUPTA. "A Compact Gas-Cooled Fast Reactor with an Ultra-Long Fuel Cycle". In: *Science and Technology of Nuclear Installations* 2013.1-3 (2013), pp. 1–10.

[20] J. PARMENTOLA and J. RAWLS. "Energy Multiplier Module (EM2) Capping the Waste Problem and Using the Energy in U-238". In: *15th International Conference on Emerging Nuclear Energy Systems (ICENES2011), San Francisco, May 15-1* (2011).

[21] Y. KIM and D. HARTANTO. "A Compact Sodium-cooled Traveling Wave Reactor". In: *Transaction of Korean Nuclear Society Autumn Meeting, Gyeongju, October* (2011).

[22] D. HARTANTO and Y. KIM. "Physics and Design Studies for a Small Breed-and-Burn Reactor". In: *Transactions of the American Nuclear Society vol. 107, San Diego, CA, USA, November 11-15* (2012).

[23] H. Van DAM. "Self-stabilizing criticality waves". In: *Annals of Nuclear Energy* (2000).

[24] W. SEIFRITZ. "Solitary burn-up waves in a multiplying medium". In: *Kerntechnik* 65.5-6 (2000), pp. 261–264.

[25] S. FOMIN et al. "Investigation of self-organization of the non-linear nuclear burning regime in fast neutron reactors". In: *Annals of Nuclear Energy* 32.13 (2005), pp. 1435–1456.

[26] X N Chen, E Kiefhaber, and W Maschek. "Neutronic model and its solitary wave solutions for a CANDLE reactor". In: *Proceeding of ICENES 2005* (2005).

[27] K. FUCHS and H. HESSEL. "THE POSSIBILITIES FOR THE OPERATION OF A NATURAL URANIUM BREEDER REACTOR WITHOUT FUEL ELEMENT PREPARATION". In: *Kernenergie (East Germany)* 4 (1961).

[28] B. ATEFI. "Evaluation of the breed/burn fast reactor concept". PhD thesis. Massachussets Institute of Tecnnology, 1979.

[29] H.J.C KOUTS, G.J. FISCHER, and R.J. CERBONE. *Fast mixed spectrum reactor concept*. Tech. rep. Brookhaven National Laboratory, 1979.

[30] W.T. LOH. "An evaluation of the fast-mixed spectrum reactor". MA thesis. Massachussets Institute of Tecnnology, 1980.

[31] R. AVERY et al. *Coupled fast-thermal power breeder critical experiment*. Tech. rep. Argonne National Laboratory, 1958.

[32] J. S. SLESAREV, V. A. STUKALOV, and V.A. SUBBOTIN. "Problems of development of fast reactors self-fuel-provision without fuel reprocessing". In: *Atomkernenergie, Kerntechnik* 45 (1984), pp. 58–60.

[33] G. I. TOSHINSKY. "Operation in the Nuclear Cycle without Fuel Reprocessing". In: *Proceedings of the International Topical Meeting on Advanced Reactors Safety, Orlando, Florida, USA* (1997).

[34] P. HEJZLAR et. al. "Traveling Wave Reactor Development Program Overview". In: *Proc. of ICAPP 2013, Seogwipo, Jeju-do, South Korea* (2013).

[35] M. J. DRISCOLL et al. *Engineering and Physics Optimization of Breed and Burn Fast Reactor Systems*. Tech. rep. MIT, UNLV, INL, 2005.

[36] P. YARSKY. "Core design and reactor physics of a breed and burn gas-cooled fast reactor". Ph.D. Thesis. MIT, 2005.

[37] R. PETROSKI. "General analysis of breed-and-burn reactors and limited-separations fuel cycles". Ph.D. Thesis. MIT, 2011.

[38] F. HEIDET and E. GREENSPAN. "Breed-and-Burn Depleted Uranium In Fast Reactors Without Actinides Separation". In: *PHYSOR 2010 Advances in Reactor Physics to Power the Nuclear Renaissance, Pittsburgh, Pennsylvania, USA: American Nuclear Society* (2010).

[39] S. A. QVIST and E. GREENSPAN. "Inherent Safety of Minimum Burnup Breed-and-Burn Reactors". In: *Proceedings of ICAPP12, Chicago, IL, June 24-28* 362.2-3 (2012), pp. 235–247.

[40] S. A. QVIST and E. GREENSPAN. "Reactivity feedbacks of breed-and-burn cores". In: *American Nuclear Society Annual Meeting, Hollywood, FL, US* (2011).

[41] S. A. QVIST. "Reactivity Coefficients of the Berkeley Traveling-Wave Reactor". MSc. Thesis. 2010.

[42] E. GREENSPAN and F. HEIDET. "Energy sustainability and economic stability with Breed and Burn reactors". In: *Progress in Nuclear Energy* 53.7 (2011), pp. 794–799.

[43] F. HEIDET and E. GREENSPAN. "Maximum Fuel Utilization in Fast Reactors without Chemical Reprocessing". In: *Proc. of Global09, Paris, France, September 6-11* (2009).

[44] F. HEIDET. "Maximum Fuel Utilization in Advanced Fast Reactors without Actinides Separation". Ph.D. Thesis. University of California Berkeley, 2010.

[45] S. GONZALEZ. "Minimum Burnup Pebble-Bed Breed-and-Burn Reactor". MSc. Thesis. 2012.

[46] F. HEIDET, R. PETROSKI, and E. GREENSPAN. "Minimum burnup required for sustainable operation of fast reactors without recycling". In: *Proc. of the International Conference on Fast Reactors and Related Fuel Cycles: Challenges and Opportunities, Kyoto, Japan, 7-11 December* (2009).

[47] J. LEPPANEN. *PSG2/Serpent A Continuous-energy Monte Carlo Reactor Physics Burnup Calculation Code*. Tech. rep. VTT, 2009.

[48] M. B. CHADWICK et. al. "ENDF/B-VII. 0: Next generation evaluated nuclear data library for nuclear science and technology". In: *Nuclear Data Sheets* 107.12 (2006), pp. 2931–3060.

[49] K. LEVENBERG. "A Method for the Solution of Certain Non-Linear Problems in Least Squares". In: *Quarterly of Applied Mathematics* 2 (1944), pp. 164–168.

[50] S. GLASSTONE and A. SESONSKE. *Nuclear Reactor Engineering: Third Edition*. Van Nostrand Reinhold Company, New York, 1981.

[51] C. BONILLA. *Nuclear Engineering*. McGraw-Hill, New York, 1957.

[52] R. STAMM'LER and M. ABBATE. *Methods of Steady-State Reactor Physics in Nuclear Design*. Academic Press, New York, 1983.

[53] R.A. KNEIF. *Nuclear Energy Technology: Theory and Practice of Commercial Nuclear Power*. McGraw-Hill Book Company, New York, 1981.

[54] T-2 Nuclear Information Service. Tech. rep. Los Alamos National Laboratory, 2013.

[55] A. E. WALTAR, D. R. TODD, and P. V. TSVETKOV. *Fast Spectrum Reactors*. Springer, New York, 2012.

[56] X-C DING et al. "High enrichment of 15N isotope by ion exchange for nitride fuel development". In: *Progress in Nuclear Energy* 50.2-6 (2008), pp. 504–509.

[57] Nuclear Data Center http://atom.kaeri.re.kr. Tech. rep. Korea Atomic Energy Research Institute, 2013.

[58] R. PETROSKI, B. FORGET, and C. FORSBERG. "Neutronic evaluation of breed-and-burn reactor fuel types using an infinite-medium depletion approximation". In: *Proceedings of Physor 2010, Pittsburgh, PA, May 914* (2010).

[59] E. SCHNEIDER, M. DEINERT, and A. SCOPATZ. "Depleted and Recycleable Uranium in the United States: Inventories and Options". In: *Proceedings of GLOBAL 07, Boise, Idaho, US* (2007).

[60] E. E. LEWIS. *Fundamentals of Nuclear Reactor Physics*. Elsevier Inc., 1908.

[61] H. van DAM. "Physics of nuclear reactor safety". In: *Reports on Progress in Physics* 55.11 (1999), pp. 2025–2077.

[62] K. HANNERZ. "Applying PIUS to Power Generation: The Secure-P LW". In: *Nuclear Engineering International* 28 (1983), p. 349.

[63] H.P. PLANCHON, G.H. GOLDEN, and J.J. SACKETT. "Demonstration of Passive Safety Features in EBR-II". In: *CONF-870415-3* (1987).

[64] W. S. YANG. "Fast reactor physics and computational methods". In: *Nuclear Engineering and Technology* 44 (2011).

[65] J. E. LYNN, F. W. K. Firk, and M. C. MOXON. "The 2.85 keV neutron resonance of sodium". In: *Nuclear Physics* 5 (1958), pp. 603–614.

[66] P.F. ROSE. *ENDF-201, ENDF/B-VI Summary Documentation, BNL-NCS-17541, 4th Edition*. Tech. rep. Brookhaven National Laboratory, 1991.

[67] H.H. Hummel and D. OKRENT. *Reactivity coefficients in large fast power reactors*. American Nuclear Society, 1970.

[68] G. J. Van TUYLE et al. *Summary of advanced LMR (Liquid Metal Reactor) evaluations: PRISM (Power Reactor Inherently Safe Module) and SAFR (Sodium Advanced Fast Reactor)*. Tech. rep. Brookhaven National Laboratory (BNL), Upton, NY, 1989.

[69] R. HILL. *Fast Reactor Physics and Core Design*. Tech. rep. Argonne National Laboratory. Argonne, IL, US., 2007.

[70] D.C WADE and E. K. FUJITA. "Trends vs. reactor size of passive reactivity shutdown and control performance". In: *International reactor physics conference, Jackson Hole, WY, USA* (1987).

[71] S. B. SHIKOV. "Calculating the effect of a change in dimensions on the critical mass of a fast reactor using the perturbation theory". In: *Atomic Energy* 6 (1959), pp. 162–168.

[72] M. REED, K. SMITH, and B. FORGET. "The Virtual Density Principle of Neutronics and Its Application to Geometric Perturbation Theory". In: *Transactions of the American Nuclear Society Winter Meeting* (2012).

[73] J. T. GOORLEY et al. *Initial MCNP6 Release Overview - MCNP6 Beta 3*. Tech. rep. Los Alamos National Laboratory, 2012.

[74] T. TAIWO (Department Manager for Nuclear Systems Analysis). *Private communication*. Tech. rep. Argonne National Laboratory, 2010.

[75] T. FANNING (Engineering Simulation and Safety Analysis Section). *SASSYS/SAS4A training, Stockholm, 2013*. Tech. rep. Argonne National Laboratory, 2013.

[76] P. HEJZLAR and C. B. DAVIS. "Performance of the lead-alloy-cooled reactor concept balanced for actinide burning and electricity production". In: *Nuclear Technology* 147.3 (2004).

[77] KAERI. *SSC-K Code Users Manual (Rev.1)*. Tech. rep. Korea Atomic Energy Research Institute, 2002.

[78] T. SATHIYASHEELA, A. RIYAS, and R. SUKANYA. "Inherent safety aspects of metal fuelled FBR". In: *Nuclear Engineering and Design* (Article in press (march 2013) (2013).

[79] A.V. KOZLOV et al. "The Effect of Void Swelling on Electrical Resistance and Elastic Moduli in Austenitic Steels". In: *Effects of Radiation on Materials: 21st International Symposium, ASTM STP 1447, West Conshohocken, PA, US* (2003).

[80] H. OHTA et al. "Development of Fast Reactor Metal Fuels Containing Minor Actinides". In: *Journal of Nuclear Science and Technology* 48.4 (2011), pp. 654–661.

[81] NEA/OECD. "Fuels and Materials for Transmutation - A Status Report". In: *Tech. report* (2005).

[82] Y.S. KIM, G.L. HOFMAN, and J.S. CHEON. "Mechanical Modeling of U-Mo Fuel Swelling in Monolithic Plates". In: *RERTR 2012 - 34th INTERNATIONAL MEETING ON REDUCED ENRICHMENT FOR RESEARCH AND TEST REACTORS* (2009).

[83] T. SOFU and J.M. KRAMER. "FPIN2: Pre-Failure Metal Fuel Pin Behavior Model". In: *Nuclear Engineering Division, Argonne National Laboratory* (2012).

[84] Argonne National Laboratory Nuclear Engineering Division. "DEFORM-4: Steady-State and Transient Pre-Failure Pin Behavior". In: (2012).

[85] J. E. CALAHAN et al. "SASSYS/SAS4A Manual, Chapter 4. Reactor Point Kinetics, Decay Heat, and Reactivity Feedback". In: *Argonne National Laboratory* (2012), pp. 1–64.

[86] T. KOBAYASHI et al. "Developement of the SESAME metallic fuel performance code". In: *Nuclear Technology* 89 (1990), pp. 183–193.

[87] B. RADHAKRISHNAN. "Modeling of Gap Closure in Uranium-Zirconium Alloy Metal Fuel–A Test Problem". In: (2009).

[88] A.A. BAUER (editor). *AN EVALUATION OF THE PROPERTIES AND BEHAVIOR OF ZIRCONIUM-URANIUM ALLOYS*. Tech. rep. Battelle Memorial Institute, 1959.

[89] J.M. FACKELMANN, A.A. BAUER, and D.P. MOAK. "LITERATURE SURVEY ON DILUTE URANIUM ALLOYS FOR SANDIA BOOSTER CONCEPT TO SANDIA CORPORATION". In: (1969).

[90] L. LEIBOWITZ and R.A. BLOMQUIST. "Thermal conductivity and thermal expansion of stainless steels D9 and HT9". In: *International Journal of Thermophysics* 9.5 (1988), pp. 873–883.

[91] H.S. KAMATH. "Recycle Fuel Fabrication for Closed Fuel Cycle in India". In: *Energy Procedia* 7 (2011), pp. 110–119.

[92] S. KAITY et al. "Microstructural and thermophysical properties of U–6wt.alloy for fast reactor application". In: *Journal of Nuclear Materials* 427.1-3 (2012), pp. 1–11.

[93] C. BASAK et al. "An evaluation of the properties of As-cast U-rich U-Zr alloys". In: *Journal of Alloys and Compounds* 480.2 (2009), pp. 857–862.

[94] P.E. ARMSTRONG, D.T. EASH, and J.E. HOCKETT. "Elastic moduli of alpha, beta and gamma polycrystalline uranium". In: *Journal of Nuclear Materials* 45.3 (1972), pp. 211–216.

[95] G. L. HOFMAN et. al. "Metallic Fuels Handbook". In: *Argonne National Laboratory Report, ANL-IFR-29* (1985).

[96] R. A. WIGELAND and T. J. MORAN. "Radial core expansion reactivity feedback in advanced LMRs: uncertainties and their effects on inherent safety". In: *Topical Meeting on the Safety of Next Generation Power Reactors, Seattle, WA* (1988).

[97] M. NAKAGAWA, H. ENDO, and M. KAWASHIMA. "Development of the core-bowing reactivity analysis code system ATLAS and its application to a large FBR core". In: *Nuclear Engineering and Design* 157.1-2 (1995), pp. 15–26.

[98] G. A. McLENNAN. "NUBOW-3D (inelastic): A FORTRAN program for the static three-dimensional analysis of bowed reactor cores, including irradiation creep and swelling". In: *Trans. Am. Nucl. Soc.; (United States)* 30 (1978).

[99] H.S. CHENG and G. J. Van TUYLE. "A simple model for radial expansion reactivity in LMRs (liquid metal reactors)". In: *BNL-NUREG-40366* (1988).

[100] J.M. CHAUMONT, D. GOUX, and L. MARTIN. "Some safety related characteristics of Phenix, a 250 MWe fast reactor 1989 and 1990 negative reactivity trip investigations". In: *ANP92: International Conference on Design and Safety of Advanced Nuclear Power Plants, Tokyo (Japan)* (1992), pp. 25–29.

[101] B. FONTAINE et al. "Description and preliminary results of PHENIX core flowering test". In: *Nuclear Engineering and Design* 241.10 (2011), pp. 4143–4151.

[102] D.C. WADE and Y. I. CHANG. "The integral fast reactor (IFR) concept: Physics of operation and safety". In: *International Topical Meeting on Advances in Reactor Physics Mathematics and Computation, April 27-30, 1987, Paris, France* (1987).

[103] D.C. WADE, R.A. WIGELAND, and D.J. HILL. "The safety of the IFR". In: *Progress in Nuclear Energy* 31.1-2 (1997), pp. 63–82.

[104] D.C. WADE. "Uncertainty reduction requirements in cores designed for passive reactivity shutdown". In: *European Organization forEconomic Cooperation andDevelopment's Nuclear Energy Agency Committee on Reactor Physics (NAECRP) Specialist's Meeting, September 23-24, 1988, in Jackson Hole, Wyoming, US* (1988).

[105] D.C. WADE. "Recent innovations in IFR safety research". In: *ARS 94' International Meeting, Pittsburg, PA, US* (1994).

[106] R.B. VILIM. "The passive response of the Integral Fast Reactor concept to the chilled inlet accident". In: *ANS 1990 Fast Reactor Safety Meeting, Snowbird, Utah, US* (1990).

[107] R. D. LEGGETT and L. C. WALTERS. "Status of LMR fuel development in the United States of America". In: *Journal of Nuclear Materials* 204 (1993), pp. 23–32.

[108] J. C. HESSON, M. J. FELDMAN, and L. BURRIS. *DESCRIPTION AND PROPOSED OPERATION OF THE FUEL CYCLE FACILITY FOR THE SECOND EXPERIMENTAL BREEDER REACTOR (EBR-II)*. Tech. rep. 1963.

[109] R. K. STEUNENBERG and L. BURRIS. *From test tube to pilot plant, a 50 year history of the Chemical Technology Division at Argonne National Laboratory*. Tech. rep. Argonne National Laboratory (ANL), Argonne, IL, 2000.

[110] T. OKAWA and E. GREENSPAN. "Feasibility of designing the encapsulated nuclear heat source reactor with negative void reactivity feedback". In: *Nuclear Technology* 160.3 (2007), pp. 257–278.

[111] YU. E. BAGDASAROV et al. "Intrinsic Safety of Future BN-800 Based Nuclear Technology". In: *Atomic Energy* 90.6 (2001), pp. 455–459.

[112] R.A WIGELAND, R.B. TURSKI, and P.A. PIZZICA. "TRADEOFF OF SODIUM VOID WORTH AND BURNUP REACTIVITY SWING: IMPACTS ON BALANCED SAFETY POSITION IN METALLIC-FUELED CORES". In: *International Topical Meeting on Sodium Cooled Fast Reactors Safety, Obninsk, Russian Federation, October 3-7* (1994).

[113] V.M. POPLAVSKY and A.M. TSIBOULIA. "Core design and fuel cycle of advanced fast reactor with sodium coolant". In: *International Conference on Fast Reactors and Related Fuel Cycles (FR09) - Challenges and Opportunities - December 7 - 11, 2009, Kyoto, Japan* (2009).

[114] S. MASSARA and D. VERWAERDE. "Physics and behaviour during a ULOF of an innovative heterogeneous annular FBR core". In: *IAEA TM on Innovative FBR, Vienna, Austria* (2012).

[115] N. DEVICTOR. "PRE-CONCEPTUAL DESIGN STUDY OF ASTRID CORE". In: *IAEA TECHNICAL MEETING ON INNOVATIVE FAST REACTOR DESIGNS WITH ENHANCED NEGATIVE REACTIVITY FEEDBACK FEATURES, Vienna, Austria* (2012).

[116] S.J. KIM, N.Z CHO, and Y.J. KIM. "A pan-shape transuranic burner core with a low sodium void worth". In: *Annals of Nuclear Energy* 27 (2000), pp. 435–448.

[117] D. SCHMITT. "Design of a Sodium-cooled Fast Reactor with innovative annular geometry and very low sodium void worth". In: *Proc. of ICAPP 2011, Nice, France* (2011).

[118] A. T. CISNEROS and E. GREENSPAN. "Feasibility of a Fast Seed High Burnup Thorium Blanket Core". In: *Presented at the 3rd International Symposium on Innovative Nuclear Energy Systems, Tokyo, Japan, October 31 November 3* (2010).

[119] J.E. DONOGHUE et. al. "Preapplication safety evaluation report for the Power Reactor Innovative Small Module (PRISM) liquid-metal reactor. Final report". In: *Office of Nuclear Reactor Regulation, U.S. Nuclear Regulatory Commission* (1994).

[120] M. KAMBE and M. UOTANI. "Design and development of fast breeder reactor passive reactivity control systems: LEM and LIM". In: *Nuclear Technology* 122.2 (1998), pp. 179–195.

[121] E. R. SPECHT et al. "Hydraulically supported absorber balls shutdown system for inherently safe LMFBRs". In: *in Proceedings of the International Meeting on Fast Reacctor Safety and Related Physics* 3 (1976), p. 683.

[122] M. J. DRISCOLL, P. HEJZLAR, and G. APOSTOLAKIS. "Optimized, Competitive Supercritical-CO2 Cycle GFR for Gen IV Service". In: *REPORT NO: MIT-GFR-045* (2008).

[123] M. TAKAMATSU et al. "Demonstration of Control Rod Holding Stability of the Self Actuated Shutdown System in Joyo for Enhancement of Fast Reactor Inherent Safety". In: *Journal of Nuclear Science and Technology* 44.3 (2007), pp. 511–517.

[124] S. NAKANISHI et. al. "Development of Advanced Loop-Type Fast Reactorin Japan (5): Adoption of Self- Actuated Shutdown System to JSFR". In: *Proc. of ICAPP 2008, Anaheim, CA, US* (2008).

[125] M. KAMBE et al. "Rapid-L Operator-Free Fast Reactor Concept Without Any Control Rods". In: *Nuclear Technology* 143.1 (2003).

[126] S. VANMAERCKE et al. "Development of a Secondary SCRAM System for Fast Reactors and ADS Systems". In: *Science and Technology of Nuclear Installations* 1 (2012), pp. 1–9.

[127] M. EDELMANN, G. KUSSMAUL, and W. VATH. "Improved fast reactor safety by passive shut-down". In: *Progress in Nuclear Energy* 29 (1995), pp. 379–386.

[128] S. V. STANKUS, R. A. KHAIRULIN, and A. G. MOZGOVOI. "Experimental study of density and thermal expansion of the advanced materials and heat transfer agents for liquid metal systems of thermonuclear reactor: Lithium". In: *Teplofizika Vysokikh Temperatur* 49.2 (2011), pp. 187–192.

[129] H.W. DAVISON. "COMPILATION OF THERMOPHYSICAL PROPERTIES OF LIQUID LITHIUM". In: *NATIONAL AERONAUTICS AND SPACE ADMINISTRATION* (1968).

[130] M. YAMADA et al. "Spatially Dense Velocity Structure Exploration in the Source Region of the Iwate-Miyagi Nairiku Earthquake". In: *Seismological Research Letters* 81.4 (2010), pp. 597–604.

[131] NIED. *Online report (retrived in march 2013)*. Tech. rep. National Research Institute for Earth Science and Disaster Prevention, 2013.

[132] M. KAMBE. "RAPID Operator-Free Fast Reactor Concept without Any Control Rods Reactor Concept and Plant Dynamics Analyses". In: *Journal of Nuclear Science and Technology* 42.6 (2005), pp. 525–536.

[133] R. G. SMITH et al. "A study of the compatibility of thermionic converter materials with caesium". In: *Journal of nuclear materials* (1963).

[134] H. OKAMOTO. "The Fe-In (Iron-Indium) system". In: *Journal of Phase Equilibria* (1990).

[135] K. NATESAN, C. B. REED, and R. F. MATTAS. "Assessment of alkali metal coolants for the ITER blanket". In: *Fusion Engineering and Design* 27 (1995), pp. 457–466.

[136] T. R. PINCHBACK and D. A. KNECHT. *The Development of Process and Storage Materials Suitable for Krypton-85 Waste Management*. Tech. rep. 1979.

[137] C. W. BALE. "The Cs-Li (Cesium-Lithium) system". In: *Bulletin of Alloy Phase Diagrams* 10.3 (1989), pp. 232–233.

[138] J. SONGSTER and A. D. PELTON. "The In-Li (Indium-Lithium) System". In: *Journal of Phase Equilibria* 12.1 (1991), pp. 37–41.

[139] F. J. SMITH. "The limits of miscibility in the lithium-potassium system". In: *Journal of the Less Common Metals* 35.1 (1974), pp. 147–151.

[140] C. W. BALE. "The Li-Rb (Lithium-Rubidium) system". In: *Bulletin of Alloy Phase Diagrams* 10.3 (1989), pp. 268–269.

[141] W. E. BROOKS. "Cesium (Cs)". In: *USGS Metal Prices in the United States Through 2010* (2013).

[142] A.C. TOLCIN. "Indium (In)". In: *USGS Metal Prices in the United States Through 2010* (2013).

[143] T. L. ROBERTS. "Global Potassium Reserves and Potassium Fertilizer Use". In: *INPNI 2008 Joint Annual Meeting* (2008).

[144] W. E. BROOKS. "Rubidium (Rb)". In: *USGS Metal Prices in the United States Through 2010* (2013).

[145] A. C. TOLCIN. "Mineral Commodity Profiles - Indium". In: *U.S. Geological Survey, Mineral Commodity Summaries, January 2012* (2012).

[146] W. C. BUTTERMAN, W. E. BROOKS, and R. G. REESE Jr. "Mineral Commodity Profiles - Cesium". In: *USGS Open-File Report 2004-1432* (2005).

[147] A. C. TOLCIN. "Mineral Commodity Profiles - Indium". In: *U.S. Geological Survey, Mineral Commodity Summaries, January 2007* (2007).

[148] A. S. BASIN and A. N. SOLOV'EV. "Investigation of the density of liquid lead, cesium, and gallium by the gamma-method". In: *Journal of Applied Mechanics and Technical Physics* 8.6 (), pp. 57–59.

[149] M. J. ASSAEL et. al. "Reference Data for the Density and Viscosity of Liquid Cadmium, Cobalt, Gallium, Indium, Mercury, Silicon, Thallium, and Zinc". In: *Journal of Physical and Chemical Reference Data* 41.3 (2012).

[150] P.L. KIRILLOV et. al. "Thermophysical Properties of Materials for Nuclear Engineering: Tutorial for students of specialty Nuclear Power Plants". In: *OBNINSK INSTITUTE FOR ATOMIC POWER ENGINEERING* (2006).

[151] Wolfram Alpha Website. *Wolfram Alpha Database at - http://www.wolframalpha.com, accessed April 2013*. Tech. rep. 2013.

[152] S. A. QVIST. "Nuclear Fuel Assembly Reactivity Control System". In: *US Patent Application Serial number 61/676,881* (2012).

[153] X-5 Monte Carlo Team. *MCNP - A General N-Particle Transport Code, Version 5*. Tech. rep. Los Alamos National Laboratory, 2005.

[154] N. E. TODREAS and M. S. KAZIMI. *Thermal Hydraulic Fundamentals 1 & 2*. Cambridge: Taylor & Francis, 1990.

[155] S-K. CHENG and N. E. TODREAS. "Hydrodynamic models and correlations for bare and wire-wrapped hexagonal rod bundles - Bundle friction factors, subchannel friction factors and mixing parameters". In: *Nuclear Engineering and Design* 92.2 (1986), pp. 227–251.

[156] S. A. QVIST. *The ADOPT code manual (rev. 2)*. Tech. rep. 2012.

[157] ASME. *Boiler & Pressure Vessel Code, Section VIII, Division 1, Subsection A, Article UG-27*. ASME. New York, 2005.

[158] V. SOBOLEV, E. MALAMBU, and H. A. ABDERRAHIM. "Design of a fuel element for a lead-cooled fast reactor". In: *Journal of Nuclear Materials* 385.2 (2009), pp. 392–399.

[159] OECD/NEA. *Handbook on lead-bismuth eutectic alloy and lead properties, materials compatibility, thermal-hydraulics and technologies*. Tech. rep. 2007.

[160] J. WALLENIUS. *Transmutation of nuclear waste*. Leadcold books and games, Stockholm, 2012.

[161] A. KISHIMOTO et al. "Solubility and Activity of Oxygen in Pb-Bi Melts". In: *Materials Transactions* 7.1 (2006), pp. 122–128.

[162] IAEA. *Thermophysical Properties of Materials For Nuclear Engineering: A Tutorial and Collection of Data*. Tech. rep. 2008.

[163] A. E. ZAIMOVSKY, A. V. NIKULINA, and N. G. RESHENTNIKOV. "Zirconium Alloys in Nuclear Power Engineering (in Russian)". In: . *Energoizdat* (1982).

[164] Y. S. TOULOUKIAN. *Thermal Expansion, Thermophysical Properties of Matter*. IFI/Plenum, New York- Washington, 2003.

[165] F. A. ROUGH. *AN EVALUATION OF DATA ON ZIRCONIUM-URANIUM ALLOYS*. Tech. rep. Battelle Memorial Institute, 1955.

[166] W. P. BARTHOLD. "Constrained nuclear design". In: *American Nuclear Society Topical Meeting, "Advanced Reactors; Physics, Design and Economics," Atlanta, Georgia, September 8-11, 1974* (1974).

[167] T. CISNEROS. "NEUTRONICS AND DEPLETION METHODS FOR PARAMETRIC STUDIES OF FLUORIDE-SALT-COOLED HIGH-TEMPERATURE REACTORS WITH SLAB FUEL GEOMETRY AND MULTI-BATCH FUEL MANAGEMENT SCHEMES". In: *Proceedings of PHYSOR 2012, American Nuclear Society* (2012).

[168] A. G. CROFF. "A versatile computer code for calculating the nuclide compositions and characteristics of nuclear materials". In: *Nuclear Technology* 62.3 (1982), pp. 335–352.

[169] R. PETROSKI, B. FORGER, and C. FORSBERG. "Evaluation of core compositions for use in breed and burn reactors and limited-separations fuel cycles". In: *Annals of Nuclear Energy* 55 (2013), pp. 151–168.

[170] M. B. TOLOCZKO, F. A. GARNWE, and C. R. EIHOLZER. "Irradiation creep and swelling of the US fusion heats of HT9 and 9Cr-1Mo to 208 dpa at 400C". In: *Journal of Nuclear Materials* 212 (1994).

[171] *Small Modular Fast Reactor Design Description*. Tech. rep. ANL / CEA / JNC, 2005.

[172] E. PITCHER. "The materials test station: A fast-spectrum irradiation facility". In: *Journal of Nuclear Materials* 377.1 (2008), pp. 17–20.

[173] J. ZHANG and N. LI. "Review of the studies on fundamental issues in LBE corrosion". In: *Journal of Nuclear Materials* 373.1-3 (2008), pp. 351–377.

[174] J. Van den BOSCH et al. "Liquid metal embrittlement susceptibility of ferritic–martensitic steel in liquid lead alloys". In: *Journal of Nuclear Materials* 376.3 (2008), pp. 322–329.

[175] A. JIANU et. al. "Creep-to-rupture tests of T91 steel in flowing Pb–Bi eutectic melt at 550 °C". In: *Journal of Nuclear Materials* 394.1 (2009), pp. 102–108.

[176] *Proceedings of the International Conference on Heavy Liquid Metal Coolants in Nuclear Technology, HLMC 1998, Obninsk, Russia*. Tech. rep. 1998.

[177] E. GREENSPAN et. al. "Innovations in the ENHS reactor design and fuel cycle". In: *Progress in Nuclear Energy* 50.2-6 (2008), pp. 129–139.

[178] Gen4Energy. *Gen4 Module Technology, 2012. Available from: http:// www.gen4energy.com/technolo* Tech. rep. 2012.

[179] J. J. SIENICKI et. al. *Status report on the Small Secure Transportable Autonomous Reactor (SSTAR) / Lead-cooled Fast Reactor (LFR) and supporting research and development.* Tech. rep. Argonne National Laboratory (ANL), Argonne, IL, 2008.

[180] T. R. ALLEN et. al. "Cladding and duct materials for advanced nuclear recycle reactors". In: *TMS JOM* 60.1 (2008), pp. 15–23.

[181] *HeLiMnet Deliverable D5.1: LFR and ADS nuclear system development: state of the art and future R& D activities*. Tech. rep. ENEA, 2012.

[182] D. De BRUYN, S. LARMIGNAT, and A. W. HUNE. "Accelerator Driven Systems for Transmutation: Main Design Achievements of the XT-ADS and EFIT Systems within the FP6 IP-EUROTRANS Integrated Project". In: *Proceedings of ICAPP 10, San Diego, CA, USA, June 13-17* (2010).

[183] M. BANDINI et. al. "Preliminary T/H and transient analyses for EFIT reactor design". In: *Proceedings of ICAPP 07, Nice, France* (2007).

[184] A. V. ZRODNIKOV, G. I. TOSHINSKY, and O. G. KOMLEV. "SVBR-100 module-type fast reactor of the IV generation for regional power industry". In: *Journal of Nuclear Materials* (2011).

[185] V. Y. ABRAMOV. "Corrosion and mechanical properties of BREST-OD-300 reactor structural materials". In: *Proceedings of the 11th International Conference on Nuclear Engineering, Tokyo* (2003).

[186] A. NAGATA, N. TAKAKI, and H. SEKIMOTO. "A feasible core design of lead bismuth eutectic cooled CANDLE fast reactor". In: *Annals of Nuclear Energy* 36.5 (2009), pp. 562–566.

[187] M. TAKAHASHI, S. UCHIDA, and Y. KASAHARA. "Design study on reactor structure of Pb–Bi-cooled direct contact boiling water fast reactor (PBWFR)". In: *Progress in Nuclear Energy* 50.2-6 (2008), pp. 197–205.

[188] H. SEKIMOTO et. al. "Long-life small reactor for developing countries, "LSPR"". In: *Proceedings of the International Seminar on Status and Prospects for Small and Medium Sized Reactors, Cairo, Egypt* (2001).

[189] J-Y. LIM and M-H. KIM. "A new LFR design concept for effective TRU transmutation". In: *Progress in Nuclear Energy* 49.3 (2007), pp. 230–245.

[190] H. M. SON and K. Y. SUH. "Evolutionary design of reactor vessel assembly for liquid metal cooled battery". In: *Progress in Nuclear Energy* 53.7 (2011), pp. 825–830.

[191] S. CHOI et al. "Long burning small modular reactor based on natural circulation". In: *Nuclear Engineering and Design* (2011).

[192] J. WALLENIUS. "ELECTRA-FCC: a centre for Generation IV system research and training". In: *Proceedings of the ELECTRA workshop presentations, Stockholm, Sweden* (2012).

[193] I. V. DULERA et al. "Compact High Temperature Reactor (CHTR)". In: *BARC NEWSLETTER* (2006).

[194] P. HOSEMANN et al. "The design, setup and operational testing of the irradiation and corrosion experiment (ICE)". In: *Journal of Nuclear Materials* 376.3 (2008), pp. 392–395.

[195] S. A. QVIST et al. "Capability demonstration of simultaneous proton beam irradiation during exposure to molten lead–bismuth eutectic for HT9 steel". In: *Nuclear Instruments and Methods in Physics Research Section A: Accelerators, Spectrometers, Detectors and Associated Equipment* 698 (2013), pp. 98–105.

[196] *Handbook on LeadBismuth Eutectic Alloy and Lead Properties, Materials Compatibility, Thermal-hydraulics and Technologies*. Tech. rep. OECD/NEA, 2007.

[197] P. HOSEMANN et. al. "Characterization of oxide layers grown on D9 austenitic stainless steel in lead bismuth eutectic". In: *Journal of Nuclear Materials* 375.3 (2008), pp. 323–330.

[198] P. HOSEMANN et. al. "Structural, electrical and magnetic measurements on oxide layers grown on 316L exposed to liquid lead–bismuth eutectic". In: *Journal of Nuclear Materials* 421.1-3 (2012), pp. 140–146.

[199] B. F. GROMOV et. al. *Use of Russian Technology of Ship Reactors with lead-bismuth coolant in nuclear power, On the basis of authors reports at Conference on Heavy Liquid Metal Coolants in Nuclear Technologies (HLMC-98), Obninsk, Russia.* Tech. rep. 1999.

[200] N. LI et al. *Corrosion Test of US steels in lead-bismuth eutectic (LBE) and kinetic modeling of corrosion in LBE systems*. Tech. rep. LA-UR-02-2028, 2002.

[201] P. HOSEMANN et al. "Corrosion of ODS steels in lead–bismuth eutectic". In: *Journal of Nuclear Materials* 373.1-3 (2008), pp. 246–253.

[202] V. ENGELKO et. al. "Surface modification/alloying using intense pulsed electron beam as a tool for improving the corrosion resistance of steels exposed to heavy liquid metals". In: *Journal of Nuclear Materials* 415.3 (2011), pp. 270–275.

[203] J. ZIEGLER. *SRIM Monte Carlo software (http://www.srim.org)*. Tech. rep. 2011.

[204] V. SOBOLEV. "Thermophysical properties of lead and lead-bismuth eutectic". In: *Journal of Nuclear Materials* 362.2-3 (2007), pp. 235–247.

[205] D.B. PELOWITZ. *MCNPX Users Manual, LA-CP-07-1473, version 2.60*. Tech. rep. Los Alamos National Laboratory, 2008.